Direct-Write Electrospinning of Highly-Loaded Ceramic Slurries for Additive Manufacture

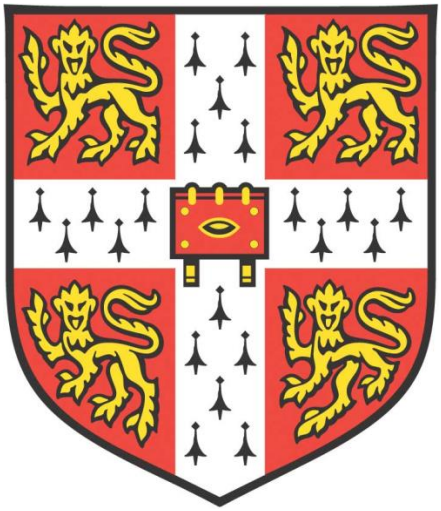

Jonathan Peter Waite

Clare College

Institute for Manufacturing

Department of Engineering

University of Cambridge

This dissertation is submitted for the degree of Doctor of Philosophy

September 2018

DECLARATION

This dissertation is the result of my own work and includes nothing that is the outcome of work done in collaboration except where specifically indicated in the text.

It is not substantially the same as any that I have submitted, or is being concurrently submitted, for a degree or diploma or other qualification at the University of Cambridge or any other University or similar institution. I further state that no substantial part of my dissertation has already been submitted, or is being concurrently submitted, for any such degree, diploma or other qualification at the University of Cambridge or any other University or similar institution.

In accordance with the Department of Engineering guidelines, this thesis does not exceed 65,000 words and it contains less than 150 figures.

Signed:

_____

Date:

_____

Jonathan Peter Waite, Master of Engineering

University of Cambridge

DIRECT-WRITE ELECTROSPINNING OF HIGHLY-LOADED CERAMIC SLURRIES FOR ADDITIVE MANUFACTURE

Jonathan Peter Waite

ABSTRACT

Ceramics are desirable materials for a range of mechanical, electrical and biomedical applications, but they can be difficult to form and process. Additive manufacture is increasingly being explored for producing ceramic parts without moulds. In this work, a method for controllably patterning filaments containing high volume fractions of ceramic particles was explored, using electrospinning as the deposition method.

Inks containing 50 vol% alumina powder in mineral oil or wax were deposited from a 200 μm inner diameter blunt, grounded needle at distances from 0.5 to 5.0 mm from a conductive plate with positive voltages of up to 10 kV applied to it.

For the oil-based ink, jets with widths down to 25 μm were produced and an empirical relationship between the minimum jet width, nozzle height, flow rate and voltage was established. An average electric field of 2.0-2.5 kV/mm was found to give the most stable jets. The substrate speed was found to have a major effect on the jet width and entirely determine the deposit diameter due to the ink still being molten upon impact, as predicted by thermal modelling.

Patternable features were explored with the wax-based ink. It was found that filaments deposited within 0.5 mm of each other would be attracted together and that the ability to bridge gaps was limited. Sharp corners were rounded to a radius of 0.4 mm, with deviations up to 2 mm from the corner. Investigation was constrained by the speeds achievable with the motion platform used, resulting in filament diameters around 100 μm.

Several lattices produced by this process were successfully sintered to pure alumina, although little consolidation was achieved and the filaments were very porous. These samples had approximately 15 % of the strength expected if they were made of solid alumina.

ACKNOWLEDGEMENTS

I first want to thank my supervisor, Professor Ian Hutchings, for all the time, effort and critical thought he has put into this thesis. I am very grateful to the KACST partnership with the University of Cambridge for funding this work, and to the Worshipful Company of Engineers for their financial support. I also want to thank my colleagues at the Institute for Manufacturing for their help with my experiments, particularly Dr Ronan Daly.

I am so grateful to my mother, Kathrin, and my grandparents, Roy and Audrey, for their love and support throughout my university career, and indeed throughout my life. Last, but definitely not least, I want to thank Esther for her love, encouragement and advice, in this and all things.

CONTENTS

LIST OF TABLES

List of Figures

LIST OF SYMBOLS

Symbols

A	Maximum solid volume fraction; Area
c	Specific heat capacity
D	Diameter
d	Distance between axes
E	Electric field; Young's modulus
F	Force
g	Acceleration due to gravity; Edge-to-edge gap
G'	Storage modulus
G''	Loss modulus
h	Convective heat transfer coefficient
I	Second moment of area
k	Thermal conductivity
K	Electrical conductivity
L	Latent heat of fusion; Length
m	Mass
N	Contact ratio
Nu	Nusselt number
Pr	Prandtl number
Q	Volume
q	Thermal energy
r	Radius
Ra	Rayleigh number
s	Centreline spacing
t	Time
T	Temperature
w	Minimum jet width
y	Distance from neutral axis
α	Thermal diffusivity
β	Thermal expansion coefficient
γ	Surface tension
δ	Displacement
ε	Emissivity; Permittivity
ε_0	Permittivity of vacuum
θ	Angle
μ	Dynamic viscosity
ν	Kinematic viscosity; Velocity
ρ	Density
σ	Stefan-Boltzmann constant; Stress
ϕ	Volume fraction

Non-standard units

1 L = 1 dm^3

1 mL = 1 cm^3

vol%	Volume percentage
wt%	Weight percentage
wt/wt%	Weight percentage based on the weight of another ingredient of a mixture

LIST OF APPENDICES

1 INTRODUCTION

Additive manufacturing (AM) is a family of technologies that are creating new routes in almost every area of manufacture. Their defining trait is that they create physical geometries by adding material, rather than removing it from a larger piece, but they have other common features. For example, there is no use of moulds or masks, allowing for economical production of small numbers of parts and individual customisation. As they are computer-controlled processes, the actual manufacture is automated and human interaction is only needed for ancillary operations. They are capable of easily producing internal as well as external geometries of a complexity that would be difficult, time consuming or impossible with conventional techniques. However, these processes have other common traits such as being relatively slow and producing parts with material properties that are inferior compared to the same materials processed with other methods, although these areas are being improved.

AM is a broad category of process and covers a similarly broad range of materials. Polymers are very widely used and are the basis of many of these technologies, including the oldest methods. Metals are also well utilised, although with more limited options. However, ceramics are still a niche material, despite the potential for excellent performance in certain applications.

The term ceramic covers a variety of different materials such as clays and concrete, but this work focuses on what will be referred to as ‘technical ceramics’. All ceramics share some characteristics, including good mechanical properties at high temperatures, high hardness and brittleness. Technical ceramics are those with most applicability in engineering as they have the highest strengths and service temperatures. They are usually simple metallic compounds such as oxides, nitrides and carbides. Notable examples are aluminium oxide, zirconium oxide, silicon nitride and tungsten carbide. Arguably porcelain could fit into this category as it is widely used, e.g. for high voltage isolation components. However, as a clay-based material which undergoes an irreversible chemical change during production, processing it is very different to the other mentioned ceramics and so it will not be considered here.

The properties of technical ceramics give them relevance in a number of areas. Their high melting points and temperature stability is of great use in heat engines, where higher temperatures lead to higher thermodynamic efficiencies. Their high hardness is useful for cutting and grinding tools, as well as bearing surfaces, where they give longer component lives than metals or polymers. However, technical ceramics are not very prevalent in practice, partly because these same desirable properties make them very difficult or expensive to form into useful parts. Their brittleness also leaves them sensitive to impact and tension loads, requiring more care in the handling and use of ceramic components.

We can add materials like hydroxyapatite (HA), which is a form of calcium phosphate, to our definition of technical ceramics. HA has a unique application in producing artificial biological hard tissues, i.e. bone, which can seamlessly integrate with existing tissue. This has several advantages over implants made of other materials, but primarily it gives much more secure attachment. Another ceramic with a specific engineering use is lead zirconate titanate (PZT), a common piezoelectric material that is widely used in transducers and sensors. Processing these functional materials by AM presents the opportunity for easy production of individually tailored parts and components with complex interiors, such as lattices with variable pores.

The main objective of this research is to develop a novel AM method for patterning technical ceramics to allow for their wider use and enabling geometries that are more advanced, improving performance in existing applications and making these materials a viable option for others.

1.1 Research aims

To achieve the objective of this work we will develop an extrusion-based direct writing system to deposit ceramic powder in a fluid carrier and binder material as a specially formulated ink. Electrospinning will be combined with this process to reduce the minimum feature size the system can produce.

1. **Create a system capable of producing patterns with high resolution**

The common Fused Deposition Modelling (FDM) 3D printers currently have difficulty using nozzle diameters smaller than around 200 µm due to the large pressures created by forcing a viscous molten polymer through such a small orifice. Powder bed AM systems typically also have track widths around 100 µm, limited by factors such as particle size and the spread of binder or heat. Therefore, to improve on existing techniques the system developed here should provide a resolution smaller than 200 µm.

2. **Formulate a suitable ink**

The material being deposited by the system, comprising ceramic powder, a carrier fluid and additives, has many conflicting requirements. Our ultimate aim is to produce a solid part, so maximising the ceramic content of the ink is of great importance. However, to produce fine features we need the ink to flow freely and not have an excessive viscosity. Further to these opposing needs, the shape of the ink must be fixed shortly after leaving the nozzle and the part must retain its shape while the carrier is removed and the powder bonded together. The large electric field needed for electrospinning also requires the ink to have low conductivity. Easy handling and stability during storage are also desirable. Suitable ingredients must be identified, the mixture optimised and the resulting ink characterised. Of particular interest are its

response to the high and low shear, as will be seen in the nozzle and due to self-weight once deposited respectively.

3. Investigate electrospinning conditions

Electrospinning uses a simple experimental setup but the physics is complex and involves many variables. Trying to understand and predict the results from theory alone is beyond the scope of this work, especially when considering the behaviour as the jet hits a moving substrate. An operating window for this process must be established, the limiting factors identified and recommended conditions under which to carry out subsequent work should be identified. The properties of the ink will have a significant effect on the behaviour of the electro-jet and so this aim is closely coupled with the previous one.

4. Investigate patterning ability

Once the deposition mechanism is finalised and understood it needs to be translated into a method of direct writing. The nature of electrospinning, particularly the distance between the nozzle and substrate, mean that there will be some limits on what geometries can be produced. Exploring these limits is key to determining the usefulness of the process and the most suitable applications.

5. Produce pure ceramic parts

For the shapes produced by the process to be of use, they must be converted to pure ceramic with the binder and carrier components removed. This will be done through sintering and will cause a combination of shrinkage and porosity, possibly leading to shape changes and cracking. The viability of the sintering step needs to be verified and the resulting effects on the parts quantified.

1.2 Thesis outline

Chapter 2 gives a more detailed background to this research, including an overview of the more prominent AM technologies. It reviews the literature covering existing ceramic AM processes and electrospinning in particular. In Chapter 3, simulation and modelling will be used to make some predictions about important parameters of the

process, informing its viability. Chapter 4 documents and discusses the custom apparatus developed for this work and used for the later chapters. The experimental work begins in Chapter 5 with the optimisation of the inks for deposition, including model inks, trial compositions and the final ink selected for ceramic part production. Chapter 6 analyses the behaviour of these inks when electrospun, characterising their response to different conditions and thus identifying a preferred operating region for use in the direct writing process. Direct writing is investigated in Chapter 7, particularly how the nature of electrospinning affects the patterning ability compared to other processes. Chapter 8 covers converting the shapes produced in Chapter 7 to final, pure ceramic parts and provides verification of the products. Chapter 9 summarises the results of the thesis and discusses options for future work.

2 BACKGROUND

This chapter gives the context for the present work and consider the relevant available literature. It will cover the wider field of additive manufacture, including several existing methods for using ceramics, discuss the electrospinning process and describe some conventional ceramic manufacturing techniques. Finally, an overview of the full process developed in this work will be given.

2.1 Additive manufacture

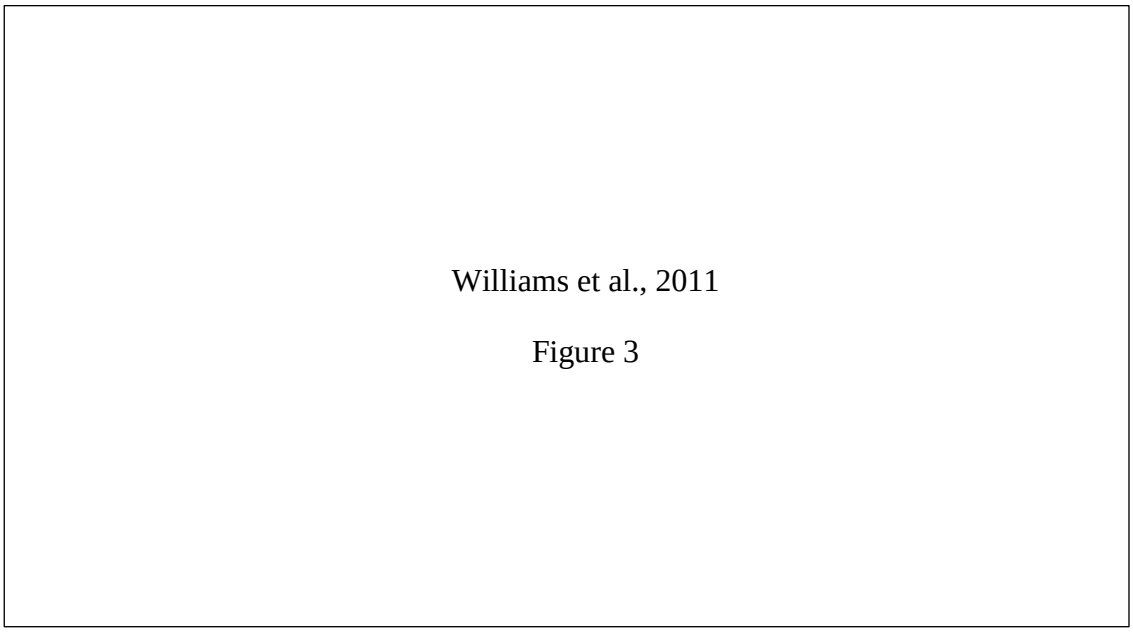

Figure 2.1 Morphological matrix for AM processes (Williams et al., 2011).

Additive Manufacture (AM) has been used in manufacture since the early 1980s as a method for producing prototypes. It is increasingly being used for producing end-use parts, a transition that in part relied on the many new AM methods that have been developed. In order to group these processes, various classification schemes have been proposed (Hon et al., 2008; Medellín-Castillo and Pedraza Torres, 2009). Different

classification schemes focus on different characteristics, such as material phase or deposition method. One of the most useful classifications was presented by Williams et al. (2011). They identified the major sub-functions required for an AM process and the common techniques for achieving these, then compiled them into the matrix shown in Figure 2.1. Any existing AM process can be described by drawing a line connecting a box from every row. This concept is most useful for identifying similarities in process, such as Selective Laser Melting and Electron Beam Melting, or for conceptualising new AM processes.

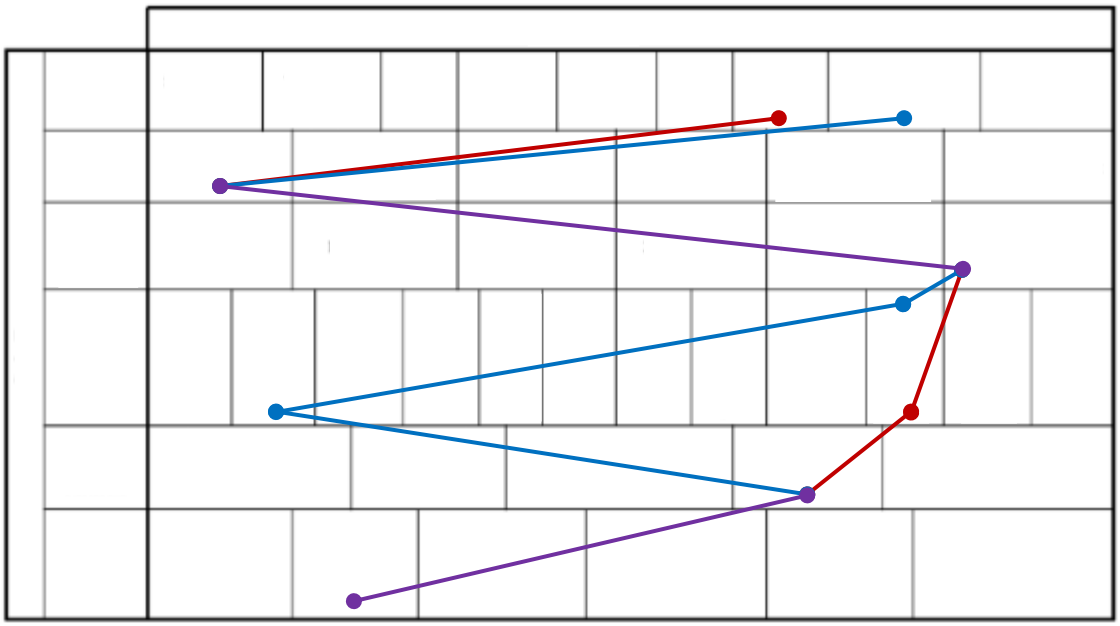

Figure 2.2 Completed Williams matrix for this process (blue) and FDM (red), with purple lines indicating overlap between the two processes. Modified from (Williams et al., 2011).

An example of using the matrix is shown in Figure 2.2, where FDM and the electrospinning process developed in this work are mapped out. We can see the similar shapes the processes trace out, and where the lines of the different processes meet there is an opportunity for knowledge transfer leading to process improvements. One criticism of this matrix is that the sub-function labels are rather abstract. This is because the matrix is a high-level tool designed to cover a range of processes with very different details, but exact knowledge of the definition is required for proper use. There

is also some overlap between categories; for example, a laser can be either a light source or a heat source depending on how it is utilised and the ‘Create Primitive’ row contains both ‘Freeze’ and ‘Solidify melt’, which are fundamentally the same process. Despite this the matrix is currently one of the most developed and informative classifications.

There are many different AM processes now in existence. Many are variations on previous processes and trace the same path on the Williams matrix. For example, Precision Extrusion Deposition (PED) (Hamid et al., 2011) is very similar to FDM, but instead of using a filament of polymer, PED uses granules fed by a screw extruder. There are several reviews of these techniques which usually focus on one application, such as micro-scale AM (Vaezi et al., 2013), ceramic materials (Travitzky et al., 2014) or direct material addition methods (Hon et al., 2008). Table 2.1 is taken from one such review, giving examples of the feature sizes attainable with current ceramic direct writing.

Lewis et al., 2006

Table 1

Table 2.1 Summary of direct writing methods using ceramic materials (Lewis et al., 2006).

Of these methods, only four achieve a minimum feature size of less than 100 μm. First there are inkjet based methods, using a volatile solvent with 14 vol% solids (Zhao et al., 2002) or a molten wax with 40 vol% solids (Reis et al., 2005). While drop-on-demand inkjet has many advantages, such as high resolution and up to thousands of

nozzles working in parallel, it has some significant disadvantages for AM applications. The drops tend to spread significantly, leading to very thin layers. This derives partly from the fact that the ink must fall within a tight range of viscosities and surface tensions, which prevents the use of high viscosity or gelatinous inks that will not slump. This also limits the maximum solid loading, keeping the rate at which solid material can be deposited low.

The alternative approach is to deposit filaments or lines of ink directly from a nozzle. Micropen writing is claimed to achieve 25 μm, but the paper referenced by Table 2.1 actually demonstrated using a nozzle of 8 mil (200 μm) to deposit continuous tracks of approximately 1000 μm width (Morissette et al., 2001). The Micropen system has nozzles available down to 25 μm, which may have caused the confusion (King et al., 1999). On the other hand, work by Lewis et al. (2006) with nanoparticle gels did achieve a line width down to 30 μm using 50 vol% solids, but they report frequent nozzle blockages at this resolution. Therefore, they were only able to extrude for long enough to produce 2D patterns, instead using a 100 μm nozzle for 3D objects. Due to their continuous flow and tolerance of higher solid loadings, filament methods can likely achieve higher build rates than inkjet methods. This is especially true in the vertical direction, as the inks used in filament methods usually retain their cross-section during deposition. Filaments also lend themselves to building smooth-walled objects and have the potential to bridge gaps without supporting material, whereas inkjets can only deposit onto existing material. On the other hand, point features such as narrow columns are more challenging for filament methods.

2.1.1 Ceramic Additive Manufacture

2.1.1.1 Extrusion Free-Forming

Fused deposition modelling (FDM) is one of the most widely used forms of additive manufacture for several reasons, including low cost, low waste and simplicity. As shown in Figure 2.3, complex 3D objects are built layer-by-layer with molten polymer deposited through a small nozzle. The resulting parts can be weaker than the bulk

polymer due to poor inter-layer bonding and their sparse interior structure. Very similar methods to FDM include Precision Extrusion Deposition (PED), which replaces the polymer filament feedstock with pellets driven by a rotating screw (Shor et al., 2005), or replacing the molten polymer with a monomer liquid that polymerises instead of freezes (Lombardi and Calvert, 1999). These techniques can all be categorised as Extrusion Free-form Fabrication (EFF), a method of solid free-form fabrication characterised by patterning lines of material directly from a nozzle.

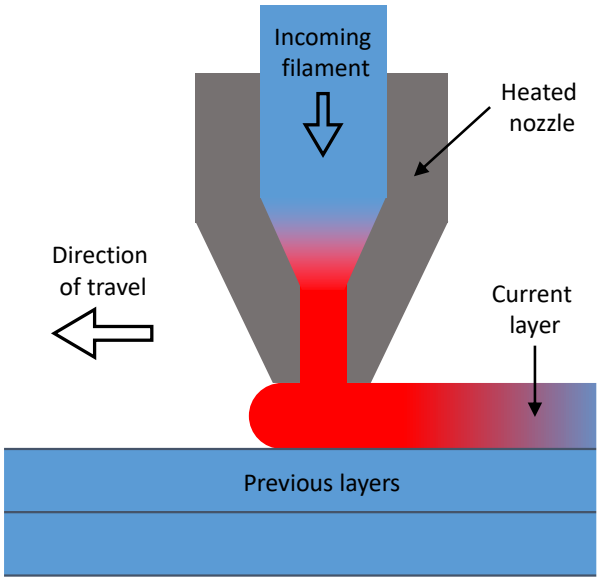

Figure 2.3 Schematic of Fused Deposition Modelling. A polymer filament is pushed into the heated nozzle as the nozzle traces the shape of the current layer, then the nozzle is raised for the next layer. Red indicates molten polymer whereas blue indicates solid polymer. Note the constraint of the molten polymer by the nozzle.

Methods have been developed to allow an EFF system to pattern materials other than plastics. Fused Deposition of Ceramics (FDC) is most similar to FDM, only adding a high volume fraction of ceramic particles to the polymer filament (Bellini, 2002; Jafari et al., 2000). Multiphase Jet Solidification (MJS) carries powdered ceramics or metals in wax or a low-melting point metal alloy, but feeds from a cartridge rather than a spool of filament (Greulich et al., 1995). This puts a tighter limit on print volume but avoids the difficulties of producing a consistent filament.

The core principle of these processes is to use a polymer as a carrier for particles of the desired material. This allows the patterning of materials with higher melting points at less than a few hundred degrees Celsius. The particles could be metallic, ceramic or indeed another polymer with a higher melting point. The resulting shape, usually described as a 'green body', must have the binder removed and then undergo sintering to produce the final part. This obviously adds extra steps and potentially significant time to the process, as well as introducing the potential for part failure during de-binding and sintering from the shrinkage that occurs as the powder consolidates. There is also often difficulty in producing fully consolidated parts, as will be discussed in Section 2.3.2.

These processes are still limited by the problems of the original FDM process, such as difficulty using fine nozzles and the need for support material to be added below overhanging geometry. Nozzle diameter is particularly likely to be an issue, as conventional FDM machines typically use nozzles with an inner diameter of 0.4 mm and are generally no smaller than 0.2 mm. Below this the pressure drop through the nozzle becomes problematic for the feed mechanism and it is more likely impurities will cause a blockage. Adding a solid filler will increase the viscosity of the molten material and the particles themselves can cause blockages.

2.1.1.2 Robocasting

While using the same principles as the previously mentioned EFF methods, Robocasting (RC) is different in two ways. First, it is one of few AM process developed for and commonly used with ceramic materials. Second, it uses gelation instead of freezing to lock deposited material in shape. The latter point makes it particularly useful for biological applications, as the low temperatures allow for the incorporation of proteins or live cells.

Usually the gelation of the ink is reversible and due to the entanglement of large molecules in the ink. The lack of a drastic change in properties seen during freezing means the inks used in RC must be carefully formulated. When under high shear the ink needs to have low viscosity so that it can easily pass through fine nozzles, but once

stationary the viscosity must be very high to retain the shape, i.e. the ink should be strongly shear-thinning (Smay et al., 2002). Ideally, the ink will also have a high enough yield stress that there is negligible flow due to gravity or surface tension. Typically, the desired rheology will be achieved with an organics content of only a few percent of the mass of ceramic. This means that after drying there is little material to be burnt out if the part is sintered.

Alternatively, gelation may be induced by a chemical reaction. This is normally an irreversible change and allows for a more drastic transition of ink properties, potentially giving better results. The disadvantage is the requirement for mixing two components in the deposition process, either just before the nozzle (Morissette et al., 2000) or by extruding into a liquid bath containing the gelation agent (Gratson and Lewis, 2005).

The resolution of RC is determined by the internal diameter of the nozzle, as with other EFF methods. With the comparatively low viscosity of the inks used, the limiting factor is usually the particle size, rather than the pressure drop as with polymer melts. It has been found empirically that problems begin to occur when the particle to nozzle diameter ratio is below 1:100 (Nadkarni and Smay, 2006, p. 103). Beyond this point, deposition becomes inconsistent and clogging is likely to occur.

2.1.1.3 Powder-bed processes

This category of AM processes builds the object in a bed of powder. A layer of the object is fused, and a new layer of powder deposited on top. One arrangement for achieving this is shown in Figure 2.4. This has the major benefit of the un-fused powder fully supporting the object during the build process. However, this excess powder must be removed to free the object, which can be a messy and hazardous task that will inevitably waste powder. Any powder-bed process will have a resolution limited by the particle size of the powder. As the particle size is reduced, electrostatic and Van der Waals forces cause it to agglomerate, which hinders even recoating, and it becomes difficult and possibly hazardous to handle.

The powder can be fused by one of two methods: directed energy beams or binder addition. The energy beam usually takes the form of a laser (or an electron beam for metals) with high energy density that directly melts the powder to fuse it. The melting can be limited to the surface of the particles as in the (misnamed) Selective Laser Sintering (SLS), creating a porous body that needs further sintering or infiltrating with a lower-melting point material to produce a fully solid final product. With different parameters, the melting can be complete and leaves a continuous track of solid material. This is called Selective Laser Melting (SLM) and results in higher density, stronger parts, but the large temperature gradients and freezing of the melt pool can cause stresses within the part. The use of these techniques with metals is the subject of much research (Gu et al., 2012).

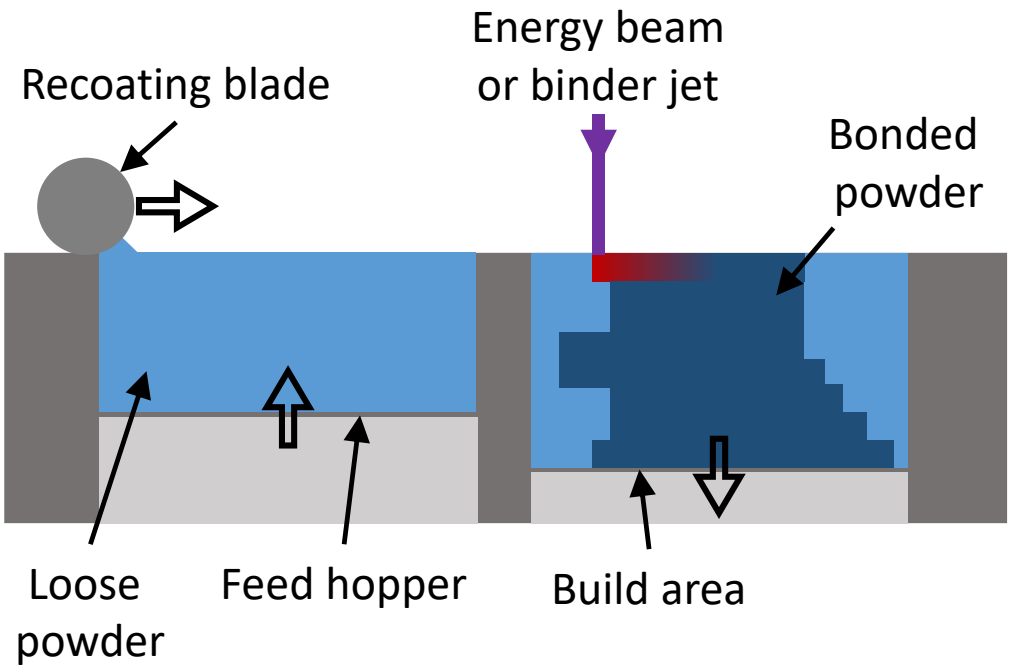

Figure 2.4 Schematic of a generic powder-bed process. The build area moves down one layer thickness and the feed hopper moves up, then the recoating blade scrapes a layer of loose powder over the top of the build area. An energy beam or jet of binder bonds the powder into the shape of that layer, then the process repeats until the full object is built.

When working with high-melting point materials the bed of powder is often heated to near its melting point to reduce the energy that needs to be delivered by the laser, which

increase build speed and reduces thermal differentials, decreasing residual stress. With metals, an inert atmosphere or vacuum may be used to prevent oxidation of the hot powder. The resolution of the process is determined by the width of the melt pool, which is affected by many variables such as laser power and the thermal conductivity of the powder, as well as powder size.

SLM is more difficult for ceramics than for metals due to their brittle nature. In metals, stress from thermal gradients can be relieved by plastic deformation, but in the same situation, a ceramic will tend to fracture. This requires the powder bed to be heated to a greater proportion of the material's melting point, which for technical ceramics is usually in excess of 1,000 ^{o}C. This leads to much higher power consumption and challenges in producing a powder recoating mechanism that can operate in these conditions.

The alternative binder addition method is most often performed with an inkjet print head passing over the powder surface that deposits the binder under computer control. The clear advantage is the lack of thermal gradients during the build process, leaving the part stress-free and with accurate dimensions. The same machine is capable of working with a wide range of powders, whereas a laser will be optimised for absorption by specific types of material. Furthermore, higher build rates can be achieved by using wider inkjet heads, which is much simpler than trying to coordinate multiple lasers. The disadvantage is that, at least for high melting point materials, the 'green' part must be sintered to bring it to full density and strength, adding a long post-processing step. The powder bed is sometimes heated, but only to control the moisture content of the powder and enhance binder cure. Difficulties in this approach arise in ensuring the binder penetrates into the powder but does not spread too far due to capillary action.

2.1.1.4 Laser Powder Forming/Laser Engineered Net Shaping

There are several names for this technique, which uses a deposition head containing a laser and powder delivery system aimed at the same point in space. When building an object, the laser provides energy to create a melt pool into which the arriving powder melts. As the head moves, the deposited material cools and solidifies, with the

incoming powder replenishing the melt pool. The process is comparable to FDM, in that a nozzle moves through space heating and depositing material that then freezes. These techniques are unusual in that they are used to add material to an existing part, for example to build up an area for repair. They suffer from the same thermal stress issues as SLM but heating the material out of the deposition zone is more difficult. Ceramics can be used with this process but are usually mixed with a metal to produce a composite material that avoids the brittleness and poor resistance to thermal shock of pure ceramic.

2.1.1.5 Stereolithography

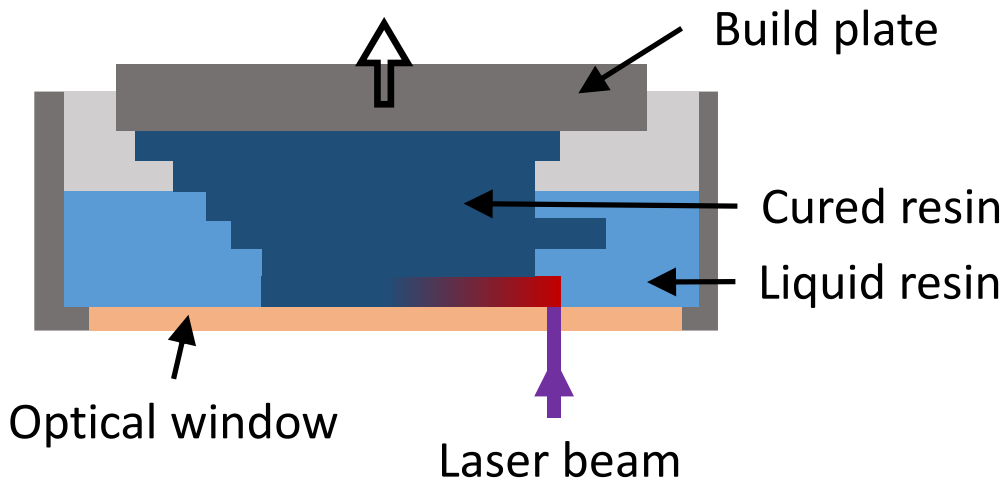

Figure 2.5 Schematic of a stereolithography process. The resin is selectively cured by the laser and then the build plate is raised, allowing liquid resin to flow in ready for the next layer.

Stereolithography (SLA) uses a photo-reactive polymer resin that is selectively cured by an ultraviolet light source, either a scanned laser or a projected image. Layer heights are set by controlling the thickness of the liquid layer between the light source and the previous layer, as seen in Figure 2.5. One of the difficulties with the process is recoating the layer of liquid resin, which is usually quite viscous. SLA can be adapted for use with metals (Lee et al., 2006) or ceramics by adding a fine powder to the resin (Griffith and Halloran, 1996). This increases the viscosity, exacerbating the recoating issue, and the opacity, limiting the layer thickness and build rate. As with many of the

other methods discussed here, SLA produces a green body that requires de-binding and sintering to produce the final part.

2.2 Electrospinning

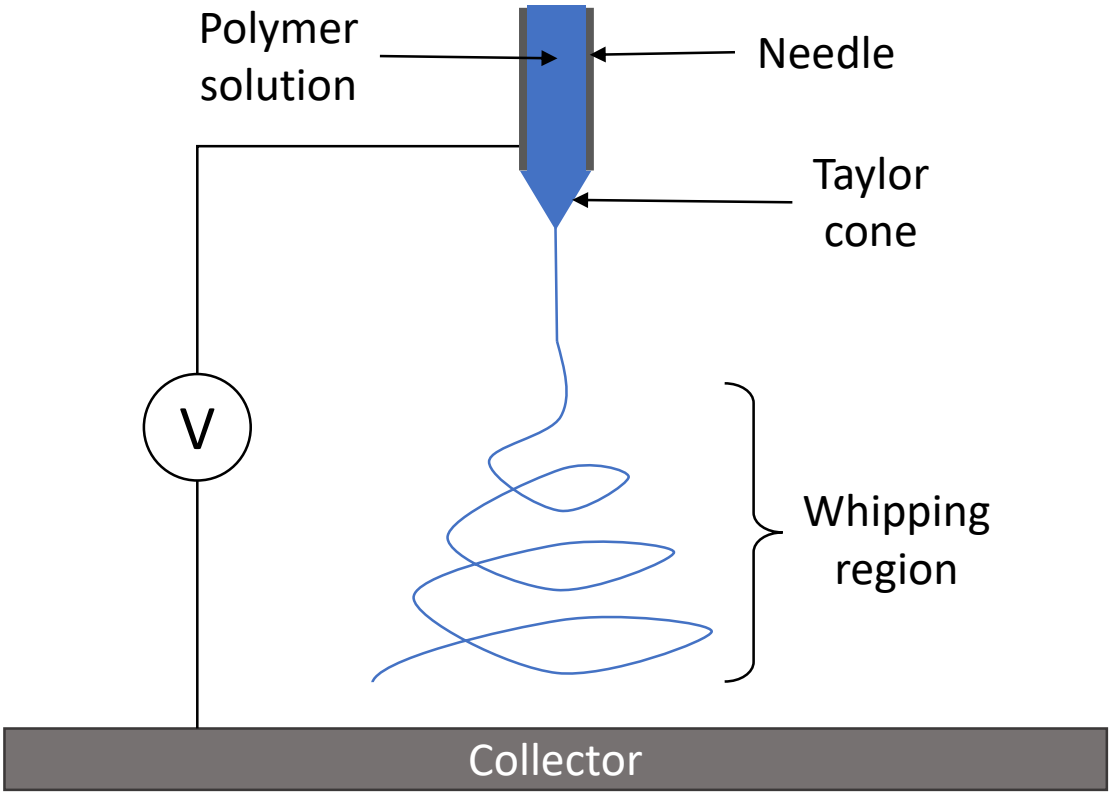

Figure 2.6 A typical electrospinning setup with a whipping filament of polymer solution.

Electrospinning has been described in published literature for many decades, the phenomenon being first investigated over a century ago (Zeleny, 1914) and applied practically since the 1930s (Anton, 1934). The core principle is the stretching and thinning of a liquid filament due to an electric field in an arrangement similar to Figure 2.6, with the 'Taylor cone' formed at the nozzle being a defining feature. In practice, the apparatus is often a hollow metal syringe needle pointed at a conductive plate with a separation on the order of 1 to 100 mm. A potential difference in the range of 1 to 30 kV is applied between the two, and sometimes a flow rate is imposed on the ink. The shape and path the fluid takes as it travels between the electrodes depends on the

parameters of the experiment and has several distinct forms, but the term ‘electrospinning’ is usually used to describe the needle ejecting a straight and continuous filament of liquid. The filament becomes thinner than the internal diameter of the nozzle and it may begin to whip in a circular motion, causing further stretching.

2.2.1 Modes

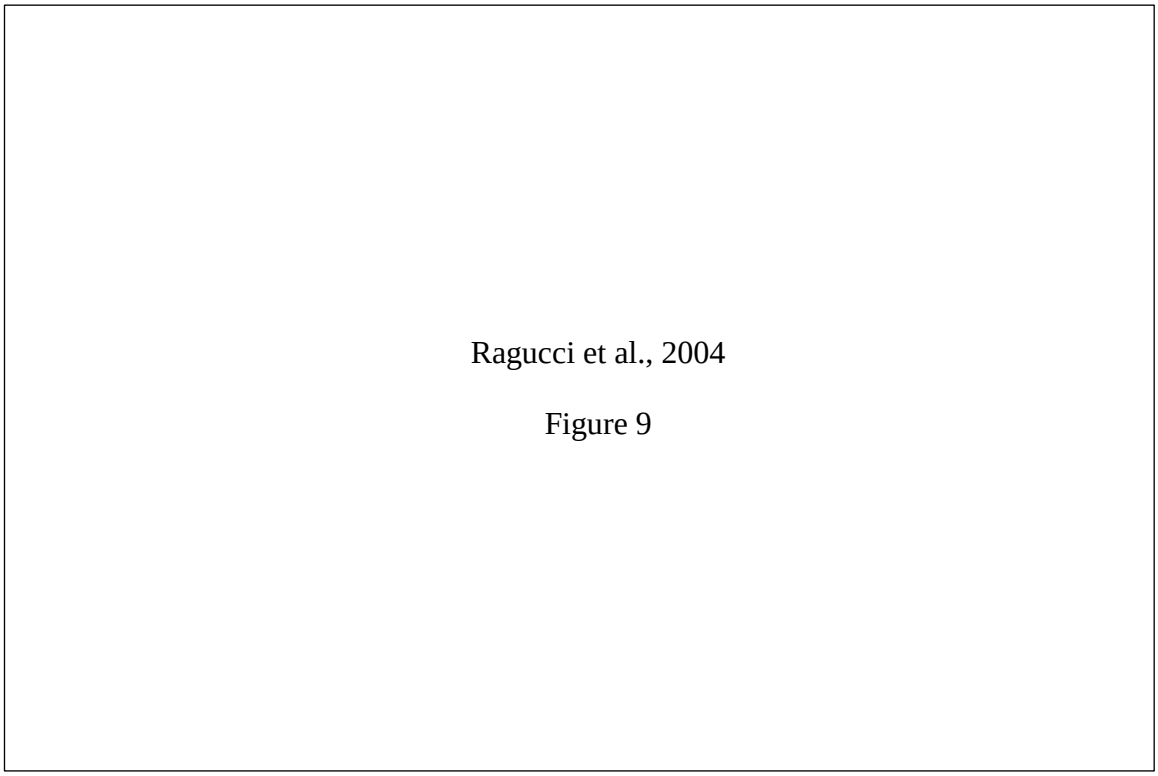

Figure 2.7: Operating map of electro-jetting modes for heptane with a conductivity additive (Ragucci et al., 2004).

The same experimental setup can generate several different electrohydrodynamic behaviours. Only a subset of these behaviours may be achieved in a given experiment and their order of appearance can vary, making it useful to plot ‘operating maps’ of how the jetting mode varies with flow and voltage (Shin et al., 2001). These maps can be quite complex with the area of interest being relatively small, such as the ‘Taylor cone-jet’ mode on the left of Figure 2.7. The easiest distinction that can be made is between the steady state ‘jet’ modes and the pulsating modes, which often involve dripping. Within the steady jet modes, there can be a single jet or multiple jets issuing from the

nozzle, multiple jets being seen at higher electric fields. The mode of interest for this work is usually referred to as a 'cone-jet', in reference to the distinctive Taylor cone formed at the nozzle with a jet emitted from its point. The exact distinctions and names for each mode have caused confusion in the past (Cloupeau and Prunet-Foch, 1994). Ragucci et al. (2004) showed that the polarity of the nozzle affects the shape of the operating map, with a nozzle that is negative with respect to the substrate needing higher voltages to achieve the same modes, but giving a wider voltage range for a given mode compared to a positive nozzle for heptane.

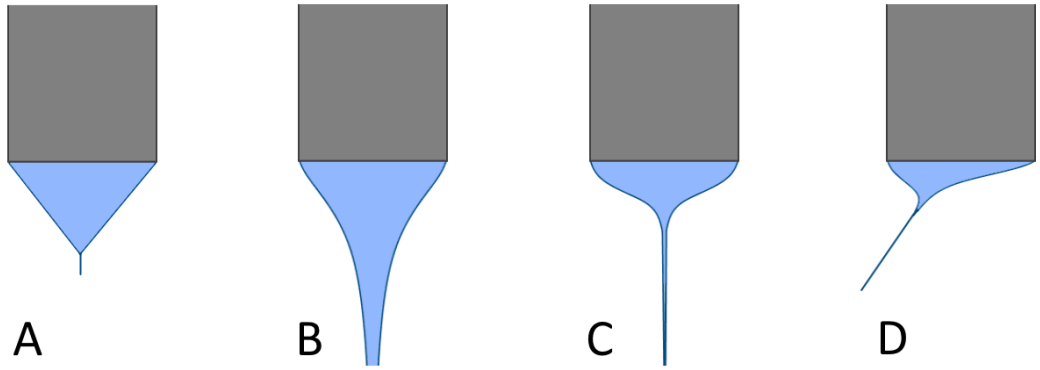

Figure 2.8 Possible forms of the nozzle meniscus in the cone-jet mode. (A) shows the classic Taylor cone with little to no jetting. (B) shows how the cone can deform due to a high flow from the tip. As the electric field increases the cone resembles (C) and eventually (D). Based on Cloupeau and Prunet-Foch, 1994.

In the cone-jet mode, a Taylor cone forms at the nozzle due to the balance of forces from the charged ink in the electric field and from surface tension. Figure 2.8 shows how the appearance of the cone can vary, but the definition of this mode is that just before a jet forms, the steady-state meniscus forms a straight-walled cone with an included angle of 98.3º (Taylor, 1964). It is important to note that Taylor's analysis was for a static droplet without any flow, with a precise volume and in a carefully shaped electric field. Clearly, the geometry will differ from this ideal in practical electrospinning, but the extent of deviation depends on the fluid properties, flow rate and electric field vectors. Generally, fluids that are more viscous will cause greater deformation, demonstrated by comparing (A) and (B) in Figure 2.8. Lower flow rates

or stronger electric fields reduce the cone as seen in Figure 2.8 (C). Very high electric fields can cause the jet to angle, as seen in (D), or cause multiple jets to form.

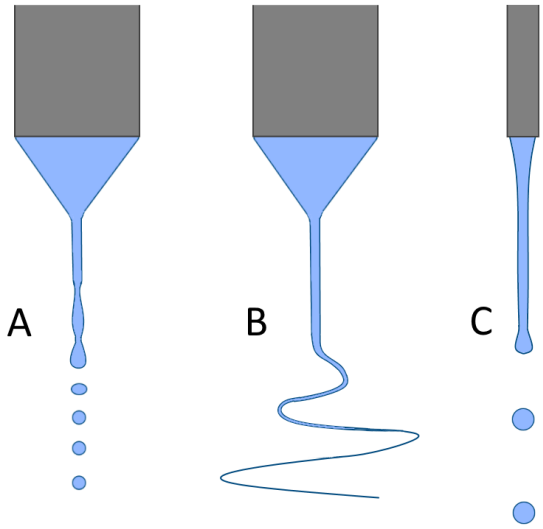

Figure 2.9 Breakup of electro-jets. A) Rayleigh breakup B) Whipping instability C) Simple jet, with a higher flow rate from a smaller nozzle. Based on Cloupeau and Prunet-Foch, 1994.

The tip of the cone feeds into a straight column of liquid that travels toward the collector electrode, thinning as it does so (Spivak and Dzenis, 1998). Given a sufficiently long flight time, the jet may break up in one of two ways; first, through the Plateau-Rayleigh instability as shown in Figure 2.9 (A), in which surface tension causes the cylinder of fluid to collapse into spherical droplets of a characteristic size dependent upon the cylinder dimensions and fluid properties. Second, it may deflect from the direct path and whip around in a chaotic spiral due to the repulsion of charges in the jet, as seen in Figure 2.9 (B). The whipping accelerates and stretches the jet, which when using fluids such as polymer solutions leads to an even finer solid filament. Other inks may undergo whipping and then Rayleigh breakup. The material deposited from a whipping jet is spread over a larger area of the collector due to the random nature. Higher viscosity and lower surface tension will tend to favour whipping over Rayleigh breakup.

Another mode that is relevant to the present work is the simple jet (Cloupeau and Prunet-Foch, 1994). At sufficiently high flow rates, the laminar flow of fluid from a

nozzle forms a continuous jet even without an electrical potential. Such a jet may also undergo Rayleigh breakup but has no Taylor cone, exhibits little thinning after clearing the nozzle and produces larger droplets at a lower frequency, as seen in Figure 2.9 (C). Weak electric fields can accelerate droplet breakup or cause some whipping.

Even when only considering the steady Taylor cone-jet, the outwardly simple process involves some complex physical phenomena. The stability of the jet filament is due to a careful balance of electric field, flow rate and fluid properties (Mestel, 1996). Predictive equations and models have been developed for such electro-jets, but they often fail to account fully for the observed behaviours. The problem is further complicated by the consideration of real inks, which are often non-Newtonian fluids (Feng, 2002). These models tend to provide little information about the conditions needed to establish an electro-jet with a given ink and are usually compared to experiments with relatively simple, low viscosity inks, which are quite different to the inks used in this work, so these models will not be considered in further detail.

2.2.2 Scaling laws

While developing a full model of the electro-jet is difficult, it is possible to derive scaling laws for specific aspects. One key parameter of the process is the conductivity of the ink. For the electric field to cause the ink to accelerate, the ink must be able to carry some charge and cannot be a perfect insulator. Similarly, for the charge in the ink to feel a force, the electric field lines must cross the fluid surface and therefore the ink cannot be a perfect conductor. These conditions imply limits on the conductivities of the ink, which might be as wide as 10^{-11} to 10^{-1} S/m (Cloupeau and Prunet-Foch, 1989).

Within the range of conductivities that form stable jets, the conductivity affects the behaviour of the jet. Current flows through the electro-jet in two ways. First, there is a convective current due to the bulk flow of liquid carrying charged particles from needle to substrate. Second, there is a conductive current due to the transfer of charge between particles within the jet. The different dynamics of these two currents leads to the current scaling differently in fluids with high (Equation 2-1) versus low (Equation 2-2)

conductivities, where *I* is the total current and *Q* is the volumetric flow rate. For this purpose, a fluid has a high conductivity if the equality given in Equation 2-3 is true, where γ is the surface tension, ε_0 is the permittivity of vacuum, μ is the viscosity and *K* is the conductivity (Gañán-Calvo et al., 1997). As a point of reference, sunflower oil with a conductivity additive is considered high viscosity. In addition to the change in current scaling, increasing the conductivity of the ink generally results in the cone-jet forming at lower flow rates and with a cone angle closer to the theoretical angle of 98.3º (Cloupeau and Prunet-Foch, 1989).

2-1 $$I \propto Q^{1/2},\ d \propto Q^{1/3}$$

2-2 $$I \propto Q^{1/4},\ d \propto Q^{1/2}$$

2-3 $$(\gamma^3 {\varepsilon_0}^2/\mu^3 K^2 Q)^{1/3} \leq 1$$

It is notable that the jet current only depends upon the flow rate and fluid properties in either conductivity regime, although which fluid properties are relevant changes. As well as the current, the jet diameter is observed to scale with the flow rate, again in two different regimes depending on whether the fluid is high or low conductivity. The corresponding relations are given in 2-1 and 2-2, where *d* is the diameter of the emitted droplets, which is directly proportional to jet diameter for low viscosities (Gañán-Calvo et al., 1997, p. 257).

While simple, these scaling laws are not perfect, as a small range of powers produce a satisfactory fit with the data (Gañán-Calvo et al., 1997, p. 258). Other work has recommended the same fit, with a power of 1/3 (Mora and Loscertales, 1994), or a different power, up to 2/3 for a salt doped glycerol (Fernandez De La Mora et al., 1990). The different fits can be potentially explained by the other properties of the fluids in question, particularly the viscosity. These scaling laws are based on data from a range of fluids, but in absolute terms they all have relatively low viscosities.

Given dependence of jet diameter on flow rate, one might consider how far the jet can be thinned by reducing the flow rate. However, to maintain the jet a minimum flow

rate is required. As with the jet diameter, the exact form is not universally agreed but generally of the form given in Equation 2-4, where ε is the relative permittivity and ρ is the density of the ink (Ku and Kim, 2002). Higher viscosity fluids may have a minimum flow rate that exceed this limit by several times.

2-4 $$Q_{min} \propto \frac{\varepsilon \gamma \varepsilon_0}{\rho K}$$

2.2.3 Inks

Historically electrospinning has mostly been performed with polymers dissolved in organic solvents. A combination of low viscosity at the nozzle, long-chain molecules and solidification in flight produces very fine continuous filaments without Rayleigh breakup. When conditions lead to whipping, the filaments can have diameters on the order of nanometres (Huang et al., 2003). These inks are often used to create non-woven mats for biological, filter and electrode applications.

More recently polymer melts have been used in electrospinning with viscosities in the range of 40 to 200 Pa s, compared with up to 5 Pa s for a polymer solution (Hutmacher and Dalton, 2011, p. 47). This produces thicker filaments, but they remain straight and continuous over much longer distances than polymer solutions, especially when allowed to cool in flight. The jet diameters are typically in the 10 to 100 μm region, but by using low molecular weight polymers diameters of micrometres down to hundreds of nanometres have been achieved (Hutmacher and Dalton, 2011, pp. 47–48). The straight jet path allows easy control over the point of deposition and melt electrospinning can be used as a method of direct writing (see Section 2.2.5). Alternatively the jet can be heated in flight to encourage whipping and create nano-scale fibres that are comparable to those produced with polymer solutions, but without the use of solvents (Zhou et al., 2006). Due to the improved material properties and lack of solvents, this approach is rapidly gaining popularity in many fields (Brown et al., 2016). One particular area is tissue scaffolds, where good biocompatibility is a major advantage (Hochleitner et al., 2015; Pokorny et al., 2017; Wei and Dong, 2013).

The electrospinning process is affected by the properties of the ink, particularly the viscosity, surface tension and conductivity. When depositing directly onto the collector electrode, the conductivity of the ink must be low enough that the conductive path the jet creates does not allow excessive current to flow, which could cause heating of the ink in the jet or short the high voltage source. However, the conductivity of the ink can be a great aid in producing fine and well-formed filaments. Increasing the conductivity of the ink means a higher density of charge carriers, which will be acted upon by the electric field to stretch the ink and produce thinner jets. Increasing the stretching in this way can also be used to avoid the formation of beads in the jet (Angammana and Jayaram, 2011). The advantage of changing the ink conductivity, rather than its viscosity, for example, is that it can be done with very small quantities of additive and with little effect on the other properties of the ink, provided that a suitable additive can be found for the ink in question.

Sol-gel inks can allow electrospinning to pattern ceramics instead of polymers. The sol-gel ink is formulated with soluble ceramic precursor compounds, such as metal nitrates. Metal oxides can then be easily produced by calcinating the precursor compounds in air. Dissolved polymer may (Kolathodi et al., 2016) or may not (Son et al., 2006) be added to aid electrospinning; adding polymer relaxes the requirements on the rheology of the sol-gel but adds more organic material that must be burnt out. This method can produce ceramic fibres with diameters in the nanoscale due to the combined effects of stretching in the electro-jet, solvent evaporation and material burn-off, but it is limited to materials for which suitable sol-gel precursors can be made.

Another way to incorporate non-polymer materials into the fibre is to add fine solid particles to a polymer solution. This route is applicable to materials that cannot be produced by a sol-gel process, but is limited by the size of the filler particles and their effect on the ink properties. The solid fraction of the ink is usually kept low to avoid problems, as demonstrated in Table 2.2. Both of the papers used to produce Table 2.2 demonstrate that a low solid loading of small particles tends to result in encapsulation of the particles rather than exposed particles on the fibre surface, which is problematic for

catalytic and some bio-active applications. Higher solid loadings can allow for electrohydrodynamic jetting without a polymer component, for example 20 vol% in glycerol (Nangrejo et al., 2010) or 10 vol% in ethanol (Wang et al., 2005). Combining this approach with a volatile solvent means the deposited fibres will contain almost entirely solid filler material (Kim et al., 2005), reducing or eliminating the need for a burnout step as would be required with a polymer solution.

Powder	Particle size (nm)	Polymer	Ink		Dry deposit	
			Weight %	Volume %	Weight %	Volume %
Barium sulphate	430	PVA	7.2	1.7	37.5	13.8
Silver acetate	279	PVA	6.7	2.13	42.0	20.5
Boron Nitride	347	PVA	15	7.73	63.8	49.6
Cobalt	50	PVA	5	0.60	34.5	6.6
Zinc	< 50	PVA	5	0.74	34.5	8.1
Titanium	< 100	PCL	2	0.51	16.9	4.9
Hydroxyapatite	1167	PVA	7	2.35	45.5	23.9
Hydroxyapatite	1167	PU	7	2.18	42.9	22.1

Table 2.2 Solid content of polymer solutions used for electrospinning. First line taken from Sato et al. (2010) and others from Barakat et al. (2010).

A potentially useful feature of electrospinning is the flow profile in the jet. Repulsion forces the charges in the jet to the surface while causing stretching, resulting in faster flow at the jet surface than the core. This differential flow aligns long particles with the jet flow and the alignment can be maintained through to the deposited filament. Used with materials like carbon nanotubes this could create fibres with high stiffness and tensile strength, or used with materials like silver nanowires to add conductivity (Lee et al., 2014).

2.2.4 Equipment setup

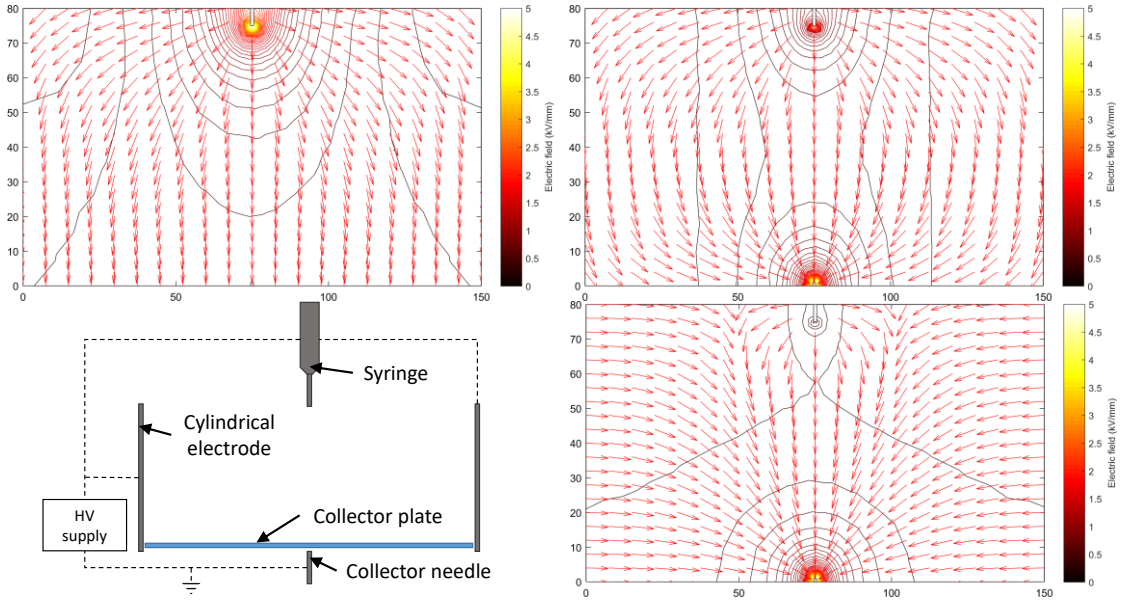

Figure 2.10 Clockwise from top left: Electric field with flat plate collector; field with pin electrode; field with pin and sidewall electrode; apparatus schematic. Contours indicate field strength and arrows indicate field direction. Recreated based on Lee et al., 2012, using the same techniques described in Section 3.2.

In its simplest form, electrospinning needs no more than a conductive point coated in liquid above a conductive plate, with a potential difference between them. Usually a hollow metal syringe needle is used to deliver the liquid ink from a syringe, allowing for a much greater duration of spinning or continuous operation. An alternative to a conductive needle is to use a glass capillary, which can be comparatively easily produced in much finer diameters than metal needles. This then requires an electrode to be placed inside the capillary to make electrical contact with the liquid (Doshi and Reneker, 1993). Electro-jets can also be formed without pointed geometry, such as from the outer curved surface of a cylinder (Niu et al., 2009). Authors normally report collector distance and applied voltage, although the average electric field strength is arguably more comparable. Field strengths reported in the literature vary from 200 to 2,000 V/mm (Hutmacher and Dalton, 2011, p. 48)

The collecting electrode can have an even wider range of forms. The simplest is a flat plate, which collects randomly oriented fibres when used with a whipping electro-

jet. Attempts to align these chaotic fibres have used rotating disks (Theron et al., 2001) and cylinders (Edwards et al., 2010) or auxiliary electrodes to shape the electric field (Deitzel et al., 2001). Another approach is to use a solid needle as a collector electrode below a non-conductive plate, which can help to focus the electric field and the jet down to a single point. Lee et al. demonstrated the use of such a pin collector in combination with an auxiliary electrode to focus a whipping polymer solution jet to a well-controlled point (Lee et al., 2012). Simulations of the field produced are reproduced in Figure 2.10. There are many papers investigating the effects of collector geometry on aligning fibres, but we will not consider them further here because we are interested in mask-less deposition of the ink.

Another variable of the apparatus is the polarity of the needle. Typically, the collector is grounded and the nozzle raised to a large positive potential with respect to the collector. However, reversing the polarity and making the nozzle negative can cause an observable difference. Specifically, the voltages at which the jet transitions from one mode to another are increased and the range of voltage over which a given mode is stable is larger (Ragucci et al., 2004). It is suggested that this asymmetry is due to the differing mobility of positive and negative charge carriers in the fluid, implying that the effect is dependent on the ink used. Alternatively, changing the polarity of the needle can completely change the operating map, as seen in Figure 2.11 (Jaworek and Krupa, 1999). Here the same modes are present, but with a negative needle the spindle mode is far more dominant at high electric fields.

Figure 2.11: Electro-jetting modes for distilled water with different needle polarities (Jaworek and Krupa, 1999)

2.2.5 Electrospinning as direct writing

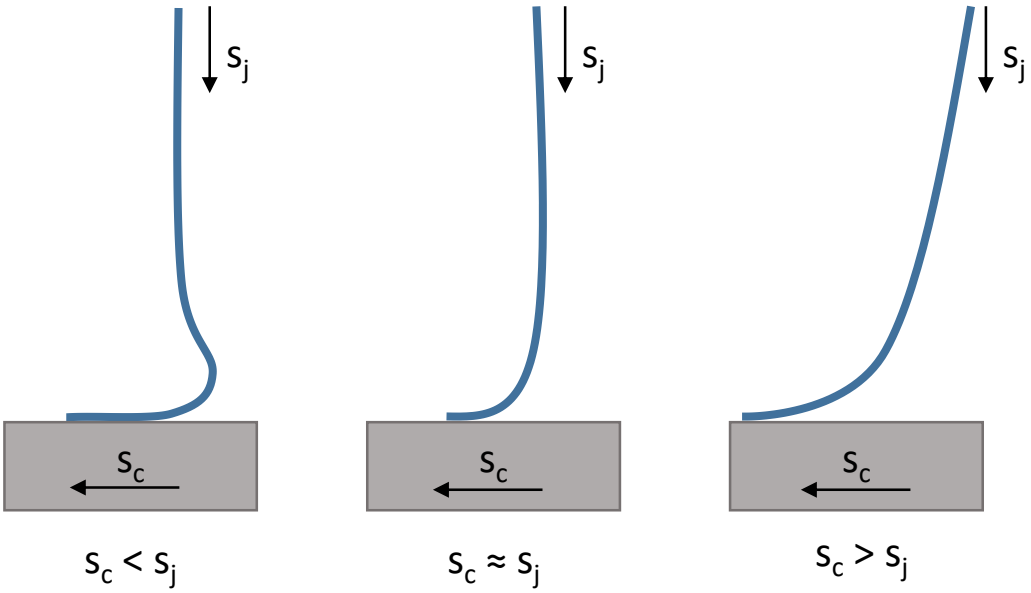

Figure 2.12: Shape of filament impact for a range of collector speeds (s_c) versus jet speed (s_j), based on Brown et al., 2011, p. 5653.

A major attraction of electrospinning is the small fibre diameters produced. There is increasingly more work on adapting the process to the direct writing of objects over a range of scales and for a variety of materials, particularly for biological applications (Dalton et al., 2013). The main challenge is the control of the point of deposition. Particularly with polymer solutions, the gap between the electrodes is often much reduced compared to previous arrangements to avoid deflection of the jet. The applied voltage is also reduced to result in electric fields comparable to those achieved for larger gaps, such as 600 V across a 500 µm electrode gap giving 1,200 V/mm (Sun et al., 2006). Smaller gaps allow a tighter achievable turning radius of the deposited filament, with an electrode gap of 170 µm enabling radii of 10 µm while depositing 5 µm filaments (Wei and Dong, 2013, pp. 6–7). Here the voltage was also reduced to 200 V, keeping the field strength around 1,200 V/mm.

The nozzle should maintain a speed over the substrate that approximately matches the speed of the jet. This ensures the filament lays neatly on the substrate in the direction of travel with good positional accuracy (Brown et al., 2011). A higher nozzle

velocity creates a large suspended region, hindering accurate placement and the patterning of tight corners, although this can be used to mechanically stretch and thin the jet. When the nozzle velocity is lower than the jet velocity, the filament buckles in the region just above the substrate, causing waves or regular circular motions of the point of impact (Huang et al., 2013). This can be used to pattern lines of coiled mesh. The shapes of the impacting jets are shown schematically in Figure 2.12.

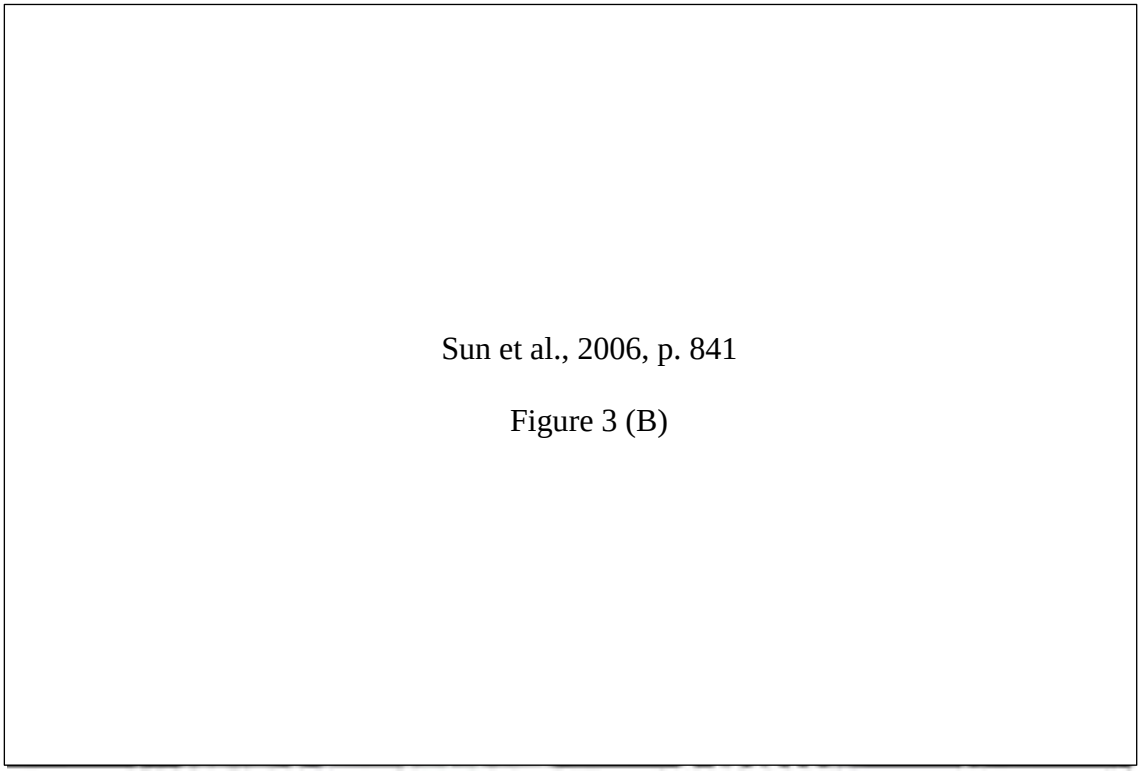

Figure 2.13 Spiralling of jet from a stationary nozzle due to retained charge (Sun et al., 2006, p. 841).

While many fluid jets will tend to coil when they hit a flat substrate, in electrospinning the charge carried by the filament can cause the coils to grow in size instead of depositing on top of each other. The effect is worst when the substrate surface is non-conductive or the deposited filament otherwise retains its charge, which then repels the charge in the incoming filament. For a stationary nozzle this mostly results in an evenly-spaced spiral pattern, such as that seen in Figure 2.13 (Sun et al., 2006, p. 841). In situations where it is not possible to use a conductive collector

surface, for example when using a conductive ink, the problem can be reduced by lowering the voltage used (Bisht et al., 2011, p. 1833).

2.3 Ceramic materials

The term ‘ceramic’ covers a huge range of compounds, including clays and glasses. All are inorganic and non-metallic, which leads to some general properties such as low ductility. Obviously not all ceramics are suitable for high performance applications. Those that are suitable are often called ‘technical ceramics’, which is also a fairly broad definition. A Versailles Project on Advanced Materials and Standards (VAMAS) report on classification of these materials defines an advanced technical ceramic as “a highly engineered, high performance, predominantly non-metallic, inorganic, ceramic material having specific functional attributes” (*Technical basis for a unified classification system for advanced ceramics*, 1993). Most technical ceramics have high hardness, high melting points, high elastic moduli and good chemical resistance. Their stiffness and minimal ductility make them brittle, but they generally retain their mechanical properties at elevated temperatures. Many have poor or mediocre thermal conductivities and are good insulators.

These properties make technical ceramics useful in many applications. Wear resistance makes them effective as long-lasting cutting edges, in bearing components and other moving components. Their sustained performance at high temperatures makes them excellent high-speed cutting tools and of great interest to engine and turbine designers, where higher operating temperatures allow for greater thermal efficiencies. The combination of stiffness and biological compatibility is driving investigation into their use in hard tissue replacement and regeneration. Ceramics with piezoelectric, magnetic or superconductive properties are widely used in sensors, motors and other electronic devices. Other ceramics can be used as dielectrics for insulation or durable capacitors. These electronic applications are usually less sensitive to the mechanical properties of the ceramic than the structural applications mentioned earlier.

Ceramic	Chemical formula	Melting point (°C)
Aluminium oxide (alumina)	Al_2O_3	2,070
Zirconium dioxide (zirconia)	ZrO_2	2,715
Silicon carbide	SiC	2,730
Silicon nitride	Si_3N_4	1,900
Tungsten carbide	WC	2,800
Boron carbide	B_4C	2,765
Boron nitride	BN	2,975

Table 2.3 Common structural ceramics.

In this work, we are interested in technical ceramics for the more structural applications. Common ceramics used in these areas are listed in Table 2.3 along with their melting points. For research purposes, we primarily need a ceramic that is readily available and easy to work with while retaining practical relevance. This immediately draws us to alumina and silicon nitride because of their relatively low melting points, making sintering significantly easier. However, silicon nitride tends to decompose at temperatures just below its melting point, leaving us with alumina. As it is commonly used as an abrasive, alumina is readily available in fine particle sizes.

2.3.1 Conventional processing

Processing of technical ceramics usually starts with a powder of the desired ceramic. The powder is formed and then bonded in separate steps. One of the oldest forming techniques is slip casting, where an aqueous slurry of the ceramic powder is poured into a mould made from plaster. Capillary forces pull the water out of the slurry, increasing the solid content and converting it from a flowing liquid to a soft solid. The process can be used to produce hollow objects by removing the remaining slurry after a fixed time, or solid objects by leaving a reservoir of slurry above the mould cavity to account for

the settling of the dried slurry. The process is very slow, requiring hours to days for sufficient water to be removed to produce a stable green body. Even then, the mould must be dried before it can be re-used. A modern adaption is Pressure Slip Casting, which replaces the pull of capillary forces with the push of applied pressure as the driver for water removal. This requires a mould with specific pore and mechanical characteristics, but brings the moulding time down to minutes for thin-walled parts (Rak, 2000, p. 11)

There are other mechanisms used to induce a phase change in a moulded ceramic part. Mixing the powder with a polymer allows the injection moulding of ceramic parts, a fast and automated process. A similar mixture can be extruded through a die to produce high aspect ratio parts. However, this requires expensive machinery and moulds that can withstand the pressures and abrasion, as well as needing a long burnout treatment to remove the polymer binder. The latter issue can be overcome by using a temperature sensitive gel instead of a polymer, such as agar. This reduces the organic content from near 50 vol% to only a few percent, the rest being replaced with easily evaporable water (Rak, 2000, p. 7). A range of other gelation reactions (e.g. pH change, polymerization, hydrolysis reducing the water content) can be used in batch moulding.

Simple geometries can be produced by pressing of the dry powder, forming a ‘compact’ that is then directly sintered. Heat can be applied during the pressing in a one-step process where the pressure aids the consolidation of the powder. It is possible to apply this to reasonably complex parts with Hot Isostatic Pressing, where the powder is contained within a semi-flexible, impermeable mould that is then placed in a heated pressure chamber. While able to produce well-consolidated parts quickly, the moulds are difficult to form and generally must be destroyed to extract the part, making the process expensive.

In a more exotic process, ceramics may also be deposited by Chemical Vapour Deposition (CVD). Precursor compounds are vaporised in a low-pressure chamber and decompose into the desired ceramic on a heated surface. CVD is most suited for

applying ceramic coatings or producing parts over a sacrificial form. While expensive, it produces fully solid, high quality ceramic parts.

A limitation common to all the discussed methods is the need for a mould or form to impart the desired shape. Mould production adds an extra step in the overall process and can significantly add to the cost for single part or small batch production runs. Unlike plastics and metals, ceramic materials are difficult to work or machine. Their high hardness leaves few materials able to cut them effectively. Furthermore, their poor ductility means cutting processes that stress relatively large areas can create and grow cracks that lead to chipping or complete breakage of the part. This leaves abrasive processes such as grinding, which is slower and therefore more expensive than sawing or milling.

2.3.2 Sintering

Sintering is a method of bonding loose particles into a solid mass without melting the material. It takes place at temperatures below but near the melting point of the material. It is fundamentally a diffusion-based process, driven by the higher surface energy of many particles compared to a continuous bulk. As the rate of diffusion increases with temperature, so does the rate of sintering. The initial particle size also affects the rate, with smaller particles having a higher surface energy and shorter diffusion distances.

The goal of sintering is typically one of two possibilities. Usually it is desired to achieve as strong a part as possible, in which case the aim is to achieve the full density of the bulk material and minimise voids. Alternatively, an open porous network may be desired, for filtering or similar applications. These correspond to late and early stages of the sintering process respectively. The common challenge with sintering is getting to, or close to, full material density in a reasonable time. Depending on conditions, it may take hours or days to bring a part to full density and because the surface energy that drives the change reduces with time, it may never be achieved.

One powerful technique to improve the ability of a material to be sintered is to add a liquid phase to the process (German et al., 2008). The liquid provides two main

benefits; first, the surface tension acts to pull particles into closer proximity. Second, the liquid phase should at least partially dissolve the solid phase, allowing for a much higher rate of diffusion than the solid state. The resulting material will be a composite, with grains of the primary material surrounded by the, now solidified, liquid phase. In systems where the solubility is higher, the liquid phase may be a new mixture or alloy.

As well as improving speed and reducing pores, careful selection of the liquid phase can drastically lower the required temperature. The ceramic of interest in this work, alumina, has a melting point just over 2,000 ^{o}C and in pure form usually needs to be sintered above 1,500 ^{o}C to achieve good consolidation (Yalamaç et al., 2014). Adding quantities of compounds such as titanium oxide, manganese oxide or copper oxide at as little as a few mole percent can bring this temperature down to 1,300 ^{o}C (Cutler et al., 1957; Erkalfa et al., 1995). More complex mixtures, such all three previous oxides plus boric acid, can reduce the temperature even further to less than 1,100 ^{o}C (Xue and Chen, 1991). The second two studies use the interesting method of adding the sintering aids via an aqueous solution of appropriate salts with the alumina powder suspended within it. This avoids the need to source or produce fine powders of each component and reduces the chance of their agglomerates creating areas devoid of alumina.

2.4 Process outline

Of the general AM approaches, a method that directly places material such as extrusion has the major benefits of less wastage and easier handling of the input material compared to methods using resin vats or powder beds. One drawback with this approach is that typically the material must pass through some kind of nozzle, with the internal diameter limiting the minimum feature size. It is also desirable to work with solid powders of the intended ceramic because this gives the process compatibility with the widest range of materials and reduces the sensitivity of the final material properties on the processing, as would be the case with using a precursor compound.

Fluid containing solid particles flowing through a small nozzle creates a new limitation on our process, as if the orifice is not significantly larger than the particles

they can jam and block further flow. Electrospinning provides a solution to this problem, as the stretching of the fluid causes the jet to be narrower than the nozzle. In this way, we can reduce the minimum feature size compared to a direct extrusion method, without using finer powders that are more difficult to produce. With an ink of suitable viscosity and a relatively small distance between the nozzle and substrate, the jet should remain straight, giving good control over the impact point.

The other key aspect of the process is the fixing of the jet as it is deposited on the substrate. This must happen quickly enough to prevent significant flow of the ink, which would cause difficulty when trying to build three-dimensional objects. Over a longer timescale, the deposit needs to resist deformation due to gravity, from either its self-weight or the weight of material deposited on top. Additionally, the ink should have a low viscosity while inside and just after leaving the nozzle to allow for significant stretching and thinning by the electric field.

In this research, we will investigate inks that use freezing or evaporation to fix the material after leaving the nozzle. The freezing approach is attractive because the phase change is easily controllable and reversible, avoiding nozzle blockages due to premature fixing of the ink. Frozen ink will also have a longer storage life, as separation and sedimentation cannot occur. The evaporation mechanism could suffer blockages due to evaporation from the nozzle, but has merit because it removes the carrier fluid during deposition, leaving less material to be removed before sintering. Particularly in the case of freezing, an additional fixing process will be needed to prevent the ink melting during sintering. This will be provided by a UV curable component. UV curing is not used to fix the ink during deposition for several reasons, primarily difficulty curing the material quickly enough, the comparatively high viscosity of available compositions and the potential for curing to occur in the nozzle. A flow-chart for the process is shown in Figure 2.14, with optional routes if the final ink does not need UV-curing or a separate binder burn-out step.

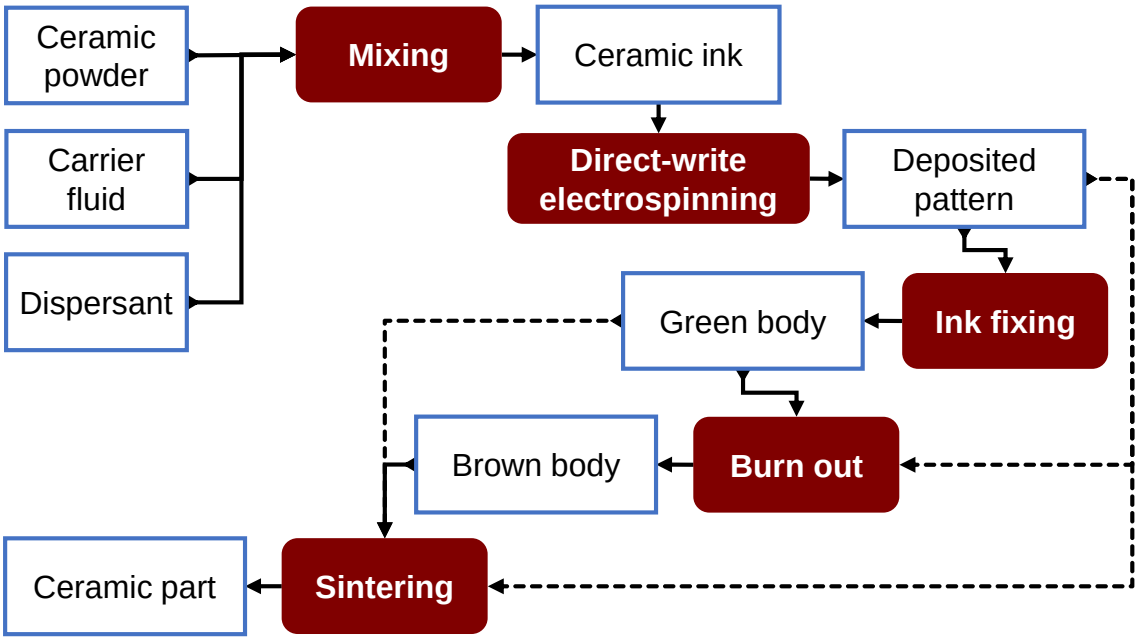

Figure 2.14 Process flow-chart. Outlined boxes are materials, shaded boxes are processes and dashed lines are optional routes.

3 MODELLING OF DEPOSITION PROCESS

This chapter will cover mathematical modelling and simulation of several aspects of the electrospinning process. This gives some insight into the behaviour of the process and aids in identifying the most important conditions. The areas to be considered are how the solid loading affects the ink rheology, the electric field between nozzle and substrate, and how the ink cools during deposition.

3.1 Effect of solid loading on ink viscosity

To minimise shape changes during consolidation and voids in the final part, the ink should have a solid content that is as high as possible while having a suitable rheology to achieve the desired behaviour when electrospun. We can use previous work to predict the solid volume fractions that can be achieved for given carrier liquids. If we assume the particles of the powdered solid are spheres of uniform size, it has been long thought and more recently proven (Hales et al., 2017) that the maximum volume fraction occupied by the solid is just over 0.74, as found in face-centred cubic and hexagonal close-packed lattices. This requires perfect ordering of the spheres, which is

common in crystal lattices, but unlikely in poured powders. The random placing of particles reduces the volume fraction and the 'random close-packed' limit has been empirically determined to be 0.637 (Finney, 1970). The solid volume fractions achievable in practice will be different due to both the non-spherical particles and variance in particle size. While it is possible that it could be higher, for example by smaller particles filling the spaces between larger particles, it will be lower for a powder of particles of a single size.

The solid volume fraction of the ink in this work is further limited by the need to flow easily through a small orifice. The addition of solid particles to a liquid increases the viscosity by reducing the volume of fluid undergoing shear, by introducing additional boundary layers and, at higher volume fractions, by interactions between the solid particles. There have been several equations proposed for the viscosities of slurries, generally adding more terms to predict the effect of higher solid loadings. Conversely the equation proposed by Kitano et al. (1981), has a single term:

3-1
$$\mu_r = \left(1 - \frac{\phi}{A}\right)^{-2}$$

Here μ_r is the factor by which the viscosity is increased, ϕ is the solid volume fraction and A is the maximum possible solid volume fraction. To estimate the slurry viscosity, μ_r must be multiplied by the viscosity of the carrier liquid. This equation was proposed to fit measurements taken from molten polymers with a variety of solid fillers at volume fractions of up to 0.4 and at shear stresses above 1,000 Pa. This means that it is not entirely applicable to the conditions used in this work, but was chosen for its simplicity and because it gives the expected behaviour of infinite viscosity (i.e. no flow) at the maximum solid volume fraction. The value of A is dependent on the filler properties, with the highest value of 0.68 applying to spherical glass beads and balloons with diameters between 36 and 74 μm (Kataoka et al., 1978). Note that this is higher than the theoretical random close-packed limit, although no measurements were taken at solid volume fractions very close to this limit.

Carrier liquid	Measurement temperature (°C)	Viscosity (mPa s)	Solid volume fraction at 750 mPa s
Mineral oil	25	20.4	0.54
Paraffin wax	100	4.5	0.62
Water	25	1.0	0.65
Ethyl acetate	25	0.4	0.66

Table 3.1 Base viscosities and theoretically achievable solid loadings for different carrier liquids, as determined by equation 3-1.

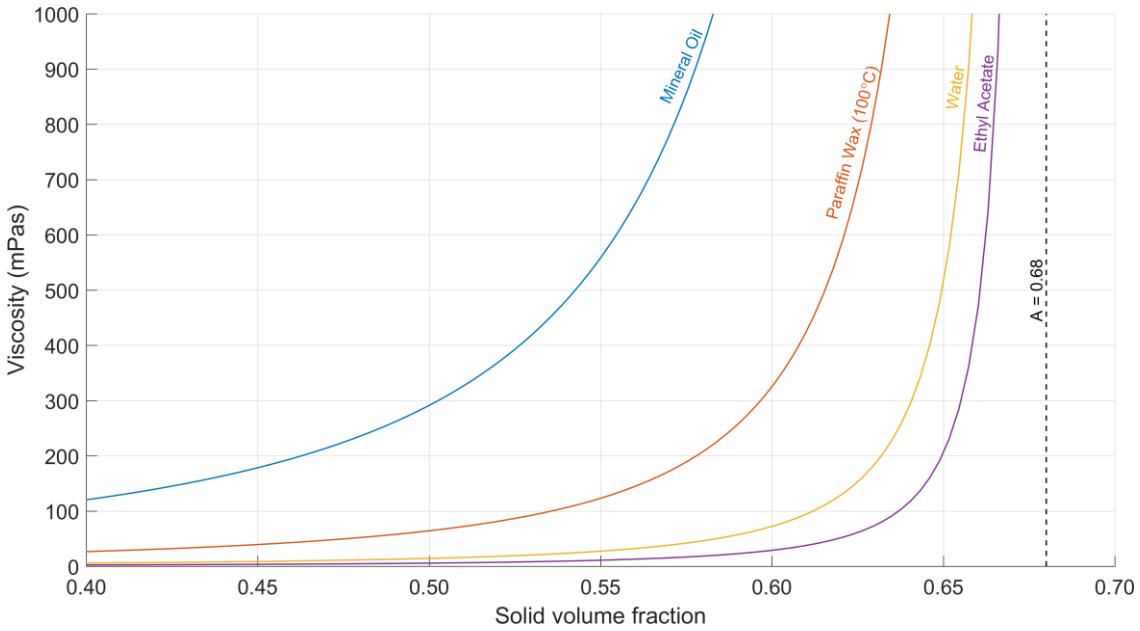

Figure 3.1 Estimates of slurry viscosities for various carrier liquids using equation 3-1, assuming a maximum possible solid volume fraction of 0.68.

Taking the highest observed value for *A* in the work of Kataoka et al., the expected viscosity of inks based on different carrier fluids could be plotted. The viscosities of the carrier fluids are listed in Table 3.1. The predicted ink viscosities are shown in Figure 3.1, which indicated that it should be possible to achieve quite high solid loadings if a low viscosity fluid was used. It was also clear that the viscosity would become very

sensitive to the solid content at high solid volume fractions, meaning that small errors in ink production could cause significant variance in process performance. Early experiments for this work suggested ink viscosities in the range of 500 to 1,000 mPa s produces good results, so the final column of Table 3.1 compares the expected solid loading each liquid would achieve in the middle of this range according to the equation from Kitano et al. Note that the mineral oil and paraffin wax had almost identical viscosities at the same temperature, provided they were above the melting point of the wax (around 55 ^{o}C, see Section 5.1.3).

3.2 Electrostatic fields around the nozzle

Electrospinning can be performed with a wide variety of emitter geometries, but the shape of the emitter and collector determine the shape of the electric field that drives the process. Therefore, some consideration should be given to the field shape to ensure it is consistent between experiments and to look for possible improvements. Of interest to this work was the effect of a shroud around the nozzle, which was required to heat the nozzle for deposition above room temperature. In Section 2.2.4 we saw how using a pin instead of a plate as the collector electrode helps to guide the impact point of the electro-jet. The high viscosity of the ink and short distance between the nozzle and substrate in this work reduced the need to control the impact point in this way, so this section will focus on nozzle geometries. The aim was not to accurately model the fields around the jet or predict how they would affect the jet.

Two-dimensional simulations were carried out within MATLAB using the Partial Differential Equation Toolbox in electrostatics mode. Appendix C gives the script used to produce the simulation. Figure 3.2 shows the geometry and boundary conditions of the simulation and Figure 3.3 shows the results for five different geometries. The nozzle was 0.4 mm across, the substrate set to 5 kV and the nozzle, along with any shroud, was set to 0 V for all simulations. The remaining boundaries were set to be Neumann boundaries with zero charge. As well as the default case of the bare needle (a), two shroud geometries were considered, with their surfaces at the same potential as

the nozzle. A pointed shroud (b), with minimal material near the nozzle, was chosen to minimize changes to the electric field. A flat-bottomed shroud was chosen to make the electric field closer to vertical around the nozzle to reduce the tendency of the jet to deviate from the vertical. This shroud should also provide better heating to the nozzle because of the extra material. The flat shroud was simulated both flush with the nozzle (d) and with the nozzle 1 mm proud of the shroud (c and e). The nozzle was 2 mm above the substrate in cases (a) to (d) and 3 mm above the substrate in case (e).

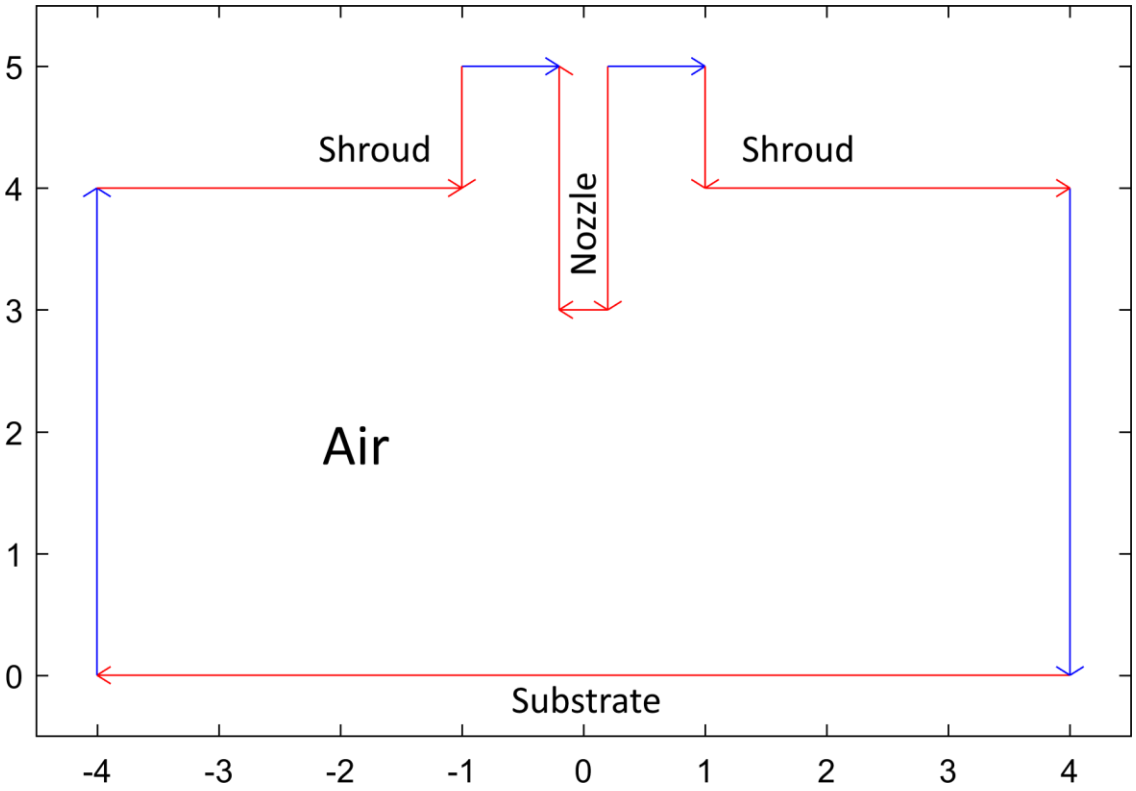

Figure 3.2 The geometry and boundary conditions used for electrostatic modelling, taken directly from the MATLAB PDE Toolbox. The red lines indicate Dirichlet boundary conditions (fixed potential) and the blue lines indicate Neumann boundary conditions (fixed charge). In the simulations the substrate boundary is set to 5 kV, the nozzle and shroud boundaries are set to 0 V and the Neumann boundaries are set to zero charge. The relative permittivity of the air is assumed to be 1.0. The width of the nozzle is 0.4 mm. The axes are in mm and the geometry shown corresponds to Figure 3.3 (e). The arrows have no significance for this application.

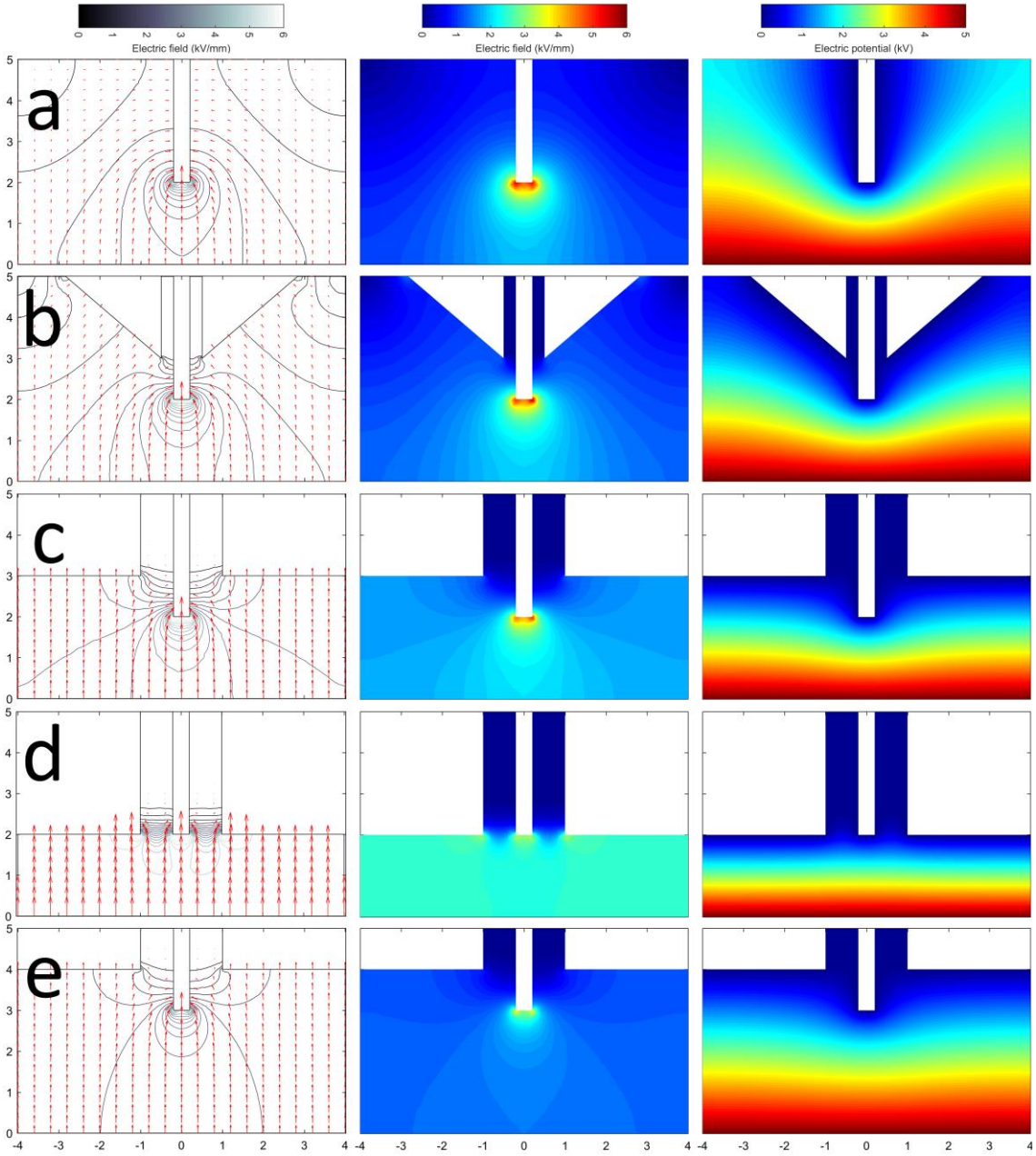

Figure 3.3 Electrostatic simulation of different nozzle geometries.
Axes are in mm and colour scales are consistent within each column.
a) Bare nozzle 2 mm above substrate b) Pointed shroud c) Recessed shroud d) Level shroud e) Recessed shroud with nozzle 3 mm above substrate.

From case (a) of Figure 3.3, we can see the electric field gradient is most intense around the nozzle, which has several implications for later experiments. First, most of

the acceleration and stretching of the ink will probably occur near the nozzle, rather than being evenly distributed along the flight path of the electro-jet. Second, assuming a given field gradient at the nozzle is needed to form the Taylor cone-jet for any experiment, the voltage needed to initiate electrospinning does not directly scale with the distance between nozzle and substrate. Third, it is likely that the voltage at which the air begins to breakdown will be lower than expected. With a constant electric field, such as between parallel plates at the same separation of 2 mm, we would expect dielectric breakdown of the air to occur near a potential of 6 kV between the plates, assuming this occurs at the commonly accepted field strength of 3 kV/mm. In this bare needle case, we see a peak field of 6 kV/mm at a potential of 5 kV, so we might expect breakdown at a potential as low as 2.5 kV.

Adding a shroud reduces the peak electric field, necessarily increasing the field strength further from the nozzle. In Figure 3.3 (d), with the flat shroud flush to the nozzle, the field is almost constant between the nozzle and substrate, at the expected 2.5 kV/mm. Conversely, in case (b) the pointed shroud has much less effect on the electric field below the nozzle, although there is still a reduction in peak gradient compared to the bare needle. The left column of Figure 3.3 demonstrates that the more constant the electric field between the nozzle and substrate, the closer to vertical the field is.

Evening out the electric field gradient may not be beneficial when trying to produce the thinnest electro-jet possible, as a molten ink will be most fluid near the nozzle. Once solidified no practical level of electric field will cause further stretching, so the stronger field around the nozzle is preferred. Balancing this with avoiding dielectric breakdown of the air and the need for good heat delivery to the nozzle means the recessed flat-bottomed shroud provides a good compromise.

Figure 3.3 (e) models the recessed flat-bottomed shroud at the same voltage but with the nozzle 3mm above substrate. As expected, we see the average and peak electric fields are reduced. The reduction is approximately proportional to the factor by which the distance has changed, although the geometry has not been simply scaled. The nozzle is narrower and the shroud closer to the nozzle height compared to a faithful

scaling, which would lead to a higher and lower peak field respectively. The opposing errors appear to be similar in magnitude in this situation.

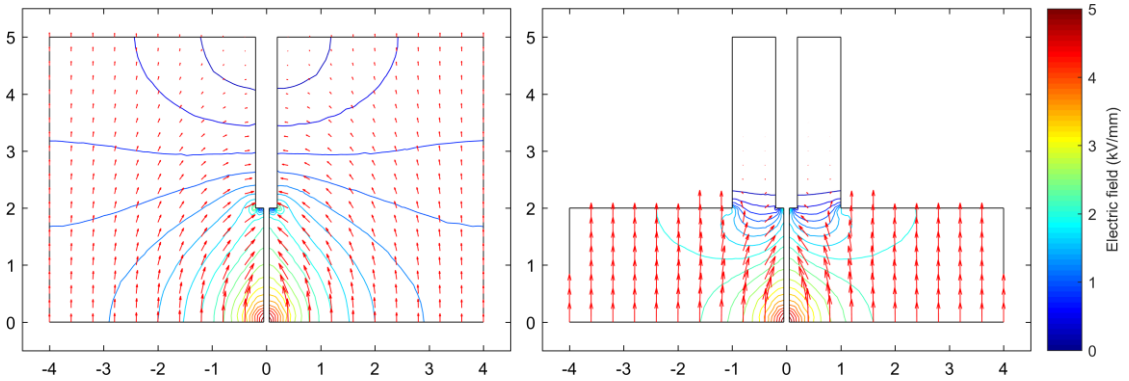

Figure 3.4 Simulations (a) and (d) of Figure 3.3 re-run with the filament modelled as 0.1 mm strip with a surface charge of -2.2 mC/mm^2.

There were several simplifications in this approach. The first was the reduction of a 3D axisymmetric process to a 2D simulation, which would not change the overall results but would affect the exact values. The second was the omission of the ink filament. By the nature of electrospinning the filament must carry charge, which will affect the electric field. Measurement of the jet current was not attempted in this work, but the high voltage supply could only supply 1 mA. Assuming the lowest flow rate and smallest diameter of 0.25 µL/s and 100 µm respectively, this gave a maximum surface charge of 2.2 mC/mm^2. This was added to the simulation and gave the results seen in Figure 3.4, which shows similar behaviour to the results of Figure 3.3. The addition of the shroud has a lesser effect on the field near the jet because the surface charge dominates, but the electric field is brought closer to vertical.

3.3 Heat loss from the jet

For an ink that is fixed by freezing, the temperature of the ink during deposition has a large effect on the final shape. The ink must be above its melting point, but by raising the temperature its viscosity can be lowered, which will improve flow through the nozzle and produce thinner filaments. If the ink is too hot, it will take a long time to freeze and will be able to flow on the substrate, producing flat deposits and possibly re-

melting previously deposited material. Therefore, it is beneficial to have an estimate of temperature changes the ink will undergo during deposition to ensure the nozzle temperature is as high as possible while ensuring rapid freezing on the substrate. For these calculations, the ink is assumed to be a simple mixture of alumina and paraffin wax at 50 vol% with the properties given in Table 3.2. Although the practical work will be taking placing in a room air conditioned to 21 °C, the ambient temperature will be taken as 25 °C to give a conservative estimate and allow for some localised heating of the air.

Property	**Symbol**	**Value**	**Units**
Density	ρ_i	2,400	kg m^{-3}
Specific heat capacity	c_i	1.12×10^3	J kg^{-1} K^{-1}
Flow rate	$\dot{Q}$	0.25 - 1.00	mm^3 s^{-1}
Temperature	T_i	353 (80)	K (°C)

Table 3.2 Ink properties for thermal modelling

3.3.1 Convection and radiation from the jet in flight

Ideally, the ink should cool to just above its melting point as it reaches the substrate. The surface of the electro-jet will be modelled as a vertical cylinder in free air, using the values for its properties given in Table 3.3. Forced convection due to entrainment of air by the flowing ink will be ignored. The thermal power loss by natural convection, $\dot{q}_{conv}$, can be calculated from equation 3-2, where *h* is the convective heat transfer coefficient and *A* is the surface area. The heat transfer coefficient depends on the problem geometry. We can make a good estimate of *h* by calculating the average Nusselt number, *Nu*, as shown in equation 3-3. For a vertical cylinder of length *L* and diameter *D*, this is given by equation 3-4 ("Thermal-FluidsPedia | Natural convection on cylinders and spheres," 2018), where the Rayleigh number *Ra* and Prandtl number *Pa* are given by equations 3-5 and 3-6 respectively. Note that the Rayleigh number is

evaluated at the 'film temperature', taken as the average of the surface and ambient temperatures.

3-2 $$\dot{q}_{conv} = hA(T_i - T_a)$$

3-3 $$h = \frac{Nuk}{L}$$

3-4 $$Nu = \frac{4}{3}\left[\frac{7RaPr}{5(20+21Pr)}\right]^{1/4} + \frac{4(272+315Pr)L}{35(64+63Pr)D}$$

3-5 $$Ra = \frac{g\beta}{\upsilon\alpha}(T_i - T_a)L^3$$

3-6 $$Pr = \frac{\upsilon}{\alpha}$$

For very thin filaments, the surface area to volume ratio becomes very large and the radiative thermal power, $\dot{q}_{rad}$, might become significant. The calculation of this is relatively straightforward:

3-7 $$\dot{q}_{rad} = \varepsilon_i \sigma A({T_i}^4 - {T_a}^4)$$

The Stefan-Boltzmann constant is $\sigma = 5.67\times10^{-8}$ W m^{-2} K^{-4} and the emissivity of the ink, ε_i, will be assumed to be 1.0 for simplicity. With the thermal power losses established, the change in temperature of the ink at steady state is given by equation 3-8, where $\dot{m}$ is the mass flow rate.

3-8 $$\Delta T_i = \frac{\dot{q}}{\dot{m}c_i} = \frac{\dot{q}_{conv}+\dot{q}_{rad}}{\dot{Q}\rho_i c_i}$$

Property	Symbol	Value	Units
Thermal expansion coefficient	β	$1/T$	K^{-1}
Kinematic viscosity	ν	1.57×10^{-5}	$m^2\ s^{-1}$
Thermal diffusivity	α	1.90×10^{-5}	$m^2\ s^{-1}$
Thermal conductivity	k	2.60×10^{-2}	$W\ m^{-1}\ K^{-1}$
Temperature	T_a	298 (25)	K (°C)
Acceleration due to gravity	g	9.81	$m\ s^{-2}$

Table 3.3 Properties of air for calculation of natural convection

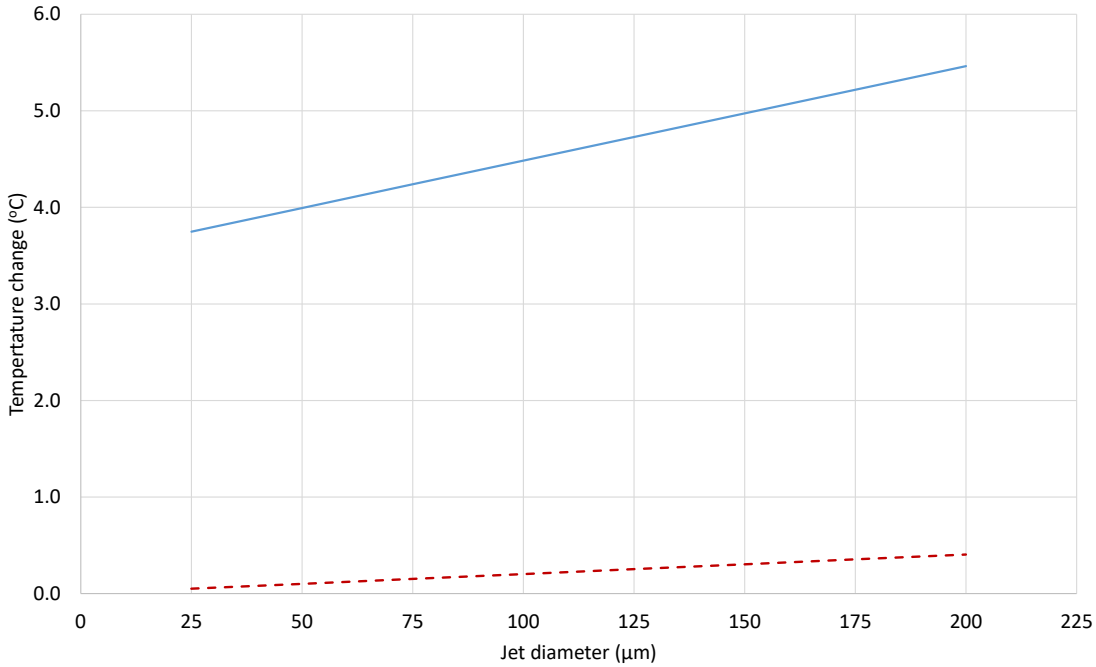

Figure 3.5 Effect of diameter on the temperature loss of a jet at a nozzle height of 1.0 mm and with a flow rate of 0.25 µL/s. The solid blue line is the total change and the dashed orange line is the radiative contribution.

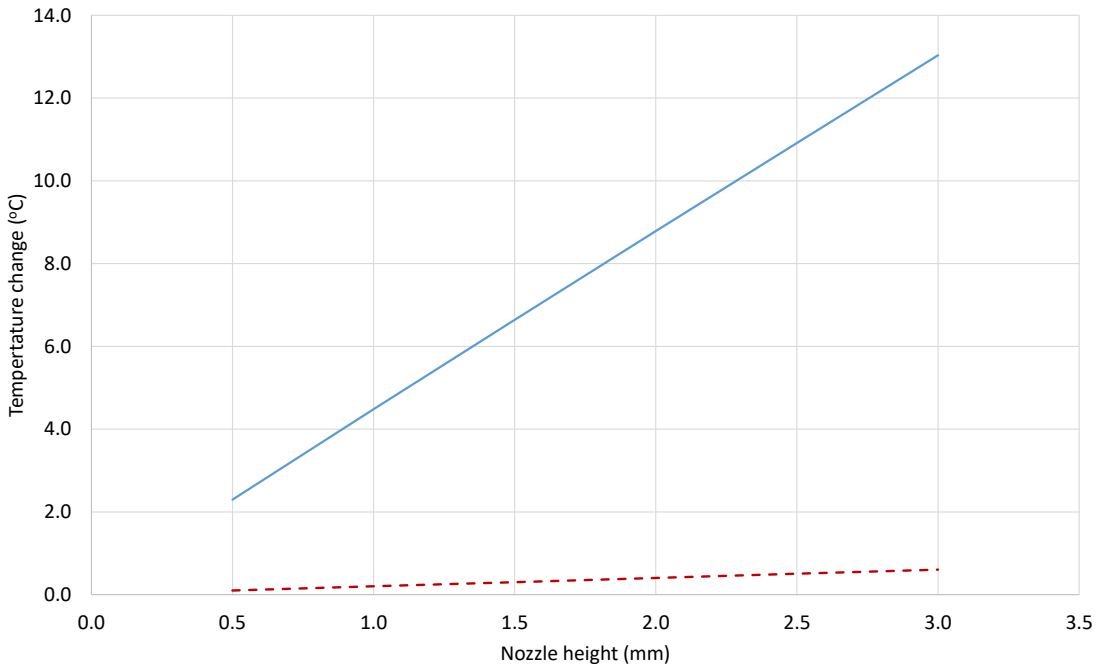

Figure 3.6 Effect of nozzle height on the temperature loss of a jet with a diameter of 100 µm and flow rate of 0.25 µL/s. The solid blue line is the total change and the dashed orange line is the radiative contribution.

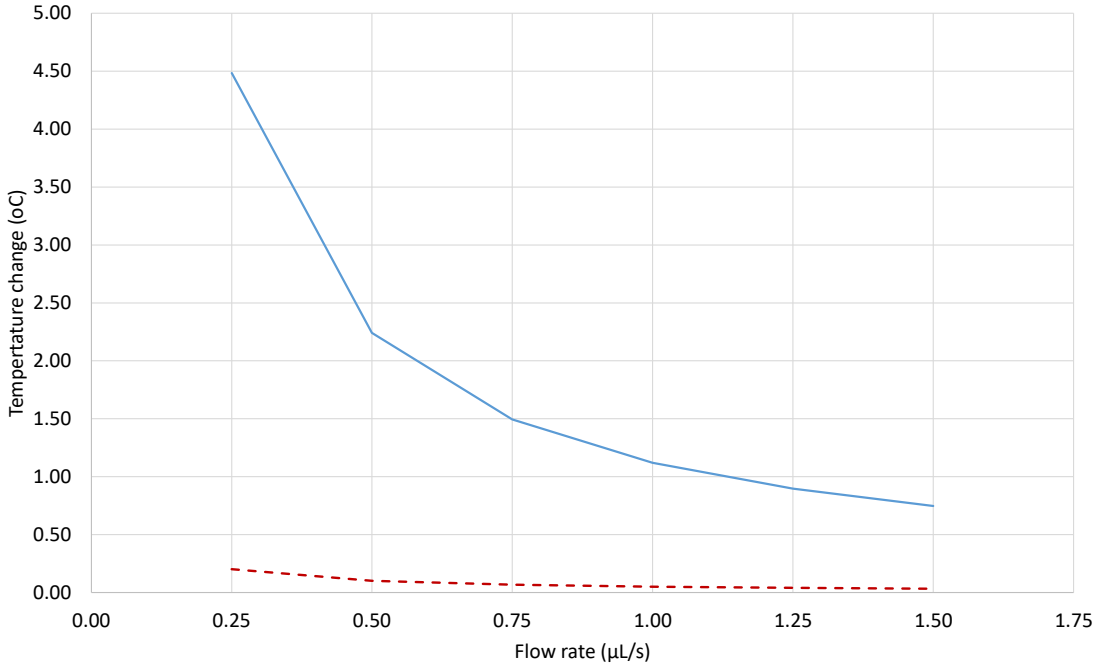

Figure 3.7 Effect of flow rate on temperature change for a jet at a nozzle height of 1.0 mm and with a diameter of 100 µm. The solid blue line is the total change and the dashed orange line is the radiative contribution.

We can now examine the effect of changing the jet geometry on the temperature of the ink. The constant variables in each case are a nozzle height of 1.0 mm, jet diameter of 100 µm and a flow rate of 0.25 µL/s. These are chosen as typical values from later work, except for the flow rate, which is set to a low value to amplify the trends. First, Figure 3.5 shows that increasing the diameter causes a small linear increase in the temperature drop of the ink as it travels from nozzle to substrate. It can be seen from the equations that this is because the second term of the average Nusselt number is proportional to $1/D$, while the jet surface area is proportional to D. This cancels out and leaves only the first term of Nu, scaled by the increased area, to increase the heat loss. Note that this also gives a non-zero y-intercept. For a smaller jet, there is a relatively greater volume of air into which the heat can diffuse. We can see that the radiative losses are small compared to the convective losses, only really becoming significant above 100 µm, although they do contribute about a third of the gradient.

Second, we plot the effect of nozzle height above the substrate in Figure 3.6. Again, we see a linear increase in temperature drop. The second term of the expression for Nu is proportional to L, as is the area, but the convective heat transfer is proportional to $1/L$. This accounts for the hot air rising up the jet being less able to absorb heat from the top of the jet than the ambient air at the bottom. Here the y-intercept is zero because it is assumed in deriving the Nusselt number that heat flows are perpendicular to the curved cylinder surface and so there is no heat flow on the flat surfaces. This means the volume of air available to remove heat is directly proportional to the nozzle height in this model.

Finally, in Figure 3.7, we see the effect of flow rate on temperature change. The jet geometry is constant; therefore, so are the heat flows and we only need consider equation 3-8. As the temperature change is inversely proportional to the mass flow, the graph takes the shape of a simple reciprocal curve and doubling the flow halves the temperature change.

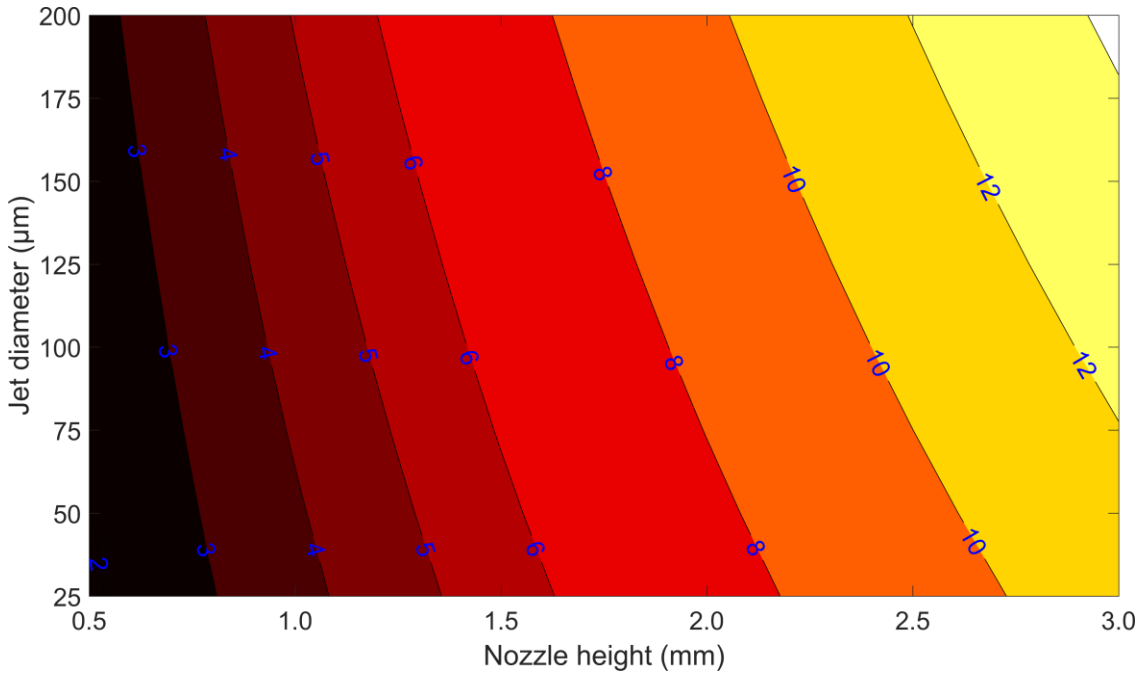

Figure 3.8 Contour plot of temperature drop during flight for a jet at different nozzle heights, different diameters and a flow rate of 0.25 µL/s.

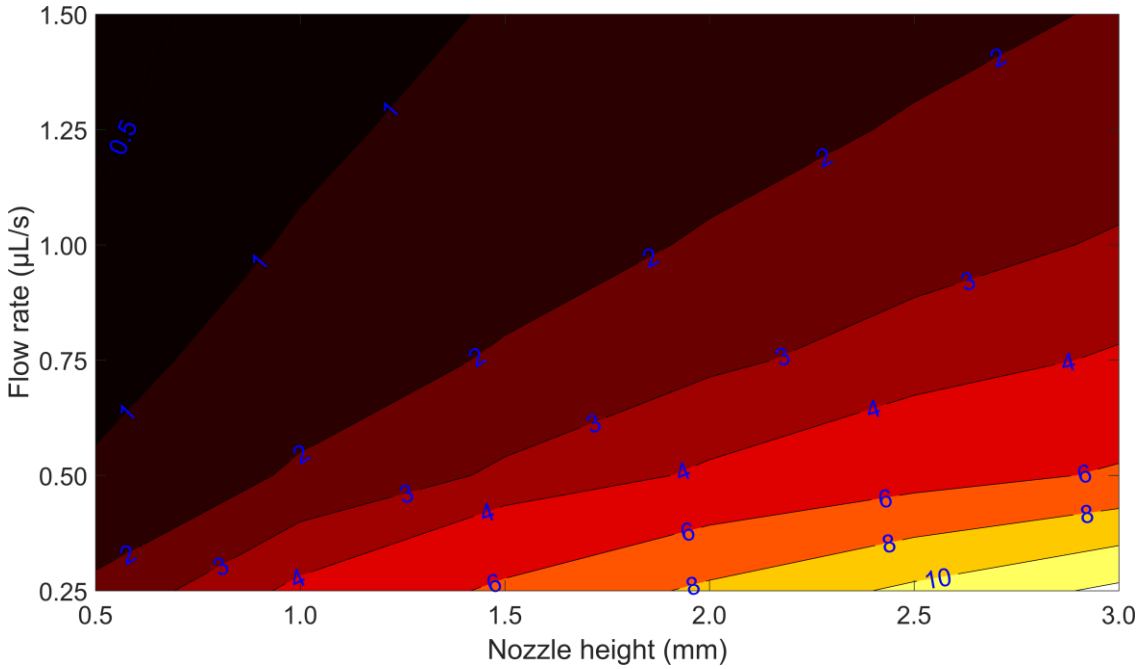

Figure 3.9 Contour plot of temperature drop during flight for a jet at different nozzle heights, different flow rates and a diameter of 100 µm.

These results can also be visualised as contour plots, which can demonstrate the relationship between a pair of variables. This is shown for jet diameter and nozzle height in Figure 3.8 and for flow rate and nozzle height in Figure 3.9. As expected, the jet diameter has a comparatively small effect on temperature loss, giving contour lines mostly aligned with its axis.

Figure 3.9 shows a significant area of the parameter space with very little temperature loss. In practice this region of high flow and small nozzle height is not very interesting, as it should give little chance for the jet to thin and will require very high substrate speeds. For both contour plots, the maximum temperature drop is in the range of 12-14 ^{o}C. Again, this might not be useful in practice as longer jets will be thinner and need higher flow rates to be stable, whereas maximum temperature drop is for a jet that is long, thick and has low flow. For the conditions that are likely to be used in experiments, the temperature drop is between 1-5 ^{o}C. When compared to the difference between the initial temperature and melting point of the ink, which is 25 ^{o}C, this is a small to negligible reduction. The temperature loss is driven by the larger difference between initial temperature of the ink and ambient temperature, so lowering the initial ink temperature slightly would amplify the effect of convective heat loss. This weak cooling also means that under most conditions the ink will still be molten at the point which it contacts the substrate.

3.3.2 Conduction on the substrate

Once the ink is on the substrate, there are two important points to consider. The first is when the ink begins to freeze, which will occur at the interface with the substrate and can have a significant effect on the spreading of the deposit. The second is when the whole cross-section of the deposit has frozen, at which time the shape is fully locked and cannot be affected by, for example, additional deposits on top of it.

In this model, we will only consider conduction through the deposit to the substrate, assuming the substrate to be fixed at ambient temperature and that there is no interface resistance. The geometry of the problem is set out in Figure 3.10. The distance x is not

used directly; instead it is used to define the contact ratio, *N*, as shown in equation 3-9. The values of the required properties are given in Table 3.4 and the ink is assumed to have a sharp melting point.

3-9 $$N = \frac{x}{D}$$

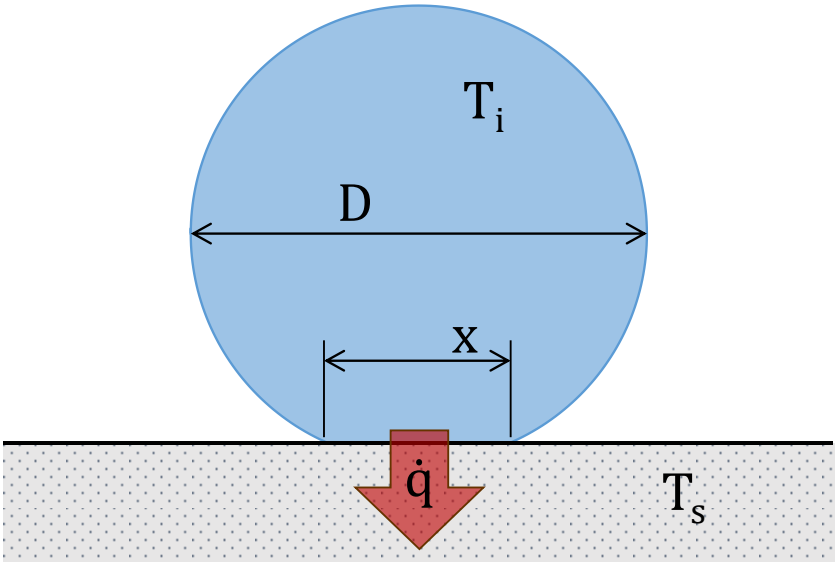

Figure 3.10 Cross-section of deposited ink on the substrate, showing the dimensions for modelling the conductive heat loss from the deposit on the substrate.

Property	Symbol	Value	Units
Density	ρ_i	2,400	kg m^{-3}
Specific heat capacity	c_i	1.12×10^3	J kg^{-1} K^{-1}
Thermal conductivity	k	15.1	W m^{-1} K^{-1}
Latent heat of fusion	L_f	4.00×10^4	J kg^{-1}
Ink temperature	T_i	353 (80)	K (°C)
Melting point	T_m	328 (55)	K (°C)
Substrate temperature	T_s	298 (25)	K (°C)

Table 3.4 Ink properties for modelling solidification on the substrate

The thermal power due to conduction between parallel surfaces is defined as:

3-10 $$\dot{q} = \frac{kA_{contact}(T_1 - T_2)}{d}$$

Where $A_{contact}$ is the area over which conduction is occurring, T_1 and T_2 are the hot and cold temperatures respectively and d is the distance between the surfaces. This assumes a constant cross-sectional area along the path of conduction and constant temperatures, neither of which are the case in this model. To produce an estimate for a given length of deposit, l, the conduction distance is assumed to be half the deposit diameter and the high temperature is taken as the melting point, resulting in equation 3-11. Until a portion of the deposit has finished freezing, T_m is the lowest temperature any portion of the deposit can be, so using it as the high temperature will give a conservative estimate of heat flow.

3-11 $$\frac{\dot{q}}{l} = \frac{kN(T_m - T_S)}{2}$$

The energies that must be removed to cool a given length of deposit to the melting point, q_{cool}, and subsequently for it to freeze, q_{freeze}, are given by equations 3-12 and 3-13 respectively, where $A_{section}$ is the cross-sectional area of the deposit. This is a circle with a segment removed, the area of which is given by equation 3-14. The central angle of the segment in radians, θ, can be neatly expressed in terms of the contact ratio, as shown in equation 3-15.

3-12 $$\frac{q_{cool}}{l} = c_i \rho A_{section}(T_i - T_m)$$

3-13 $$\frac{q_{freeze}}{l} = L_f \rho A_{section}$$

3-14 $$A_{section} = \pi(\frac{D}{2})^2 - \frac{D^2}{8}(\theta - sin\,\theta)$$

3-15 $$\theta = 2sin^{-1} N$$

Finally, the time to reach the point of interest, *t*, is simply given by equation 3-16, with q either being q_{cool} or $q_{cool} + q_{freeze}$, corresponding to the assumed inception and completion of deposit solidification.

3-16 $$t = \frac{q}{\dot{q}}$$

Figure 3.11 shows how these times vary with the contact ratio. The chosen range of contact ratios was informed by visual inspection of a broken deposit under an optical microscope and the X-ray images presented in Section 8.2.1. The freezing time is not very sensitive to the contact ratio for contact ratios above 0.2, so it does not need to be tightly controlled to ensure consistent results.

The effect of diameter on freezing time is shown in Figure 3.12. By using the contact ratio to eliminate the diameter from equation 3-11, changing the diameter only varies the area and thus the energy that needs to be lost. This results in a parabolic curve passing through zero.

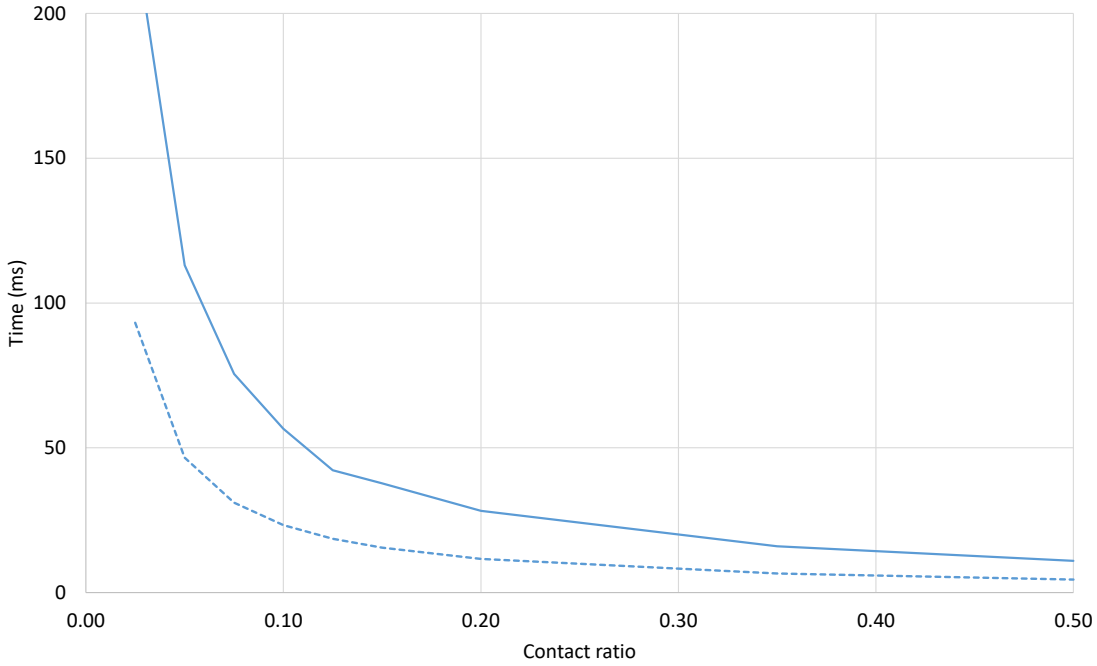

Figure 3.11 Effect of contact ratio on freezing time for a deposit of 100 µm diameter, starting at 80 °C. The dashed line is the start of freezing and the solid line is complete freezing of the deposit.

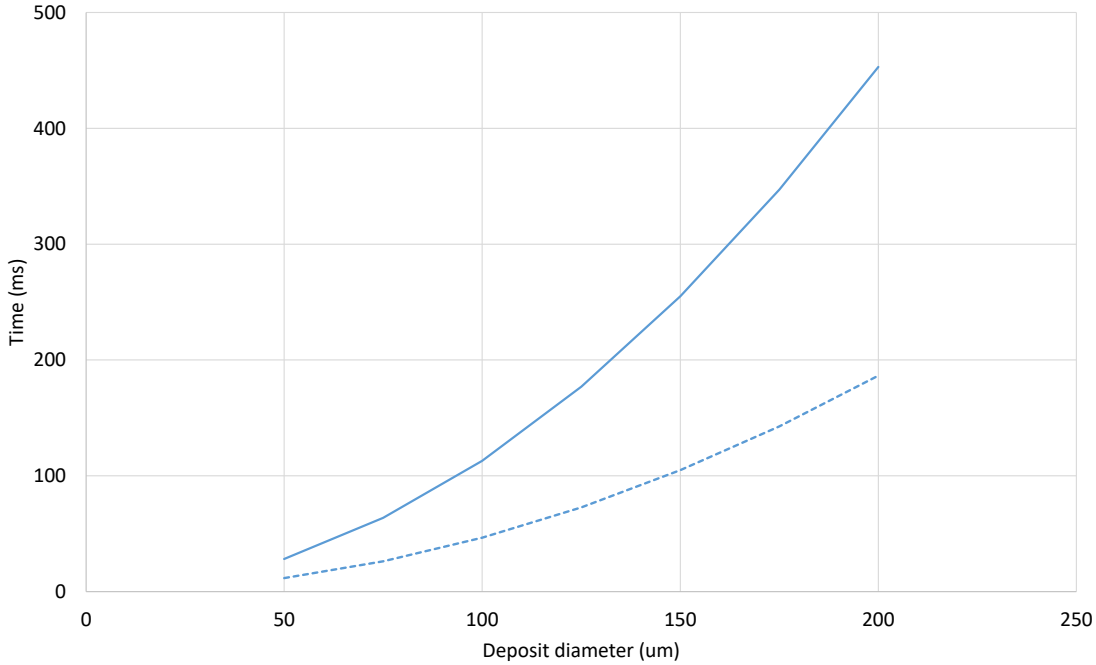

Figure 3.12 Effect of deposit diameter on freezing time for a contact ratio of 0.05, starting at 80 °C. The dashed line is the start of freezing and the solid line is complete freezing of the deposit.

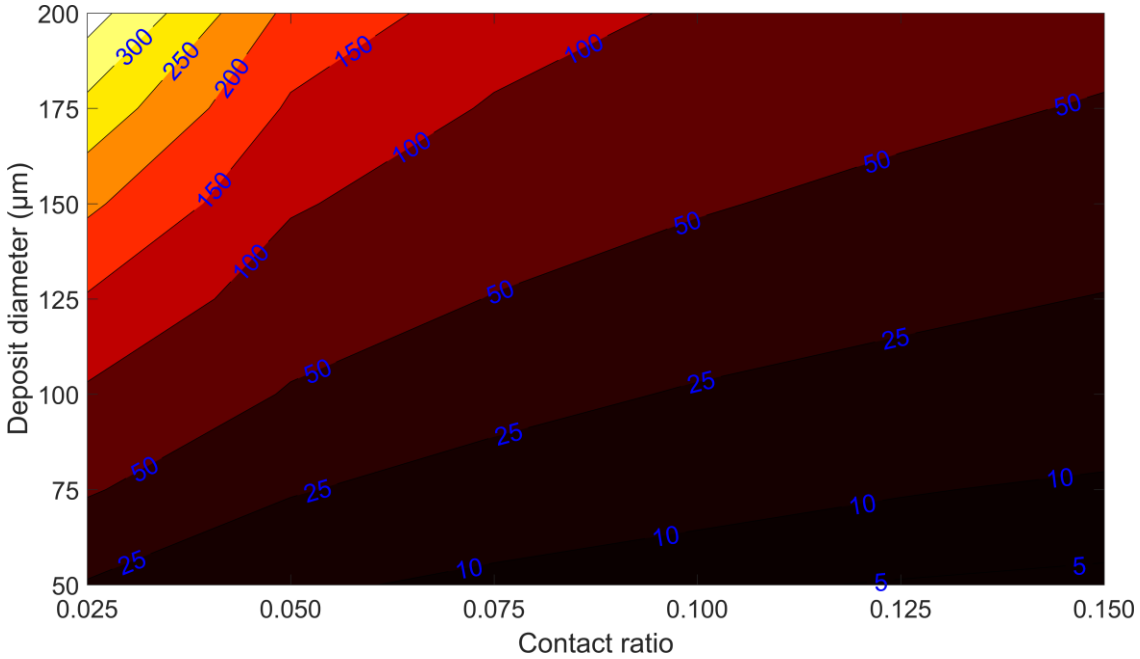

Figure 3.13 Time for a deposit to cool to its melting point for various diameters and contact ratios. The blue numbers are time in milliseconds.

For deposits with a diameter as large as 200 µm, it is estimated to take less than 200 ms to pin the contact area and less than 500 ms to solidify the entire deposit. Assuming the nozzle is moving at 50 mm/s relative to the substrate, this equates to deposition distances of 10 and 25 mm respectively. Compared to the intended nozzle heights of a few millimetres, this is quite a large distance. For example, if patterning a hollow cylinder with a circumference of less than 25 mm, which is a diameter of around 8 mm, the first layer will not have fully solidified when the second layer begins. Note that for this model we have not included any cooling that occurs while the jet is in flight, which would reduce the cooling time on the substrate. However, the heat of fusion is unaffected by the temperature of the incoming ink and accounts for almost half of the time it takes to fully solidify, limiting the overall reduction. On the other hand, if the top surface of the deposit is molten or close to melting when more ink is deposited on top of it, there will be a stronger bond between the layers. Furthermore, if the pinning of the contact area is more important for determining the shape than full freezing, the minimum cylinder diameter reduces to 3.2 mm. The problems this slow freezing might cause will also be minimised by the increase in viscosity of the molten ink as the temperature drops, which will limit any flow due to self-weight or additional layers of ink. Figure 3.13 replots the cooling times for both the contact ratio and the deposit diameter as a 2D contour plot. The region in which cooling takes long enough to cause potential problems is clearly visible to the top left, but for the given parameter space this region is small.

3.4 Conclusions

A shroud around the nozzle with a flat lower face and slightly recessed from the nozzle tip (Figure 3.3 (c) and (e)) provides a good compromise between high electric fields at the nozzle to exaggerate stretching of the ink, vertically aligned electric field to promote the electro-jet travelling straight downwards and maintaining a suitable temperature at the nozzle. Due to the high electric fields around the nozzle, dielectric breakdown of the air might occur at a lower potential difference than expected.

While travelling from the nozzle to the substrate, cooling of the ink varies from negligible, for a small nozzle height and high flow rate, to around 10 ^{o}C, for a low flow rate and a nozzle height of 3 mm. The cooling increases with the diameter of the jet but the effect is smaller than that of these other two variables. Radiative losses are negligible, except for jets with diameters over 200 μm. Under practical conditions, the cooling effect is expected to be a few degrees Celsius, suggesting it may be useful to use an ink temperature less than 80 ^{o}C and that it is expected the ink will still be liquid as it hits the substrate.

The time taken for the ink to solidify fully on the substrate may be as high as 0.5 s for large deposits with small contact areas, but will be around 0.2 s for more typical deposit sizes. Reducing the contact ratio only causes a small increase in the freezing time if it is above 0.2 and drastically increases it when below that value. For ink at 80 ^{o}C, around half of the time to solidify fully comes from dissipation of the heat of fusion, limiting the ability to reduce the freezing time by lowering the temperature of the ink in the nozzle. It is expected that in practice, full solidification will occur sooner due to cooling while the ink is in flight and the conservative heat flow used in this modelling. Furthermore, increases in ink viscosity due to cooling will limit any potential problems from slow solidification.

4 EQUIPMENT DEVELOPMENT

This chapter will discuss the design of equipment produced for this work and the considerations that drove its development. This equipment included a custom syringe pump, capable of high driving force and of heating the syringe; a high voltage supply and the connection of its outputs; and two stages for ink to be deposited onto, the first a rotary stage for observing the electro-jets and the second a three-axis system for creating 3D patterns.

4.1 High pressure heated syringe pump

Most commercially available syringe pumps are intended for use with low viscosity fluids and are not capable of exerting large forces on the syringe plunger. Few of them are designed to heat the syringe and combining these two features is rare. Therefore, one was custom built for use in this work.

The basic components of a syringe pump are the syringe, a motor, a leadscrew and nut to convert from rotational to linear motion, and a support structure. Placing the motor, leadscrew and syringe along the same axis provides the most direct transfer of force but results in a very long piece of equipment. As the pump would be mounted on a moving gantry, it was designed to be compact, so the motor and leadscrew were

positioned off-axis. To counter the torque produced by the off-axis forces, guide rails were added to either side of the syringe. The final embodiment is shown in Figure 4.1 and dimensioned drawings of the components are provided in Appendix A.

A stepper motor was chosen to drive the pump because of its intrinsic positional accuracy. With a suitable driver, such as the Allegro A4988 used here, it could also be easily controlled directly from a signal generator or from common 3D printer hardware (see Section 4.2.2). The specific motor used here was a Nanotec LS4118S1404-T6X2-150 (RS Components, Northamptonshire), which had an integrated leadscrew with a diameter of 6 mm, pitch of 2 mm and usable stroke of around 125 mm. This removed the need for a coupler to an external leadscrew and reduced the overall size. The motor had a NEMA17 faceplate and produced 0.2 Nm of torque at 1.4 A, which gave a theoretical linear force of 628 N on the leadscrew nut when ignoring friction.

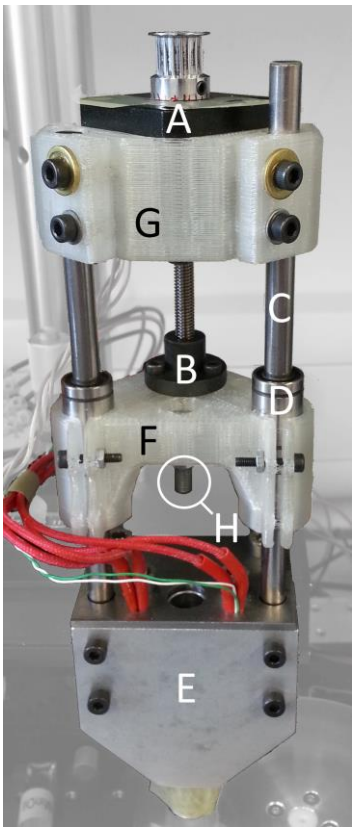

Figure 4.1 Syringe pump mounted above the rotary stage with heating electronics installed. A) Stepper motor. B) Leadscrew nut. C) Guide rail. D) Linear bearing. E) Heater block. F) Drive plate. G) Motor mount. H) Plunger mounting screw.

The pump was designed to use 3 mL plastic-bodied syringes, chosen due to their availability, standard sizing and as a compromise between higher volumes, for patterning larger objects, and narrower diameter, to produce higher pressures for a given force. At a flow rate of 1.0 µL/s, this syringe size held enough material to dispense continuously for 50 minutes. The inner diameter of the syringes was 9.6 mm, giving a pressure of over 8.6 MPa at the theoretical peak force of the motor. The real pressure would be somewhat lower due to friction between the leadscrew and nut as well as between the plunger and syringe wall, but it was sufficient to burst the walls of the syringe at room temperature if it was not well supported. To achieve the rated capacity, the plunger needed to move around 41 mm within the syringe, but the body of the syringe was 58 mm long. Leaving this extra distance empty ensured proper sealing and guidance of a standard plunger, although the plunger used here was rigidly mounted to the pump so the syringe could be filled to around 4 mL without causing issues.

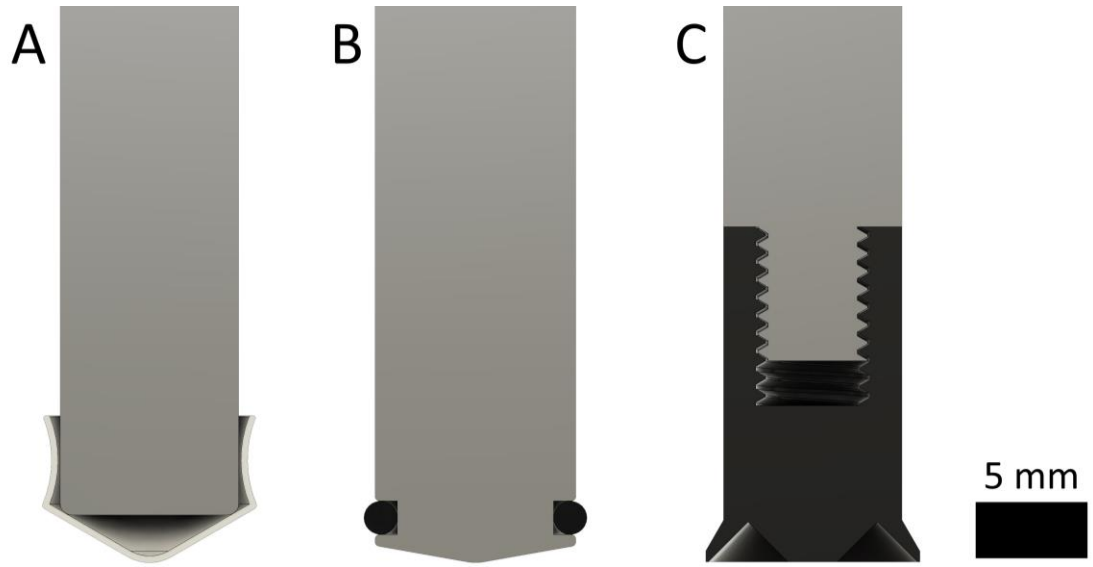

Figure 4.2 Cross-sections of the different plunger designs. A) Pneumatic piston pressed onto metal rod. B) Rubber O-ring seated in a groove on a close-fitting rod. C) Custom machined acetal tip with thin, downward-angled flange threaded onto metal rod.

Design of a suitable plunger tip took several iterations. A typical syringe plunger for handheld use was not able to transmit the level of force this pump can produce. Some preliminary work was done using pneumatic pistons placed in front of or pressed onto

the tip of a metal rod, as shown in Figure 4.2 (A), but the rod did not provide support in the areas needed for the piston to provide a good seal. The first iteration of a custom-made plunger used a butyl rubber O-ring located in a groove near the tip of an aluminium rod, shown in Figure 4.2 (B). The first problem with this design was that the O-ring could be pushed out of the groove, breaking the seal, unless the diameter of the rod was very close to that of the inside of the syringe. The second problem was that some ink formulations, particularly those including limonene or esters, and the elevated temperatures caused the O-rings to swell and soften, also causing failure. Changing the O-ring for one made of a different material could have circumvented this, but a more versatile solution was developed instead. This consisted of a short piece of acetal rod with a thin, downward-angled flange, screwed onto the end of the aluminium rod. The exact geometry can be seen in Figure 4.2 (C) and a dimensioned drawing is provided in Appendix A. Acetal has a service temperature in excess of 80 ^{o}C, is very durable and has good chemical resistance. The flange was thin enough to have some flexibility and provided the sealing surface against the syringe wall. Being angled downward, the pressure below the plunger pressed the flange into the wall to increase the sealing force at higher pressures.

To provide mechanical support and heating to the syringe, it was held in a block of aluminium. The heater block is shown in Figure 4.1 (E) and the main features are laid out in Figure 4.3. The main block was a simple cuboid with a series of vertical holes. Arranged around a central hole for the syringe were pairs of holes for heater cartridges (H), mounting bolts (G) and the guide rails (F) of the pump. The holes for the syringe and guide rails were through-holes; the other holes stopped around halfway through the block. There were cross-holes into the guide rail mounts for screws to lock the rails in place, as the rails also counteracted the drive force of the pump. On the bottom face of the syringe block, two edges were chamfered to improve access to the nozzle area. The bottom end of the syringe hole had an M16 thread, into which different nozzle shrouds could be threaded. The shroud, also made of aluminium, conducted heat from the syringe block to the proximity of the nozzle itself and provided the vertical constraint of

the syringe. A small cross-hole near the nozzle end was included in the shroud to allow access for a wire to ground the syringe tip.

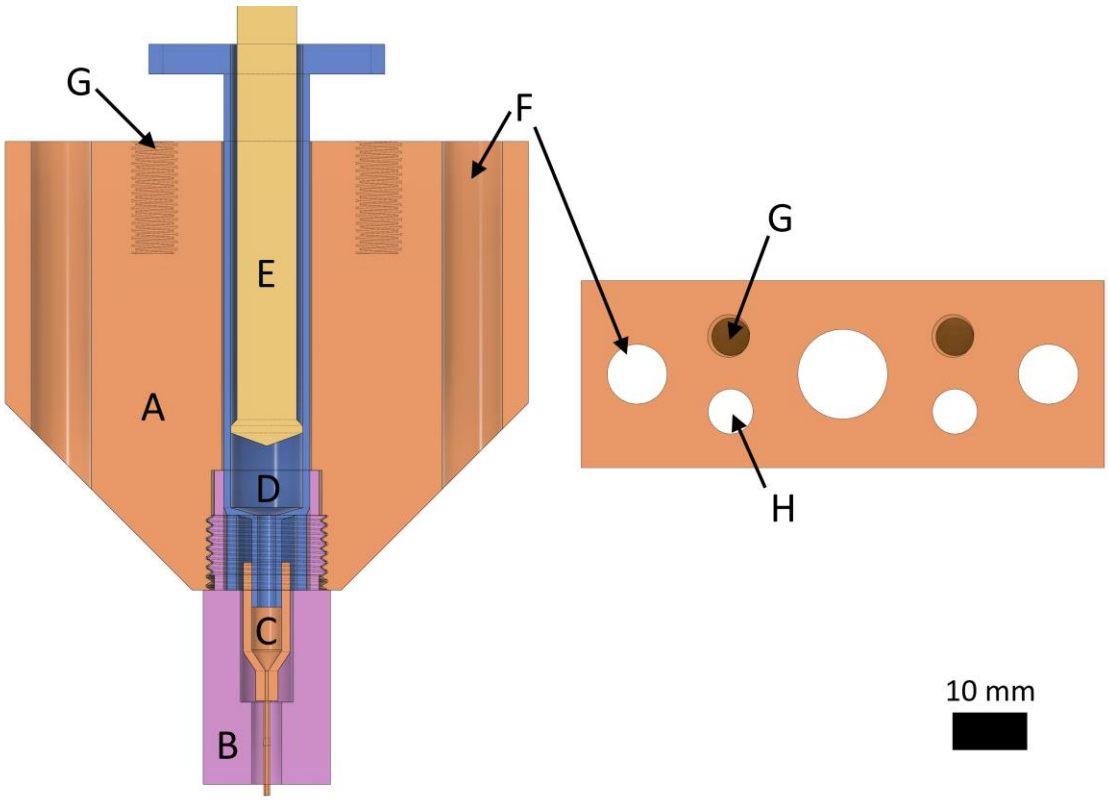

Figure 4.3 Section view (left) and top-down view (right) of heated syringe block. A) Heater block. B) Nozzle shroud. C) Blunt needle tip. D) 3 mL syringe. E) Plunger. F) Guide rail mounting holes. G) Threaded mounting holes, behind cross-section plane. H) Heater cartridge holes, in front of cross-section plane.

The drive plate and motor mount, seen in Figure 4.1 as (F) and (G), were 3D printed in PLA on a consumer-grade FDM machine. They wrapped around the guide rails and linear bearings respectively, clamped in both cases by bolts and nuts. The motor was screwed to its mounting bracket and the leadscrew nut and plunger were screwed to the drive plate.

Control of the heating was provided by a Red Lion PID controller. One or two 40 W heater cartridges were powered in parallel from a DC power supply via one output of the PID controller. A K-type thermocouple was inserted into the same hole as one of the heater cartridges to provide feedback to the controller. It was positioned touching

the top edge of the cartridge and held in place by the compression of the wire insulation of the cartridge. During use, the control loop maintained a constant temperature of 85 ^{o}C according to its display, even with only one heater cartridge. At a target temperature of 85 ^{o}C, the temperature at the bottom of the shroud was 80-81 ^{o}C. Wiring connections are given in Appendix B.

In testing with an oil-based ink containing 50 vol% alumina powder, as used in Section 6, the pump produced flow rates that were on average 91 % of the demanded flow rate, with a standard deviation of 3 %. For example, this means setting the pump to 1.00 µL/s would typically produce 0.87 – 0.94 µL/s. This testing was carried out at 85 ^{o}C and flow rates of up to 2.0 µL/s as worst-case conditions, with samples taken over periods of one to six minutes. The pump was allowed to settle for five to ten minutes after changes in demanded flow rate, but the low flow rates and flexibility of the syringe meant that some transient behaviour likely increased the variability of these results. In most experiments the run time was much longer than this, giving time for these transients to decay. Furthermore, the dispensed volume was calculated based on densities at room temperature. At 85 ^{o}C, the paraffin wax will have a density considerably lower than at room temperature, accounting for the majority of the offset ("Viscosity of Paraffin Wax – viscosity table and viscosity chart," n.d.).

4.2 Deposition stages

4.2.1 Rotary stage

In order to observe the electro-jet for an extended period, the nozzle needed to be stationary so that a camera and light source could be aimed at the jet. Therefore, the substrate needed to move, and the easiest way to achieve arbitrarily long deposition distances was with a rotating stage. The stage itself was an aluminium disk, 3 mm thick and 120 mm in diameter, which was screwed onto a short section of acetal rod. This rod had a small protrusion on the top surface to locate the disk, a hole in the bottom surface to mount onto the motor shaft and a cross-hole for a screw to lock the motor shaft in place. The motor was a Trinamic QSH4218-35-10-027 NEMA17 stepper motor

(Farnell, Leeds), which was mounted inside a bracket 3D printed in PLA that in turn mounted to an optical breadboard. The motor mount was designed such that the motor was electrically isolated from the breadboard, which was grounded, and the acetal piece isolates the motor from the substrate, which was held at a high positive voltage. The motor mount and coupler are shown in Figure 4.4. The motor was driven by a stepper driver with step pulses coming directly from a signal generator, as shown in Appendix B.

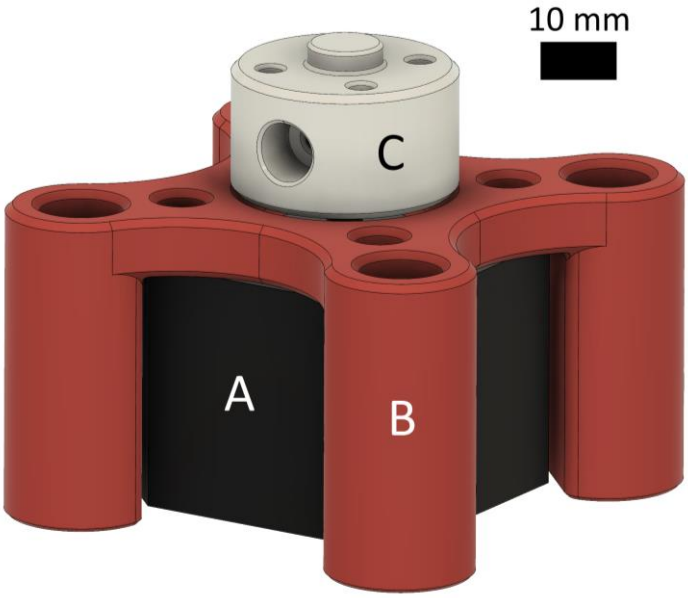

Figure 4.4 The stepper motor (A) for the rotary stage, with its motor mounting (B) and coupling block (C).

To allow for deposition onto a clean substrate for more than one revolution of the stage, a wiper was set up touching the top of the substrate on one side. This was again 3D printed in PLA and presented a vertical wall to the approaching substrate. The bottom face was angled up away from the substrate, so that only the leading edge of the wiper contacted the substrate surface. The wiper clamped onto a metal rod screwed into the optical breadboard, allowing for adjustment to the height, different angles of the wiper and moving the wiper to different positions around the stage. A typical position of the wiper is shown in Figure 4.5 and the practical setup is shown in Figure 4.6.

Electrical contact with the substrate disk was made through a solid copper wire sliding on the underside. Good electrical contact was ensured by making the aluminium surface smooth and positioning the wire so that it was sprung against the substrate disk.

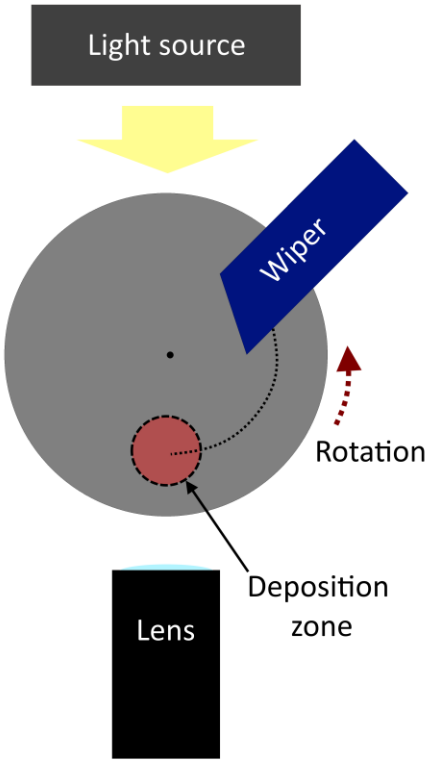

Figure 4.5 Schematic of the rotary stage apparatus.

To capture images of the electro-jet, the syringe pump was positioned upright with the nozzle at the desired height. A Nikon D40 DSLR camera was set up on one side of the stage with a Navitar 12X Zoom microscope lens and 2x F-mount tube (part numbers 1-50504 and 1-62922 from Close-Ups, Berkshire), adjustable from 1.2 to 14 times total magnification. For all experiments, the camera was positioned slightly above the top surface of the substrate so that it was looking downward by a couple of degrees. This reduced the need to match the camera height exactly to the height of the substrate and allowed for imaging the reflection of the deposit. This helped to establish the otherwise difficult to distinguish surface of the substrate in captured images without introducing significant distortion of the image. An ARRILUX Pocket PAR 125 light source was set up diametrically opposite to the camera, aimed at the lens. The nozzle and wiper were

arranged as shown in Figure 4.5, so that the nozzle was directly in front of the camera lens over the near side of the rotary stage. Note that the distance of the nozzle from the centre of the stage sets the linear speed of the substrate at a given motor rotational speed, so required careful adjustment or at least accurate measurement. In all experiments, the nozzle was set to be 40 mm away from the centre of rotation. The imaging axis intentionally passed through the centre of rotation of the stage, so that the section of jet that the camera captures was moving as close to perpendicular to the imaging axis as possible. The wiper was positioned to remove the deposit before it passes through the imaging line a second time, avoiding it being visible in captured images, and so that the wiper was outside of the camera's field of view. The practical setup is shown in Figure 4.6.

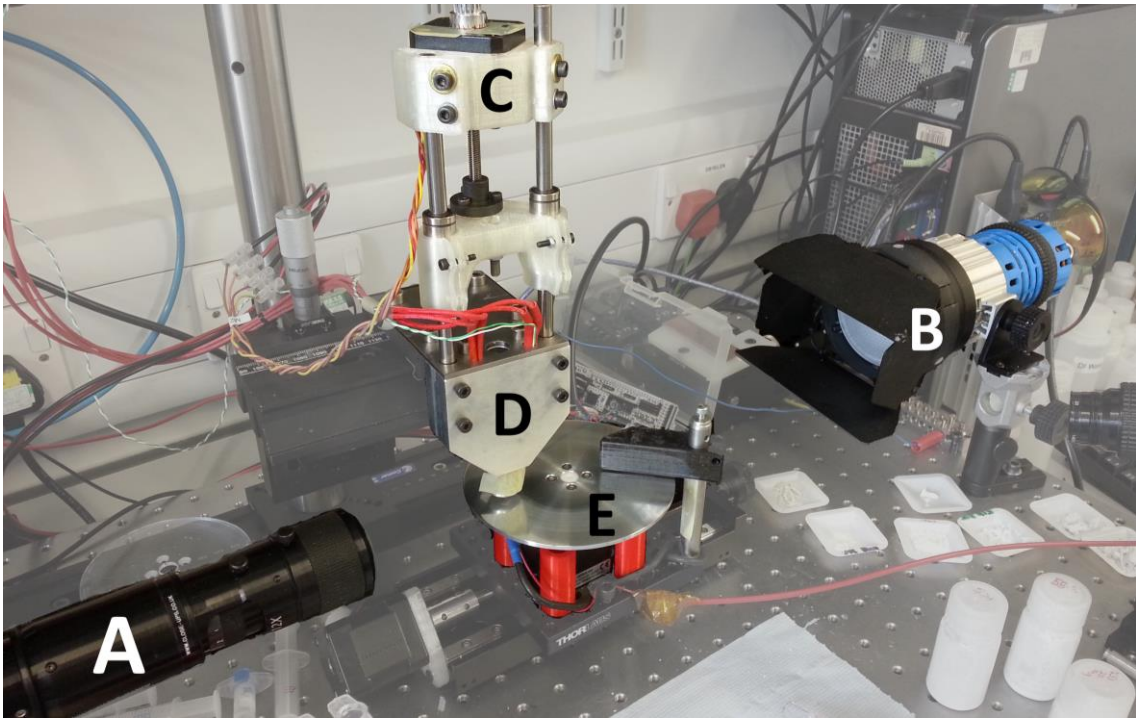

Figure 4.6 Arrangement of the rotary stage apparatus.
A) Camera lens. B) Light source. C) Syringe pump motor. D) Syringe heating block. E) Rotary stage.

4.2.2 Three-axis stage

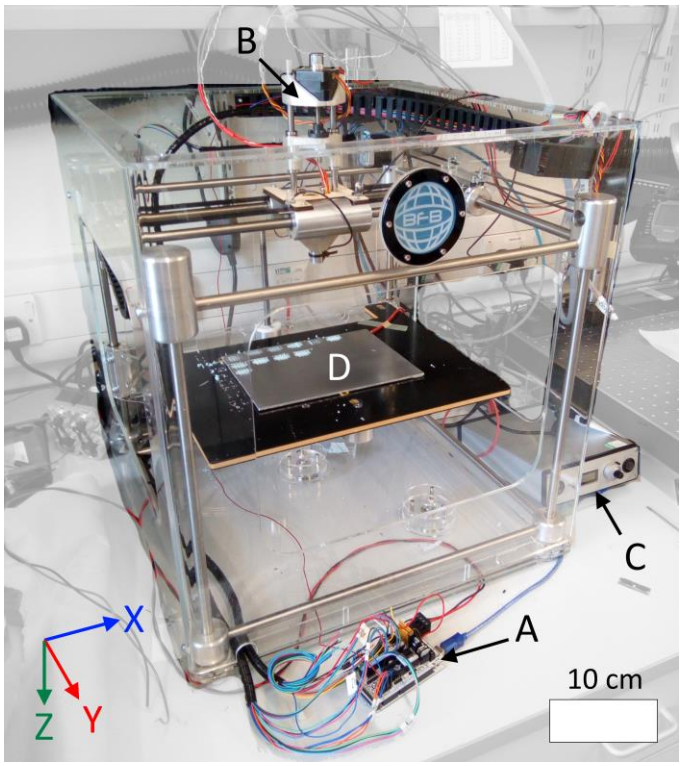

Figure 4.7 The modified BFB 3000 printer. Lower left shows the coordinate system of the motion axes, with the arrows indicating increasing coordinates. A) Replacement control electronics. B) Heated syringe pump. C) High voltage supply. D) Aluminium substrate.

For producing useful patterns, two horizontal axes were needed (X and Y). To allow for patterns with multiple layers, an additional vertical axis (Z) was also desirable, making three axes in all. A surplus FDM 3D printer was modified to fit the custom syringe pump for this purpose. The original machine was a 'Bits from Bytes' BFB3000 printer, which is now discontinued. The tool moved in the horizontal plane on two perpendicular pairs of round rails and linear bearings at the top of the machine, driven through belts by NEMA17 stepper motors. The X-axis moved the tool carriage with a single motor and the Y-axis moved the X-axis with two motors. The bed of the machine moved vertically on another pair of round rails, driven by a small ball-screw and NEMA23 motor. The build-plate was removable, and its mounting system included three points for manual height adjustment, allowing the top surface to be adjusted to

match the plane of the nozzle. Each axis had an inductive end-stop sensor for homing. The original electronics required proprietary code to run and were not easy to modify, so were removed from the machine along with the original extrusion heads. A 3 mm thick aluminium plate was placed onto the bed as a conductive substrate, with a wire pressing against the top surface of the plate providing electrical contact without distorting it. The weight of the plate was enough to keep it in place under printing conditions. A plywood plate was fabricated to mount the custom syringe pump in place of the original extruders. The printer is shown as used in this work in Figure 4.7.

The motors and sensors were wired to a RAMPS 1.4 interface board with Allegro A4988 stepper motor drivers and mounted onto an Arduino Mega 2560 microcontroller (Ooznest Ltd, Essex), as laid out in Figure 4.8. Wiring connections are provided in Appendix B. This open-source solution was chosen for its low cost, customisability and compatibility with freely available FDM slicing software. The Arduino was flashed with Marlin 1.0.2 firmware ("Marlin," 2018) after modifying the configuration files to use appropriate values for the motion settings. Additionally, features that prevent cold extrusion were disabled. The E-axis is normally used to control the feeding of plastic filament and moving it while the nozzle is cold could damage the filament or machine. The E-axis could have been used to drive the syringe pump, but the heating control was done externally in the presented setup and this feature would have blocked E-axis motion if not disabled. The controller has no file storage, so commands in the form of g-code were streamed over USB from a PC running host software. Many suitable FDM printer host programs are freely available, but here Repetier-Host 0.95 was used ("Repetier-Host," 2018). This software provided on-screen buttons for live control of the machine as well as streaming of g-code files. The currently loaded file could be previewed with a 3D visualisation and the material flow-rate and motion feed-rate could be scaled during file streaming.

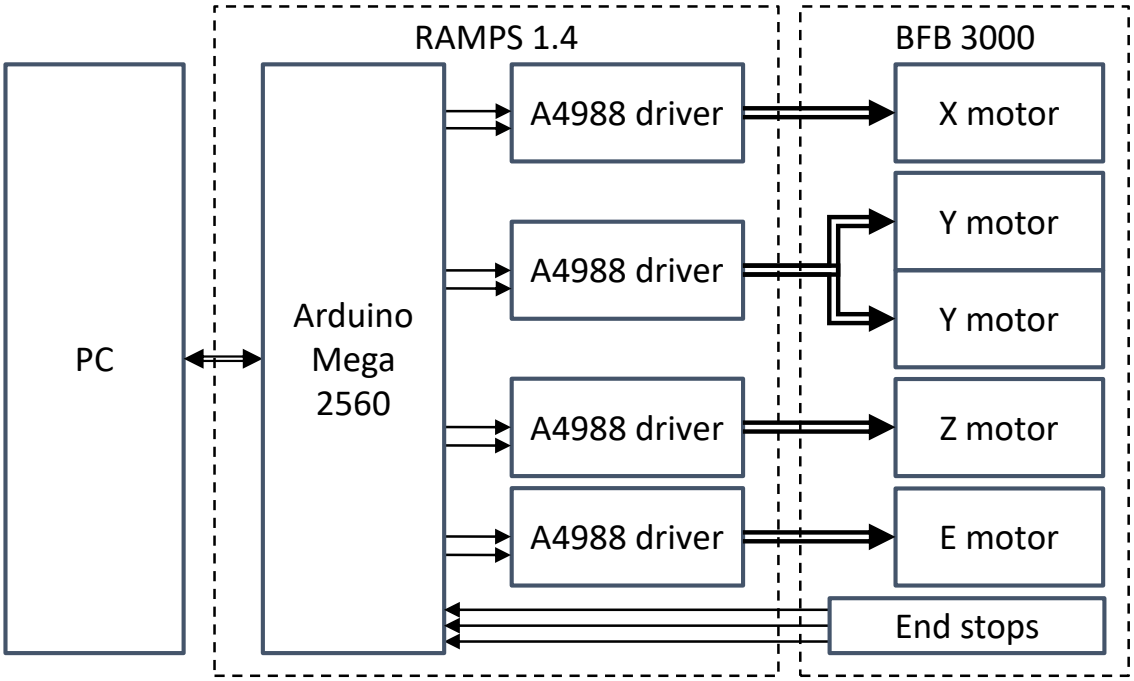

Figure 4.8 Schematic of the electronics for the three-axis stage used in this work, including the dual Y-axis motors and optional E-axis motor.

The use of common FDM machine firmware meant that the three-axis stage was compatible with any slicing software capable of outputting the Marlin (or generic 'RepRap') format g-code. Some adjustment of the slicing parameters was needed, for example setting the nozzle diameter to the expected diameter of the deposit and setting the filament diameter to the internal diameter of the syringe. To prevent unexpected errors or waiting, all instructions pertaining to temperature control should be removed from the g-code, either with settings before slicing or by editing the output file after slicing. In theory, using slicing software would allow arbitrary shapes to be produced with the process that is the subject of this thesis. However, the stopping and starting of the ink flow may present difficulties and there are limits on what geometries can be patterned with this process, as explored in Section 7. This also did not give an easy way to create patterns of individual lines or precise geometries to test the process.

To gain precise control of the motion of the stage, MATLAB was used to program scripts that would automatically generate repeating patterns. Several examples are

given in Appendix F. These scripts include control of the E-axis and setting a nominal speed for all motion. Patterns that are more complex require more complex scripts and curves are cumbersome to program by hand, although this could be addressed with a dedicated function. The provided scripts all use relative coordinates, but the g-code implementation allows absolute coordinates referenced to the machine home position as well as free switching between the two, letting the g-code generator use either at any time for preference and convenience.

The controller was set up so that it could be used to drive the syringe pump, synchronising the flow of ink with the motion of the nozzle. This includes the acceleration ramps that the controller generates, ensuring a constant volume of ink per distance of travel throughout a print. While this approach has great benefits in FDM, it can cause problems for this electrospinning process because the ink flow rate affects the properties of the electro-jet. Therefore, only preliminary work was done with the syringe pump driven by the E axis, and later work used an external signal generator and motor driver to give a constant flow rate, as shown in Appendix B. The errors this approach introduced can be minimised by using low deposition speeds and high acceleration values in the controller firmware, although the latter was limited by the machine mechanics.

4.3 High voltage system

To provide a wide voltage range, a power supply was assembled around a Hitek Power PSM10/103 module as shown in Figure 4.9. This module could output up to 10 kV at 1.0 mA, consuming up to 1.0 A at 24 V. Among other features, it provided a 0-10 V analogue input for voltage control and an independent 0-10 V output for voltage monitoring. The output was protected against short circuits and arcing, which were likely to occur with the nozzle moving above the substrate at electric fields approaching the dielectric breakdown field of air.

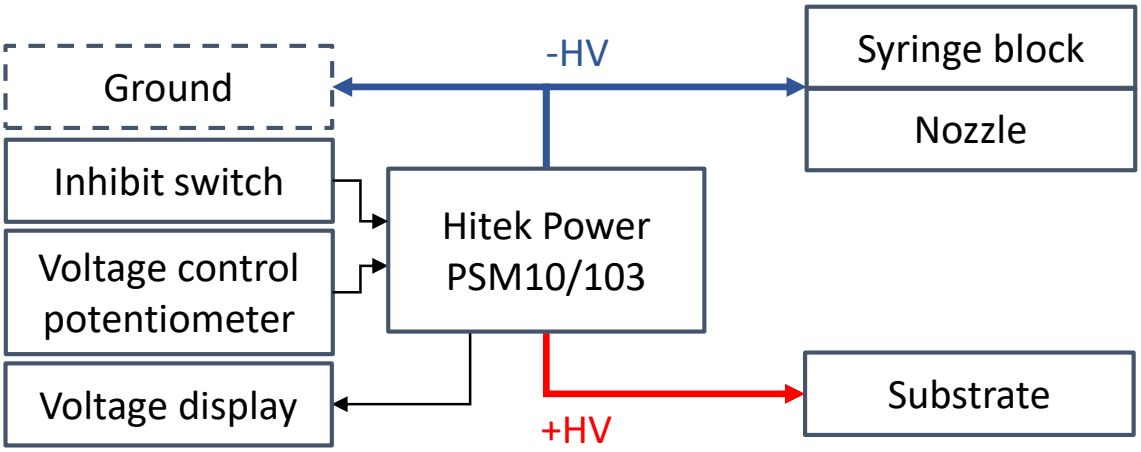

Figure 4.9 Schematic of the high voltage system.

The negative output of the supply was connected to ground along with the heater block and nozzle. With either motion stage, only the aluminium substrate plate itself was connected to the positive output of the high voltage supply. This was primarily done to avoid problems with the heater electronics becoming connected to a high potential, which could cause shorting of the high voltage supply or potentially damage the PID controller. Most methods of electrically isolating the heater components from the heater block would also add an inconvenient level of thermal isolation. Putting the heater block at high potential would also increase the size of the high voltage object, increasing shock risk, and would necessitate isolating it from its mounting. The Hitek module weakly referenced the high voltage outputs to ground internally, so that reversing the polarity, to make the substrate negative with respect to the nozzle, caused the entire experimental setup to sit at an elevated voltage.

5 Ink Formulation

This chapter covers the development and characterisation of the inks used in this work, including details of the materials used. The inks include: an oil based ink to act as an easy to work with model fluid described in Section 5.2, evaporative inks which offered easier post-processing but were unsuitable in Section 5.3, and a UV curable ink that is stable through the high temperature sintering process in Section 5.4.

5.1 Techniques and materials

5.1.1 Materials

Aluminium oxide powders were sourced in two sizes. A 1 kg sample of 1200 grit Duralum White was provided by Washington Mills, Manchester. This grit size translates to an average particle diameter of 4 µm. A second kilogram batch of AP-D alumina was purchased from Struers, Rotherham, with an average particle size of 0.3 µm. Both powders are intended for use as abrasives and are produced by grinding. Figure 5.1 shows scanning electron microscope (SEM) images of the two powders. The particles of the 4 µm powder were at or below the expected size, including many particles down to 1 µm. The 0.3 µm powder had a more consistent particle size but also showed large agglomerations. The particles of both powders were angular, which

would limit their ability to flow and pack densely. The range of particle sizes in the 4 µm powder potentially allowed for better packing, with the smaller particles able to fill gaps between larger particles given sufficient chance to reorganise. Conversely, the large clumps of the 0.3 µm powder would hamper packing of the particles and if not properly broken up in an ink would act as much larger particle with very high surface area and roughness, making production of high solid fraction inks challenging.

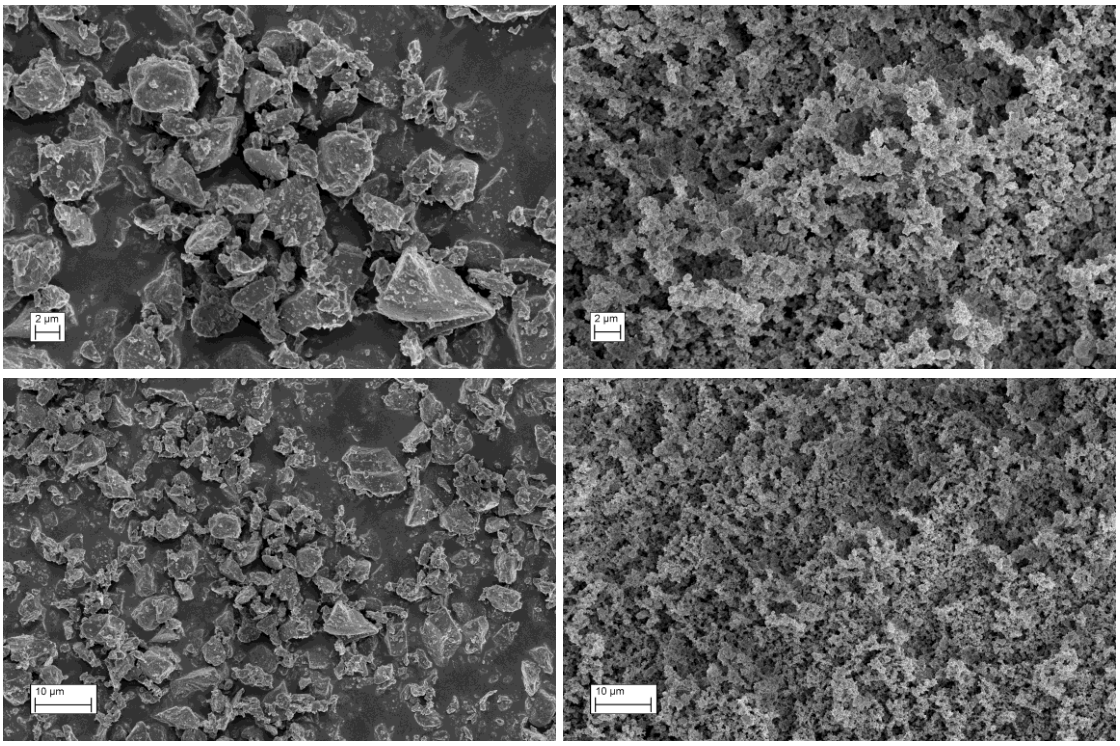

Figure 5.1 SEM images of the two powders, the '4 µm' powder on the left and the '0.3 µm' powder on the right. The powder was sprinkled onto contact cement and sputter-coated with a gold-palladium alloy. Full details of the SEM procedure are in Section 8.1.

For the liquid components of the inks, light mineral oil and n-octane were purchased from Sigma-Aldrich, Dorset. Two paraffin waxes, with nominal melting points of 52 and 60 ^{o}C, and D(+) limonene were purchased from Fisher Scientific, Loughborough. For dispersion of the powder in the liquids, 95 % stearic acid was purchased from Sigma-Aldrich and a sample of Hypermer KD4 was provided by Croda International Plc, East Yorkshire. These dispersants were selected based on the work of Seerden et al. (2001), with KD4 as the currently available equivalent to

Hypermer LP1 used by those authors. Lithojet 210 etch resist (LJ210), a poly-acrylic wax manufactured by The Dow Chemical Company, Derbyshire, was used as a UV-curable component. Key properties of these materials are presented in Table 5.1. To measure the density of a material, 3 to 5 mL of the material were placed into a 5 mL syringe and weighed. All material quantities in this work were measured by weight; where volume percentages are given, they have been calculated using the values in Table 5.1.

Material	**Density (kg m^{-3})**	**Melting point (^{o}C)**	**Supplier code**
Alumina	3,900*	1,700*	-
Paraffin wax (52 ^{o}C)	900*	51-53	P/0600/90
Paraffin wax (60 ^{o}C)	900*	55-65	P/0680/90
Lithojet 210	985**	65-72	-
Light mineral oil	833	-15	330779
Limonene	841	-74	L/1860/07
Octane	703	-57	74821
Stearic acid	845	67-72	175366
Hypermer KD4	900**	26	-

Table 5.1 Properties of the materials used for ink formulation in this work. Data were either taken from material datasheets, generic values (*) or experimentally determined (**).

5.1.2 Rheometry

All rheometry work was carried out on an Anton Paar MCR 302 rheometer. The lower plate was temperature controlled with a P-PTD200/80/I/AIR Peltier module. All samples containing solid powders were measured between 25 mm parallel plates using a PP25 tool set with a gap of 0.3 mm. Lower viscosity samples, such as pure

liquids or mixtures of liquids, were measured with a 50 mm cone with a 1^{o} angle and flat lower plate using a CP50-1 tool set. For samples containing volatile components such as limonene or octane, a FDM 3D printed two-piece cover, as shown in Figure 5.2, was used to enclose the measuring plates. The surface around the lower plate was flooded with the volatile liquid to saturate the atmosphere within the cover.

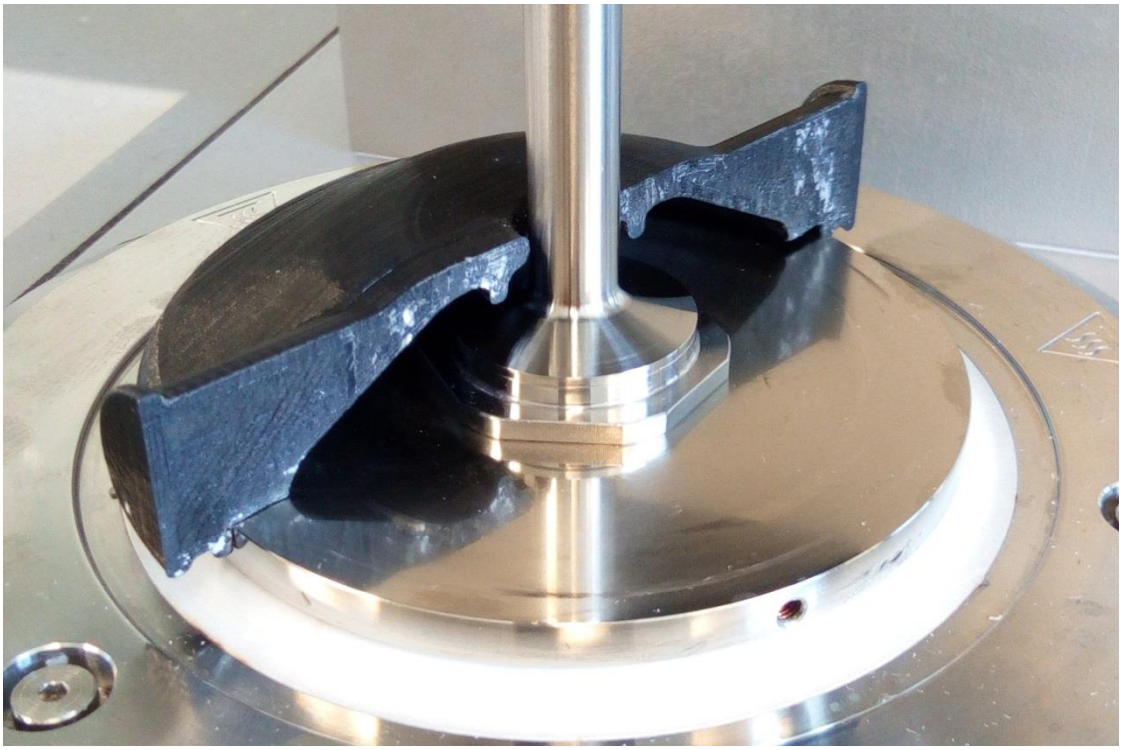

Figure 5.2 Half of the 3D printed cover and PP25 tool installed on the rheometer.

The control software for this rheometer provided a wide range of predefined tests and the ability to define custom tests with many stages. In this work, we made use of only a few measurement types. The simplest measurement was a 'flow curve', measuring the viscosity of the sample over a range of shear rates. As it passed through the nozzle, the ink saw shear rates above 100 /s, which can be estimated by dividing flow velocity by nozzle radius. For example, a liquid flow of 1.0 µL/s through a 200 µm tube will experience shear rates around 318 /s. The ink also experienced very low shear rates when on the substrate after deposition. Ideally, both regimes would have been covered by the flow curve. However, at some rotational speed the sample was

ejected from between the measuring plates of the rheometer by inertial forces, putting a hard limit on the maximum shear rate to which a sample could be exposed. Additionally, very low shear rates required very long measurement times to produce a good signal to noise ratio, putting a soft limit on the lowest shear rates for which we could obtain data. This low-shear issue could be somewhat addressed by taking fewer data points in this region. The rheometer software supported measurements with constant, linear or logarithmic spacing with respect to the independent variable. Figure 5.3 gives an example flow curve, with the corresponding shear stress, showing the noisy data at low shear rate and a maximum shear rate that consistently did not eject any of the sample for the tested inks.

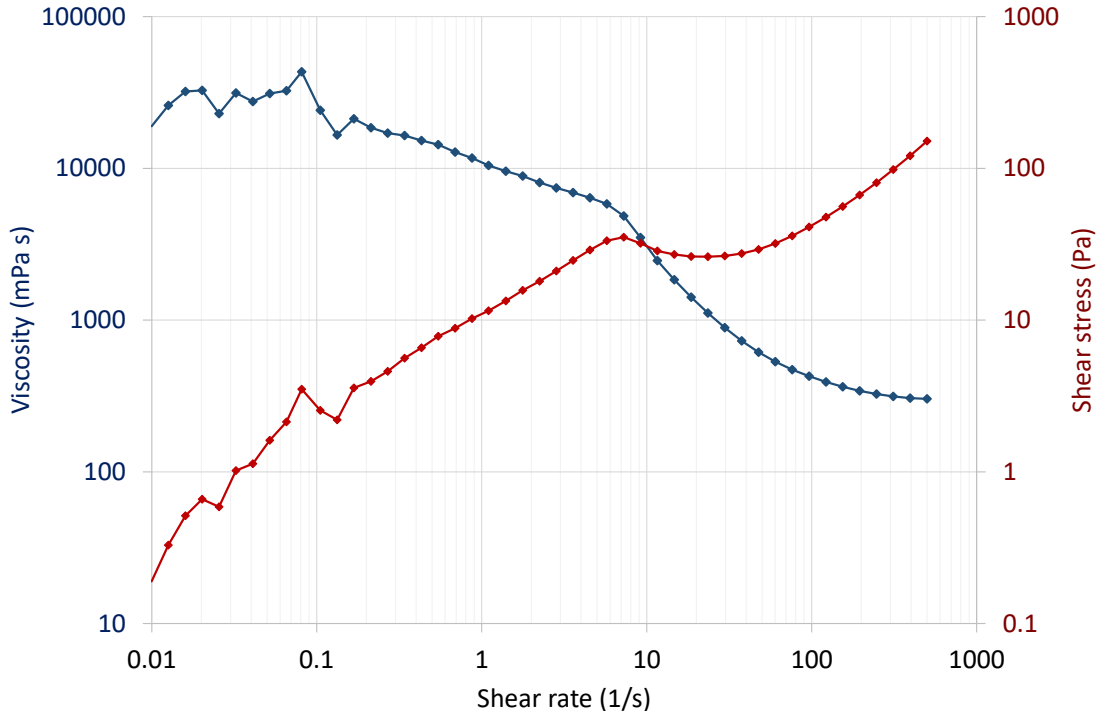

Figure 5.3 Example viscosity and shear stress curves, using a logarithmic spacing of data. The low shear data is noisy due to insufficient sampling times. The ink comprised 50 vol% 4 µm alumina, 1.0 wt% KD4, 1.0 wt% stearic acid and the rest a 60:40 mix of paraffin wax and LJ210, with a final addition of limonene at 10 wt% of the whole mixture. See Section 5.4 for full details of this ink.

The second measurement type used was a 'temperature ramp'. In such a test, the sample was sheared at a fixed rate while the temperature was steadily changed. The

temperature could be increased or decreased during the test, with decreasing temperatures having two advantages. First, if the sample solidified within the temperature range, the effect of solidification on viscosity could be captured, whereas with increasing temperatures it was necessary to ensure the sample begun the test molten throughout. The increasing viscosity as the sample solidifies can be seen in Figure 5.4. Second, for a temperature range that was entirely above ambient, it was likely that the temperature across the sample will be more consistent. The MCR 302 heated the sample from the lower plate only, so there would be a temperature gradient across the sample and minimising the heat input would reduce this gradient. This also meant the rate of temperature change should have been low enough to allow the whole sample to equilibrate at the new temperature.

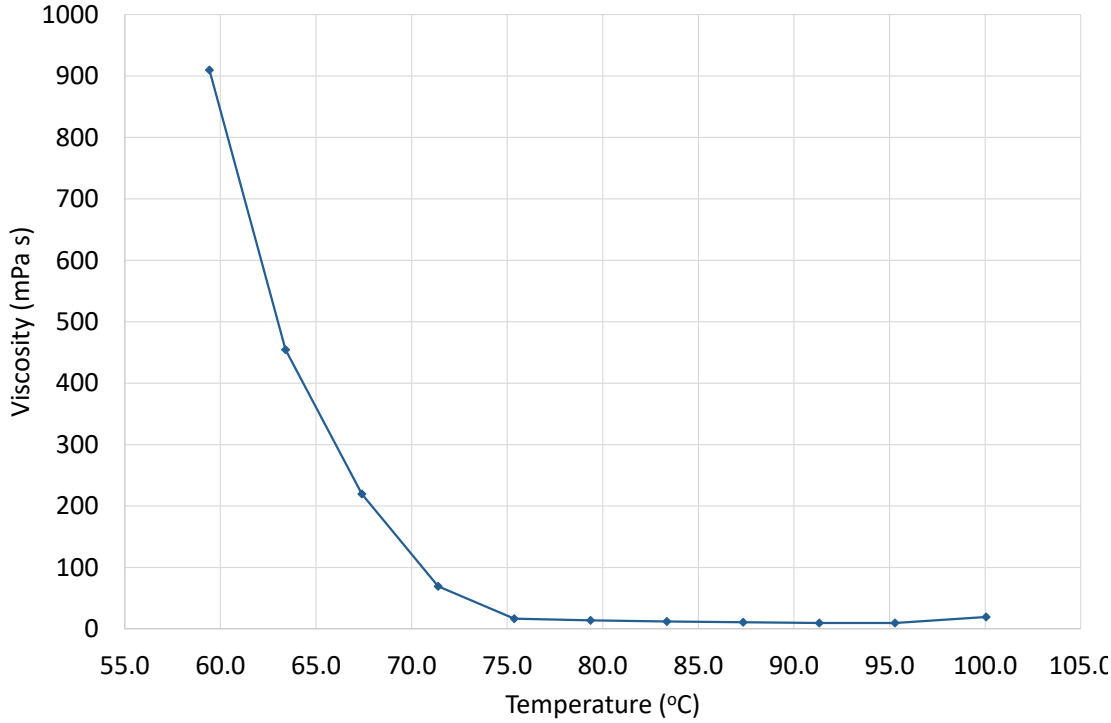

Figure 5.4 Temperature ramp for Lithojet 210, showing the sharp viscosity increase as the mixture solidified. The melting point for LJ210 is 65 to 72 °C according to its datasheet and the ramp was conducted at 2 °C/min.

The final two types of measurement are linked, both being oscillatory measurements. As might be expected, oscillation rheometry moves the measuring

plate in alternating directions, rather than one direction as in the previously described tests. By comparing the shear and stress over time in the sample, its viscoelastic behaviour can be measured; in simple terms, whether it is fluid-like or solid-like and how this changes with shear rate. A viscous, fluid-like material dissipates the energy put into it, whereas an elastic, solid-like material will store and return the energy, until the shear stress exceeds its yield point. This means that, when the applied shear is varied sinusoidally, the peak shear stress and peak strain are simultaneous for purely elastic materials whereas peak shear stress occurs at zero strain for purely viscous materials. Almost all real materials show some blend of these behaviours, so the phase shift between the stress and strain waveforms will be somewhere between 0 and 90^{o} (0 and $\pi/2$ radians). The sample response can also be fully described with the storage (*G'*) and loss (*G"*) moduli as functions of the frequency of oscillation. Which of these moduli is larger determines which behaviour is dominant, so for example a self-supporting gel would have a larger storage modulus (*G' > G"*).

There are two approaches to measuring these moduli, which are described by Anton Paar as an 'amplitude sweep' and a 'frequency sweep'. In an amplitude sweep, the sample is sheared to an increasing extent, controlling either the shear rate or the shear stress, at a fixed frequency. For most samples, there will be a point at which the structure of the material undergoes a change, leading to a change in the loss and storage moduli. A typical gel sample, with a storage modulus that is initially higher than the loss modulus, will have *G'* drop below *G"* above some oscillation amplitude, signalling the collapse of the gel structure and its transition to a fluid-like state. Before these structural changes occur at a certain shear amplitude, γ_L, the magnitude of the moduli is usually roughly constant with shear amplitude and this is termed the linear viscoelastic region (LVER). An idealised amplitude sweep is shown in Figure 5.5, reproduced from the Anton Paar reference website ("Amplitude sweeps," n.d.). The values of the moduli and γ_L will depend on the frequency at which the amplitude sweep is conducted. Frequency sweeps, where the peak shear is constant and the frequency of the oscillations is increased, are usually conducted in the LVER,

therefore follow an amplitude sweep. This provides information about the response of the sample at different timescales. For example, a sample that has lower moduli at low frequencies is more likely to allow suspended particles to sediment than a sample for which the moduli stay high over the frequency range.

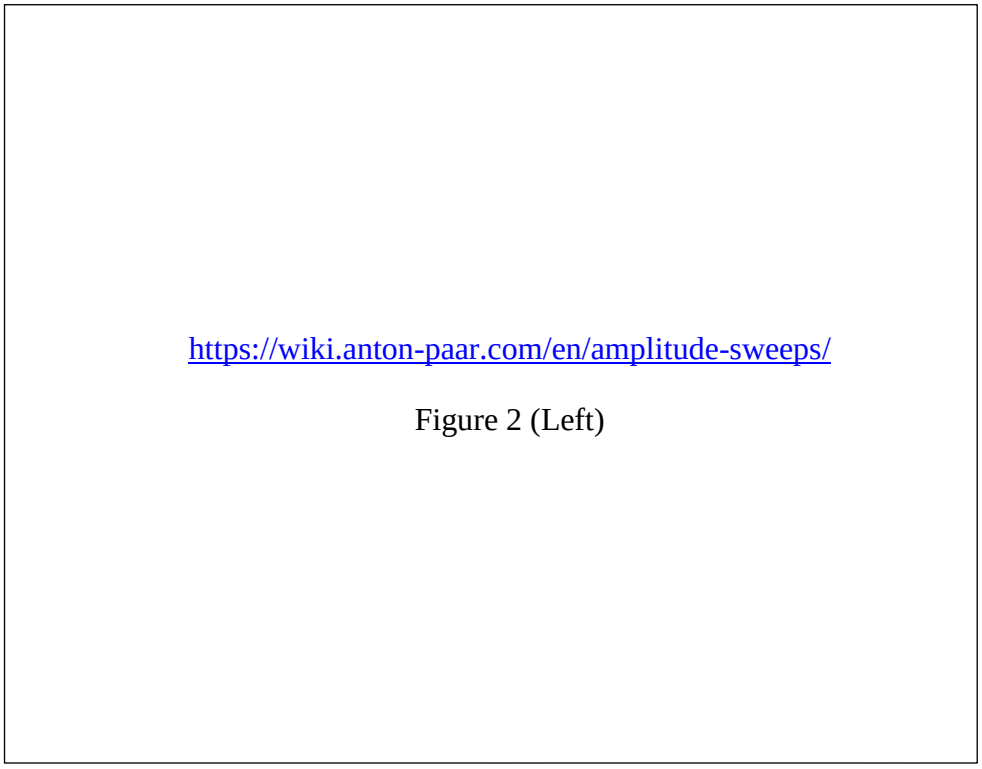

Figure 5.5 A theoretical result of an amplitude sweep showing the LVER below γ_L and the transition from solid-like (G' > G") to liquid-like (G' < G"). Reproduced from the Anton Paar Wiki ("Amplitude sweeps," n.d.).

5.1.3 Differential Scanning Calorimetry

Thermal analysis was carried out on the two waxes and LJ210 using a TA Instruments Q2000 Differential Scanning Calorimeter. Differential Scanning Calorimetry (DSC) is a technique in which the sample to be tested and a reference are heated such that their temperatures are equal and increase at an equal rate. The difference in heat flow required to make the temperature of the sample match that of the reference is continually measured. From this, it is possible to identify phase transitions in the sample, quantify the associated latent heats and measure specific heat

capacities as a function of temperature. The reference needs to have a precisely known heat capacity over the temperature range of interest. Small sample sizes and low heating or cooling rates lead to more consistent and accurate results as this allows time for heat to diffuse fully through the sample. For this work, sample sizes were less than 2 mg and a heating rate of 10 °C/min was applied from -10 to 120 °C.

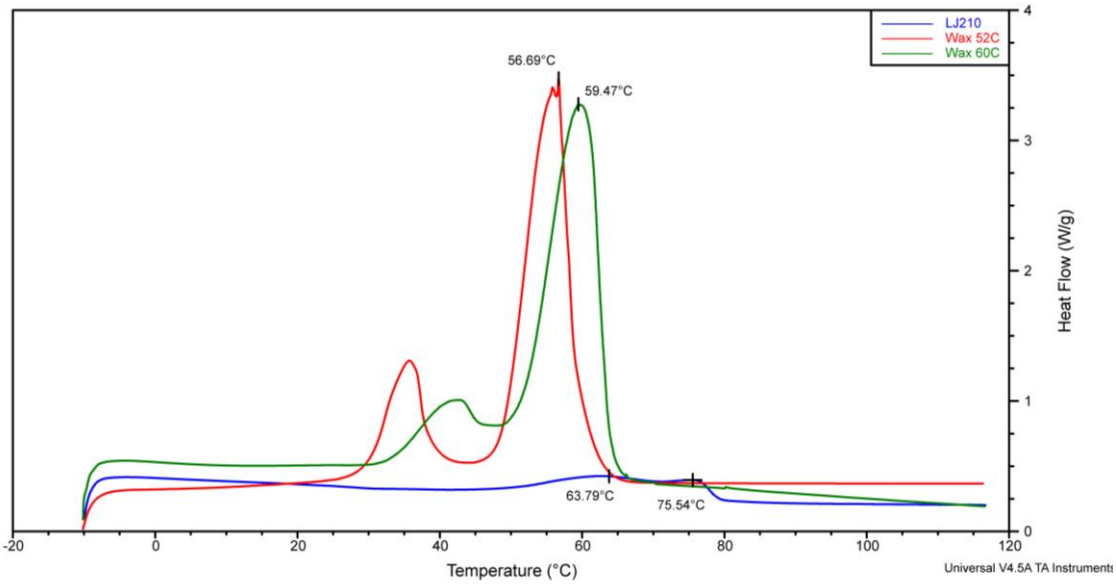

Figure 5.6 DSC of two paraffin waxes, with nominal melting points of 52 and 60 °C, and LJ210. The marked temperatures indicate peaks in the curves as a simplistic measure of melting point. Heat flow is positive for energy flowing into the sample.

The results of the DSC for the three materials are shown in Figure 5.6. A reasonably high heating rate was used to keep the experiment time practical, so the peak of the graph will actually occur slightly above the true melting point. The higher temperature wax appeared to be accurately labelled and did melt just below 60 °C. However, the low temperature wax melted almost 5 °C above the expected melting point, only a few degrees below the higher temperature wax. The smaller endothermic peaks seen in both waxes before the melting peak are likely to be due to loss of crystallinity.

The LJ210 showed a much broader melting point than the paraffin waxes, with increased heat flow over the range of 63 to 76 °C. This was to be expected, as the

waxes were relatively simple and mostly pure, giving a sharp melting point, whereas the LJ210 was a mixture of compounds with different melting points. This also correlates with the temperature ramp of LJ210 shown in Figure 5.4, where the viscosity sharply increased below 75 ºC and became unmeasurably high below 60 ºC, as well as with documentation from the manufacturer. Another noticeable result is the latent heat of fusion, represented by the area under the melting peak, which was much lower for LJ210 than for the waxes. Paraffin wax is known for having a high heat of fusion and is used for thermal ballast or energy storage because of this. One result of the lower heat of fusion of LJ210 was that the deposit freezing times predicted in section 3.3.2 represented a worst case, as addition of LJ210 to the ink formulation would significantly decrease the overall heat of fusion. Assuming half of the paraffin wax was replaced with LJ210, that both materials have the same heat capacity and that the latent heat of fusion of LJ210 was negligibly small, the time between cooling to melting point and fully freezing would be halved. For the right-most data of Figure 3.12, which considers a deposit with a diameter of 200 µm and a contact ratio of 0.05, the total time would be reduced from 450 ms to 325 ms. The higher melting point of LJ210 would also contribute to the faster freezing of deposits, although estimating this effect was difficult, especially as the LJ210 also had a range of temperature over which it melted.

5.2 Alkane based inks

Ink formulation experiments were initially done with mineral oil, which was later replaced with paraffin wax to produce an ink that would solidify. Using a carrier liquid that is fluid at room temperature made mixing and working with the ink much more convenient and reduced potential measurement errors due to temperature variations. At the same temperature, mineral oil and paraffin wax have similar viscosities, as shown in Figure 5.10. In this section, a solid fraction will be chosen to give a high solid content without raising the viscosity of the ink to an extreme, and the concentration of the dispersants set to minimise the viscosity.

For the mixing of the oil-based inks, hand stirring at the room temperature of 21 ^{o}C was sufficient. Dispersants were added to the oil first, with gentle heating in a beaker of hot water to aid the dissolution of the stearic acid, where it was used. Alumina powder was then added to the liquid mixture. This was made easier by thoroughly mixing between adding portions of the powder. For high solid loadings, adding all the powder at once produced a putty-like clump of material that required significant mixing before becoming a free-flowing ink.

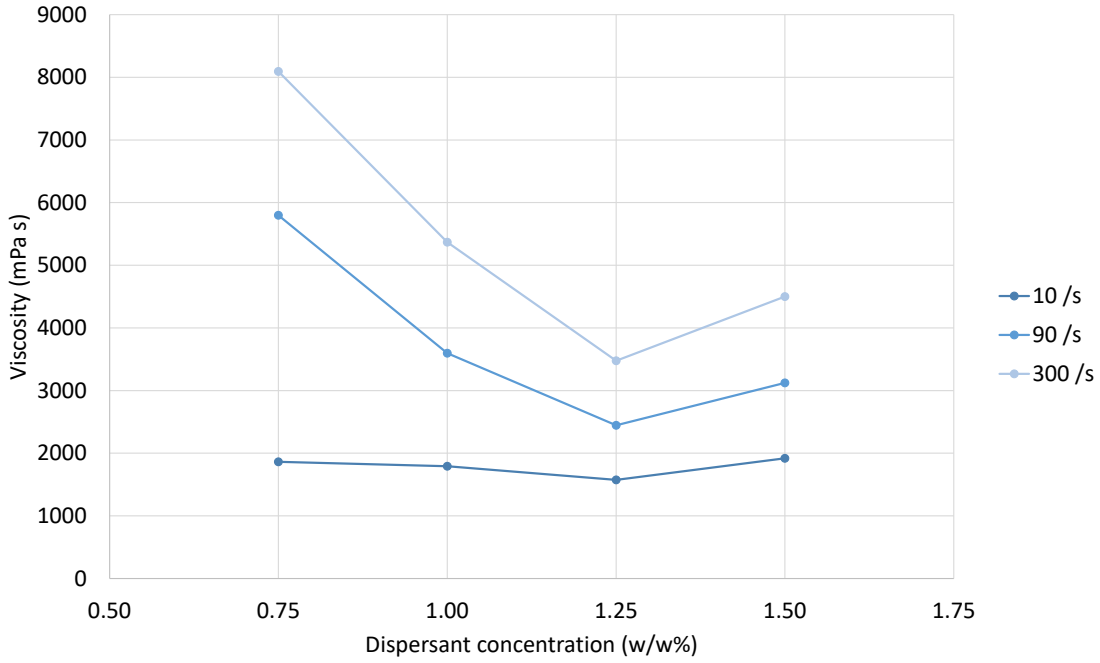

Figure 5.7 Effect of KD4 concentration on mixture viscostity in mineral oil with 50.0 vol% 4 µm alumina. The KD4 concentration was measured as a percentage of the weight of the alumina..

The effect of KD4 concentration was investigated first. Based on the work of Seerden et al. (2001), additions of KD4 from 0.75 to 1.50 % of the weight of the alumina were examined. The viscosity of these inks at different shear rates is shown in Figure 5.7. At low shear rates, the concentration of KD4 had little effect, but it became drastically more important at high shear rates. At 300 /s, around the magnitude of shear rate expected through the nozzle during deposition, the optimal KD4 concentration of 1.25 wt/wt% reduced the viscosity by more than half compared

to the lowest concentration tested. An excess of KD4 was also seen to increases the viscosity of the ink. In excess, not all the KD4 is bound to alumina particles and the very high viscosity of pure KD4 raises the viscosity of the carrier fluid (see Figure 5.10). Therefore, a concentration of KD4 of 1.25 wt/wt% was used for the oil-based ink.

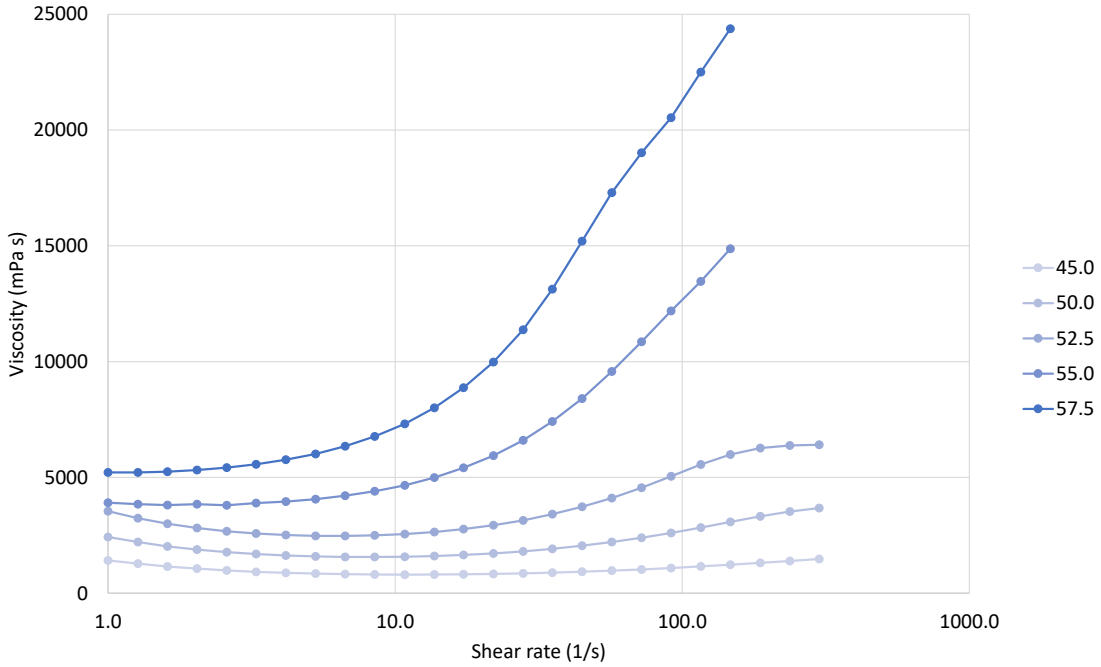

Figure 5.8 Flow curves for mineral oil inks with different solid fractions from 45.0 to 57.5 vol% and 1.25 wt/wt% KD4.

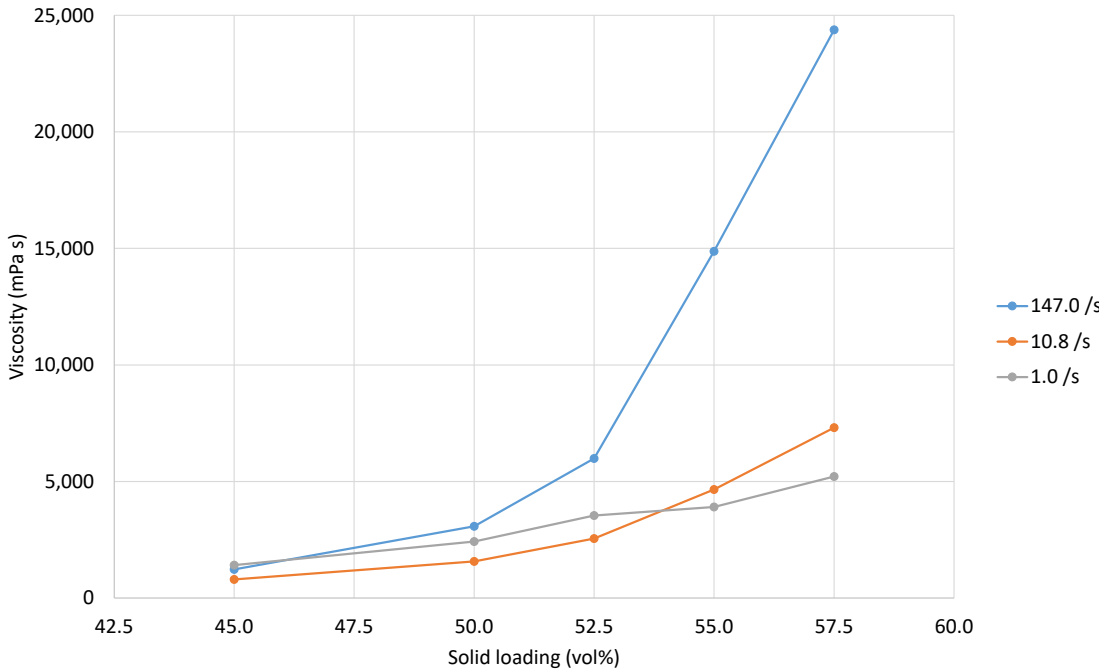

Figure 5.9 Oil-based ink viscosities against solid loading for different shear rates.

Figure 5.8 shows the flow curves for inks with different solid loadings, which can be replotted to give the more informative Figure 5.9. The shear thickening caused the relation between solid loading and viscosity to change with the shear rate, so it was necessary to consider several shear rates. At the lowest shear rate, representative of the ink sitting on the substrate after deposition, viscosity appeared to increase roughly linearly with solid loading. Increasing to a mid-range shear rate brought out the dilatant behaviour, although the viscosities were similar to the low shear rate case. At the high shear rate, comparable to flow through the nozzle, the dilatant effect was much stronger and at the highest solid loading, the viscosity was four to five times higher than it was at any of the lower shear rates. The high shear rate results are the limiting factor for solid loading of the ink. The shear thickening also disrupts predictions of slurry viscosity made in Section 3.1, as it is not possible to fit the Kitano equation to data measured at different shear rates.

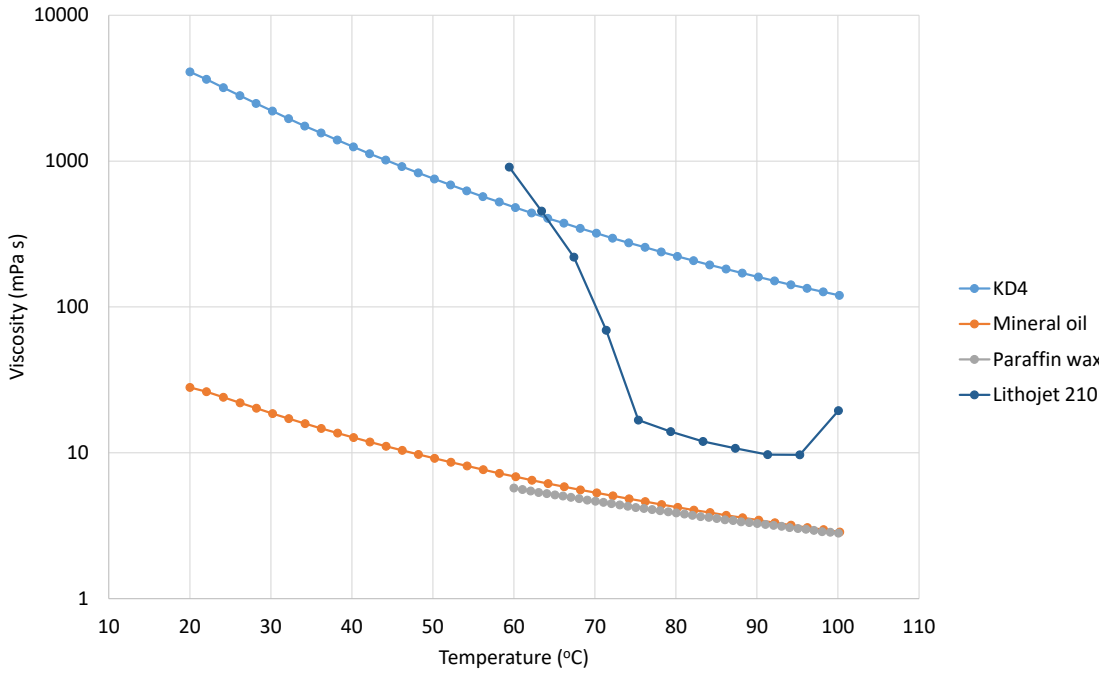

Figure 5.10 Temperature ramps for various liquids used in ink formulation. Measurements were carried out at a shear rate of 50 /s.

One way of reducing the viscosity of the ink while maintaining a high solid loading was to reduce the viscosity of the carrier liquid. At this stage, it was desirable to avoid volatile components to ensure a consistent ink during measurements, leaving few options for diluting the mineral oil. Increasing the temperature of most liquids causes a drop in viscosity and this is true for all those considered in this work, as shown in Figure 5.10. It should be noted that the paraffin wax and mineral oil had very similar viscosities at the temperatures above the melting point of the wax. By increasing the temperature from 20 to 100 °C, the viscosity of the mineral oil could be reduced by a factor of 10. In practice, the maximum temperature that could be used was limited by the syringes used to dispense the ink, as the plastic began to soften at temperatures near 100 °C. The resulting deformation could cause the syringe tips to detach under high pressure and prevented the plunger sealing well against the syringe walls.

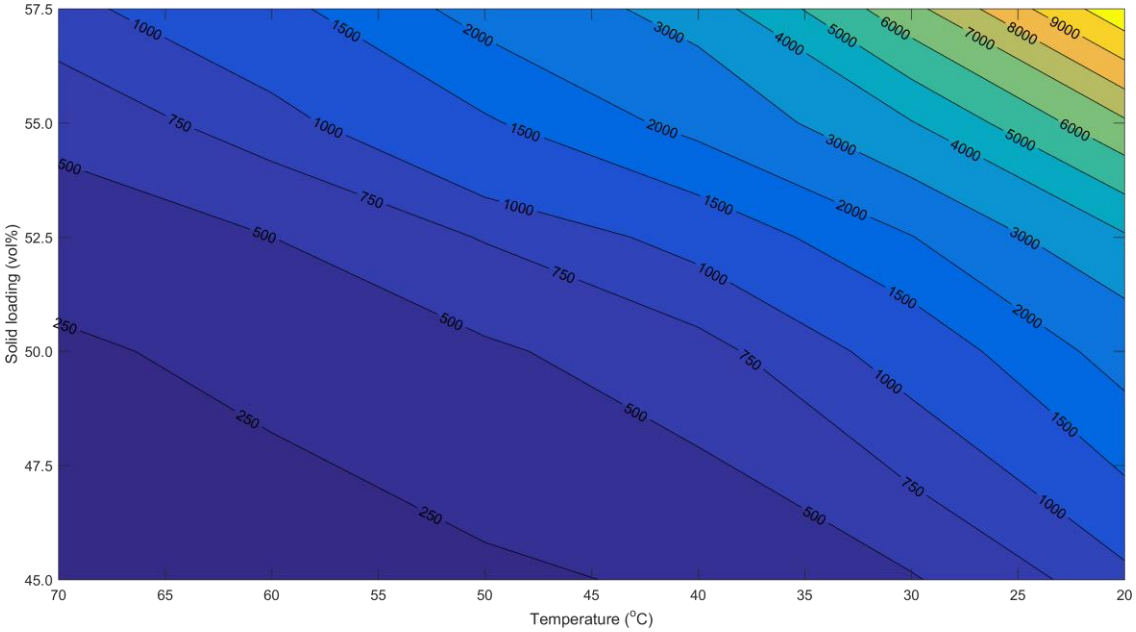

Figure 5.11 Contour map of the measured ink viscosity in mPa s for a range of solid loadings and temperatures. The ink contained 4 µm alumina powder in mineral oil with KD4 added at 1.25 % of the weight of the alumina. Data were measured every 10 °C and every 2.5 vol%, excluding 47.5 vol%, at a shear rate of 50 /s.

By performing temperature ramps with inks of different solid loadings and combining this with the temperature ramp for the mineral oil, a model was produced for the viscosity of the ink as a function of solid loading and temperature. The experimental data are presented in Figure 5.11. The Arrhenius equation was used as a model for the relationship between temperature and viscosity for the oil and KD4. The exact form is shown in equation 5-1, where the viscosity μ is a function of the temperature, T, in Kelvin. The curve was fitted to the data by two parameters, μ_o and x, using the values given in Table 5.2. The viscosities of the oil and KD4 were averaged, weighted by their volume fractions in the ink, a and b respectively, as defined in equations 5-2 and 5-3. The KD4 volume fraction was given by the alumina volume fraction multiplied by the ratio of the densities of alumina and KD4 and by the concentration. The mixed liquid phase viscosity was then substituted into equation 3-1, giving equation 5-4. As previously discussed, this model is only applicable for the shear rate at which the data were measured.

5-1 $$\mu(T) = \mu_0 e^{x/T}$$

5-2 $$b = 0.0125\phi \frac{3.9}{0.9}$$

5-3 $$a = 1 - \phi - a$$

5-4 $$\mu_{ink}(T, \phi) = \frac{1}{a+b}(a\mu_1 e^{x_1/T} + b\mu_2 e^{x_2/T})\left(1 - \frac{\phi}{A}\right)^{-2}$$

The KD4 content was not negligible and needed to be considered in this model, however a simple linear 'rule of mixtures' combination of the liquid viscosities yielded a poor fit, particularly at low temperatures and solid loadings. This was likely due to the adsorption of the KD4 onto the alumina particles, thus having a different rheology in a suspension than when measured in isolation. This could be accounted for by reducing the effective KD4 content by an arbitrary factor, producing a better fit of the experimental data. An empirically determined value, with accompanying value for *A*, is given in Table 5.2. Applying this correction gave a more reasonable value for *A*, an indication of the maximum packing fraction, as it was expected to below the limit for uniform spheres when applied to irregular powder particles. The percentage errors of both models are shown in Figure 5.12 and Figure 5.13.

Mineral oil		**Hypermer KD4**	
μ_1	7.7×10^{-3}	μ_2	8.0×10^{-5}
x_1	2.2×10^{3}	x_2	5.2×10^{3}
A		0.710	
KD4 reduction factor		0.390	
A for modified model		0.645	

Table 5.2 Empirical parameters for ink viscosity modelling.

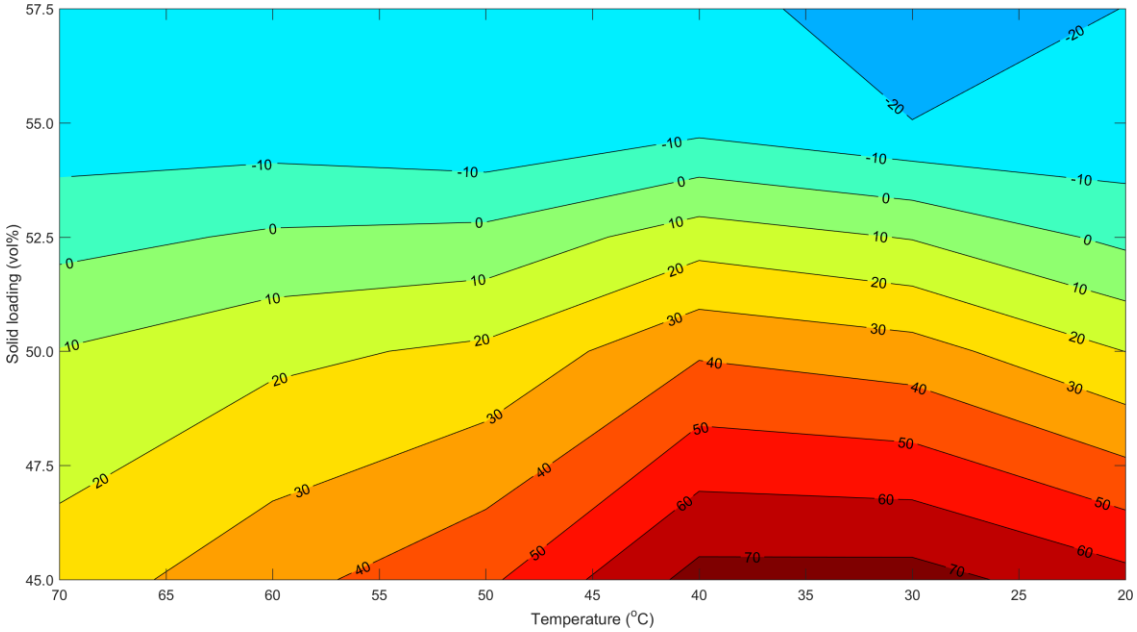

Figure 5.12 Contour map showing the percentage error for the fitted ink viscosity model using accurate proportions.

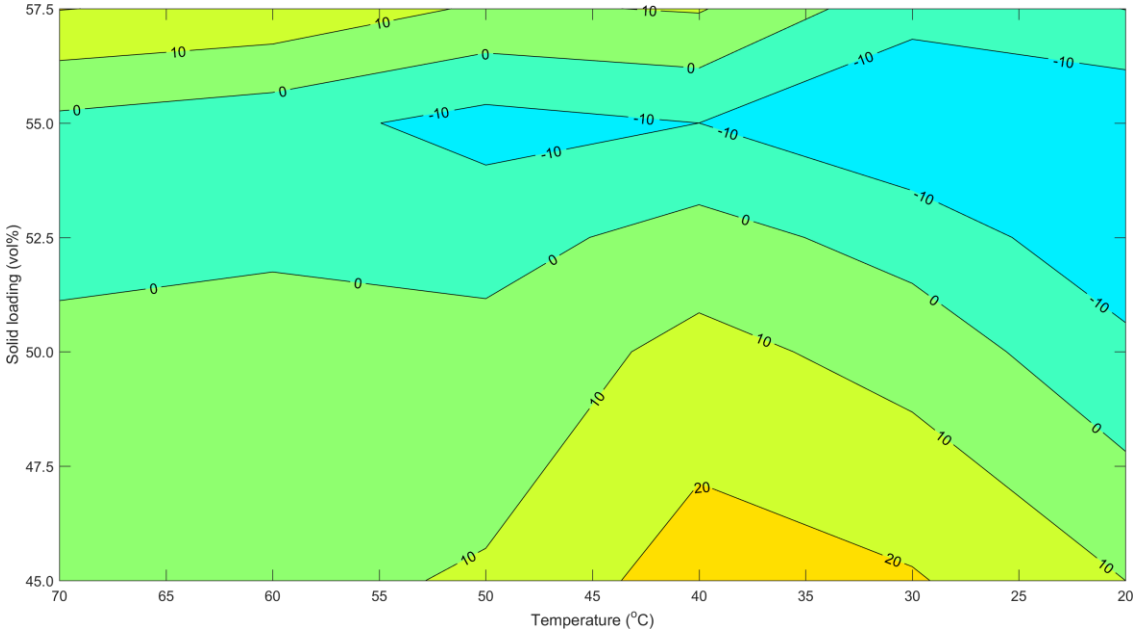

Figure 5.13 Contour map of the percentage error for the modified ink viscosity model.

A more thorough investigation of dispersant concentrations was carried out using the 0.3 µm alumina powder. Investigation with this powder was limited because suitable concentrations of KD4 could not be found for high solid loadings. Even with

a solid volume fraction of 30 %, the viscosity could not be reduced below 3,300 mPa s at any shear rate, which was a comparable viscosity to that seen with 50 vol% of the 4 µm powder. This required a KD4 concentration greater than 5 wt/wt%. At 40 vol% alumina, fluid inks were only produced with 8 wt/wt% KD4 and fluid inks could not be produced at all at higher solid loadings.

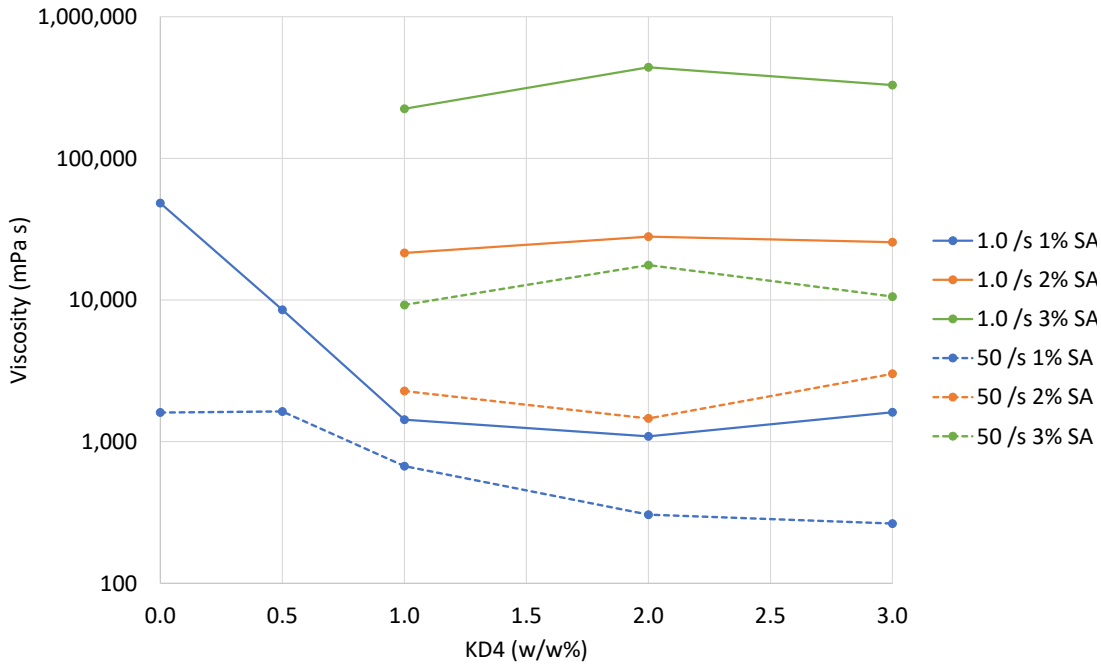

Figure 5.14 Effect of KD4 and stearic acid concentrations on viscosity of a 30 vol% 0.3 µm alumina ink. Dispersant concentraions are indicated as percentages of the weight of alumina in the ink.

The dispersant investigation was carried out at a solid loading of 30 vol% of the finer powder and both KD4 and stearic acid were added. Figure 5.14 shows the results at low and medium shear rates. The combination of dispersants was clearly much more effective than the use of KD4 alone. At 1.0 wt/wt% stearic acid, the viscosity of the ink was a third of the viscosity with KD4 alone, even when only adding a fifth of the KD4 content. Higher levels of stearic acid increased the ink viscosity. This was likely because these measurements were carried out at room temperature, at which pure stearic acid is solid. Near the melting point of stearic acid, around 70 ^{o}C, this effect would be less pronounced. With an appropriate addition of stearic acid, adding

an excess of KD4 did not reduce the ink viscosity further. Therefore, inks that contained both KD4 and stearic acid did so at 1.0 wt% based on the weight of the alumina.

5.3 Evaporative inks

As an alternative to freezing, evaporation of the carrier liquid was considered as a method for fixing the ink on the substrate. Using evaporation allows for the solid content of the ink to be much lower as the liquid component will disperse and will not be present in the green body. Thus, a lower viscosity ink can produce deposits of the same density. There is also less material that must be removed before sintering and no need to heat the ink, both of which make processing easier and more consistent.

Liquid	**Boiling point (°C)**	**Vapour pressure (kPa)**	**Viscosity (mPa s)**
Octane	126	1.47	0.5
Limonene	176	0.40	0.92
Octanol	196	0.019	-
Butanol	118	0.80	2.57
Isopropyl alcohol	82.6	5.3	1.96
Ethyl caprylate	207	0.015	-

Table 5.3 Key properties of potential volatile carrier liquid. Vapour pressures and viscosities are given at 20 °C and boiling point at 1 atmosphere.

An evaporative ink requires a liquid that is sufficiently volatile that the viscosity of the ink will significantly increase a short time after leaving the nozzle. However, the ink in the nozzle itself needs to stay fluid, putting an upper limit on the volatility of carrier that is practical. Several liquids were considered, as shown in Table 5.3, with a preference for hydrocarbons as their chemical similarity to mineral oil allows the existing dispersant optimisation to be applied. Esters and alcohols were also

considered, but could not be successfully incorporated into stable suspensions with alumina and the available dispersants.

Attempts to electrospin inks using octane or limonene alone as the liquid phase suffered from frequent nozzle blockages, even when using solid fractions as low as 30 vol%. Limonene-based inks retained too much liquid and were still fluid minutes after leaving the nozzle, but an octane-based ink with 35 vol% 0.3 µm alumina successfully produced dry filament deposits that retained their circular cross-section at a nozzle height of 2.5 mm. However, this ink was very difficult to work with because any pause in the flow of ink through the nozzle would cause a blockage. During electrospinning, build-up of dried ink on the nozzle tip would affect the jet geometry and lead to additional blockages.

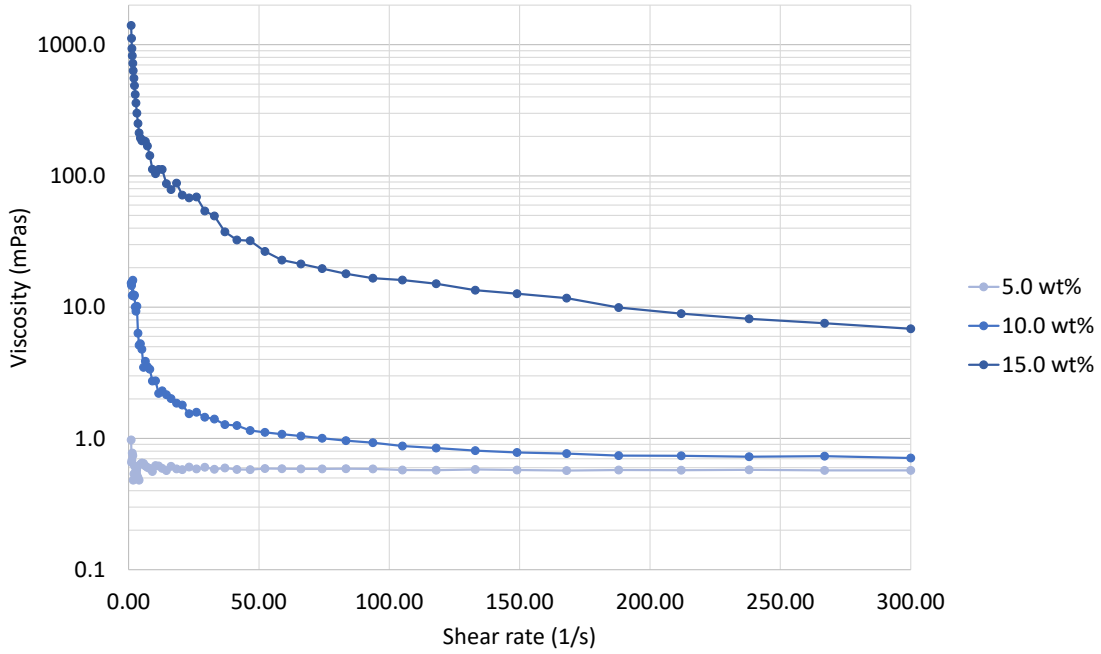

Figure 5.15 Flow curves of octane/paraffin wax mixtures with wax contents of 5 to 15 wt% at room temperature.

One strategy for producing an ink that was fast drying while minimizing nozzle blockages was to dissolve a quantity of paraffin wax in the liquid. This was attempted with octane, in which paraffin wax is miscible at room temperature. An excess of wax results in solidification, forming a gel or soft wax depending on the ratio of wax and

octane. The wax reduced the volatile content of the ink, but less liquid needed to evaporate to cause solidification. Furthermore, the wax helped bind the dry ink together. The addition of wax increased the viscosity of the mixture as shown in Figure 5.15, causing gelation with wax contents above 15 wt% in octane-wax mixtures. The viscosity could be reduced and wax content increased by heating the mixture, although this increased the evaporation of the octane and required additional process control. Without heating, the addition of wax did not significantly reduce the chances of nozzle blockages, so an octane-wax blend was not used to formulate an ink.

The difficulty in achieving stable electro-jets with the explored liquids meant that evaporative inks were not investigated further. It is possible however that this route could be successful using a medium volatility liquid, such as limonene, deposited onto a heated substrate, such that high rates of evaporation are not seen at the nozzle. Blending the limonene with wax, to provide faster drying and a binding agent, and mineral oil, as a non-volatile liquid, may be required to achieve the exact properties desired. These mixtures could be investigated in a future project.

5.4 UV curable inks

To produce pure ceramic parts, the deposited ink (also referred to as the 'green body') needed to be sintered. This process includes burning out all the organic material, i.e. the wax and dispersants. However, the ink was designed to flow freely at temperatures above 70 ^{o}C, whereas burning of the organics occurs at hundreds of degrees. This meant that the wax-based inks described in section 5.2 would not hold their shape during sintering. Therefore, an extra additive was needed that would prevent flow of the ink in the furnace. For ceramic injection moulding, small amounts of polyethylene or similar long-chain polymers are added to increase the viscosity of the material when molten. This is practical for injection moulding because high pressures can be used to force the material into the mould. In this work however, it was critical the ink had a low viscosity for electrospinning. Thus, some kind of curing after electrospinning was preferable, causing a chemical change in the ink that

prevented future melting. Polymers that cure on exposure to UV light are easily controllable and increasingly common.

Lithojet 210, as described in section 5.1.1, was chosen as a UV-curing additive for this work as is had wax-like properties, including a similar melting point to the paraffin waxes and a low viscosity when molten, as well as being miscible with alkanes. On the other hand, LJ210 was more than three times more viscous than paraffin wax at the same temperature and less durable when solid. Thin filaments of solid wax-based inks were somewhat flexible and could be easily peeled off an aluminium substrate, whereas when the wax was completely replaced with LJ210 the filaments were brittle and snapped into short lengths. To address the issues of high viscosity and low green body strength, paraffin wax was blended with the minimum quantity of LJ210 needed to prevent melting after UV curing. This was reliably achieved with a mixture of 60 wt% wax and 40 wt% LJ210. When heated after curing, this mixture still produced some liquid, but the overall shape was not noticeably changed, even without a high volume fraction of alumina powder.

At this ratio of LJ210 and wax, the viscosity of an ink with 50 vol% alumina was higher than with wax alone, as expected. To maintain similar performance to the other inks during electrospinning and when hitting the substrate, the LJ210 ink was thinned with a small addition of limonene. It was desirable to minimise the quantity of limonene added so that the solid content of the ink was not reduced. From the trials with evaporative inks, it was known that limonene evaporates slowly at room temperature. Although the ink was hot when leaving the nozzle, accelerating the evaporation, it was likely that the ink would solidify before all of the limonene had evaporated. With a large proportion of limonene in the ink, it was possible that this would lead to voids, other defects or deformation of the filaments of deposited ink as the limonene evaporated from the solid wax. Figure 5.16 shows how adding 10 wt% limonene reduced the viscosity of the LJ210-based ink. Below shear rates of 1.0 /s, the LJ210 ink was still more viscous than the alkane inks, but it was significantly less viscous at shear rates higher than this. This level of limonene was chosen for the final

formulation because of this crossover. An additional benefit of the lower viscosity was more consistent rheology, which indicated better mixing and a more homogenous ink. In this work, the limonene was added in addition to a complete ink, as a percentage of that ink's mass, such that 1.0 g of ink with 10 wt% limonene gave 1.1 g of thinned ink.

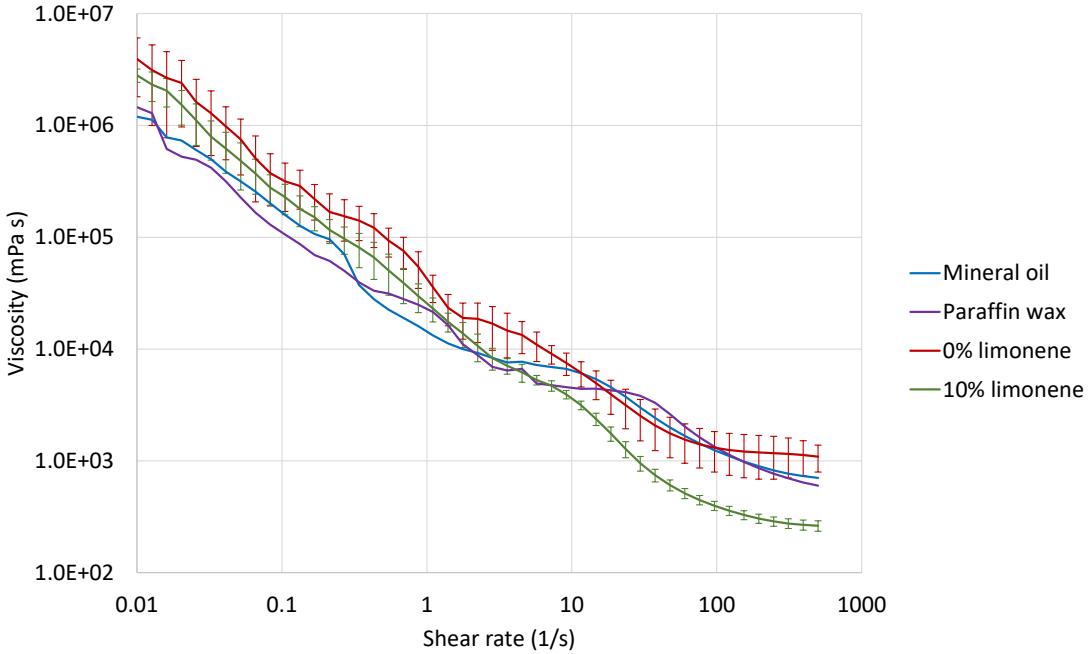

Figure 5.16 Comparison of flow curves for 50 vol% alumina inks with different carrier liquids at 80 °C: mineral oil, paraffin wax and 60:40 paraffin wax/LJ210 mixtures and either 0 or 10 wt% limonene. The error bars show standard deviation over four measurements.

The addition of limonene had an unexpected effect on the viscosity of the ink during a temperature ramp, as demonstrated in Figure 5.17. As well as lowering the overall viscosity, the temperature at which the viscosity began to rise sharply due to solidification was also reduced. This led to an ink that was still fluid at lower temperatures, which potentially allowed for the use of a lower nozzle temperature. However, this was in comparison to an ink containing LJ210. An ink with only paraffin wax as the binder would also have had a lower viscosity and melting point.

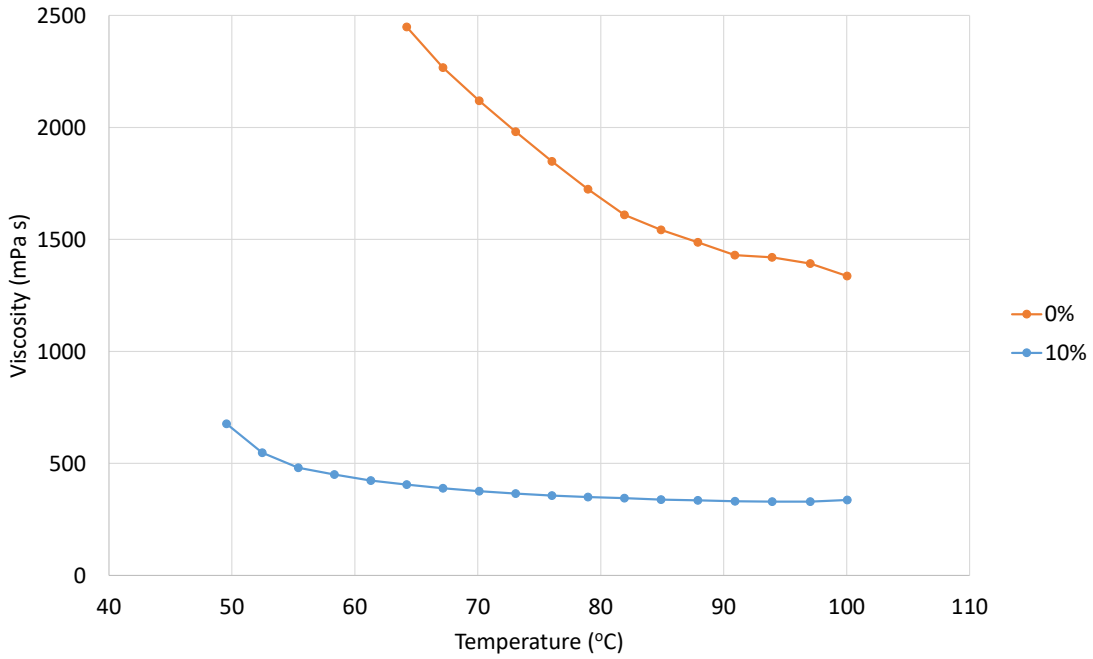

Figure 5.17 Temperature ramps for an ink with 0 or 10 wt% limonene, measured at a shear rate of 250 /s. The ink contained 50 vol% 4 µm alumina powder, 1.0 wt% of each KD4 and stearic acid based on the alumina weight and the remainder was a 60:40 mix of paraffin wax and LJ210.

Limonene	0 wt%		10 wt%	
Ingredient	**Volume %**	**Weight %**	**Volume %**	**Weight %**
Aluminium oxide (4 µm)	47.9	79.6	45.5	78.1
Lithojet 210	19.2	7.9	18.2	7.8
Paraffin wax	28.7	10.9	27.3	10.7
Hypermer KD4	2.1	0.8	2.0	0.8
Stearic acid	2.1	0.8	2.0	0.8
Limonene	0.0	0.0	5.1	1.8

Table 5.4 Default composition of nominal 50 vol% alumina inks containing LJ210 and either 0 or 10 wt% limonene.

From this point forward in this thesis, unless otherwise noted the default composition for an LJ210 based ink was 50 vol% alumina, with KD4 and stearic acid each added at 1.0 wt% of the alumina and the remainder as a 60:40 mixture by weight of paraffin wax and LJ210. Where limonene was added, it was done so in addition to a mixed ink, i.e. 1.0 g of the above ink with 10 wt% limonene produced 1.1 g of final ink. This gave the final proportions laid out in Table 5.4.

5.4.1 Ink stability

With typical ink flowrates below 1.0 µL/s during electrospinning, a full 3 mL syringe of ink provided almost an hour of printing. For the patterns and substrate size used in this work, this quantity of ink or duration of printing was far in excess of what was useful for a single run, meaning the same syringe of ink was used in multiple runs. Therefore, the stability of the ink was investigated. There were two aspects in particular of concern: possible settling of the alumina due to gravity and loss of limonene due to evaporation.

5.4.1.1 Sedimentation during heating

Alumina is around four times as dense as paraffin wax, and so without opposing forces from interactions with the liquid it will tend to sink to the bottom of container of ink. As it was solid when at room temperature, the ink could only settle or separate while in the heated syringe pump. This limited the period of interest to hours, rather than days or weeks. A full syringe of ink with a capped tip was loaded into the heated syringe pump and left undisturbed at 85 ^{o}C for two approximately 6-hour periods on subsequent days, totalling 12.5 hours of heating. The syringe was cooled and removed from the pump overnight, as it would be during experiments. At the end of this, the syringe body was cut away from the solidified ink with a razor blade and the ink split into four roughly equal cylindrical segments along its length. Each sample was weighed and then the volume was measured by an Archimedean method, with the sample hanging into a beaker of water from an external support. To reduce errors from air bubbles being trapped in the rough sections of the samples, they were each

submerged, fully removed and submerged again before measuring the weight of displaced water. This did not eliminate surface air bubbles due to the low surface energy of paraffin wax and high surface tension of water, with subsequent measurements giving smaller volumes as a greater area was wetted with each submersion. Furthermore, there was evidence on the cut surfaces of air bubbles trapped during loading of the ink into the syringe, causing internal voids that increased the error in volume measurements.

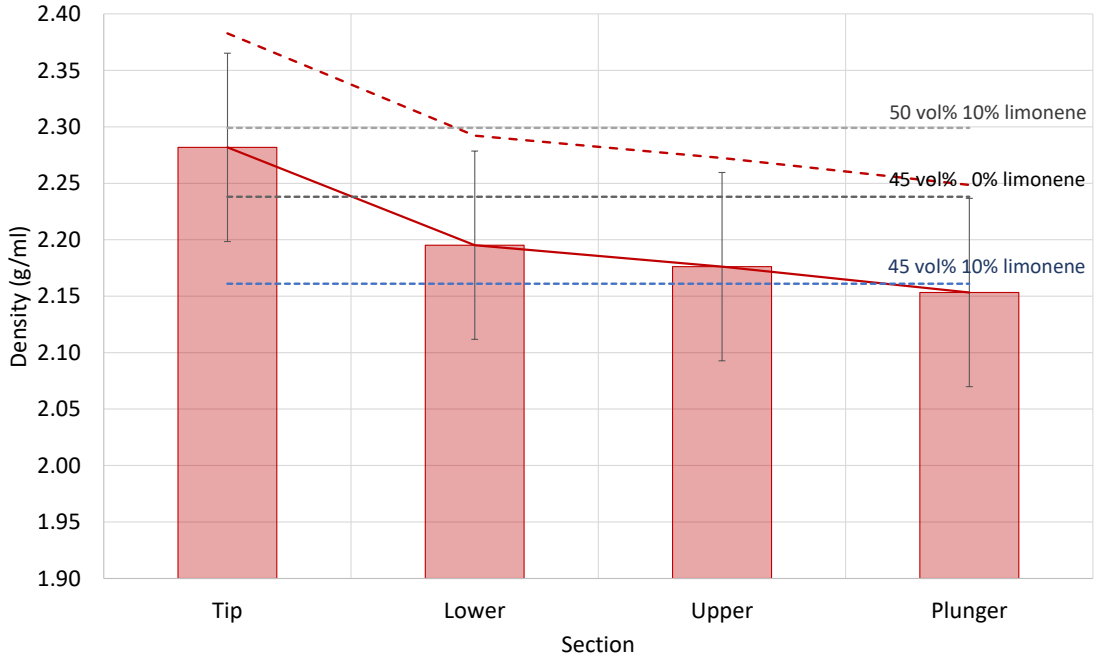

Figure 5.18 Density measurements of sections of a 50 vol% alumina LJ210 ink after resting in a heated vertical syringe for 12.5 hours. The dashed line shows the ink densities adjusted to have the expected average density and the dotted horizontal lines show the expected density of inks with various compositions for comparison. The error bars show the average difference between first and second volume measurements.

The resulting measured densities are shown in Figure 5.18 with the expected densities of inks with different alumina and limonene contents for comparison. All of the densities were below what would be expected for this ink, which was due to the air trapped during volume measurements. The dashed line shows the results shifted to have an average density matching that expected from this ink. There was a clear trend

of increasing density toward the bottom of the syringe, suggesting sedimentation of the alumina powder was taking place. The greatest deviation from the expected density, by 3.5 %, was toward the tip of the syringe. In practice, when ink was being dispensed, the lowest portion of ink would be continuously removed from the syringe. This limited the time over which sedimentation can cause the density of a given segment of ink to increase before it was dispensed. Therefore, the increase in density during electrospinning experiments would never reach the magnitude seen in this experiment.

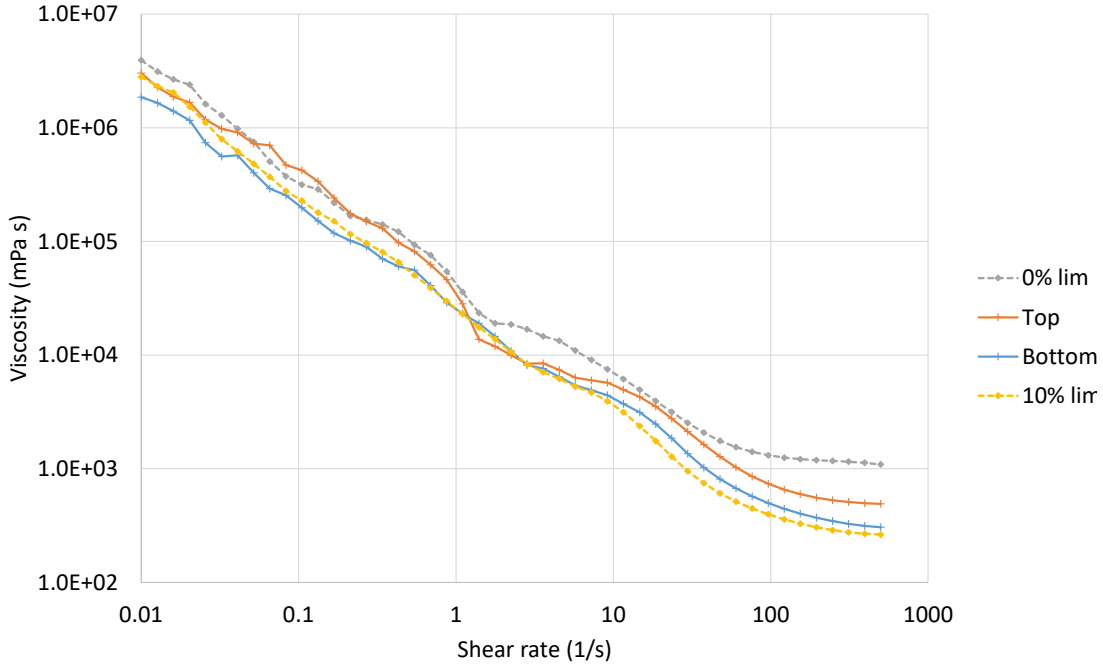

Figure 5.19 Changes in viscosity of a 50 vol% alumina LJ210 ink after sitting in a heated vertical syringe for 12.5 hours.

However, sedimentation was not the only change in the ink after prolonged heating. Figure 5.19 shows the flow curves for the same samples from the top and bottom of the syringe after being molten for 12.5 hours, compared to fresh samples of the same composition with different limonene contents. Here we see the opposite trend to what would be expected from the density measurements, as the sample from the top of the syringe had a higher viscosity than the bottom. This effect was probably caused by evaporation of the limonene around the plunger seal, which was poor compared to the

Luer lock cap on the tip of the syringe, and as discussed in section 5.4.1.2 the evaporation of limonene was a significant concern. Note that for this experiment the ink in the syringe was not under pressure, but that pressure on the plunger helped to create the seal.

Due to the issues with plunger design discussed in section 4.1, it would be difficult to improve on the current design, although adding a second seal could be possible. As it would not have to contain the pressurised ink, this seal could be a comparatively soft O-ring that would form a vapour-tight seal.

To avoid complications in this work due to this loss of limonene and the smaller changes from sedimentation, the topmost portion of ink in the syringe was not electrospun and was discarded. This was typically around 0.5 mL of ink.

5.4.1.2 Evaporation during storage

In addition to changes in the ink in the syringe pump, inconsistency in measurements suggested changes might be occurring during storage. In earlier work with the LJ210-based ink, the ink was stored in 30 mL HDPE bottles or in syringes capped at both ends. These were stored in a lab with air conditioning set to 21 ^{o}C and not inside any other container. Due to the ink being frozen solid, any changes were attributed to the loss of limonene. As a non-polar molecule, limonene can diffuse through the polyethylene and polypropylene of the storage bottles and syringes respectively, with similar organic solvents doing so on a timescale of days to weeks (Prasad et al., 1994).

To investigate the loss of limonene from the solid stored ink, samples of LJ210 ink with 10 wt% limonene were placed into three 30 mL HDPE bottles. Each sample weighed between 15.2 and 15.5 g and all were gently heated after being put in the bottles to re-melt the ink, so that the exposed ink surface was similar for each sample. After this, one bottle had its lid placed on top, but not screwed down. The second bottle had the lid tightly screwed onto it. The third bottle had the lid screwed on and was then placed inside a larger HDPE bottle along with a few millilitres of limonene

before the larger bottle was also screwed shut. This provided an environment saturated with limonene vapour around the third sample, preventing the loss of limonene from the smaller bottle. After 15 days in an air-conditioned lab at 21 °C, flow curves were measured for each sample and these are presented in Figure 5.20. Note that the liquid was still present in the bottle housing the third sample, so that the air inside had remained saturated with limonene.

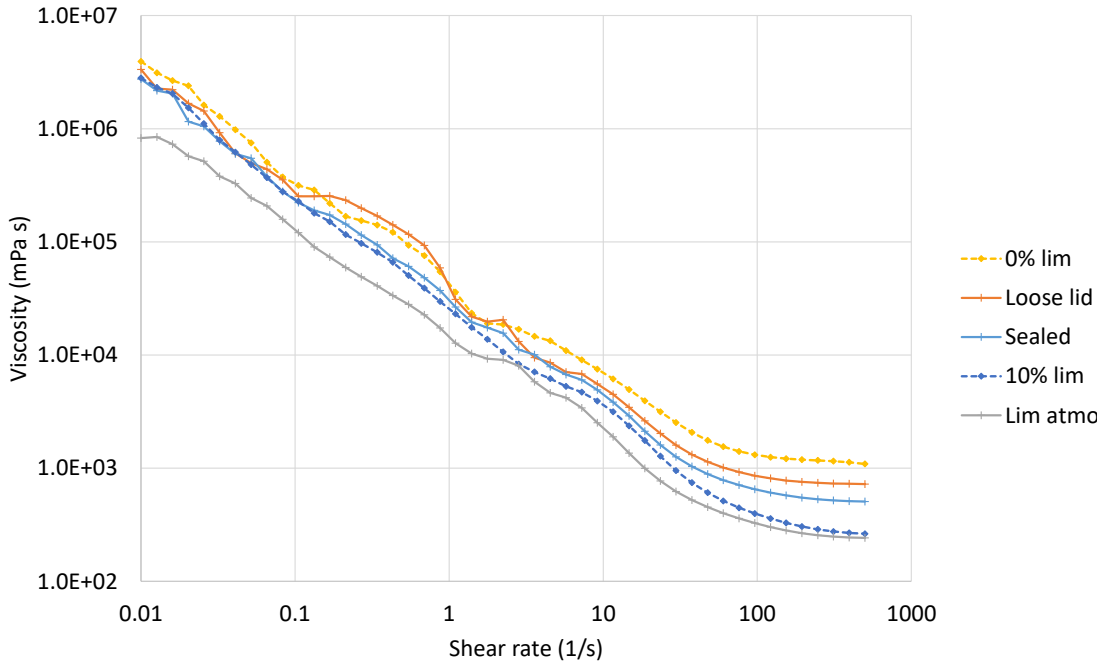

Figure 5.20 Viscosities of a 50 vol% alumina LJ210 ink after 15 days storage in HDPE bottles under different conditions: lid placed onto bottle, lid tightly screwed on, lid screwed on and placed inside another bottle containing a small amount of limonene. Inks with known limonene contents of 0 and 10 wt% are presented for comparison. All lines are an average of at least two separate measurements.

Focusing on the shear rates above 10 /s, there was a clear difference between the samples. The loose-lidded sample appeared to have lost most of its limonene content, leaving it with a viscosity approaching that of a sample without limonene. The tight-lidded sample fared only slightly better, showing that a significant proportion of the limonene had diffused through the bottle walls. Conversely, the sample stored in a limonene-saturated atmosphere had a slightly lower viscosity than a fresh sample of ink, probably due to absorbing some limonene from the outer container.

Based on these results, in subsequent work the syringes and ink storage bottles were stored inside larger HDPE containers with limonene-saturated atmospheres. The reduction in viscosity was small compared to the increase in viscosity caused by storage in open air and would be partly offset by the loss of limonene from the syringe during extended use.

5.4.2 Post-deposition curing

According to its datasheet, LJ210 requires 500 to 1000 mJ/cm^2 of 365 nm UV light to cure ("LITHOJET^{TM} 210 Etch Resist," 2018). As it is intended for use in inkjet printing, this is at an expected deposit thickness of 25 µm. This gives a UV dose of 200 to 400 J/mL. With the density of LJ210 being 985 kg/m^3, the dose in J/g is approximately the same number.

To cure them, samples were placed in a LV202-E UV illumination box from Mega Electronics, Linton. The samples were placed on a glass sheet above the light source with a white panel above, so the top of a sample received reflected light. This unit used two T5 florescent tubes rated at 8 W input power each. Taking the luminous efficiency of a generic florescent tube to be 20 %, the combined luminous power was 3.2 W. Only a fraction of this energy would be absorbed by a sample and not all of it would be at the required wavelength. Considering a typical sample weighs less than 0.5 g and the dry ink was 8 wt% LJ210, the 40 mg present in such a sample theoretically needed to absorb less than 16 J to cure completely.

An exposure time of 30 minutes was used to cure each sample. Over this period, 5.8 kJ of UV light was emitted into the box, meaning only 0.28 % of the energy was required to cure the LJ210 present. This long exposure time was used to ensure the samples were fully cured, even if only a tiny proportion of the light contributes. Compared to the hours or days needed to sinter the samples, this curing process was still relatively quick. Furthermore, the minimum UV exposure needed to cure fully a given sample depends on the sample mass, which determines the total energy required, and the sample shape, affecting the depth to which sufficient light must penetrate.

Various shapes were used in this work and given the comparatively short time required for an excessive dose, this step was not optimised. It is not known whether there is a level of exposure, far in excess of the curing requirements, that causes degradation of the LJ210.

Another reason for the high dose and cure time was that much of the LJ210 is not on the surface of the sample and was covered by opaque particles of alumina, as well as more LJ210. A large excess of UV light improved the chances of curing the ink to a good depth, rather than only on the surface, which may have been insufficient to ensure structural stability during sintering. It was probable that the UV light could only penetrate into a certain depth of ink, so that it was impossible to through-cure samples that were particularly thick, although this was not investigated here.

5.5 Conclusions

Three key types of ink were developed, based on mineral oil, paraffin wax or a blend of paraffin wax and UV-curable wax. The solid loading was investigated and a value of 50 vol% chosen to provide high solid content without raising the viscosity to the point where electrospinning was hindered. The concentration of stearic acid and KD4 dispersant were optimised to minimise ink viscosity, with the ideal concentration being 1.0 wt% each, based on the weight of alumina powder in the ink.

For the UV-curable ink, the proportion of LJ210 UV-curing etch resist in the wax blend was minimised at 40 wt%, which still prevented loss of shape at temperatures above the melting points of the waxes after curing. Due to the higher viscosity of LJ210 compared to the wax, limonene was added at 10 wt% to maintain similar ink viscosities.

Stability of this ink was investigated for two cases, first when molten for half a day to represent use in experiments, and second when solid and stored in HDPE bottles over two weeks. It was found that slow sedimentation occurs in the molten ink, with the density of lower portions of the ink in the syringe increasing by up to 3.5 %. This was not considered a serious issue as ink was removed from the bottom of the syringe

during deposition, which keeps any density increases below this level. A bigger change was found due to loss of limonene from the poorly sealed top of the syringe, resulting in a viscosity increase. The last 0.5 mL of ink in each syringe was therefore discarded. During storage, a significant proportion of the limonene was lost from even a tightly sealed plastic bottle in a room-temperature lab. To minimise changes in ink composition, syringes and bottle containing ink were therefore stored inside large bottles with liquid limonene to saturate the air with vapour.

The ink containing LJ210 was cured under UV lamp with approximately 3 W luminous output for 30 minutes. A large excess of UV light was used to ensure curing occurred through the thickness of samples and to account for losses due to absorption by the walls of the illumination box and the range of wavelengths present.

6 ELECTROSPINNING CHARACTERISATION

In this chapter, the behaviour of the electro-jet with the formulated inks is examined. Automated analysis of images of the jets was used to measure their minimum widths under different conditions, in order to identify the best conditions when using the electro-jet for direct writing as described in Chapter 7. Additionally, the range of conditions under which electrospinning can be carried out was established, providing a practical operating envelope.

6.1 Techniques

The experiments for this section were carried out with the rotary stage and imaging equipment described in section 4.2.1. The key metric used in this work was the minimum width of the jet while in flight, with a thinner jet allowing for finer patterns. The height of the deposit on the substrate was also investigated for the waxy inks, as this was a better measure of the final deposit size. The nozzles used were straight, blunt, hollow stainless-steel needles, mounted with epoxy in Luer lock hubs, bought from Intertronics, Kidlington. All the needles used were ¼ inch long, which typically left the tip of the needle about 1 mm proud of the heated shroud. Needles with internal diameters of 200, 150 and 110 μm (27, 30 and 32 gauge) were purchased.

The heated syringe pump was mounted on a vertical slide with a micrometre screw adjustment. To set the distance between the nozzle and substrate, the syringe was lowered onto the rotating substrate until the needle tip was just touching the substrate surface. The syringe was then lifted the desired distance according to the scale of the micrometre. For experiments using the heater block, at least 15 minutes were left

between inserting the syringe and setting the nozzle height, so that thermal expansion would not cause the nozzle height to drift. Additional degrees of adjustment were used to ensure the nozzle was the correct radial distance from the centre of the rotating stage, in order to achieve accurate setting of the substrate speed.

The position of the camera was adjusted with two orthogonal micrometre slides to centre the jet in the image, as well as a coarse slider to bring the camera to the appropriate focusing distance, but the exact position of the camera with respect to the electro-jet or the light source did not have a significant effect on the captured images. Once appropriately positioned and the magnification of the microscope lens set, the lens focus was set so that the silhouette of the needle was sharp, in theory putting the focus plane through the central axis of the needle. With the light source directly behind the jet, the camera captured a silhouette of the jet, which was almost greyscale due to the intensity and light quality of the lamp.

For a perfectly stable jet, in principal one image would completely capture its behaviour. However, as the jets were imaged under a range of conditions, including those at the edge of stability, three images were taken for each set of conditions. Furthermore, the incremental changes to the jetting conditions were kept small to give good data resolution and clearly establish trends. This resulted in a large number of images to analyse, and so a MATLAB script was developed to extract the key dimensions in an automated manner.

Most of the work in this section was carried out with an oil-based ink containing 50 vol% 4 μm alumina powder and 1.25 wt% KD4 dispersant. The heater block was left at room temperature (21 ^{o}C) and the nozzle height varied between 1.5 and 5.0 mm. The substrate speed was set to 40 mm/s unless otherwise specified. The oil-based ink has a similar rheology to the final ink containing LJ210 and limonene, as shown in Figure 5.16, but was simpler to produce and eliminated the need to heat the syringe, therefore improving consistency and being easier to work with.

In Section 3.2, it was established that the electric field between the nozzle and substrate is not constant, generally being stronger around the nozzle. In this chapter and subsequent chapters, the term 'electric field' is used to mean the expected average electric field, given by dividing the potential difference between nozzle and substrate by the distance between them. This is done as a method of linearly scaling results from different experiments to similar values, although one of the results from Section 3.2 was that the electric field does not linearly scale with nozzle height.

6.1.1 Automated image analysis

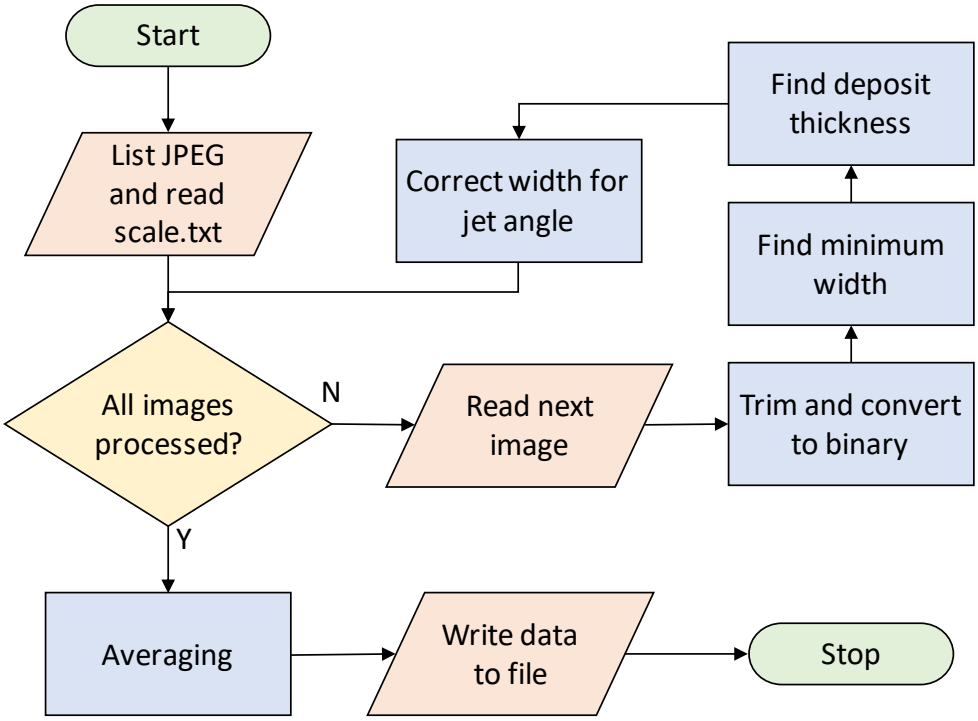

Figure 6.1 Flow diagram of the image analysis script

The final form of the MATLAB code, along with comments, is presented in Appendix D. The basic function of the script is to simplify the image and measure the jet width along each horizontal row of pixels. A flow diagram of the code is shown in Figure 6.1 and the process is demonstrated in Figure 6.2. Given sufficiently clean images, it can also measure the height of the deposit on the substrate. As well as outputting the minimum jet width for each image, the script can also provide averages

over a group. As part of the averaging, any broken jets are identified and discounted. If a given group has too many broken jets, those conditions are considered unstable and the average minimum width recorded as zero. The final feature of the script is to compensate for the angle of the jet, as width measurements are always made perpendicularly to the nozzle axis, which is vertical in the images.

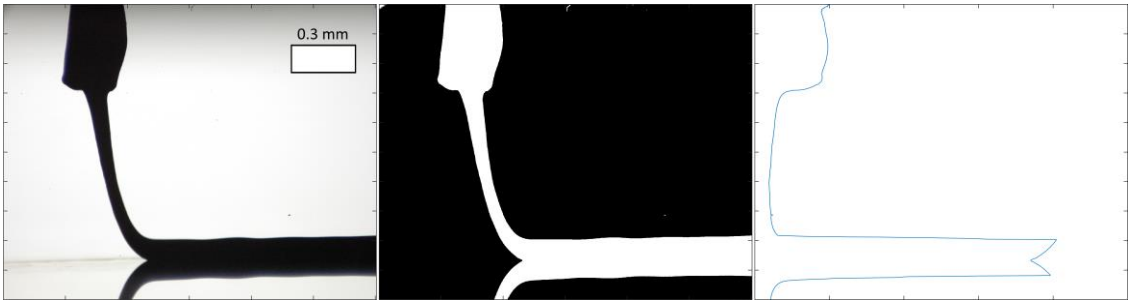

Figure 6.2 Processing of an image of an electro-jet. From left to right: colour image from camera, inverted binary image, sum of pixels along rows.

The script runs in MATLAB while the active directory contains the images to be processed. All JPEG images in the directory are processed in alphabetical order. Note that within MATLAB the rows and columns are numbered from the top left. The first step is cropping the colour image and converting it to binary. The script looks for a text file in the same directory called `scale.txt`, which contains up to four numbers on separate lines. These numbers are taken as the image scale in pixels per mm, the start row, the 'clear height' and the finish row in that order. The values of these numbers must be determined manually in a photo-editing program beforehand. Figure 6.3 shows example positions for the three height values. The start row should be at the nozzle tip, but its main function is to reduce the image size for faster processing and its value does not usually affect the results. Including some of the nozzle itself can help in aligning jet profiles at a later stage. The clear height is used to reduce the data set size for calculation of the deposit height. It can be any row below the nozzle tip and above the top extreme of the deposit, although it should be close to the deposit top for faster processing. The finish height should be below the reflection of the deposit in the substrate. In practice, this value needs to be accurate to avoid the minimum jet

thickness being found in the reflection of the jet, which can prevent the later slope correction working and cause the script to fail.

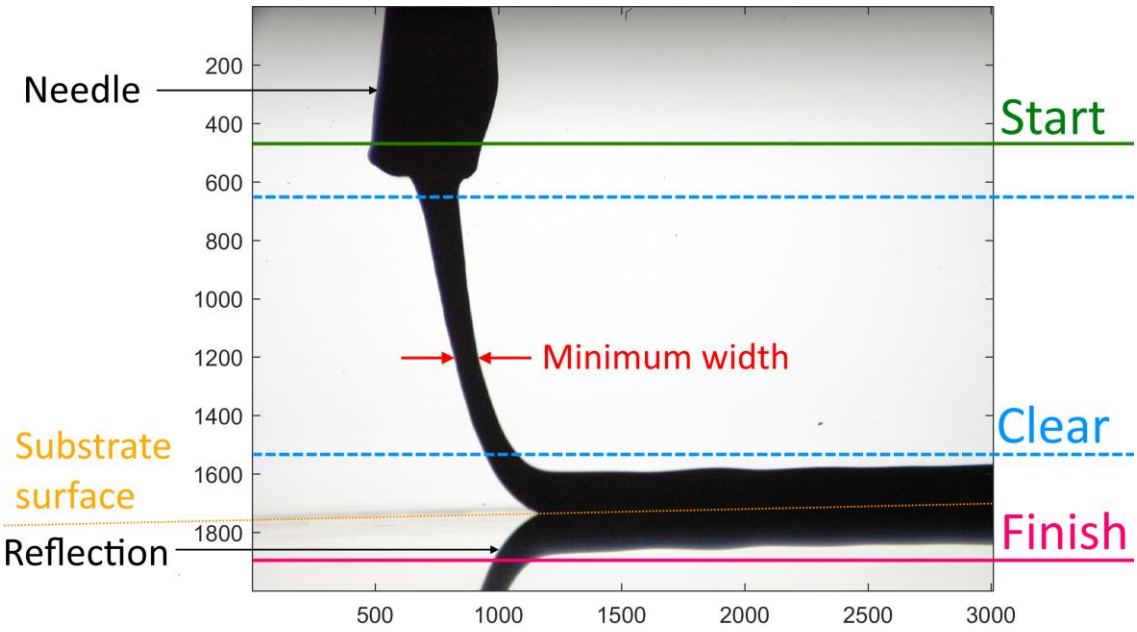

Figure 6.3 Example positions of the three height values found in `scale.txt` and other key features of the jet image. Only the finish height needs to be set precisely for accurate output. The clear height could be set to any height between the dashed blue lines. The minimum width for this jet is indicated by the orange arrows.

To reduce the image to binary, the `graythresh` function is used to determine the threshold for each image by Otsu's method. This threshold is then used to convert the image to pure black and white. This step potentially introduces some error into the width measurements, as different lens focusing and lighting conditions can affect the boundary of the silhouette, but using a variable threshold will at least account for lighting variations. Focus errors blur the silhouette boundary inwards and outwards by an equal amount, so with an accurate threshold value this should not cause significant errors. Once it is binary, the image is inverted, so that the pixels representing the jet are white (or 1) and those representing the background are black (or 0). Then the rows are summed, resulting in a column vector of jet widths.

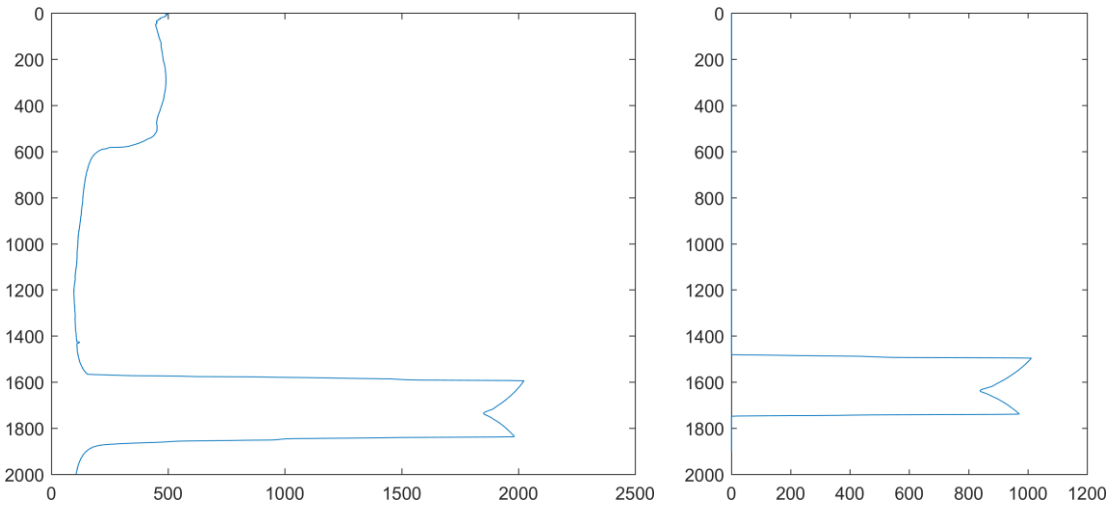

Figure 6.4 Shifting of the widths vector to identify the upper edge of the actual deposit and the 'upper' edge of its reflection, here at 1480 and 1750 pixels respectively.

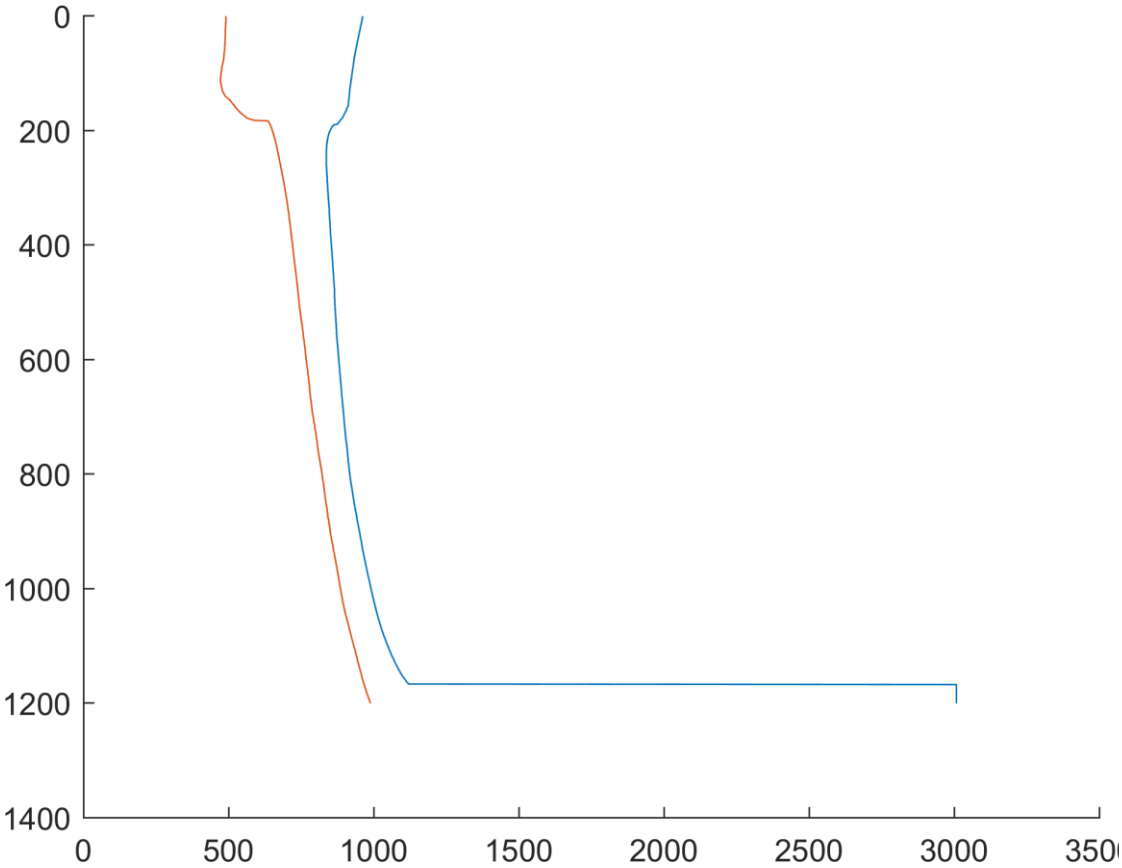

Figure 6.5 Plots of the first (orange) and last (blue) edges of the jet silhouette. The horizontal line at the bottom of the last edge is caused by the top of the deposit on the subtrate and can cause errors in the slope calculation.

Finding the minimum width of the jet is done by simply looking for the minimum value in the width column vector. Finding the average deposit height for that image is a little more involved. First the maximum width is found, which will be in one of the rows through the deposit due to the cropping of the image. All the width values are then reduced by half this maximum value, to a minimum of zero, leaving the only non-zero widths on rows through the deposit, as demonstrated in Figure 6.4. The height of the deposit can then be found by counting the rows between the first and last non-zero values in the vector. This measurement includes the reflection, so the value must be halved before being scaled to get the final figure in millimetres. This method provides an average height for deposits with variable height.

All width measurements are made horizontally across the captured image, but the electro-jets are in practice often not vertical, particularly near the substrate where the narrowest width tends to be located. To account for this and produce more accurate width measurements, the slope of the jet is estimated at the previously found minimum width and then used to adjust that minimum value. Working with the binary image, the indices of the first and last non-zero value on each row are placed into respective vectors, giving two vectors that represent the left and right edges of the jet, as shown in Figure 6.5. For each edge, the row-to-row gradient is calculated and averaged over a region centred on the row with the minimum horizontal width. The size of the region must be manually set to achieve accurate results, with 150 rows found to be suitable for the conditions used in this project, typically equivalent to 0.15 mm. Larger regions can give better accuracy, as the data is coarse due to the small number of pixels under consideration, but too large a region might give inaccurate results due to the curvature of the jet or by including a portion of the deposit. The average slope of the two edges is then averaged to give an estimate of the slope of the jet centreline at that point, which is then used to adjust the minimum width value via trigonometry. This method is only suitable for jets where the averaging region is not close to the point where the jet hits the substrate, which is accompanied by large changes in the jet shape. It is also somewhat sensitive to the size of the averaging region and does not

make direct measurements of the narrowest cross-section of the silhouette, potentially leading to errors. However, the size of the averaging region was chosen such that the output of the script agrees well with manual measurements of the images.

When compared to manual measurement of a representative set of 15 images, on average the script gave minimum widths 6.1 % larger than expected, with maximum errors of +21.8 % and -6.5 %. The large positive errors tend to occur when the true minimum width is very close to the impact point, which causes the deposit to obscure it. This could be addressed by cropping the image to remove the deposit for the minimum width analysis, but this must be done in a way that does not also remove the thinnest part of the jet or affect the measurement of it. The jets that were most affected by this error used high substrate speeds and low electric fields, which produce angled jets. As only a subset of jets will be affected, these errors would appear as a sudden change in the trend of the results and so would be easy to spot. No such changes were found in this work, but this limitation should be considered if using this method with other data. The images used for verification can be found in Appendix E.

The final processing in the script is averaging of the minimum widths and deposit heights for each group of images. There is no checking of file names at this stage, so this relies upon the image files being correctly ordered in the directory. For the minimum widths, a check is made for zero widths. This indicates a broken jet and if it were included in the average, it would erroneously reduce the average minimum width for that group. If more than one of the jets in a group is broken, which would be a majority for the group size of three used in this work, the average minimum width for that group is set to zero to indicate the jet is not stable under those conditions. Otherwise, the non-zero widths and deposit heights are separately averaged.

The last section of the script writes the data to two CSV files. One file only contains the smallest, average and largest of both the minimum widths and deposit heights for each group. The second file contains minimum width, deposit height and full list of widths for each image. The averages are then used to analyse the

relationship between jetting conditions and jet behaviour, while the full list of widths can be used to plot jet profiles for visual comparison.

6.2 Results

A typical set of results is shown in Figure 6.11, where the voltage has been varied for a set of flow rates at a fixed nozzle height. As expected, both a reduced flow rate and increased voltage caused the minimum jet width to be reduced.

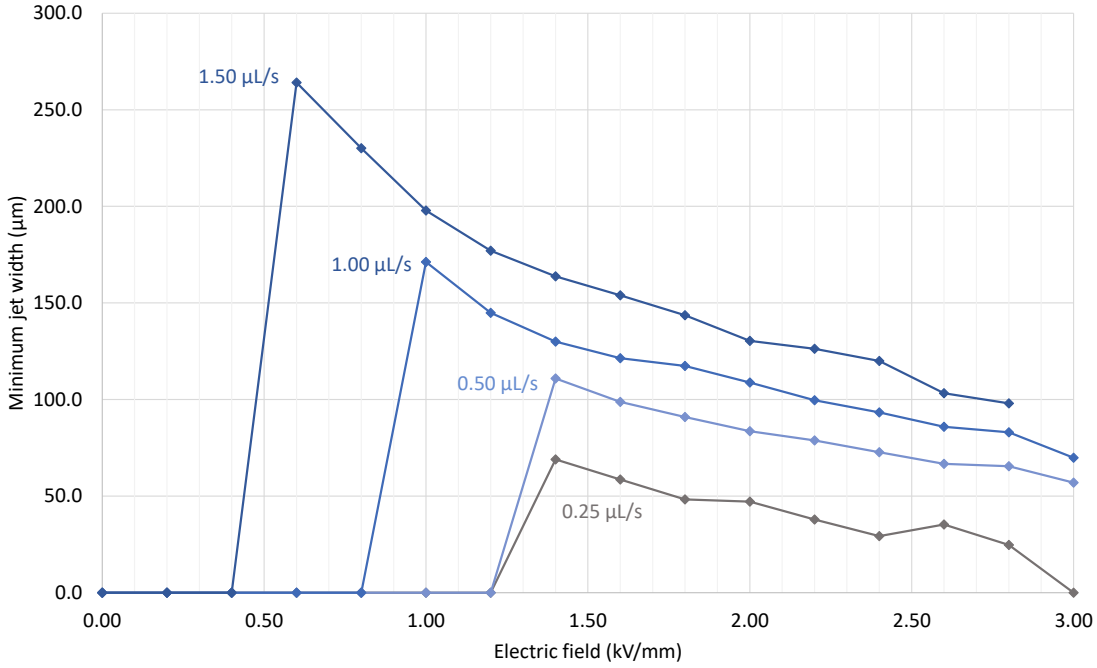

Figure 6.6 Minimum jet widths for a mineral oil ink containing 50 vol% alumina. A 200 µm nozzle at a height of 2.5 mm and a substrate speed of 40 mm/s were used, with the ink at room temperature.

With a set flow rate, by assuming the jet has a cylindrical cross-section at all points, the average speed of the ink can be calculated from the measured width at any point in the jet. The profile of a jet and the corresponding estimated speed is presented in Figure 6.7. The initial acceleration of the ink is roughly 4 m/s^2.

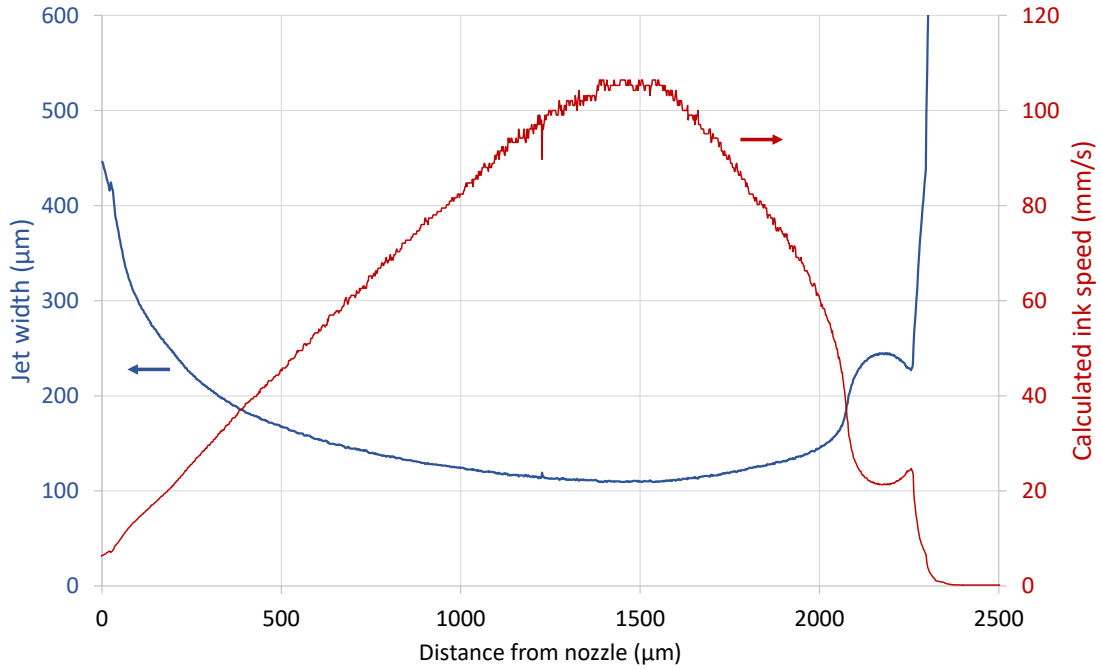

Figure 6.7 Width profile and ink speed for a mineral oil ink containing 50 vol% alumina. A 200 µm nozzle, voltage of 5.0 kV, flow rate of 1.0 µL/s and substrate speed of 40 mm/s were used, with the ink at room temperature.

To compare the relationship between applied voltage, flow rate and minimum jet width over the different nozzle heights, a three-dimensional power law equation was fitted to the data. The minimum width, w in micrometres, is related to the average electric field, E in kV/mm, and the volumetric flow rate, $\dot{Q}$ in nL/s, by a scaling factor, a, and two exponents, b and c, as given by equation 6-1.

6-1
$$w = a(E^b)(\dot{Q}^c)$$

Using the curve fitting utility of MATLAB, this equation was fitted to the data using a non-linear least squares method. The values of the parameters are shown in Figure 6.8. The exponents were found to have reasonably constant values over the range of nozzle heights, but the scaling factor varied significantly. Re-fitting the curves with the exponents set to their average values of b = -0.53 and c = 0.66 gave a' in Figure 6.8. This reduced the variance in the scaling factor, but made it clear that it

was dependent on the nozzle height, *h*. Therefore, a separate power law fit, of the form shown in equation 6-2, was used extract the height dependence from *a'*.

6-2 $$a' = m(h^n)$$

This had to be done as a separate step because the curve fitting utility only allowed up to three-dimensional data. The final scaling parameter, *a"*, could then be found by fitting the data with all the exponents fixed, as in equation 6-3.

6-3 $$w = a"(h^{-1.28})(E^{-0.53})(\dot{Q}^{0.66})$$

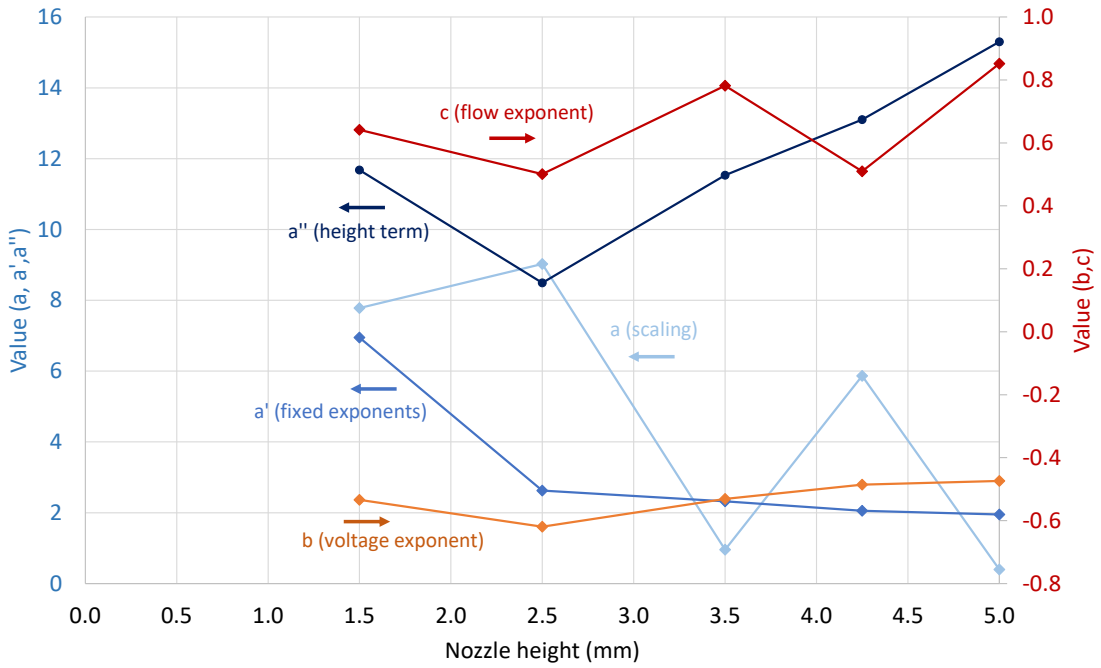

Figure 6.8 Plot of the values of the three parameters for the three-dimensional power law fit for different nozzle heights (a, b, c), plus the value of the scaling parameter when the exponents were fixed to their average values (a') and the scaling parameter when a height term was included (a").

Having found values for each of the model parameters that are reasonably consistent over the experiment conditions, equation 6-3 could be used with *a"* set to its average value of 12.0 to predict the minimum jet width under any conditions. The R squared values for each fitted curve were never below 0.84 and averaged 0.91. Plotting the measured minimum width against the calculated value gave the 'master

curve' shown in Figure 6.9. For a perfect model, all points would lie along the dashed diagonal line.

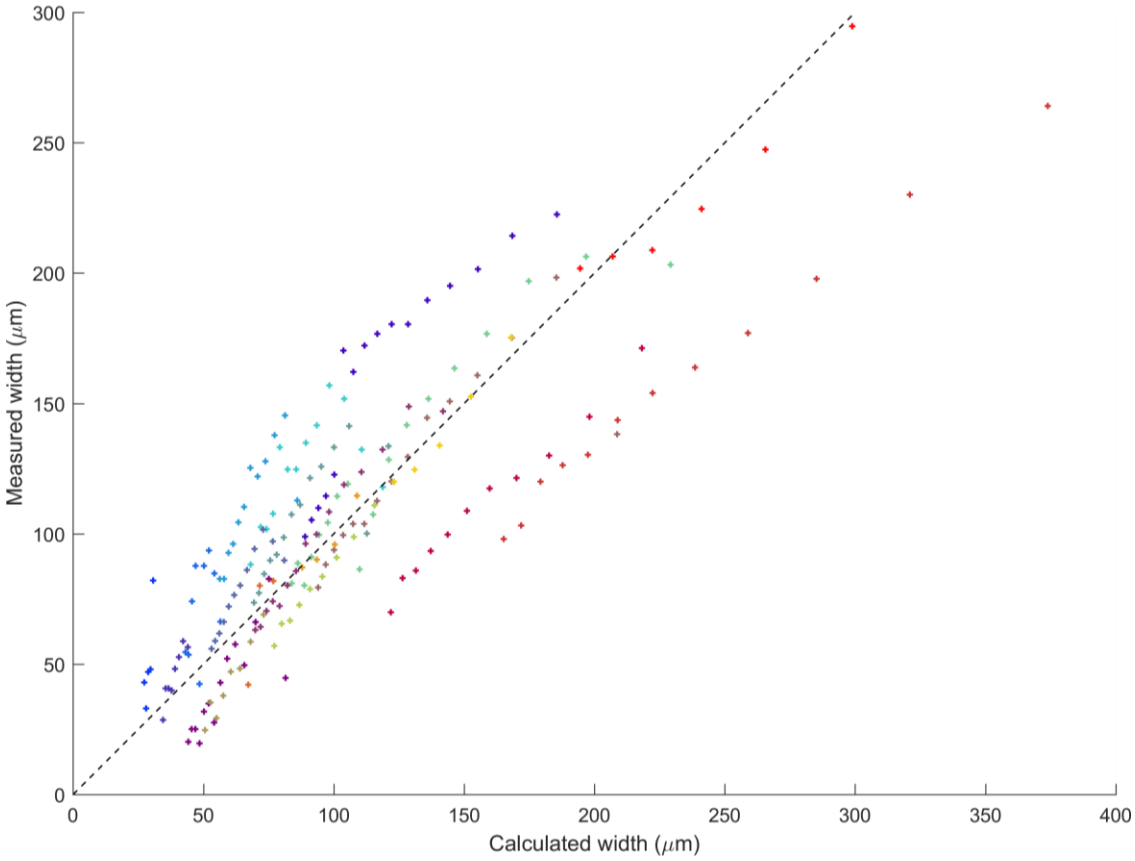

Figure 6.9 Master curve plot for the oil-based ink using equation 6-3. The dashed diagonal line indicates equivalence between calculated and measured values. Each combination of nozzle height and flow rate has a unique colour.

The agreement was generally good, although the series stretching to the top right of the plot was of some concern. This series used a nozzle height of 2.5 mm and a flow rate of 1.5 μL/s, which gave it a higher flow rate compared to the height than any other series. It might be expected that this would lead to the jet being thicker than expected, due to pooling as the jet hits the substrate, but that would push the data points above the dashed line in Figure 6.9, not below it. Possible explanations for the thinner than expected jet include a partially blocked nozzle, leakage in the syringe pump or the experiment being performed with the last portion of ink in the syringe, which it was shown in Section 5.4.1 can have significantly different properties. Re-calculating the

model with this data removed yielded equation 6-4, which has slightly different values to equation 6-3. Note that the change in exponents gives the scaling factor different units.

6-4 $$w = 11.2(h^{-1.19})(E^{-0.55})\left(\dot{Q}^{0.66}\right)$$

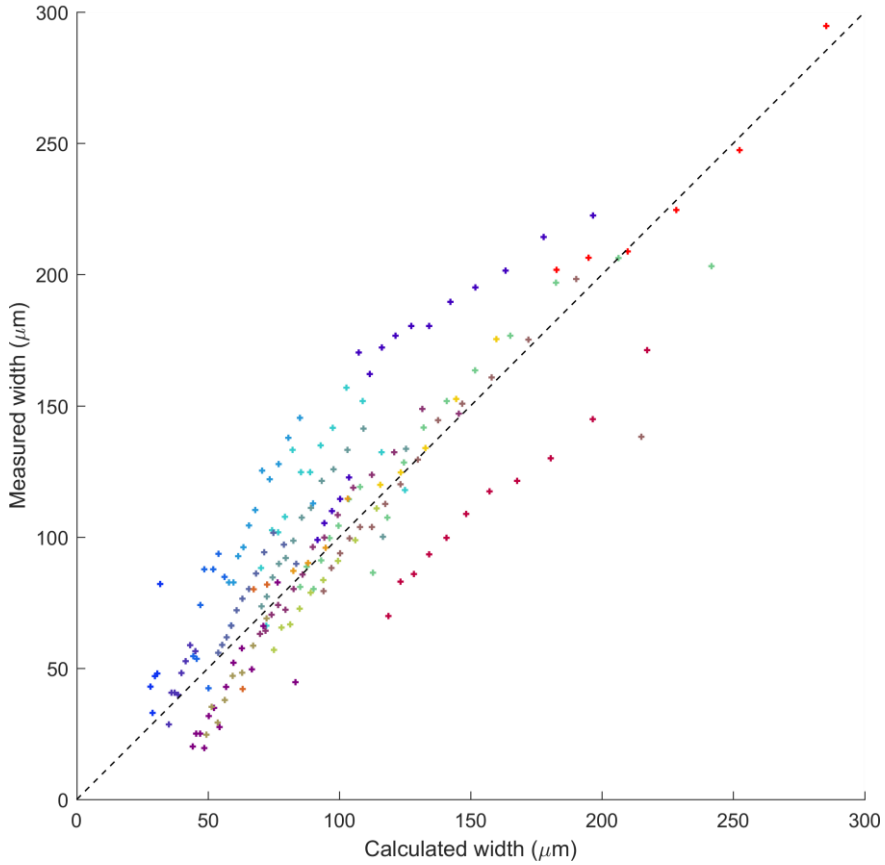

Figure 6.10 Master curve plot for the oil-based ink using equation 6-4, calculated with the outlier series of Figure 6.9 removed. The dashed diagonal line indicates equivalence between calculated and measured values. Each combination of nozzle height and flow rate has a unique colour consistent with Figure 6.9.

Replotting the master curve with this modified equation refined it to Figure 6.10, which was mostly similar to simply removing the suspect data series from Figure 6.9. Even with the refined model, there appeared to be a curve to the data points and a reasonable spread of data, suggesting the model might be incomplete, there was more anomalous data, or the two-stage fitting had introduced inaccuracy.

Taking the model as accurate, the ability to use constant exponents indicated that the effect of the applied voltage and flow rate was consistent across the different nozzle heights and that changing the flow rate by a certain factor would have greater effect on the minimum jet width than changing the voltage by the same factor. The exponent on flow rate also agrees with the highest value discussed in Section 2.2.2, although those relations did not feature the voltage or geometry. The voltage might make a difference here because the ink has a much higher viscosity than any of the work covered in Section 2.2.2. This would slow down the fluid dynamics, possibly allowing electric field effects to become visible. The height dependence may simply be due to the different methodologies, as the scaling laws were derived from jets that continued to breakup, whereas this work intentionally avoided breakup. This means the jet did not always reach its minimal diameter and how far from the minimum diameter it was depended on the nozzle height.

6.3 Operating maps

Two of the most easily varied conditions of the experimental setup were the potential of the substrate and the flow rate of the ink. By varying these conditions while holding the other variables constant the combinations that produced useful electro-jets could be identified. These could be plotted to produce an operating map for the ink, as shown in Figure 6.11 and Figure 6.12.

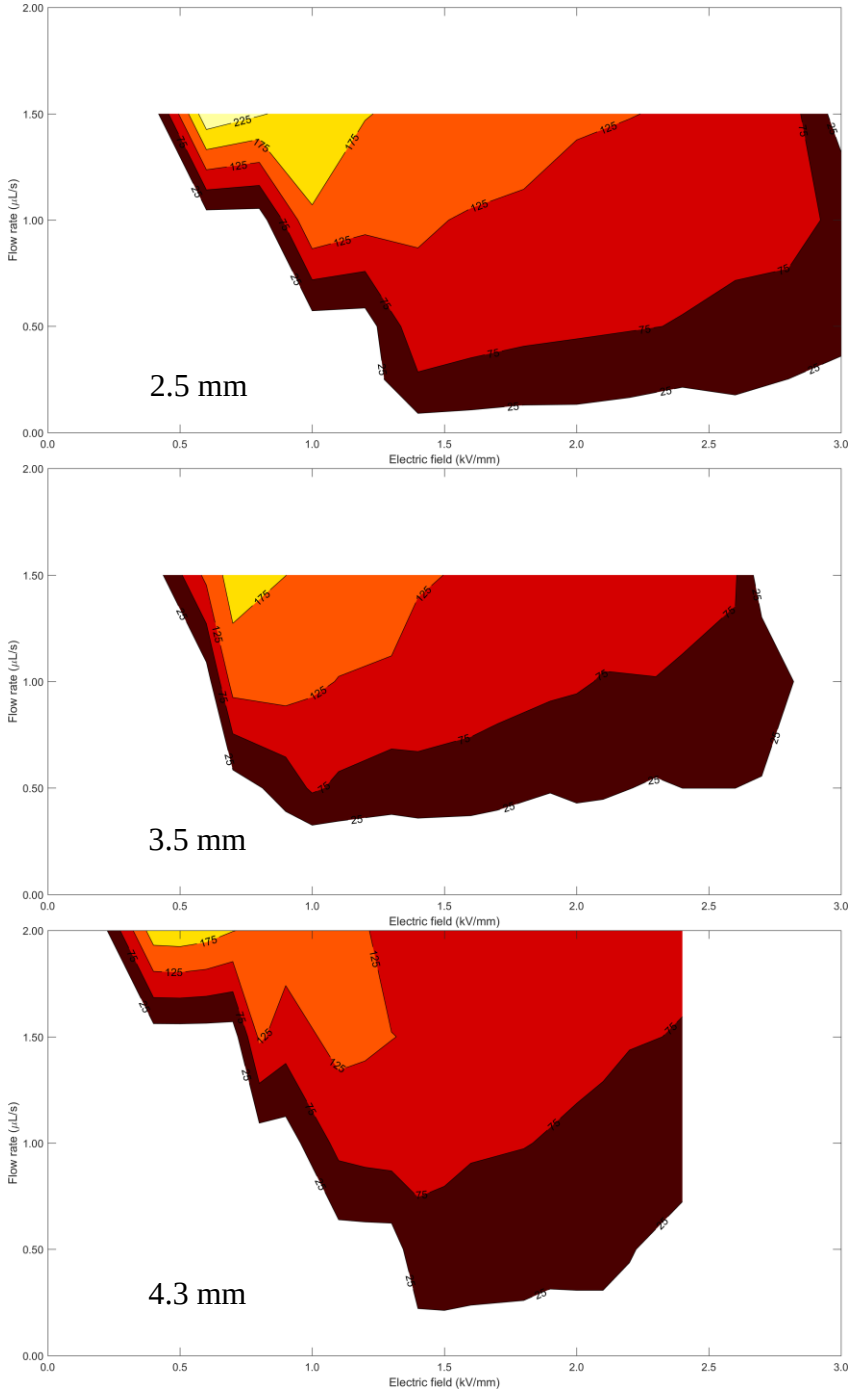

Figure 6.11 Ink flow rate opertaing map for a mineral oil ink containing 50 vol% alumina at nozzle heights of 2.5, 3.5 and 4.3 mm, from top to bottom. The labelled contours indicate the minimum jet width observed in micrometres. A 200 µm nozzle and substrate speed of 40 mm/s were used, with the ink at 21 °C.

As seen in Figure 6.11, the minimum jet diameter varied more rapidly with the ink flow rate than the electric field, particularly in the middle of the electric field range. The transition into and out of stability caused the electric field to be more important at the lowest and highest field strengths respectively. The result of this was that the electro-jet was relatively insensitive to the field strength at medium fields, giving consistent behaviour under small changes in the electric field. Additionally, Figure 6.12 indicated that the electro-jet would not be significantly affected by small changes in nozzle height, because this also implied a reduction in electric field, provided the potential of the substrate was held constant. For raising the nozzle, this corresponded to a movement upwards and to the left on Figure 6.12, in the same direction as the contours of constant jet width. These two observations were important when considering 3D patterning, where it may be necessary to raise the nozzle during deposition to accommodate the layers of previously deposited ink. An electric field of 2.0-2.5 kV/mm appeared to give the best results for this oil-based ink.

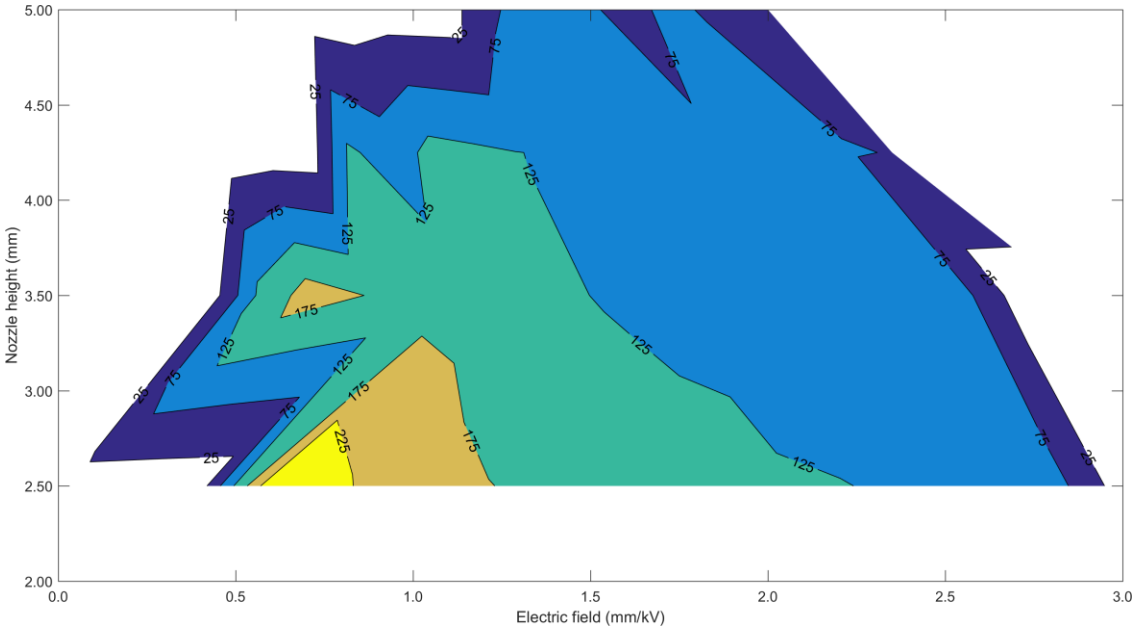

Figure 6.12 Nozzle height opertaing map for a mineral oil ink containing 50 vol% alumina at a flow rate of 1.5 µL/s. The labelled contours indicate the minimum jet width observed in micrometres. A 200 µm nozzle and substrate speed of 40 mm/s were used, with the ink at 21 °C.

6.4 Ink viscosity

The operating maps in Section 6.2 were produced using an ink based on mineral oil, with a viscosity of around 2,200 mPa s at room temperature. As the temperature dependence of the viscosity of this ink had been measured in Section 5.2, the ink could be heated to produce a lower viscosity ink with identical composition.

A summary of the effects of lower viscosity ink on the electro-jet is presented in Figure 6.13. The minimum width of the electro-jet was reduced by a lower viscosity, but the range of stable voltages was also reduced. A lower viscosity ink required both a higher electric field to form a stable jet and a lower electric field to push the jet into a dripping mode compared to a more viscous ink.

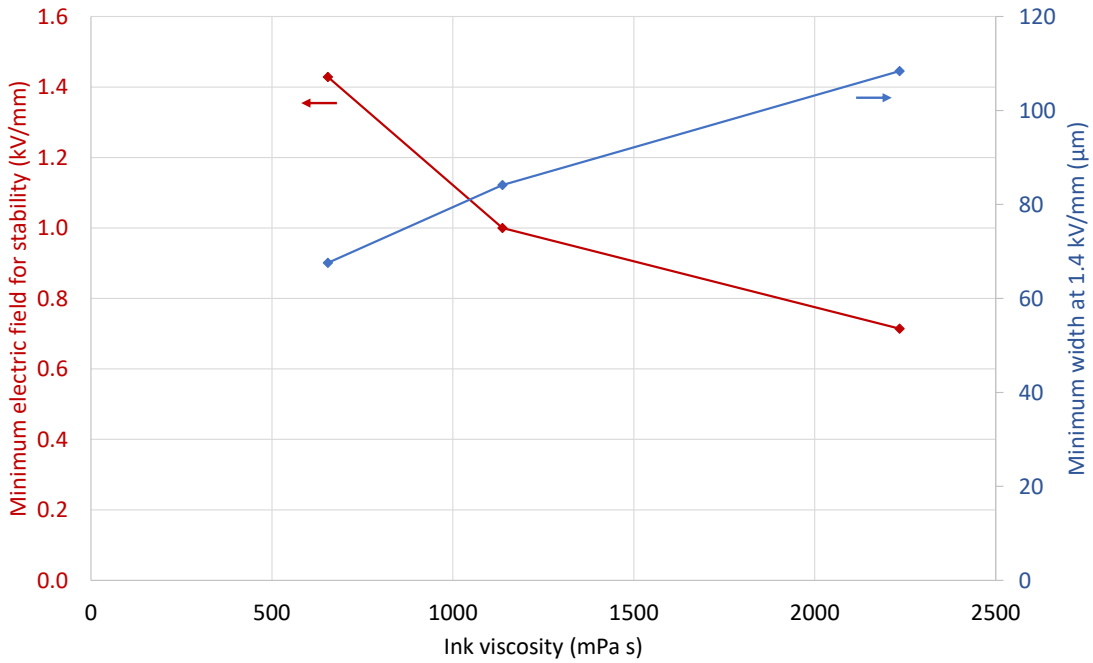

Figure 6.13 Effect of ink temperature on the voltage at which the first stable electro-jet was observed and the minimum width of the jet at an electric field of 1.4 kV/mm. The horizontal axis uses the expected viscosity based on the data presented in Figure 5.11. The ink was deposited from a 200 µm nozzle 3.5 mm above the substrate with an ink flow rate of 1.0 µL/s.

The reduction in minimum width was facilitated by the increased mobility of the ink, the lower viscosity allowing it to flow further in the same time under the same force, resulting in greater stretching. This increased mobility also contributed to the

lower electric field for the transition to a dripping mode, speeding up the development of the Rayleigh instability along the jet. The need for a higher electric field to form a stable jet was not related to this instability, as here the transition was typically from drops forming at the nozzle to a continuous filament of ink.

6.5 Nozzle diameter and polarity

When all conditions except the nozzle diameter were held constant, it would be expected that a larger nozzle would produce larger diameter jets. However, a larger diameter jet has a larger surface on which to hold charge and will have a lower fluid velocity than a narrower jet, which may cause the variation to be small or the effects to be non-linear.

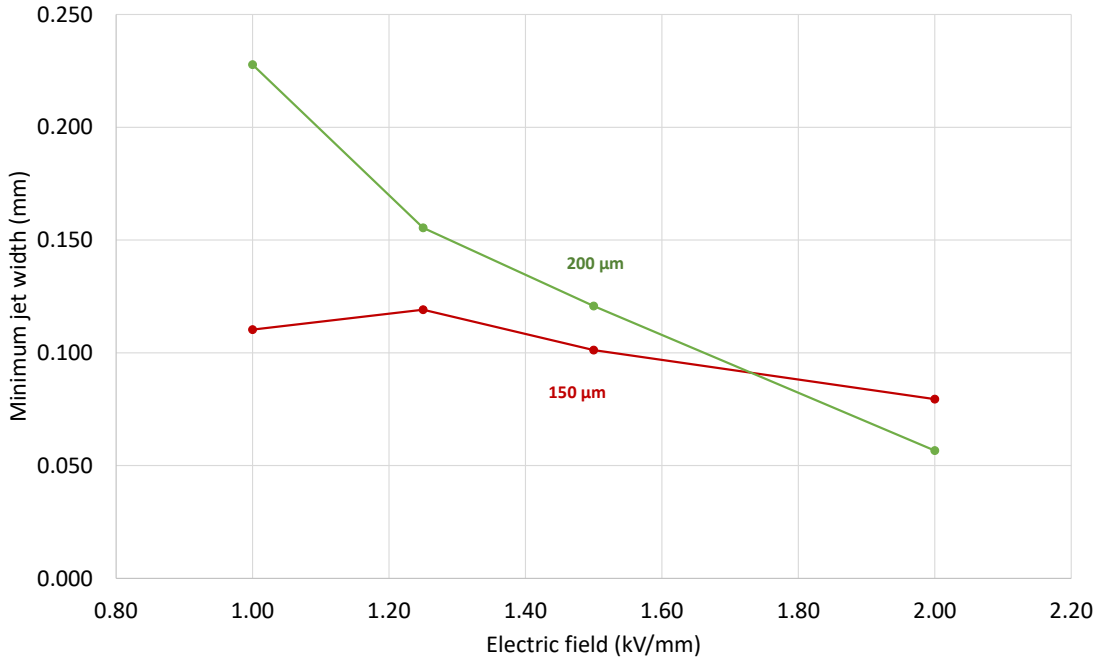

Figure 6.14 Variation in minimum electro-jet width with applied voltage for different nozzle sizes using an oil based ink with 50 vol% alumina at a nozzle height of 1.0 mm and a flow rate of 0.5 µL/s.

With the inks developed in Chapter 5, it was possible to electrospin through needles with internal diameters as small as 150 µm, although not reliably for an extended period. The next smallest diameter needle available was 200 µm, which rarely

suffered blockages. The correlation between electric field and minimum jet diameter for two nozzle diameters is shown in Figure 6.14. At lower electric fields, the larger nozzle did indeed produce larger diameter jets, but an increased field caused greater thinning such that at higher fields the larger nozzle produces jets of the same or smaller diameter than the narrower nozzle. This was likely due to the larger surface area and lower fluid velocity previously mentioned. The larger surface area carried a greater quantity of charge as the ink left the nozzle, which resulted in a greater force on the ink. The force was distributed over a larger volume of ink, but as the jet narrowed, the charge density would increase, possibly causing the acceleration of the ink to match or exceed that at the same point in a jet from a narrower nozzle. The larger diameter also meant the linear velocity of the ink was initially lower. This meant the ink was in flight for longer, particularly in the highest electric fields near the nozzle, as predicted in Section 3.2. Even if the acceleration of the ink was equal for both nozzle diameters, this resulted in the final velocities of the ink becoming closer to equal.

It has previously been reported that the polarity of the nozzle with respect to the substrate affects the electrospinning process (Ragucci et al., 2004), which was also observed in this work. Figure 6.15 shows how switching the polarity of the nozzle affects the formation of a stable electro-jet. Although the dataset was limited, it was clear a nozzle that is at a lower potential than the substrate needed lower voltages to achieve stability. It also appeared that the jet was stable over a smaller voltage range, although this was not strongly supported by the data and was likely simply the result of the reduced scale of the voltages. This result was favourable as with this particular experimental setup, making the nozzle positive with respect to the substrate caused some form of leakage current to ground, making it possible to receive mild shocks from the baseplate. For this reason, the experiment was curtailed, leading to the limited data.

Note that this result was in opposition to that found by Ragucci et al. In their work, they found that modified heptane with a negative polarity nozzle needed higher

voltages, rather than the lower voltages for the ink of mixed LJ210 and wax used here. This discrepancy, and the reason for nozzle polarity influencing electrospinning at all, was most likely due to the mobility of different charge carriers in the fluid. As the inks used in electrospinning are typically of very low conductivity, most charge transport is by movement of charged molecules or ions, rather than electron exchange. This is much slower, but importantly the speed of charge movement depends on the mobility of the ion and this is not necessarily equal for ions of different polarities. Thus, an ink with very mobile negative charge carriers but slow positive charge carriers will respond to nozzle polarity in an opposite manner to an ink with slow negative carriers but mobile positive carriers.

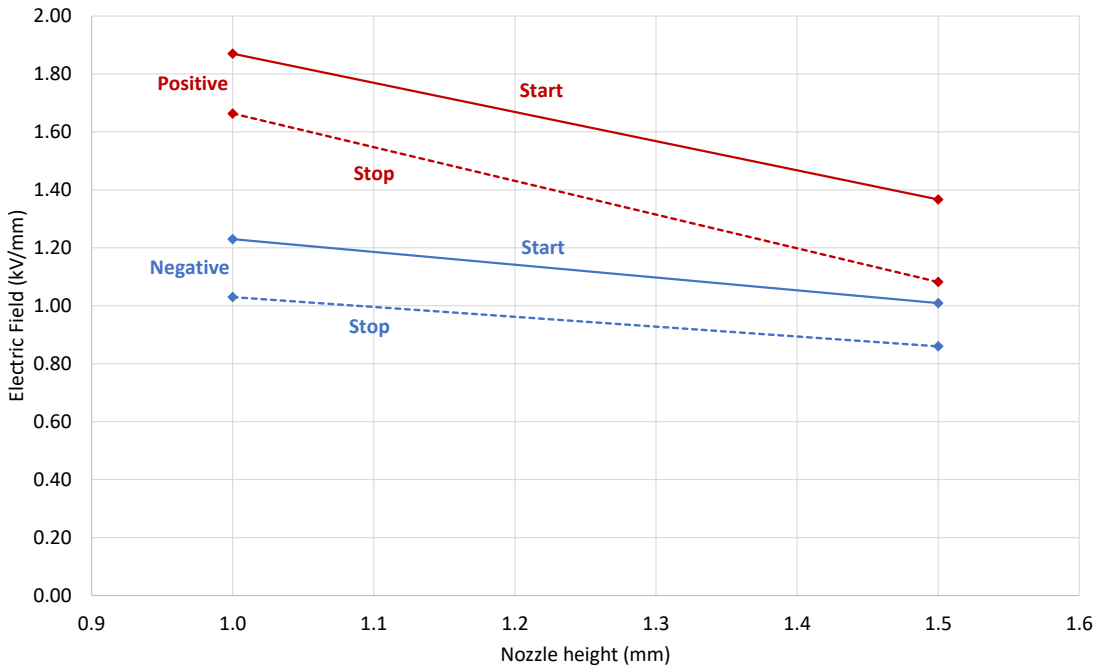

Figure 6.15 Effect of nozzle polarity on the stability of electro-jets at low electric fields. The nozzle was always grounded and the polarity of the substrate changed to make the nozzle positive (red) or negative (blue) with respect to the substrate. The voltage was raised until a stable jet was formed (solid line), then lowered until the jet became unstable (dotted line). The experiment used a LJ210 ink with 50 vol% alumina and the heater set to 85 ^{o}C, using a 200 µm nozzle and a substrate speed of 45 mm/s.

6.6 Substrate speed

For most of the preceding experiments, the substrate speed had been held constant. However, it did have an effect on the geometry of the electro-jet, mainly near the substrate. As discussed in Section 2.2.5, if the speed of the substrate does not match the speed of the fluid in the electro-jet, a semi-rigid jet will buckle or hang when the jet is faster or slower than the substrate respectively. In this work, the ink was still liquid at impact, based on the modelling of Section 3.3 and observations of how the jet impacted upon the substrate. Thus, instead of buckling, the incoming ink piled up and thickened the lowest portion of the jet. This reduced the minimum diameter of the jet and moved its location further up the jet.

The fact that the ink was molten as it hit the substrate also effectively negated the benefit of achieving a small minimum width, as the ink could still flow. The result was that the diameter of the deposit was almost entirely a function of the flow rate and substrate speed, as described in Figure 6.16. Considering that the aim of this work was to produce filaments of material with a width less than 200 μm, it was clear that very small flow rates or quite high substrate speeds are needed. These conditions were limited by the equipment available, as the syringe pump had a minimum step of about 0.045 μL, and with the pump mounted on the three-axis stage speeds above 40 mm/s caused oscillations during sudden direction changes, such as right-angled turns. These limitations could be overcome easily with redesigned apparatus. With the available equipment, the majority of work was done using a flow rate of 0.25 μL/s to achieve 100 μm diameters at substrate speeds of 40 mm/s or less. Lower flow rates risked pulsing of the ink flow due to the nature of stepper motors, one of which drove the syringe pump.

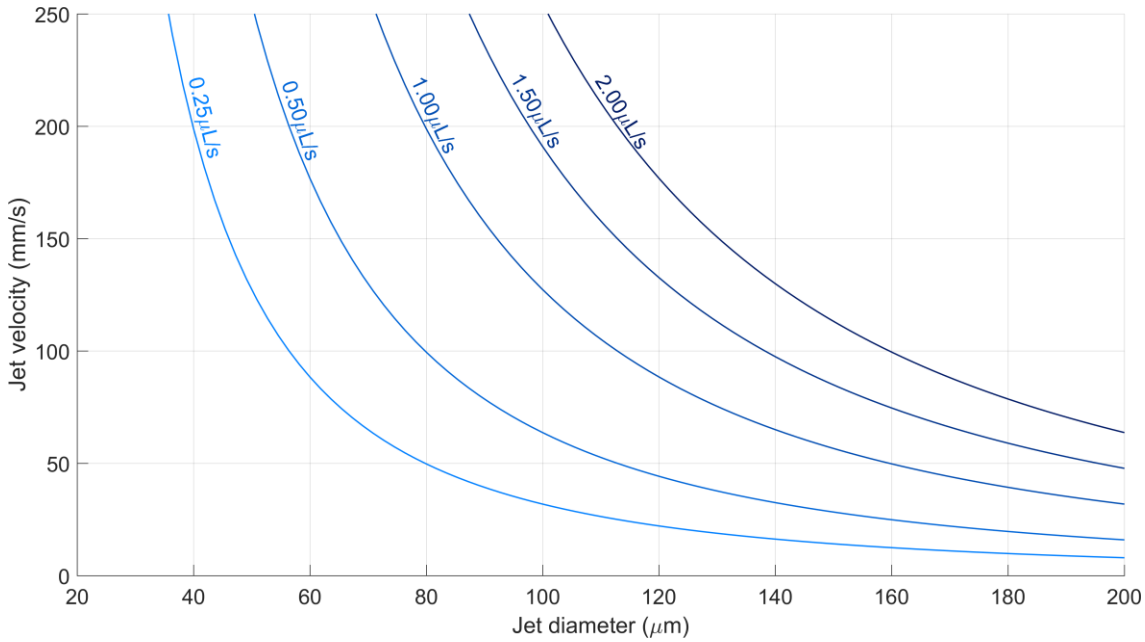

Figure 6.16 Theoretical relationship between diameter and linear velocity for a uniform cylindrical column of fluid at various volumetric flow rates.

Figure 6.17 shows the relationship between minimum width and applied voltage for speeds between 10 and 40 mm/s when using a LJ210 ink. The horizontal lines indicate the theoretical diameter of the ink at each speed, as described in Figure 6.16. The effect of substrate speed on the minimum width of the jet was pronounced, having a larger effect than the applied voltage over the range of conditions investigated. This was partly because the jets were stable at almost all speeds but only over a relatively small voltage range.

Figure 6.18 shows the deposit heights for the same run of data as Figure 6.17. In contrast to the minimum jet width, the deposit height had very little to no dependence on the applied voltage. Instead, it was entirely determined by the substrate speed, as expected if the ink was still molten upon reaching the substrate. The measured heights correlated well with the expected theoretical diameters. This lent credibility to both the measurement method and the assumption that the deposit cross-section was close to circular.

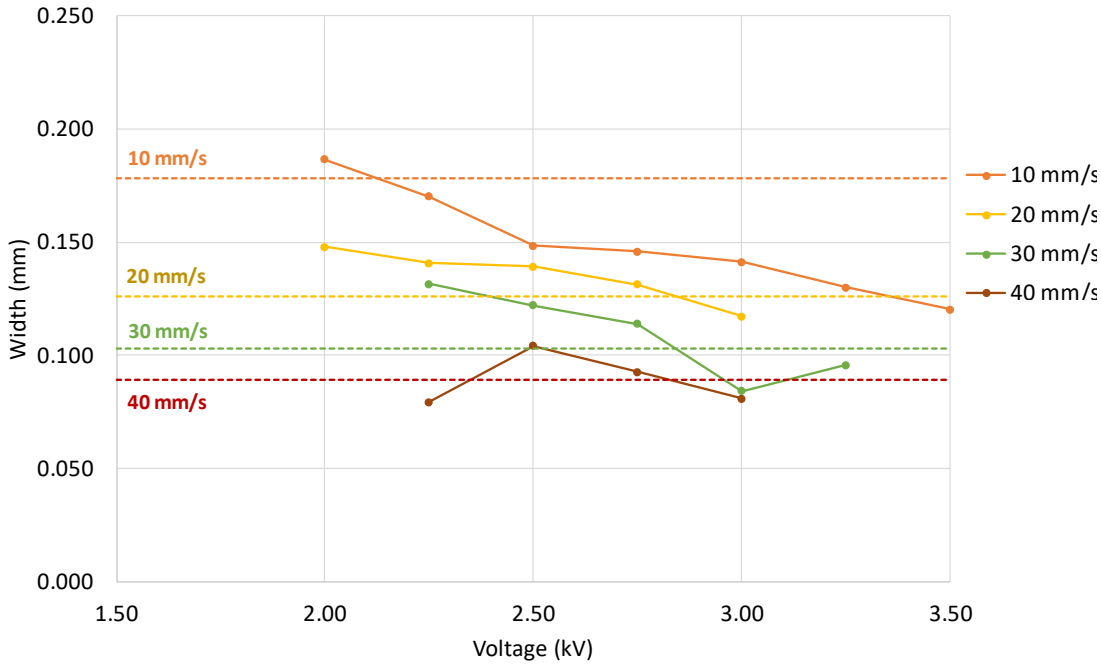

Figure 6.17 Variation of minimum jet width with voltage for a range of substrate speeds, using a LJ210 based ink with 50 vol% alumina from a 200 µm nozzle 1.0 mm above the substrate and a flow rate of 0.25 µL/s. The horizontal dashed lines indicate the expected diameter of a cylinder of ink flowing at the substrate speed with the same volumetric flow rate.

The strong dependence of deposit diameter on substrate speed, along with its independence from the applied voltage, meant that the output of the electrospinning process was robust to changes in the electrical conditions. Arguably, the applied voltage was unnecessary to control the deposit diameter, the benefit of the applied voltage instead being the forming of the ink into a continuous filament, rather than separate drops. If the conditions were changed, by reducing the syringe temperature or cooling the jet for example, it might be possible to avoid the re-flowing of the ink on impact, thus preserving the minimum diameter achieved during electrospinning. In this case, the process would become more sensitive to both the electrical conditions and the substrate speed, potentially causing greater variation but also allowing for greater control.

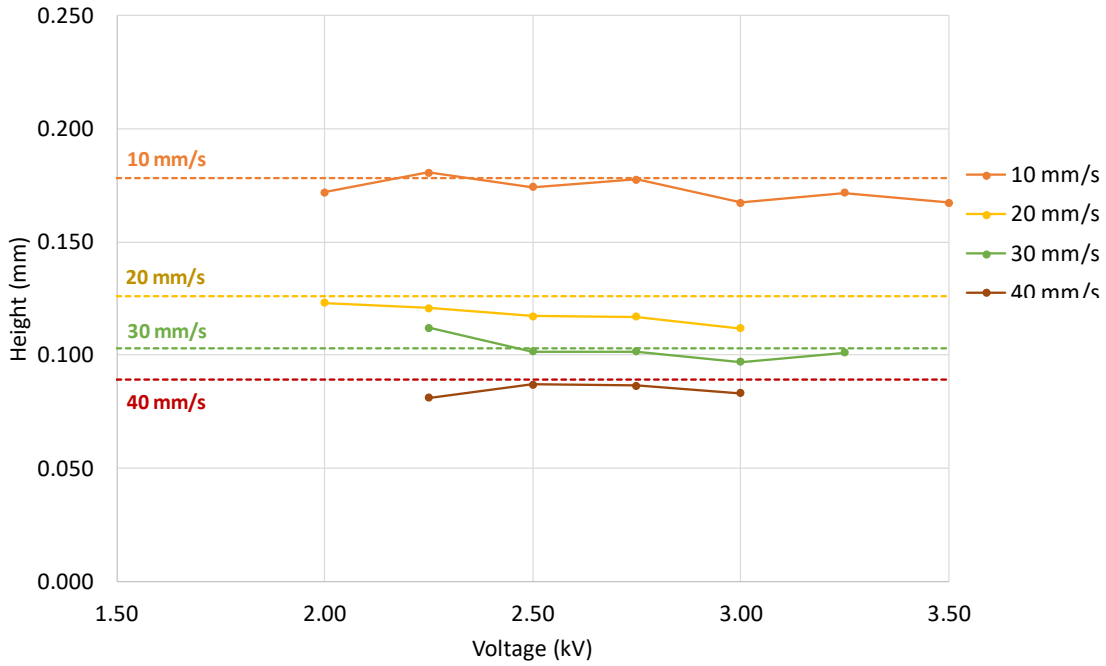

Figure 6.18 Variation of deposit height with voltage for a range of substrate speeds, using a LJ210 based ink with 50 vol% alumina from a 200 µm nozzle 1.0 mm above the substrate and a flow rate of 0.25 µL/s. The horizontal dashed lines indicate the expected diameter of a cylinder of ink flowing at the substrate speed with the same volumetric flow rate.

6.7 Conclusions

The electro-jets were reasonably insensitive to changes in voltage at electric field strengths of 2.0 to 2.5 kV/mm. At these field strengths, small changes in the nozzle height did not cause significant changes in the minimum jet width, as the extra height was offset by a weakening of the electric field. This was beneficial for 3D patterning, where deposited material might require lifting of the nozzle.

Reducing the viscosity of the ink decreased the minimum width of the jet under otherwise identical conditions, but at the cost of reducing the range of voltages over which the jet was stable, limiting the possibility of using this as a route to produce thinner filaments.

Narrower nozzles produced narrower jets, but at electric fields of 2.0 kV/mm and greater the difference was negligible and larger nozzles could even produce narrower

jets. A possible reason for this was that the larger nozzle could impart more charge to the ink, thus causing greater acceleration. Changing the polarity of the nozzle changed the electric field required to produce a stable jet. Although making the nozzle negative with respect to the substrate gave stable jets at lower voltages, the equipment used made this arrangement a shock risk. The literature also suggests the lower voltages are accompanied with narrower ranges of voltage for stable jetting, so a positive nozzle polarity was used in most of the work.

The speed of the substrate had a significant effect on the minimum jet width and entirely determined the height of the deposit. This meant almost all the conditions of electrospinning, excepting ink flow rate and substrate speed, had no effect on the final product, provided the electro-jet was stable. Lower flow rates and higher substrate speeds gave smaller deposits, but the equipment limited the flow rate to above 0.25 μL/s and the substrate speed to 40 mm/s and below, which should produce filaments of less than 100 μm diameter.

7 Direct Writing

To create arbitrary 3D geometry requires the ability to position material exactly where needed and nowhere else. However, any real method will have limits to how it can add or remove material. In this chapter the behaviour of the electro-jet and the deposits left by it are examined while creating various patterns in order to explore these limits.

7.1 Techniques

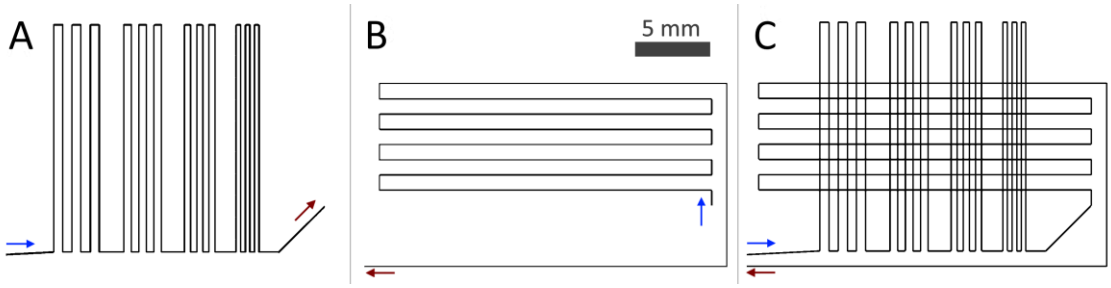

Figure 7.1 Details of the square lattice pattern. Path A was drawn first, followed by path B, resulting in lattice C. The vertical lines of A have centre-to-centre spacing of 0.6, 0.5, 0.4 and 0.3 mm. The horizontal lines of B were deposited over the lines of A with a spacing of 1.0 mm.

The patterns were created using the three-axis platform described in Section 4.2.2. The syringe pump was driven by a signal generator and separate motor driver to give a constant flow rate during deposition. For precise control of speed and position of the nozzle, MATLAB scripts were used to generate different g-code files for each desired pattern. Example scripts are given in Appendix F.

The square lattice in Figure 7.1 was used as a standard test case, as it includes multiple features of interest. First, the decreasing spacing of layer A allowed for rough determination of the minimum possible spacing of adjacent filaments. Second, layer B was deposited over layer A, showing the filaments spanning a range of small

gap sizes. Third, both layers included sharp corners followed by straight runs, which demonstrated the behaviour of the jet through corners. The full path was designed to finish at the start point, so that multiple layers of the lattice could be built up by running the script several times in succession.

References to the 'substrate speed' in this section will always refer to the relative speed of the substrate with respect to the nozzle. In practice, the substrate was stationary and all the horizontal motion was performed by the nozzle.

7.2 Electrostatic effects

The ink used in this work had a relatively high viscosity and was assumed non-conductive, which meant that the charge imparted to it when leaving the nozzle could not be easily dissipated once on the conductive substrate. This could become a problem when a jet of ink was directed toward previously deposited ink, as they would both carry the same charge and be repelled. This has been observed in other work, as discussed in Section 2.2.5 and shown in Figure 2.13.

There were two situations of interest. The first was when the incoming ink passed close to or crossed an existing filament, but contact between the old and new filaments should be minimal or non-existent. The second situation was depositing directly on top of a previously deposited filament, where good alignment was critical for building high-aspect ratio walls. This section will focus on filament crossings and the next section on layer stacking.

To investigate the behaviour of crossing filaments, the simple pattern shown in Figure 7.2 was used. A straight line was deposited, followed by a line at some angle, which crossed the first line. Enough space was left at the top turn so that the angled line could establish itself before being affected by the deposited line. The effects of the trapped charge were expected to become apparent at the crossing of the two lines. Angles from 20 to 5 degrees were investigated under different deposition conditions, with three elements patterned for each angle. The deposited patterns were photographed from above using the same camera equipment for use with the rotary

stage, described in Section 4.2.1. Measurements were taken from these images as shown in Figure 7.3.

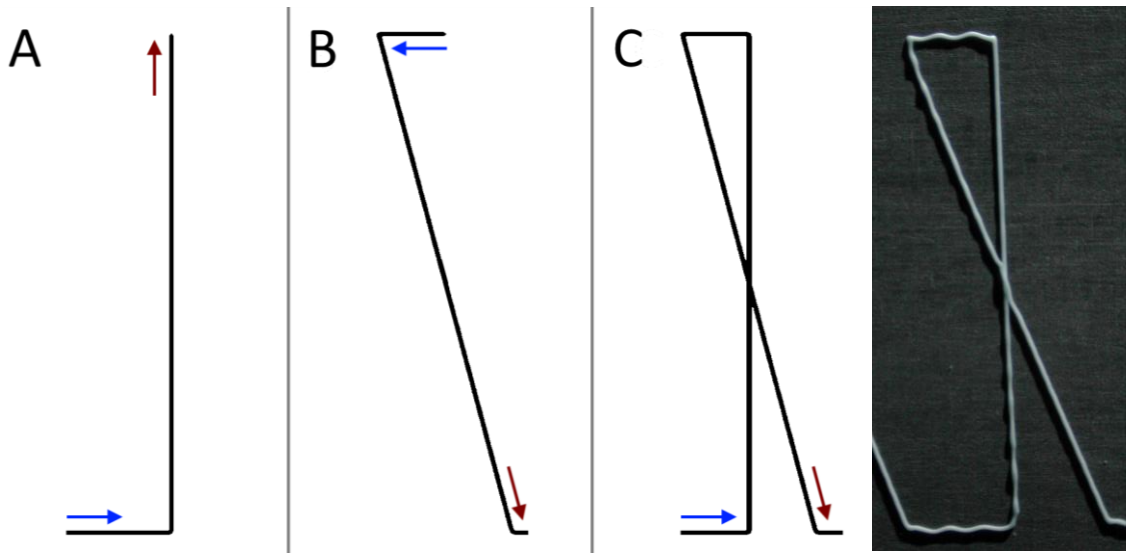

Figure 7.2 Details of the path followed for one element of the angled crossing test (left) and actual deposited pattern (right). In this example the crossing angle is 15 degrees and the element is 15 mm tall. Path A is depsoited first, then path B, resutling in path C.

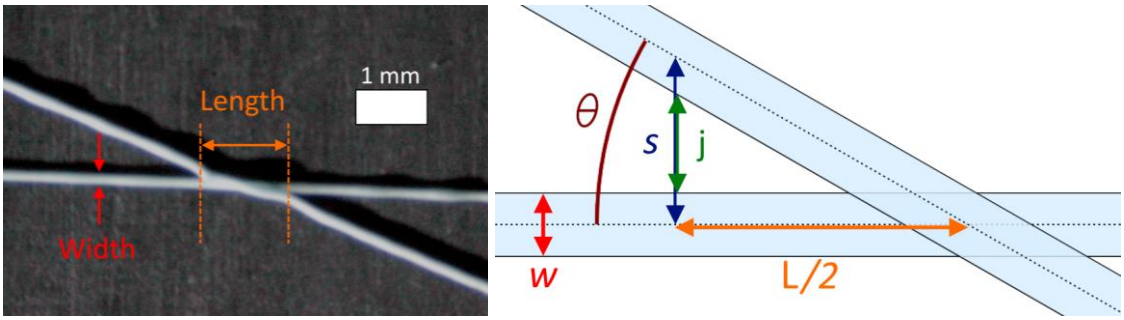

Figure 7.3 Example measurement of an element of the angled crossing pattern as deposited (left) and of the ideal geometry (right), showing the filament width w, centreline spacing s at distance from the filament crossing L/2. The gap expected between perfectly staring filaments, or the distance the deflected filament has jumped, is labelled as j.

From the left-hand image in Figure 7.3, it was clear that the main effect was attraction of the incoming filament to previously deposited ones, rather than the expected repulsion. This could be explained by the ink having some degree of conductivity, allowing the deposited material to dissipate its charge and act as a raised

grounded surface, or by the dielectric effect of the ink. Alumina has a relative permittivity of around 10 and paraffin wax of just over two, giving an average relative permittivity for the mixed ink of approximately 6. Using the same workflow described in Section 3.2, Figure 7.4 A shows how a deposit with this permittivity would affect the electric field. Additionally, simulations were carried out assuming the filament surfaces were charged (B) or that the incoming filament was charged while the deposited filament was conductive and therefore at the same potential as the substrate (C).

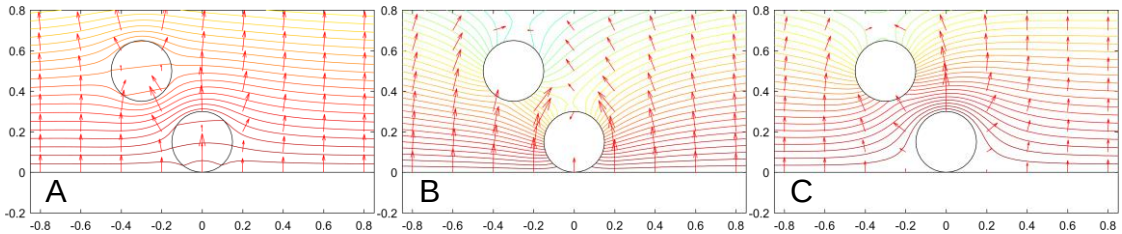

Figure 7.4 Electrostatic simulations of a pair of 0.3 mm diameter cylinders sitting on a plane at 5 kV, which is 2 mm below a grounded plane. A) Dielectric cylinders with a premittivity of 6. B) Charged cylinders with surface charges of -2.2 mC/mm^2. C) A cylinder with surface charge approaching a conductive cylinder on the plane. The contour lines show constant electric field, the arrows show the force on a positve charge and the axes are in millimetres.

Figure 7.4 A and C both show a field gradient that would attract the incoming filament toward the deposited one at similar distances to those observed, with the uncharged case showing greater forces. Figure 7.4 B is the theoretically expected case, where the like charge on both filaments causes repulsion. This suggests that the filaments carried much less charge, or the ink was more conductive than assumed. Alternatively, the deflection may be due to another effect such as surface tension pulling the molten filaments together. This could not be easily verified with the imaging arrangement used here, but the cross-sectional shape of the filaments seen in Section 8.2 suggests fast solidification on the substrate which would limit this mechanism.

The observed deviation of the filament could be quantified by calculating how much gap was expected at the point where the filaments first touch, if the filaments

were perfectly straight. Differences in filament width could be controlled for by measuring the gap between the edges of the filaments rather than the centrelines. The expected spacing, *s*, between the centrelines of the two filaments, crossing at angle θ, at a distance *x* from the crossing point, is given by equation 7-1. To find the distance the second filament has jumped, *j*, the width, *w*, of the filaments must be subtracted. Noting that *x* is half the measured length, L, equation 7-2 gives the expected gap.

7-1 $$s = x \tan\theta$$

7-2 $$j = \frac{1}{2} L \tan\theta - w$$

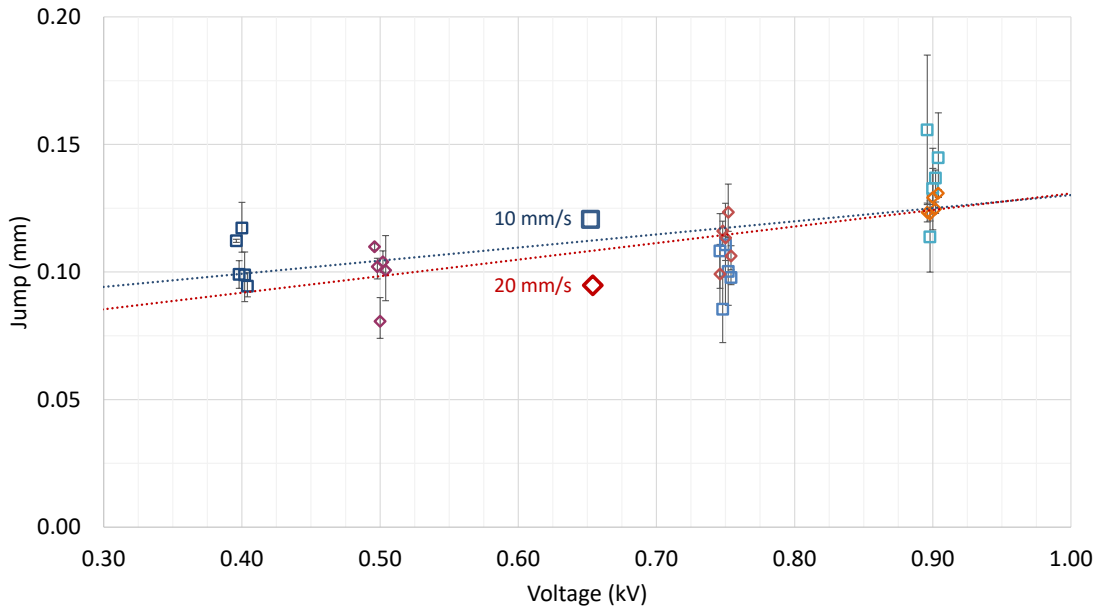

Figure 7.5 Effect of varying voltage and deposition speed on the attraction distance between filaments in the angled crossing pattern. 'Jump' was the distance between filament surfaces, not centrelines, thus accounts for varying filament width. The error bars indicate the full range of measurements. Each group of five data points represents five different angles under the same conditions, and has been spread slightly along the voltage axis for clarity. Patterns were deposited at a nozzle height of 0.5 mm and a flow rate of 0.25 µL/s.

For any pattern where the jump was greater than zero, the incoming filament had deviated from the expected impact point. Figure 7.5 plots this jump against voltage for two deposition speeds, 10 mm/s marked with squares and 20 mm/s marked with

diamonds. Note that the higher deposition speed produced thinner filaments, so that the centreline spacing was smaller than for the same jump at a lower speed and the same flow rate. It appeared that the deposition speed had negligible effect on the jump. Although the effect was small over the voltage range investigated, higher voltages produced a larger jump due to the greater charge and thus force acting on the incoming filament.

Even with three repeat measurements for each data point, the groups of data for each set of conditions in Figure 7.5 showed a significant range of jumps. Figure 7.6 replots the data against angle to prove that this was inherent variance and that there is no significant link between the angle of crossing and the deviation of the incoming filament. Figure 7.6 is also plotted based on the expected centreline spacing, rather than edge-to-edge jump, demonstrating the ability to pattern thinner filaments closer together.

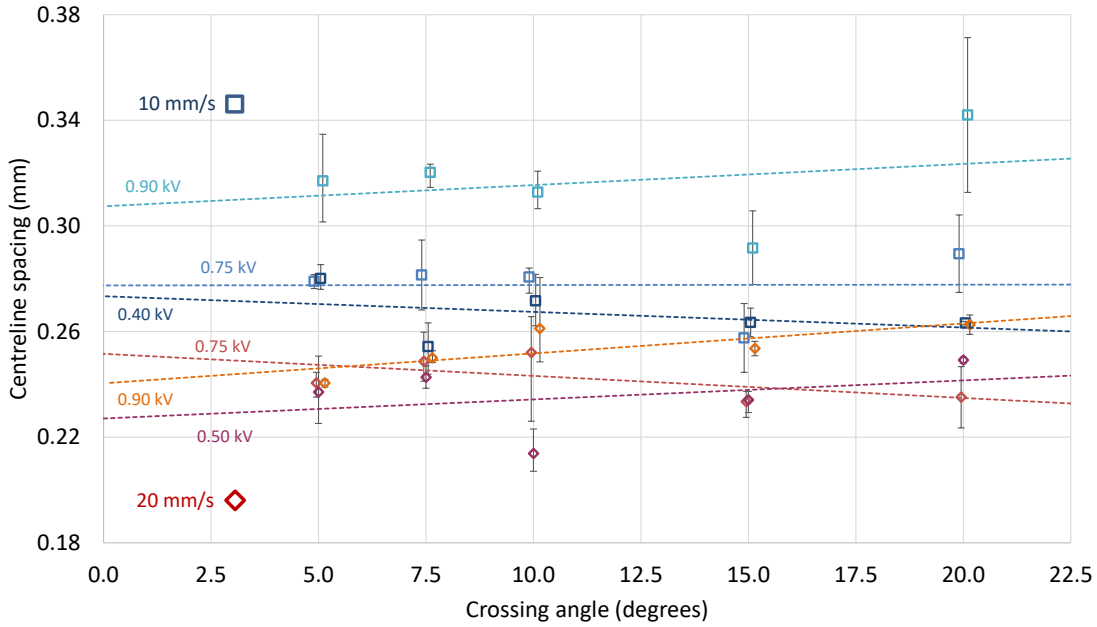

Figure 7.6 Expected centreline spacing at the first point of contact between filaments in the angled crossing pattern. The error bars indicate the full range of measurements. Points for the same angle have been spread slightly along the angle axis for clarity. Patterns were deposited at a nozzle height of 0.5 mm and a flow rate of 0.25 µL/s.

Raising the nozzle to 1.0 mm above the substrate allowed different flow rates to be used without causing major changes to the jet shape. This was also the preferred height identified in Chapter 6. Figure 7.7 plots the jump between filaments for two flow rates at two deposition speeds. It was immediately apparent that much larger jumps could be achieved compared to the lower nozzle, but that the smallest jump was similar. The larger jumps were because in this case the electro-jet was twice as long, so less stiff and more easily deviated by the same forces.

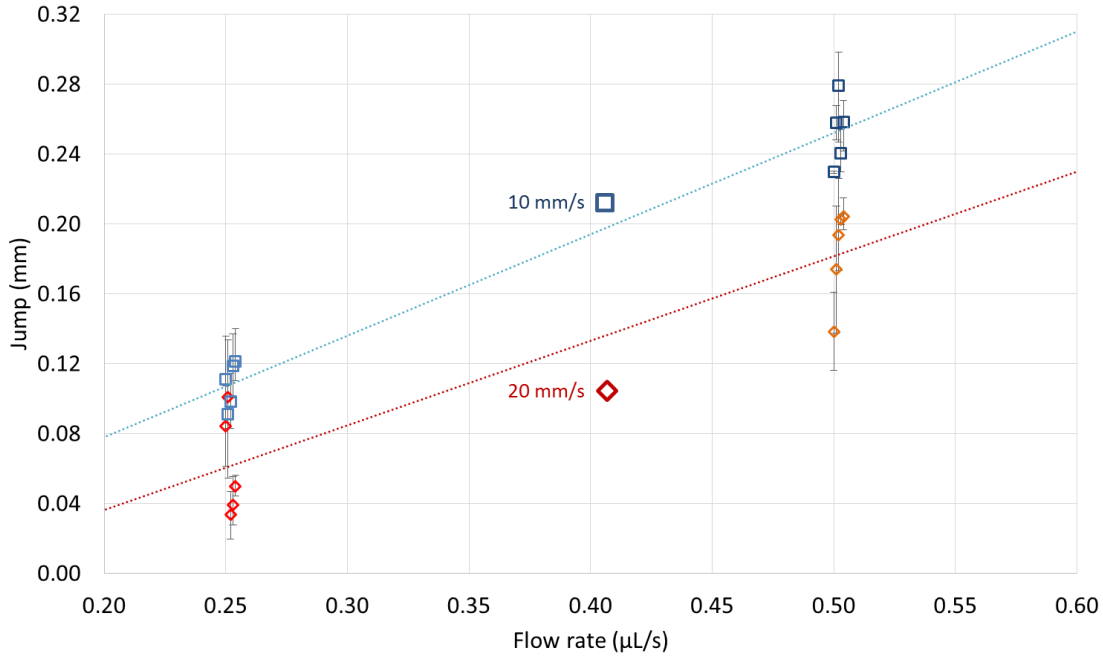

Figure 7.7 Effect of flow rate and deposition speed on jump between filaments for a 1.0 mm nozzle height. The error bars indicate the full range of measurements. Points for the same angle have been spread slightly along the flow rate axis for clarity. Patterns were deposited at 2.0 kV. Deposit diameters varied from 0.10 mm for the high flow rate, low speed samples to 0.22 mm for the low flow rate high speed samples.

At this nozzle height, there was clearly a larger jump with a lower deposition speed, as well as the jump increasing roughly proportionally with flow rate. As Figure 7.7 plots the jump, not the centreline spacing, this could not be explained by the surfaces of larger diameter filaments simply being closer together. It could be explained by the larger filaments produced by lower speeds and higher flows having a larger effect on the electric field, as predicted in Figure 7.4. Doubling the flow rate or halving the

speed both increased the diameter of the deposit by a factor of $\sqrt{2}$. Quantifying how this carried through to the electric field is difficult, but considering the two cases in Figure 7.4 the warping of the electric field due to the dielectric effect of the deposit roughly scaled with deposit diameter. Therefore, the dielectric effect of the larger deposit can fully explain the effect of deposition speed on the jump, but cannot fully explain the effect of flow rate. The discrepancy might be accounted for by considering that a higher flow rate would result in a thicker jet, which would take longer to cool and thus be more flexible as it approached the existing deposit. This would allow it to jump a larger distance. As established in Section 6.6, the substrate speed did not affect the jet width as strongly as the flow rate and so would not increase the jump in this way.

In conclusion, the incoming electro-jet was attracted to existing deposits over short distances. The attraction of the incoming filament could be attributed to the dielectric effect of the existing deposit, which distorted the electric field in proportion to the size of the deposit. The minimum distance that must be left between surfaces of the deposit for the incoming filament not to jump to the existing deposit varied based on the electrospinning parameters. The jump distance was increased by greater nozzle height, higher flow rate, slower deposition speed and higher applied voltage, in decreasing order of significance. Observed jump distances were in the range of 0.05 and 0.25 mm, equating to centreline spacings of 0.15 to 0.50 mm.

7.3 Layer stacking

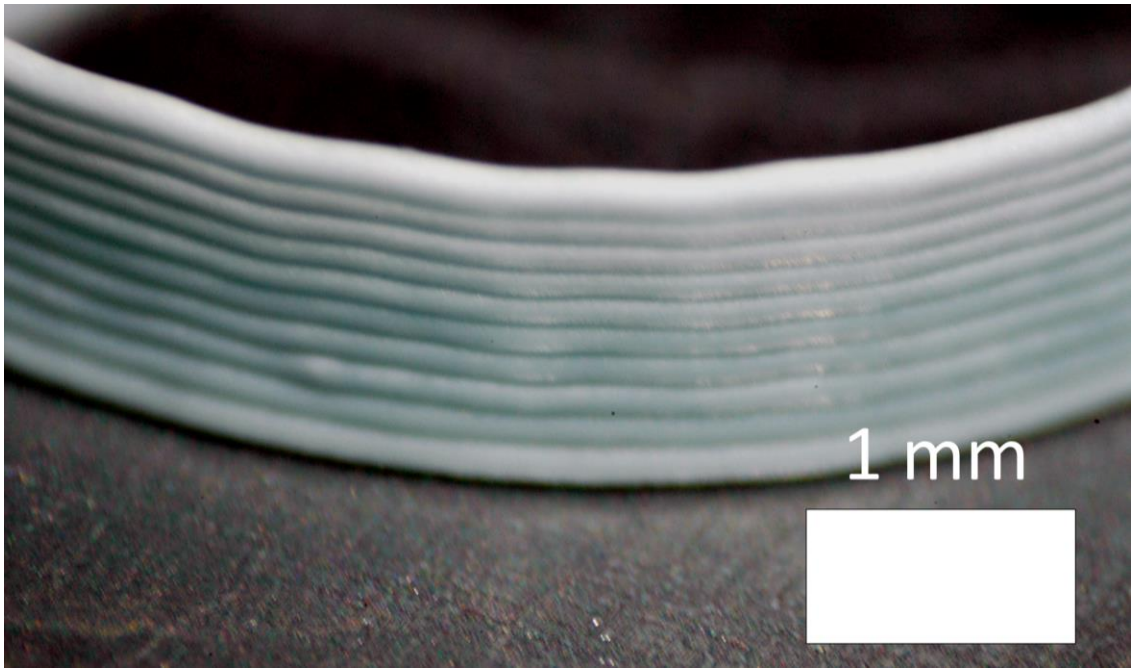

Figure 7.8 Magnified views of the walls of a single-walled cylinder with a diameter of 8 mm. There are a total of 10 layers, deposited from a 200 µm needle at a height of 1.5 mm, flow rate of 0.50 µL/s, speed of 20 mm/s and voltage of 3.8 kV.

In order to build high aspect ratio parts, such as thin vertical walls, good alignment of subsequent layers was critical. The previous section established that electrostatic effects caused the incoming jet to be attracted to deposited ink over short distances, probably due to the dielectric effect of the deposit. Considering Figure 7.4, the shape of the electric field around the deposit drove the incoming filament to a metastable equilibrium on top of the deposit. At a given height near the top of the deposit, directly above the centre of the deposit the horizontal component of the electric field was zero. Moving away from this point in either direction, the horizontal component increased and pushed the incoming filament back to directly above the deposit. This restoring force only acted over a small range, because further from directly above the deposit, by roughly the radius of the deposit, the horizontal component of the field began to reduce.

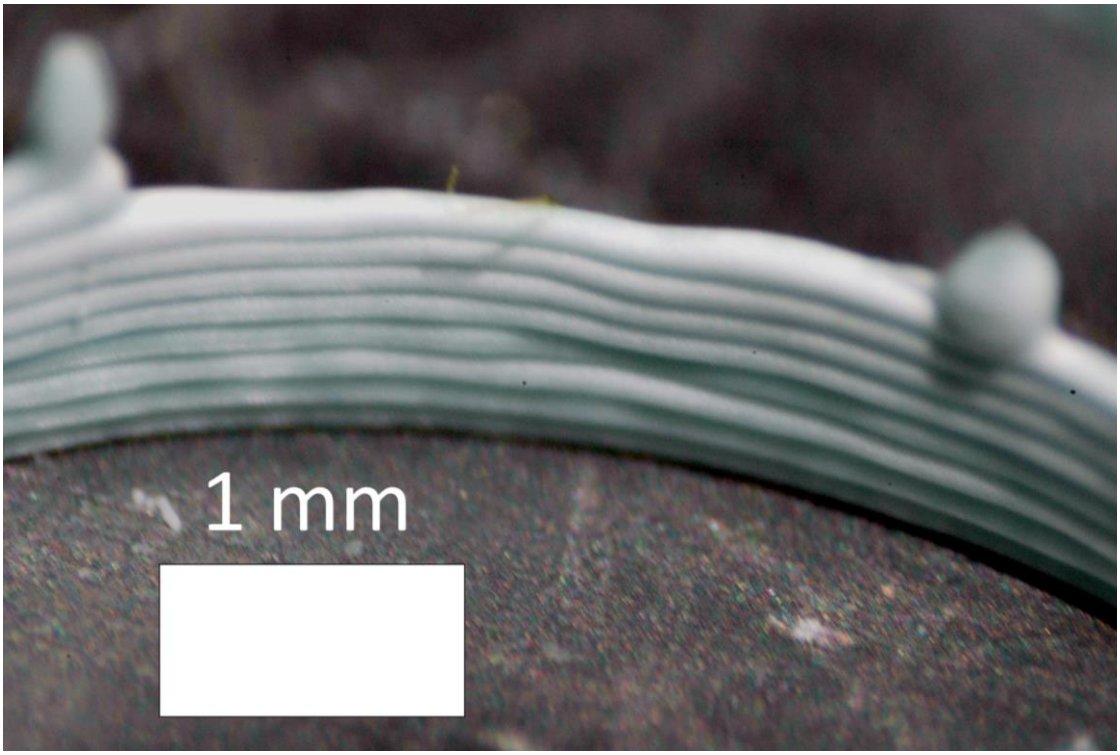

Figure 7.9 A cylinder similar to that in Figure 7.8 with a defect in the wall (centre) and ink blobs from breaking of the electro-jet (top edge).

The effect of the attraction between the deposit and incoming filament was that single filament stacks could be very stable. Figure 7.8 shows a hollow cylinder comprising 10 layers and showing very good consistency. The centre of Figure 7.9 shows a defect where the incoming filament had deviated slightly from the previous layer, but subsequent layers had been successfully deposited due to their attraction to existing features. However, tall structures required that other factors did not cause disturbances. The most common failure was caused by breaking of the electro-jet, due to the changing electric field as the deposit built up toward the nozzle, or because of transient changes in the flow rate from inhomogeneity in the ink. Whatever the cause of the break, either the jet would revert to dripping or it would restart, but the new filament would have a blob of ink at the beginning and leave a gap between it and the previous filament, as seen on the top edge of the wall in Figure 7.9. As well as being a defect, this blob would cause the jet to fail the next time it passed over it, exaggerating the problem.

Figure 7.10 shows how sudden changes in direction could also cause a similar defect, due to the extra material deposited during the slowing down and speeding up of the motion system. To avoid such problems tall structures required stable conditions or smooth changes, in practice meaning no sharp corners in the deposition path, a well-mixed ink and a properly sized nozzle. Shorter structures, containing three to four layers, were patterned with greater success because of the smaller changes to the electrospinning conditions and fewer chances for errors to compound.

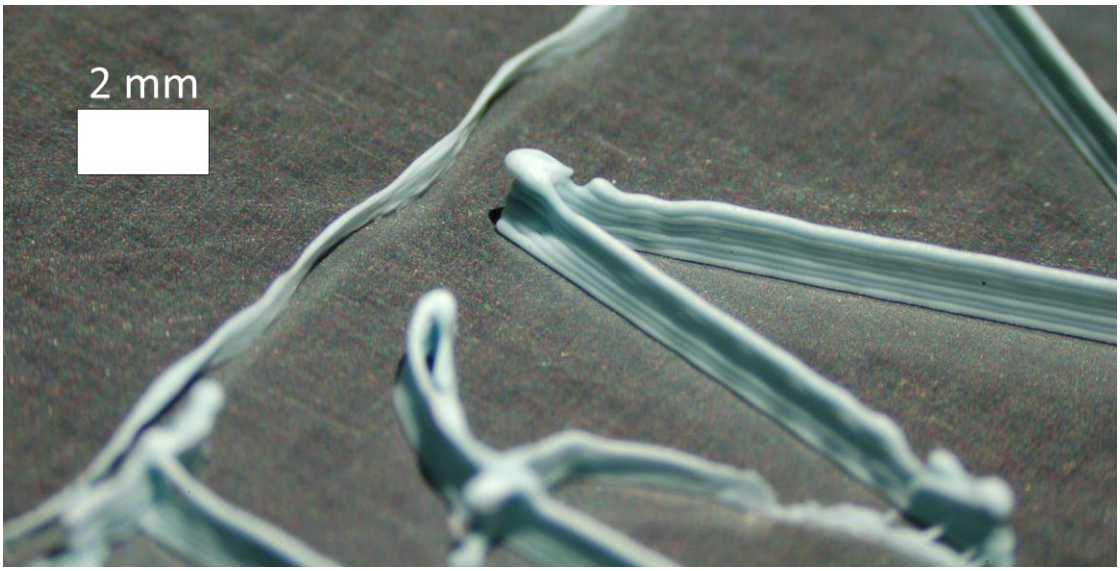

Figure 7.10 Close up of a corner of the letters "IfM", showing the defects at the top left corner of the 'M' but well formed walls before and after. The letters contained 7 layers, deposited from a 200 μm needle at a height of 1.0 mm, flow rate of 0.50 μL/s, speed of 20 mm/s and voltage of 2.0 kV.

7.4 Gap bridging

To build objects with holes through vertical walls, the incoming filament needed to be able support itself over a gap. This was an important characteristic for producing 3D lattices with fully connected space within the lattice. It was also potentially difficult because in this process the ink was still liquid as it reached the substrate, meaning it must rely on high viscosity and suspension from the nozzle to keep the filament relatively straight until it had solidified.

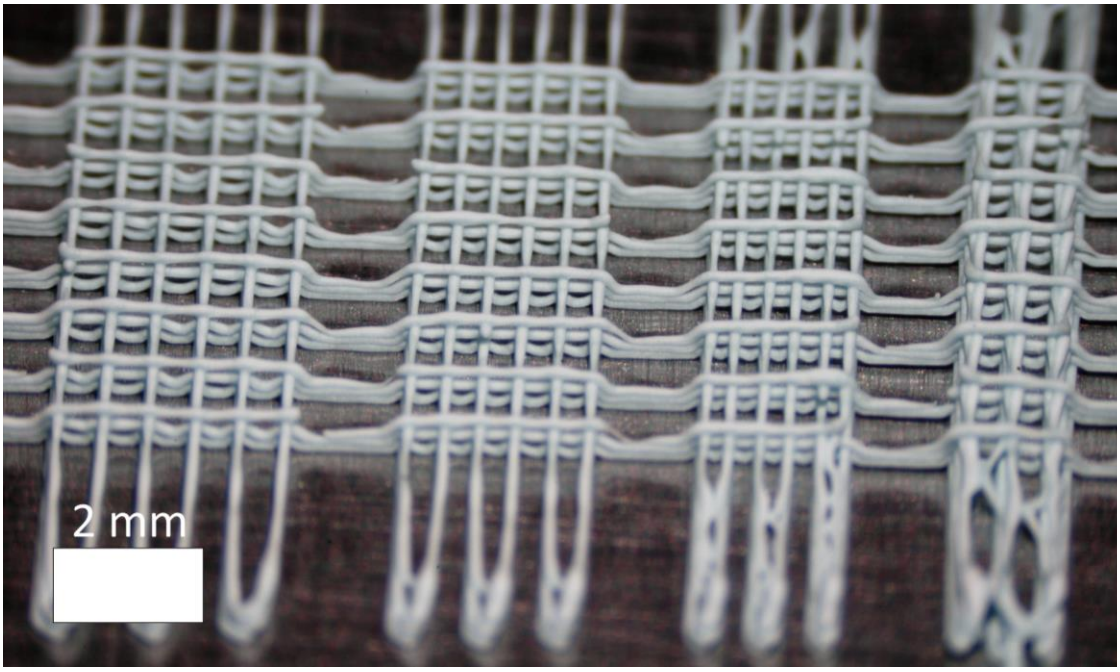

Figure 7.11 The lattice described in Figure 7.1, built up in 3 repeats. Deposited from a 200 µm needle at a height of 1.0 mm, flow rate of 0.50 µL/s, speed of 20 mm/s and voltage of 3.0 kV.

A typical lattice, as described in Figure 7.1, is shown in Figure 7.11. It was immediately clear that the proccess could successfully bridge gaps, but for good results this must be done reliably. The magnified views in Figure 7.12 show that many of the bridges sagged and that there was some variance in size. For some applications, some droop in bridging filaments would be acceptable, so to quantify the bridging ability each crossing was labelled as failed, deformed or successful. A failed crossing was in contact with the surface below it for the majority of its length, was broken or missing altogether. A deformed crossing sagged more than the radius of the filament or was of abnormal size compared to other filaments in the lattice. The remaining crossings would be close to straight and otherwise well formed, thus were considered successful. The section of 0.3 mm filament spacing was not be considered as the attraction discussed in section 7.2 caused the intended six lines to collapse to three with variable spacing.

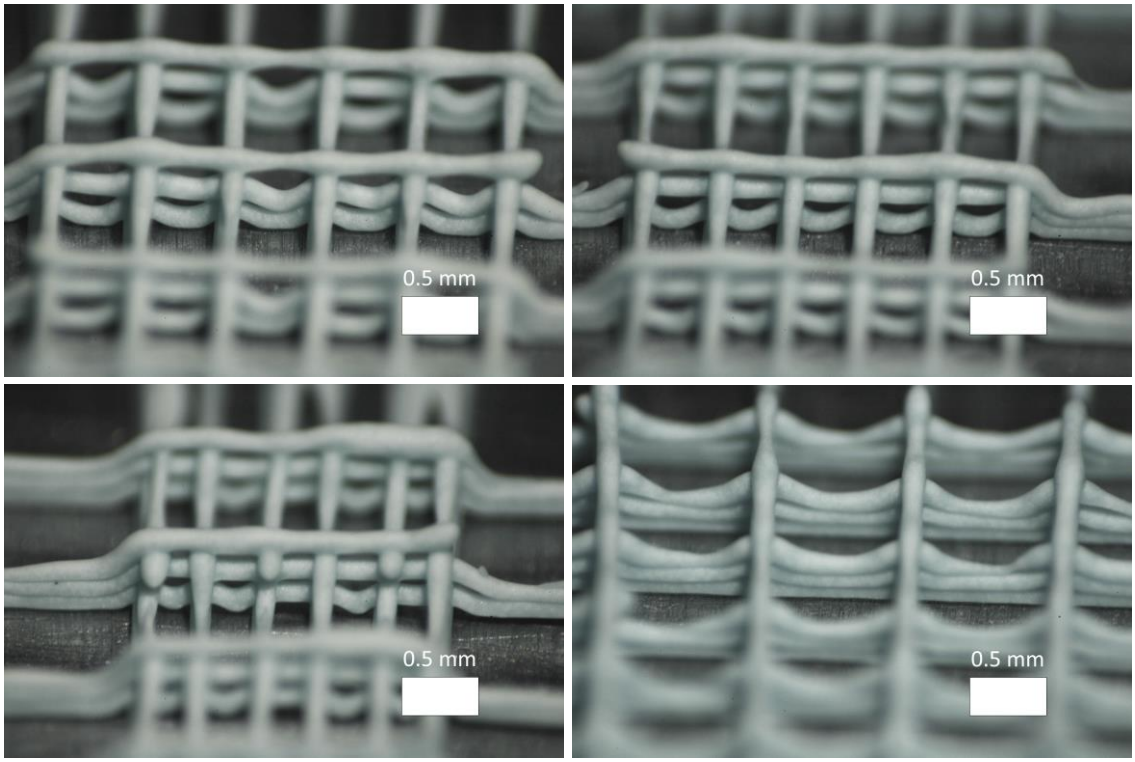

Figure 7.12 Detail of bridging filaments from the 0.6, 0.5 and 0.4 mm spacings of Figure 7.11. Bottom right is the 1.0 mm spacing between the horizontal filaments of the other images, as an example of completely failed bridging.

The categorisation of the lattice in Figure 7.11 is summarised in Figure 7.13. The overall trend was that narrower spacing gave more successful bridging, which was to be expected as the filament was hanging unsupported for less time and a small quantity of ink was suspended, reducing the tension in the jet. However, none of the investigated spacings achieved better than 71% successful bridges, which was effectively the upper limit because closer spacing led to deviation of the electro-jet. At 0.6 mm spacing, the rate of successful bridging dropped below 50 %, so this was considered not to be bridgeable. Furthermore, there were interesting trends this overview misses, so Figure 7.14 separates the data into the different layers of each section.

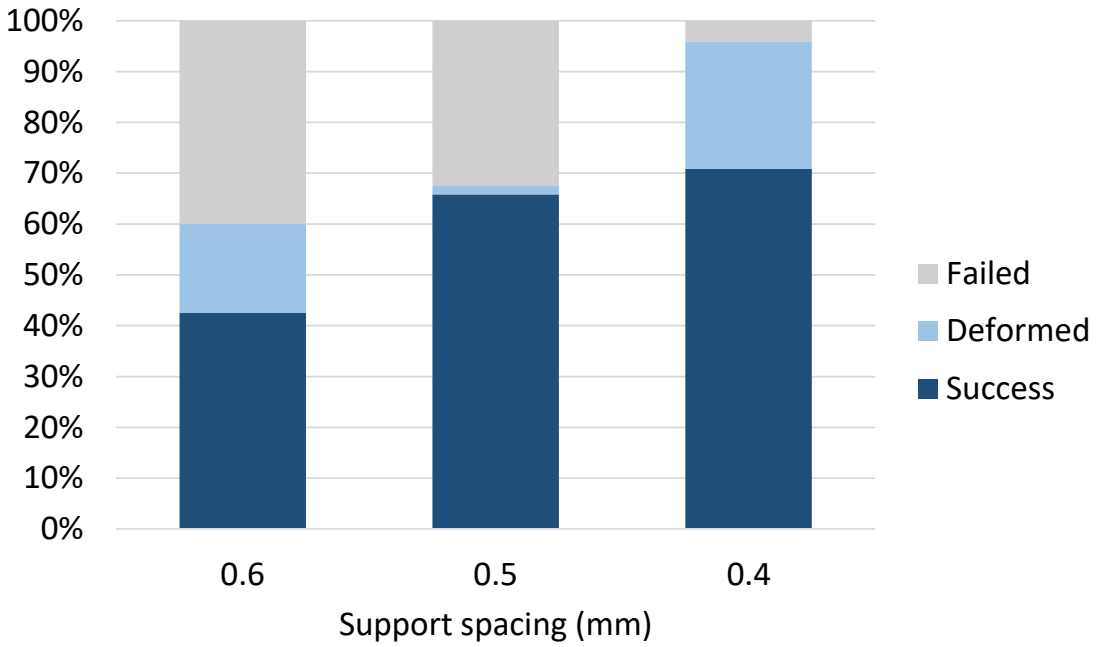

Figure 7.13 Proportion of bridges that were considered successful for each section of Figure 7.1. 'Deformed' bridges were visibly drooping, undersized or oversized and 'failed' bridges were mostly in contact with the surface below or are missing.

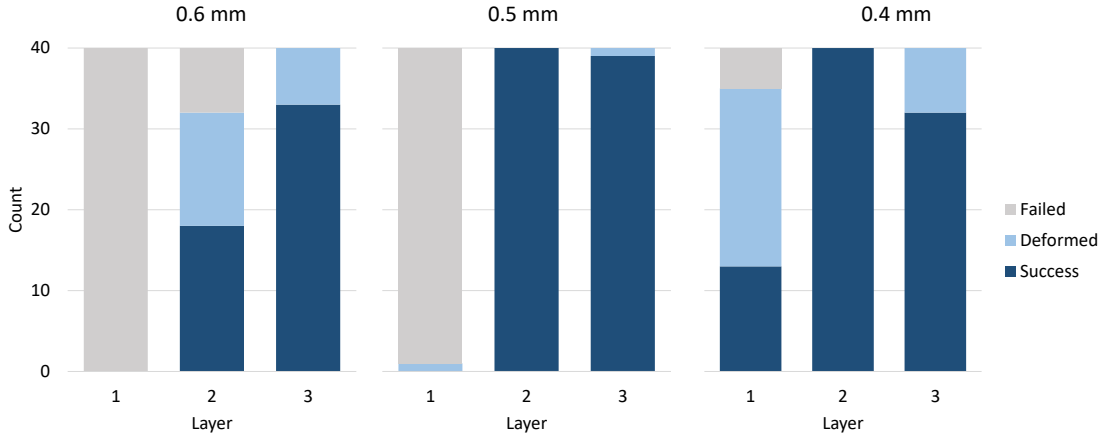

Figure 7.14 Layer-by-layer breakdown of Figure 7.13.

The first pattern to note was the poor bridging seen on the first layer, where only the 0.4 mm spacing achieved any successful bridges. The second interesting pattern is the increased proportion of deformed bridges on the third layer compared to the second layer. The deformation on the third layer was usually under or oversized filaments, whereas deformed bridges in other layers would have more pronounced sag,

but were more consistently sized. Both of these trends might be due to the deposit changing the electrospinning conditions, specifically the increasing height of the deposit reducing the length of the jet. With filament diameters above 100 μm and each repetition of the pattern adding two layers, the height of the top surface of the lattice was around 60 % of the nozzle height. For the first layer, the jet was longest and so stretched and bent more easily. This would allow the filament to sag more during bridging, leading to the first-layer bridges consistently touching the substrate. By the third layer, the jet was much shorter, so could support the suspended filament more easily but tended to form blobs of ink at the raised points. This could cause one bridge to be thicker than average and others to be thinner than average. These blobs were more common at the beginning or end of crossing each section, when the jet had just crossed the larger gap between sections.

If they were caused by variations in the effective nozzle height, these issues could be improved by changing the nozzle height during deposition. Raising the nozzle by the expected thickness of each layer would maintain a roughly constant effective nozzle height, thus keeping bridging behaviour constant. Apart from very small changes, this would also probably necessitate changing the applied voltage to maintain the same average electric field. It was established in Section 6.6 that the exact electrospinning conditions are not critical to the output of this process with this ink, but not adjusting the applied voltage over large changes in nozzle height risks destabilising the electro-jet. With the equipment available, there was no easy method to vary the high voltage supply using the controller of the three-axis stage, so this approach was left for future work.

In conclusion, the electro-jet studied in this work was capable of bridging small gaps, up to three to four filament diameters in size. However, even at the smallest gaps that could be patterned with the process, only 71 % of bridges were fully successful. For the conditions used, the second layer was most successful, with different problems arising for the first and subsequent layers. Both problems might be

addressed by adjusting the nozzle height and applied voltage during deposition to reduce the variation in electrospinning conditions.

7.5 Corner patterning

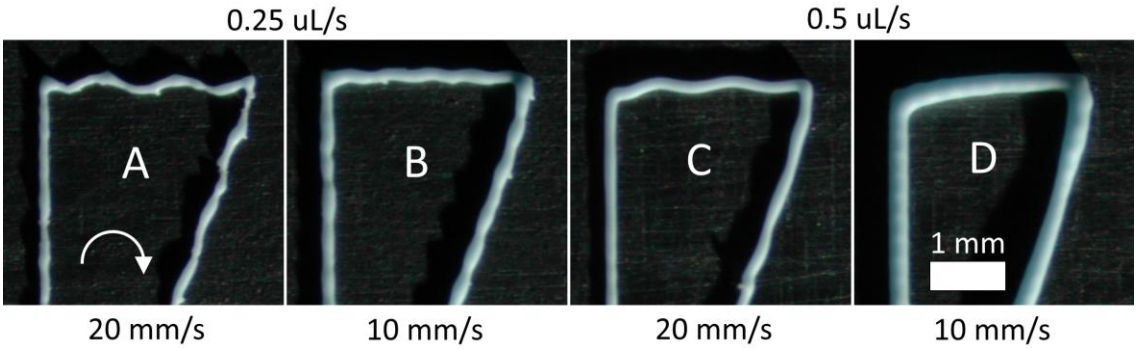

Figure 7.15 Corners of the angled crossing pattern described in Figure 7.2, deposited from a 200 µm nozzle at a height of 1.0 mm and voltage of 2.0 kV. The nozzle moved clockwise around the pattern. A and B used a flow rate of 0.25 µL/s, C and D used a flow rate of 0.50 µL/s. A and C were deposited at 20 mm/s while B and D were deposited at 10 mm/s. The horizontal lines were parallel to the X-axis of the three-axis stage.

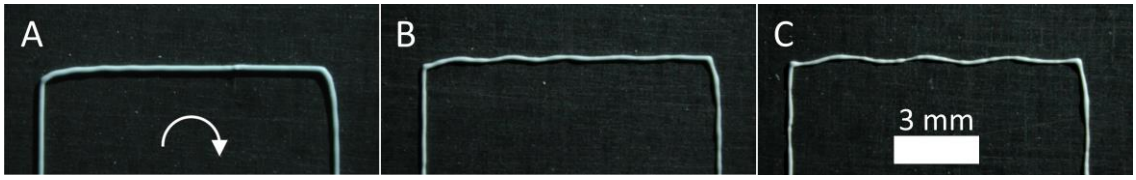

Figure 7.16 Sections of a square-wave pattern with line lengths of 10 mm. A, B and C were deposited at 10, 20 and 30 mm/s respectively, from left to right, with the horizontal lines parallel to the X axis of the three-axis stage. A 200 µm nozzle was used with a flow rate of 0.50 µL/s and voltage of 2.0 kV.

If the speed of the fluid in the jet were lower than the speed of the substrate relative to the nozzle, the jet would be dragged along with the substrate and form a long hanging section. This caused the point where the jet reaches the substrate to be some distance from the point directly beneath the nozzle. This in turn caused sharp turns in the nozzle motion to be rounded off, in the same way that the trailer of an articulated lorry follows the tractor unit around bends. Even when the jet speed was similar to that of the substrate, the fact that the jet had little stiffness could cause artefacts in tight turns or sharp corners.

In the case where the jet speed was faster than that of the substrate, generally the jet buckles and the 'slack' this produces will also cause defects, although possibly less predictably. In this work, because the ink was still fluid as it reached the substrate, a jet speed higher than the substrate did not lead to buckling or other deformation and the behaviour was similar to when the jet speed was close to the substrate speed.

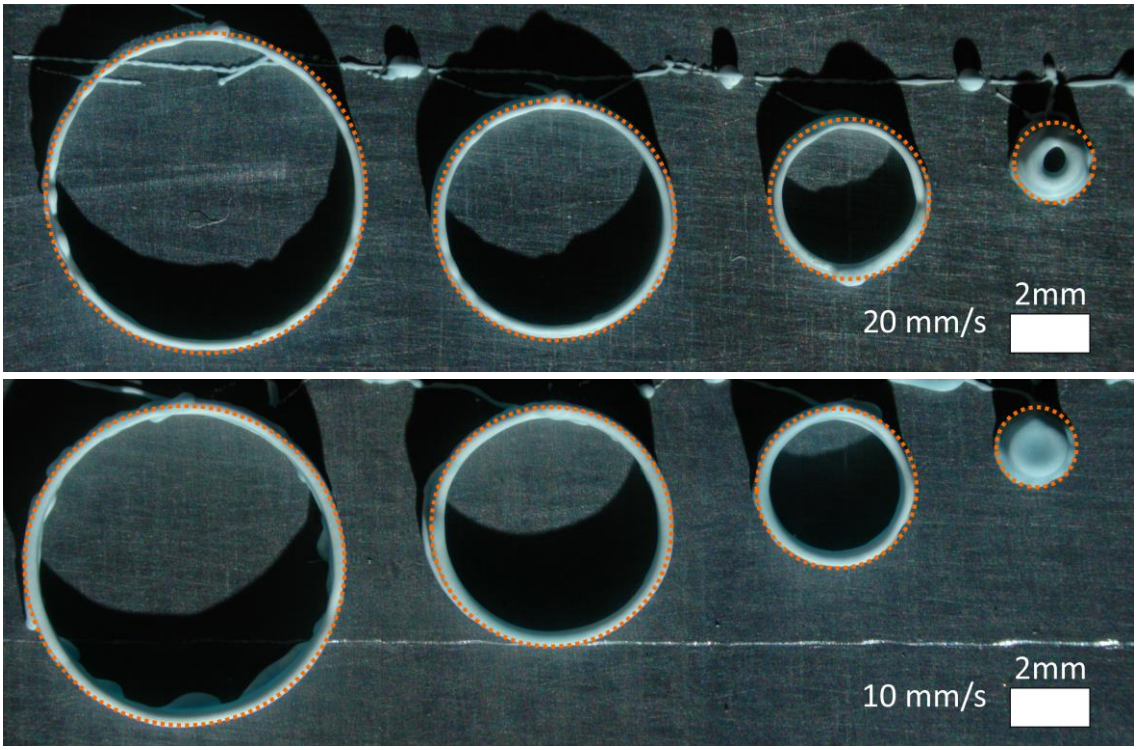

Figure 7.17 Circles of decreasing diameter deposited at 20 mm/s (top) and 10 mm/s (bottom). Each circle was built of ten layers, with the nozzle raised by 0.1 mm per layer. Deposited with a 200 µm nozzle starting at 1.0 mm height, with a flow rate of 0.50 µL/s and an applied voltage of 1.9 kV. The dotted orange lines indicate the expected centreline of each circle wall.

Examples of corner defects can be extracted from patterns previously discussed in this chapter, such as Figure 7.15, which shows corners from the angled crossing pattern at flow rates of 0.25 and 0.50 µL/s and deposition speeds of 10 and 20 mm/s. While there was clear rounding on the corners of image D, there was a significant oscillation artefact obscuring any corner defects in the other images. Figure 7.16 shows a 10 mm square wave pattern deposited at 10, 20 and 30 mm/s to investigate the

two effects. This made it clear that the oscillation was limited to one axis and dependent on deposition speed. The corners of the wave also gave clearer images of the corner rounding, showing a sharp change in direction followed by a gentler curve to the new direction. To avoid the sudden direction changes that caused the oscillation, a series of hollow cylinders were deposited, as shown in Figure 7.17. By comparing these to the expected diameter, it was possible to identify the minimum practical radius for patterns.

The oscillation was a result of how the syringe pump was mounted on the three-axis stage. The pump motor was well above the carriage and the mount itself was relatively flexible in the direction of the Y-axis. This combination caused sizeable and poorly damped vibration of the pump and nozzle in this direction whenever there were sudden changes in Y-axis velocity. Figure 7.16 is very informative about the behaviour of the oscillation, showing that at a deposition speed of 10 mm/s the oscillation was negligible and at 20 mm/s it took about 10 mm (0.5 seconds) to dissipate. When the deposition speed was increased to 30 mm/s, the oscillation deformed most of the X-axis aligned filaments, as the nozzle travelled further in the same time and the accelerations were larger, increasing the initial magnitude of the oscillation. Qualitative observations of this effect were one reason for limiting most deposition speeds to 20 mm/s and designing the patterns to have relatively long, straight sections leading into the areas of interest.

In Figure 7.15, the lower flow rate runs (A and B) appeared to show less rounding of the corners than the higher flow rate runs. This might have been due to a higher velocity of the ink in the jet, leading to a smaller suspended length. From the empirical equation obtained for the oil-based ink in Section 6.2, the relation between jet width and flow rate has the form of equation 7-3. When combined with the equation for average velocity of the fluid through a circular cross-section, given in 7-4, this results in equation 7-5.

7-3 $$w \propto \dot{Q}^{0.66}$$

7-4 $$v \propto \frac{\dot{Q}}{w^2}$$

7-5 $$v \propto \dot{Q}^{-0.32}$$

This implies that decreasing the flow rate would increase the velocity of the ink in the jet, supporting the hypothesis that this reduced the corner rounding. However, it was also clear from Figure 7.15 that at this flow rate the electro-jet was barely stable as the deposited filament was rough and irregular. Therefore, while this approach may be useful as a general method of improving accuracy, it was not useful in this work.

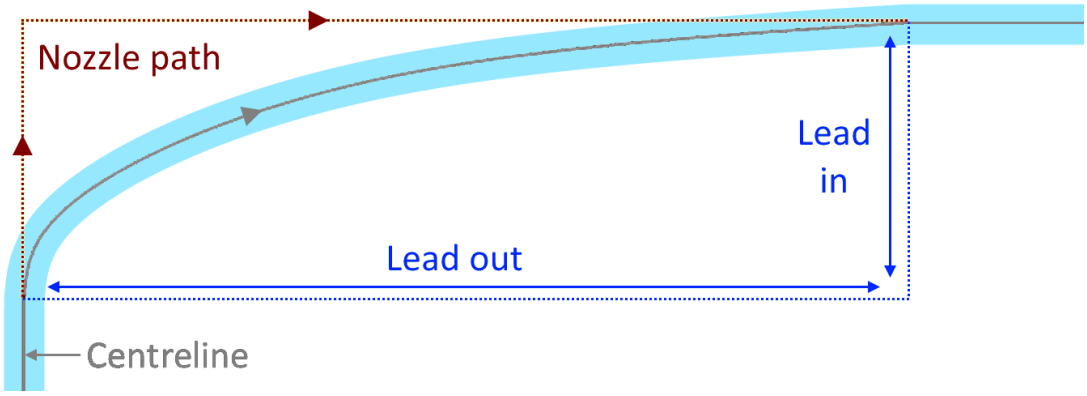

Figure 7.18 Measurement of corner rounding on the square-wave pattern. The filament would have been deposited from the lower left moving to the top right.

Close examination of the corners in Figure 7.16 revealed that the deformation caused by the suspended jet did not uniformly turn the corner under the conditions tested, instead introducing a sharp bend on the inward filament followed by a shallower curve returning to the intended path. To simply quantify this, the length of the affected region was measured along each nozzle path as outlined in Figure 7.18, with the affected length of the entry path being labelled the 'lead in' and the affected length of the exit path labelled the 'lead out'. The averaged results are presented in Table 7.1, but nozzle oscillations obscured measurements of the lead out of the first corner at 20 and 30 mm/s, so fewer samples were used for those results.

Deposition speed (mm/s)	Lead in (mm)	Lead out (mm)
10	0.57	2.04
20	0.39	1.59
30	0.35	1.50

Table 7.1 Average deformed length before (lead in) and after (lead out) a 90 degree turn at different deposition speeds, measured from experiments like that shown in Figure 7.16.

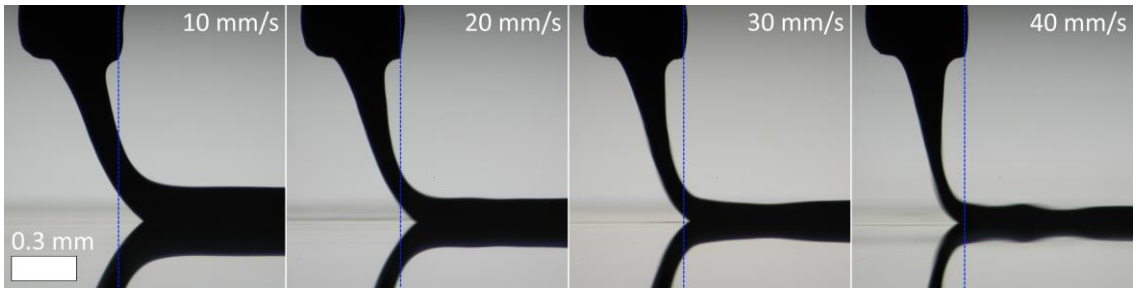

Figure 7.19 Shilouettes of electro-jets at increasing substrate speeds. The blue line is included for reference and is aligned with the trailing corner of the needle. The nozzle was 200 µm internal diameter at a height of 0.75 mm, with a flow rate of 0.25 µL/s and a voltage of 1.75 kV.

The size of the affected area decreased with nozzle speed, contrary to what would be expected, as a faster nozzle speed should have suspended a greater length of filament. However, referring to Figure 6.17, higher nozzle speeds were shown to produce thinner jets under otherwise identical conditions. A narrower jet must have a higher ink velocity at the same flow rate; this reduced the suspended length of the jet, with this data indicating that this effect was stronger than that of increasing deposition speed lengthening the suspended region. It would follow from this that increasing the substrate speed caused the impact point of the jet to move closer to directly below the nozzle. While this was counter-intuitive, it could be observed by re-examining images used to gather data for Section 6.6, such as the series shown in Figure 7.19.

The results in Table 7.1 give a large range of the filament length deformed by corner rounding, with the upper limit around four times larger than the lower limit for a given set of conditions. A more informative measure of the effect of corner rounding can be taken from Figure 7.17. The minimum achievable corner radius should be similar to the horizontal distance between the nozzle axis and the impact point of the jet. When patterning circles of decreasing size, at some point this lag distance will be equal to or greater than the radius of the circle and the impact point of the jet will tend to become stuck at the centre of the circle. From Figure 7.17, we see that at 10 mm/s, the 1.0 mm diameter circle became solid, suggesting a minimum corner radius of greater than 0.5 mm. At 20 mm/s, the same circle remained hollow, although noticeably undersized, so the minimum corner radius was slightly smaller than 0.5 mm. The lag distance had caused all the patterned circles to be undersized by several tenths of a millimetre, with the degree of under-sizing increasing with the curvature of the nozzle path. As these minimum radius estimates agreed with the lead in distances of the square-wave pattern, they could be taken as the minimum achievable corner radius. The lead out distance should be considered when designing patterns and either avoided by keeping sharp turns that far away from important features or mitigated by using curved paths instead.

7.6 Optimal patterning conditions

For the most accurate patterning, higher nozzle speeds are better. This produces a smaller lag distance, giving better corners, and causes a smaller deviation at angled filament crossings. It also produces thinner filaments when all other conditions are equal but maximum speed limited by the motion system used.

Another way to reduce the lag distance, and therefore crossing deviation, is to lower the nozzle. This also allows a reduced voltage to be applied between nozzle and substrate, which further reduces the deviation. However, without adjusting these conditions during a pattern, a low nozzle height limits the height of pattern that can be

produced. Therefore, the nozzle height should be around 50 % larger than the intended object height.

For patterns involving bridging, the spacing of the supporting filaments should be no more than 0.5 mm. It may also be beneficial to increase the nozzle height, so that conditions are more similar for subsequent layers.

7.7 Conclusions

Using electrospinning as a direct-write process was constrained by the effect of the necessary strong electric fields and raised nozzle. Probably the greatest limit demonstrated in this work was the attraction between the incoming jet and previously deposited ink. The observed behaviour matched well with the predicted effect of the dielectric properties of the ink, which deformed the electric field to direct the charged jet toward the deposit. This meant that there was a minimum spacing, which must be left between filaments of ink to ensure accurate deposition, otherwise the second filament would be attracted to the first and deposited alongside it. The spacing required was increased by a larger deposit diameter, greater nozzle height and higher voltage. Under the conditions investigated, the minimum spacing between centrelines varied between 0.15 mm and 0.50 mm.

The same effect that enforced a minimum spacing between adjacent filaments caused vertical walls to be very stable. Modelling showed that the electric field around the deposited filament caused a new filament being deposited on top of it to be guided to being vertically centred, maintaining good alignment despite small perturbations. The limiting factor for high aspect ratio vertical walls became the change in electrospinning conditions as the deposit was built up, with the jet eventually becoming unstable. Progressively raising the nozzle and adjusting the voltage during deposition could overcome this and allow for very high aspect ratio parts.

The fluidity and flexibility of the electro-jet prevented the patterning of unsupported filaments that bridged large gaps. In the best-case scenario, 71% of gaps

were successfully bridged, but the proportion dropped significantly under different conditions. This was achieved by crossing filaments whose centrelines were up to four filament diameters apart. There appeared to be an ideal length of electro-jet for bridging that was short enough not to sag excessively but also long enough not to be disrupted by interrupted contact with a substrate. As with tall objects, adjusting the nozzle height and applied voltage during deposition should improve the success rates.

Another problem caused by the geometry of the electro-jet was the introduction of a lag distance between the impact point of the jet and the nozzle axis. This led to a minimum achievable radius of around 0.4 mm in corners and cylinders, as well as deviations of the deposit from the nozzle path up to 2 mm after sharp corners. The problem could be reduced by increasing the fluid velocity of the jet, which could be counter-intuitively achieved by increasing the substrate speed. In this work, flexibility in the mounting of the syringe pump to the three-axis stage caused oscillations at the nozzle after high acceleration in the Y-axis, requiring the deposition speed to be limited to 20 mm/s. A stiffer mounting would allow for higher speeds.

8 POST-PROCESSING

To produce the final ceramic part after the electrospinning process, the wax binder must be removed and the powder particles sintered together. This chapter covers the sintering process used in this work and examines images of the samples before and after sintering. The sintered samples are also mechanically tested, as verification that the sintering process was successful.

8.1 Techniques

The literature referenced in Section 2.3.2 suggests that for the 0.3 µm alumina powder, good consolidation should be achieved above 1,500 ºC, even without the addition of sintering aids. However, the temperature required for a given degree of consolidation increases with particle size due to the reduced surface energy, and the viable inks were formulated with 4 µm powder. This meant it was expected that they would require temperatures nearer the melting point of alumina (over 2,000 ºC) or much greater times at the same temperature compared to the finer powder. Furnaces capable of reaching such high temperatures are uncommon and this became a limiting factor here. The highest temperature available for this work was 1,400 ºC, in a STF 15/75/450 tube furnace from Carbolite, Sheffield. This unit was technically capable of 1,500 ºC but it was not used at full power to protect the equipment. The tube furnace had to be run sealed, so full combustion of organic material could not be guaranteed, requiring a separate pre-treatment in a furnace with airflow. For this, a BSF12/10A from Elite Thermal Systems, Leicestershire, was used. Both of these furnaces were situated in the Process Lab of the Department of Materials Science and Metallurgy. As the available temperature was considerably lower than that expected to be required for full densification of the alumina, the aim of this sintering treatment was only to bond the particles into a single, porous piece.

To protect the samples, they were placed in alumina crucibles from Almath Crucibles Ltd., Suffolk. The crucibles were rectangular with external dimensions of 27x27x16 mm (width x length x height) and had flat lids with a central 1 mm hole. The perforated lid allowed for pressure equalisation while protecting the sample from strong gas flows. To support the samples and prevent them bonding to the crucible, a layer of coarse alumina powder was added to the bottom of the crucible. This was bought from Sigma-Aldrich and had a mean particle diameter of approximately 60 μm, as measured by optical microscopy. Due to the small mass and small thicknesses of the samples, no limit was imposed on the rate of change of temperature, allowing the furnaces to heat and cool as rapidly as they could without damage.

X-ray computed tomography (XCT) was used to capture high-resolution images of a green-body lattice, patterned as described in Figure 7.1. The imaging was carried out on a ZEISS Xradia Context microCT, with the lattice held on an expanded polystyrene block by double-sided adhesive plastic tape. The X-ray tube was run at a voltage of 80 kV and power of 7.0 W for two scans, the first an overview scan with a resolution of 5.2 μm and a second detail scan with a resolution of 1.0 μm. The same filters and lenses were used for both scans, with the magnification being adjusted by the relative positions of the source, sample and detector. Due to the nature of XCT all images have been computationally reconstructed by the accompanying software from the x-ray silhouettes captured by the scanner, leading to some image artefacts.

Scanning electron microscopy (SEM) was used to capture high-resolution images of both green and sintered lattices samples. Sections of each lattice were attached to a steel disk with a double-sided carbon-based adhesive tape, placed near one edge of the disk. The disk was mounted on a flat stub with the same carbon-based tape and then the samples were sputter coated with gold-palladium alloy from above, to an expected thickness of around 5 nm. The metallised samples were removed from the flat stubs and reattached to 45^{o} stubs, with the lattice samples toward the highest side, so that the fracture surfaces as well as the curved filament surface would be visible in the microscope. A silver paint was used to add a conductive path from the top of the

metallised disk to the new stub. The samples were imaged in a Zeiss GeminiSEM with the electron gun at 5.0 kV.

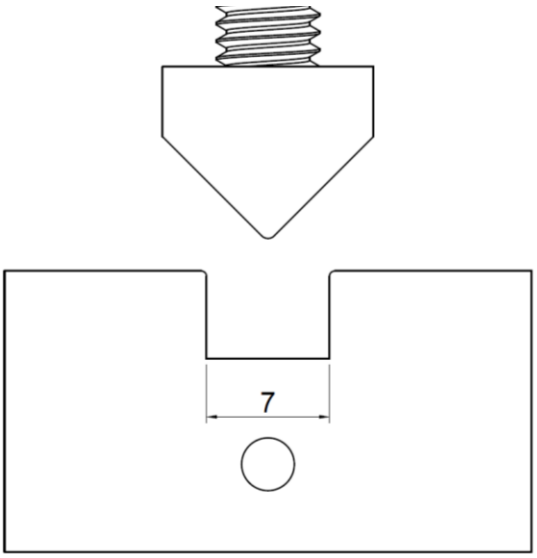

Figure 8.1 Geometry of loading fixture for the three-point bend testing. Corner radii are representative and were not precisely reproduced. Dimensions are in millimetres, with only the marked width of the channel being critical.

To measure the mechanical properties of the sintered samples, they were put through a three-point bend test. This was done on a Zwick Roell benchtop universal testing machine with a 10 N load cell. To accommodate the small size of the samples, a custom fixture was machined from aluminium with the geometry shown in Figure 8.1. Both the upper 'knife' and lower 'anvil' were wide enough to cover the samples fully and had the edges that would contact the sample lightly rounded, to avoid stress concentration7s. The tools were mounted to the machine taking care to align the knife and anvil so that their edges were parallel, and the edge of the knife was centred in the channel. Sections of the lattice described in Figure 7.1 were placed over the channel of the anvil, and then the knife was lowered at 1 mm/minute until the sample broke. The use of corners in the tooling geometry, rather than cylinders, was not ideal but was easier to fabricate.

8.2 Green body imaging

8.2.1 X-ray computed tomography

The XCT scans provided clear images of the lattice, at the scale of an entire lattice section and of a single filament. By reconstructing a 3D image from the many cross-sectional images, depth of field did not limit the clarity of the image, and the individual cross-sections provided information about the interior structure of the filaments.

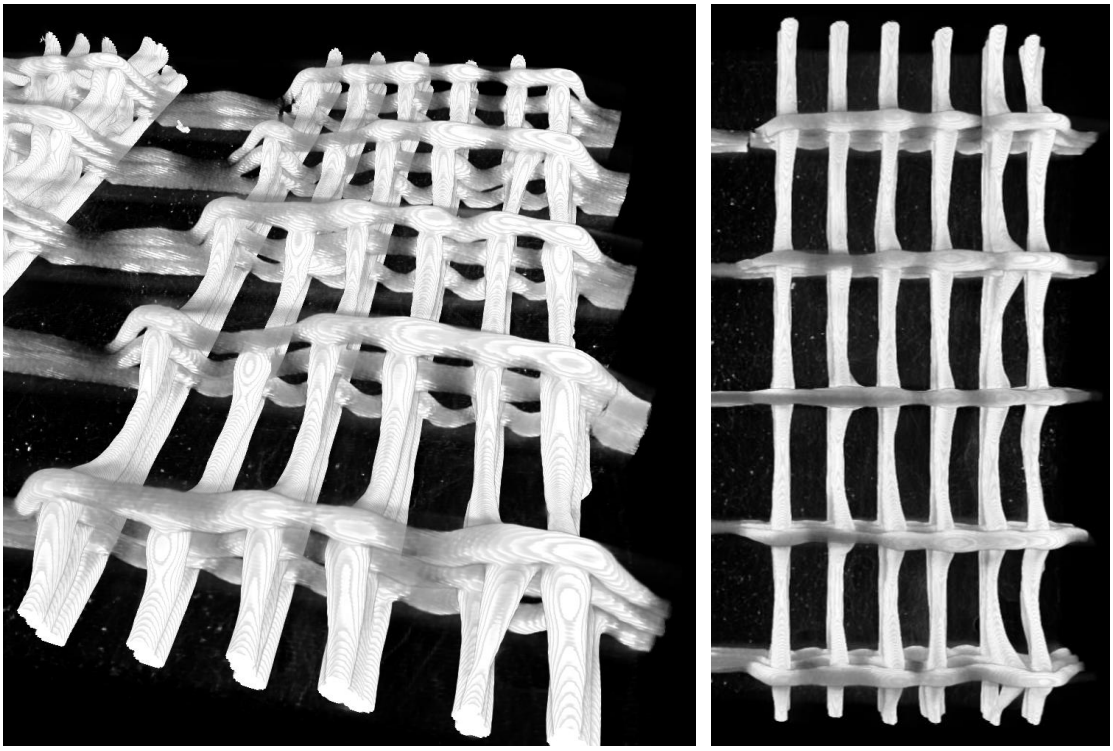

Figure 8.2 3D images from a micro-CT scan of a lattice section, deposited with a nozzle height of 1.0 mm, flow rate of 0.25 µL/s, 3.75 kV at 15.0 mm/s. The odd layers were spaced at 0.4 mm, the even layers at 1.0 mm. The right image is a plan view of the lattice section.

The reconstructed images of the overview scan in Figure 8.2 and the detail scan in Figure 8.3 gave excellent detail of the geometry, but contained artefacts from the reconstruction technique. Most notably the surfaces of Figure 8.2 had a pattern of periodically changing contrast, which appeared to be contour lines, whereas optical

images in Section Figure 7.4 of similar lattices showed no indication of this. Figure 8.3 was more difficult to interpret for two reasons. First, the density of the filaments running in different directions appeared to be different, with the filaments running across the image having noticeably greater transparency compared to the filaments with exposed cross-sections. It is likely that this was due to the orientation of the sample during imaging, as the sample was rotated in roughly the same axis as the denser filaments. As the sample was only rotated in one axis, this would lead to different information being captured about the filaments in each direction. The second ambiguity was in the exposed cross-section, where the edges of the filament again looked denser than the core. Inspection of the cross-section images, such as Figure 8.6, showed the same feature. Both images were reconstructed from the silhouettes that the scanner actually captured, so this phenomenon could have been due to the X-ray interactions, the reconstruction algorithm or an accurate reflection of the sample structure. For both scans, the 3D reconstruction was most useful for shape information rather than texture.

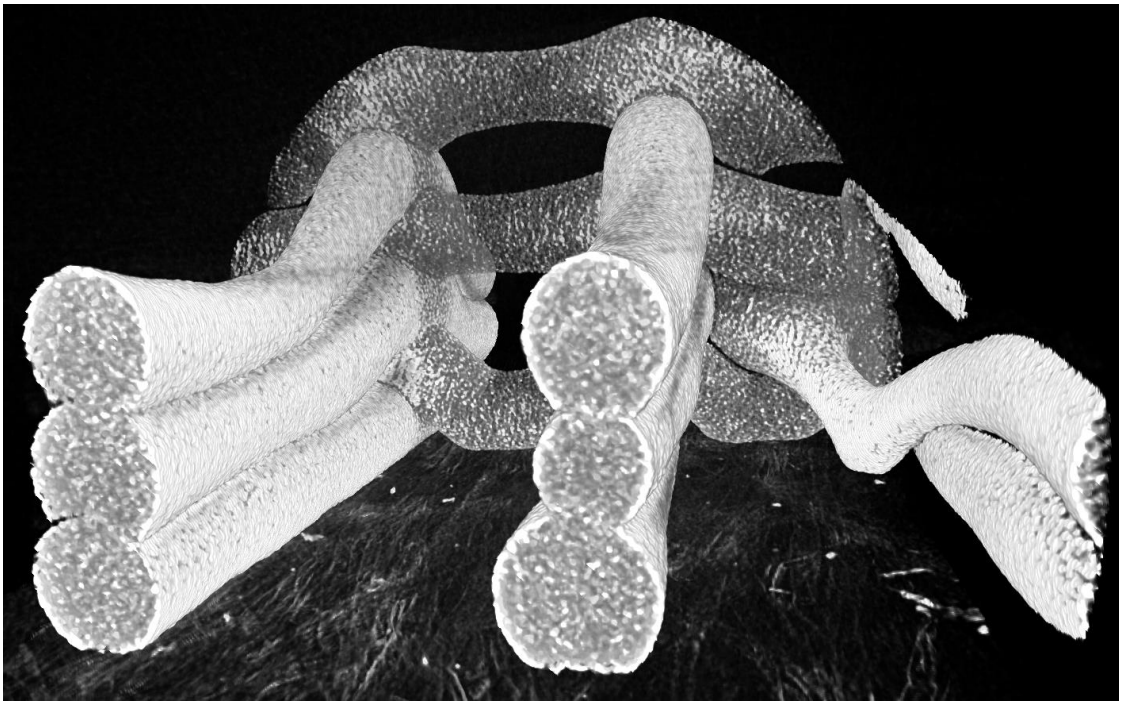

Figure 8.3 Reconstruction of the high-resolution scan of the lattice in Figure 8.2.

What could be learnt from Figure 8.2 was much the same as was concluded in Section 7.4, in that the process was capable of bridging small gaps but only did so well under very specific conditions. Figure 8.3 was more informative, being at a smaller scale than previous images. The middle of the image showed good spanning for the bridges in the second and third layers, although the thinning of the filament in both bridges was clear. The filaments running into the image showed good contact between layers, without any deformation of the previous layer. This implied the incoming filament was still fluid enough to conform to the deposited filament, and therefore at a high enough temperature to bond well with it, but did not cause significant melting of the deposited material.

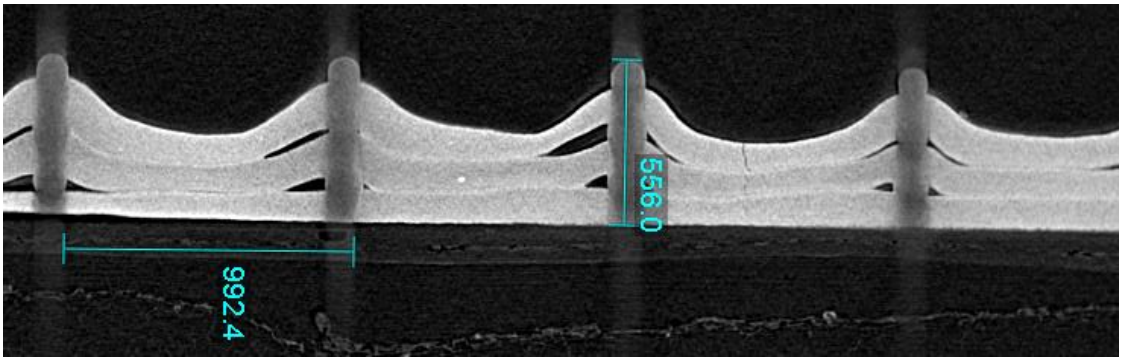

Figure 8.4 Cross section along the odd layers of the lattice in Figure 8.2. Dimensions are in micrometres.

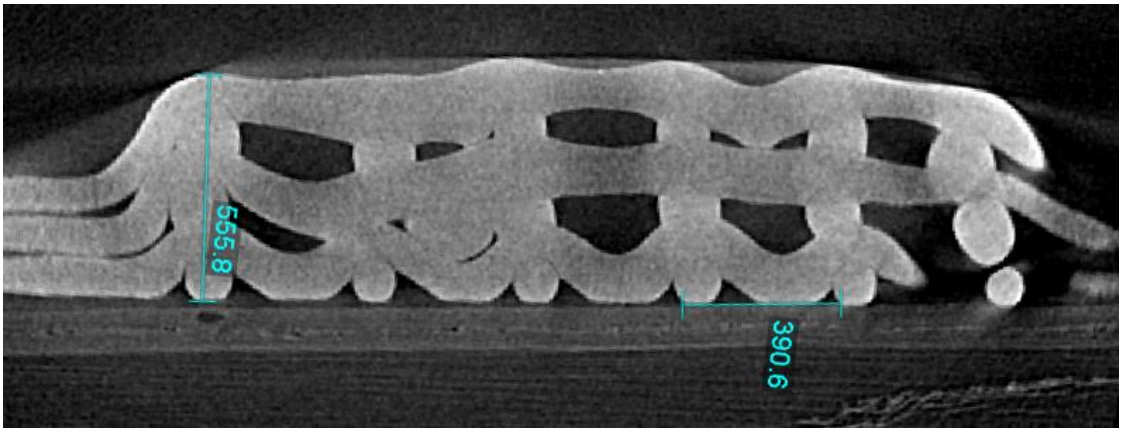

Figure 8.5 Cross section along the even layers of the lattice in Figure 8.2. Dimensions are in micrometres.

Looking at the cross-sections themselves provided better information about the interior of the lattice, but still had some artefacts. The most noticeable were the changing brightness of the material and vertical smudging in Figure 8.4. The former was caused by 'shadows' of the rest of the lattice, so in the darker sections the image was being taken along the axis of a filament and there was much more material to absorb the x-rays. The smudging was not present in all cross-sections (compare with Figure 8.5) but was most likely due to a combination of shadowing and misalignment between the axes of the scanner and the axes of the sample.

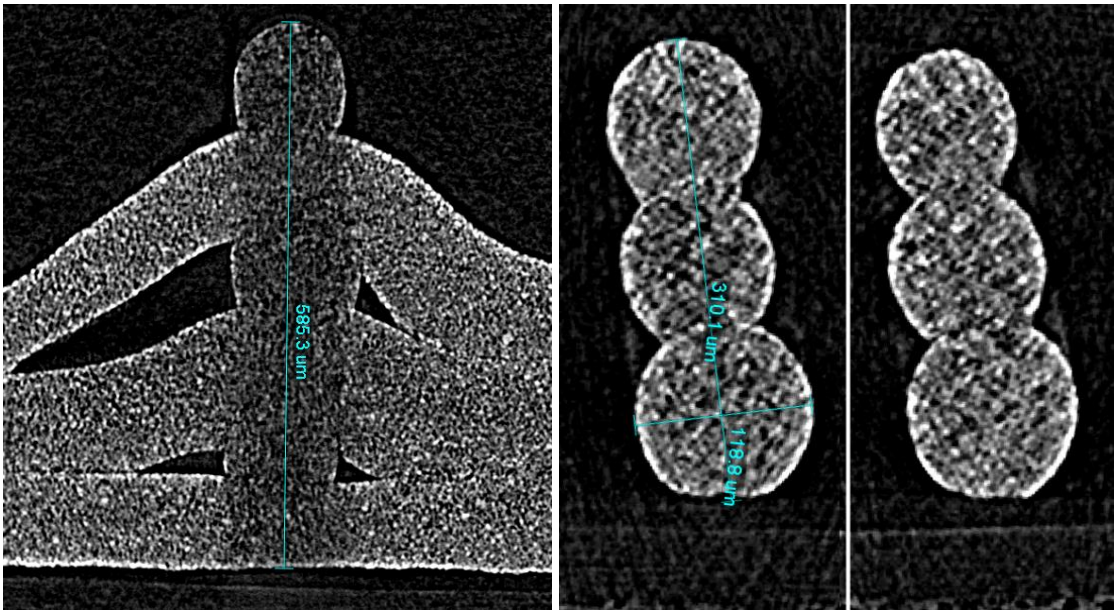

Figure 8.6 Cross section along the odd layers (left) and across the odd layers (right) from the scan shown in Figure 8.3.

Figure 8.4 and Figure 8.5 both verify the dimensions of the filaments and the edge-to-edge spacing of the filaments was within 3 % of the target dimension, even after shrinkage of the wax and filament diameter variations. The height of the filament stacks was less than the filament diameter multiplied by the number of layers due to the interface between stacked filaments. The height was reduced by as much as 8 %, which was unlikely to affect raising the nozzle with each deposited layer, but was worth considering when calculating beam strength in Section 8.5. In Figure 8.4, where the filaments were not intended to bridge the gap, each layer could be seen to

lift off from the previous as it approached the crossing points. As might be expected, the length of this distance was similar to the maximum size of bridgeable gap. Figure 8.5 provided a detailed view of the quality of the successful and failed bridging filaments. Here it was clear that the first bridging layer did fail, with the filament contacting the substrate over roughly a third of the bridging distance. The variation in the thickness of the filament as it forms bridges was also clear, with the surface tension of the ink able to pull it partly to the crossing points before it fully solidified.

Figure 8.5 shows cross-sections of several filaments, including the surface that was in contact with the substrate. Figure 8.6 does the same for fewer filaments but at higher resolution. From these the filaments can be seen to have adopted a cross-sectional shape close to a circle, except for the bottom surface. The bottom face was either flat, when the filament was directly on the substrate, or concave, when the filament was stacked on top of a previous filament. The widths of the flat surfaces that were touching the substrate were between a third and half the diameter of the filament, at the top end of the range considered in section 3.3.2. However, one conclusion of that modelling was that when the contact ratio was above 20 %, increasing it only slightly reduced the freezing time. Therefore, the estimates given in that section should be of the right order of magnitude.

Perhaps the most interesting images from the XCT scan were those in Figure 8.6, taken from the detail scan. With a resolution a quarter of the nominal particle size, these images allowed the distribution of alumina within the filament to be evaluated, although the resolution was not sufficient to identify clearly individual alumina particles. The distribution appeared uniform within the core of the filament; however, the surface appeared to be brighter, indicating a higher density. One of the challenges of XCT is to determine whether features like this are truly from the sample, an artefact of the x-rays interacting with the sample or an artefact of the reconstruction technique. It was possible that some of the alumina particles acquired a charge and were repelled to the surface of the filament during deposition, but a different imaging technique was needed to verify whether this occurs.

8.2.2 Scanning electron microscopy

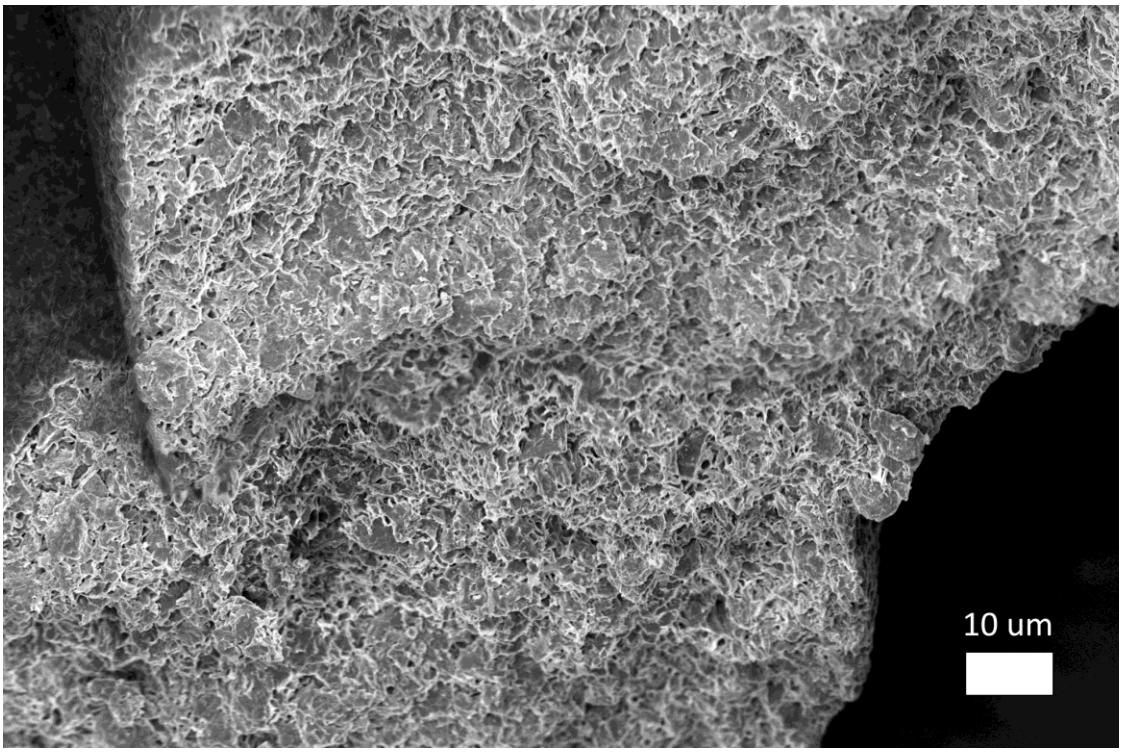

Figure 8.7 SEM image of the fracture surface of a green body lattice. Two vertically stacked filaments are visible, with the boundary between them running horizontally across the middle of the image.

While XCT provides non-destructive imaging of the interior of a sample, SEM gives more detailed and more easily interpreted information about the surfaces of a sample. For some samples, the internal structure can be examined by breaking the sample and looking at the fracture surface. The need to dissipate the electrons requires non-conductive samples to be coated in metal, poor coverage of which can lead to artefacts in the resulting images, especially in areas with overhanging or convoluted geometry.

Figure 8.7 shows the fracture surface of two stacked filaments. The XCT images suggested that the density of the ink might be higher at the surface of the filament, but this did not appear to be the case, although it was difficult to discern alumina particles from the wax matrix. This was also true in the higher magnification view in Figure 8.8. Even at the interface between the two filaments, the fracture surface looked very

similar to the core. However, the plane of fracture was different for each of the filaments, implying that the bond between them was not as strong as the filaments themselves, despite the apparent lack of a distinct boundary. The difference between the fracture planes was on the scale of a few micrometres, so the joint was probably not much weaker than the filament core, and high strength was not important in the green body. The important property was the proximity of the ceramic particles, which was consistent across the joint, leading to good strength after sintering.

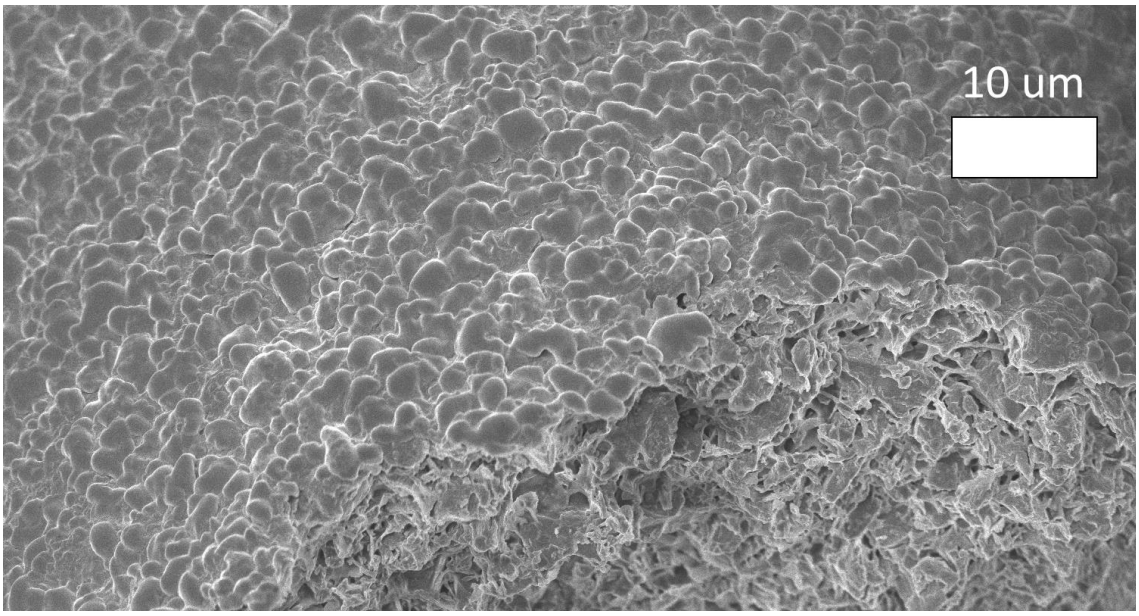

Figure 8.8 SEM image of the curved surface of a green body filament, including some of the same fracture surface shown in Figure 8.7 in the lower right.

An unexpected finding of the SEM images was the texture of the outer surface of the filament. Shown Figure 8.8 this surface was clearly seen to be bumpy with rounded protrusions, which was in stark contrast to the sharp edges of the fracture surface. A more detailed view of the surface is shown in Figure 8.9, from which it could be determined that the diameter of the bumps was around half the size of the alumina particles. It might be expected that shrinkage of the wax as it cools would allow some alumina particles to protrude from the outer surface, but these would appear sharp. The very smooth protrusions actually seen, along with observations during the original mixing of the ink, suggest that this was actually separation of the

LJ210 and paraffin wax during cooling. Ink that was kept molten without agitation for an extended period shows partial separation of LJ210 from the mixture. The same separation occurring over much shorter times and length scales was likely the cause for the two phases seen here. Other than the implication of poor long-term stability of the ink when heated, this separation did not negatively affect the direct-write process. Identifying which phase was which material was difficult by inspection alone, but considering their prevalence in Figure 8.8 it would be expected that the smooth bumps were the paraffin wax.

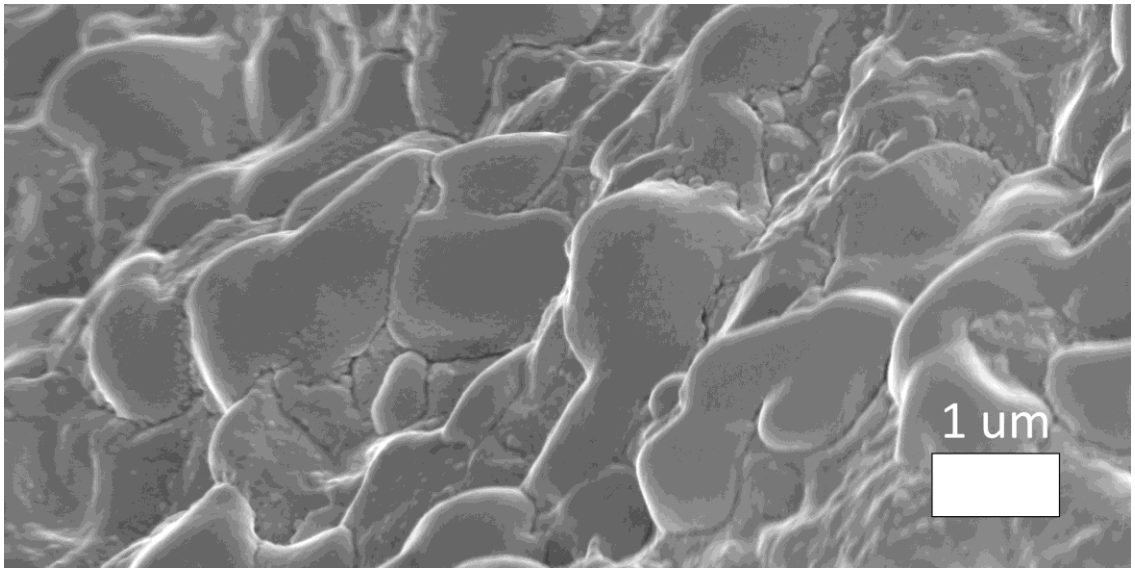

Figure 8.9 Magnified view of the outer surface of the ink, showing two distinct phases.

8.3 Sintering

For the de-binding step, the samples were brought up to 950 ^{o}C in the box furnace and left there for 2 hours to ensure complete removal of organics, moisture and other sources of outgassing, before being allowed to cool overnight. For the sintering step, the samples were sealed in the tube furnace, brought up to 1,400 ^{o}C and left overnight, then brought down to an intermediate temperature before the heating elements were turned off and the furnace allowed to cool naturally overnight.

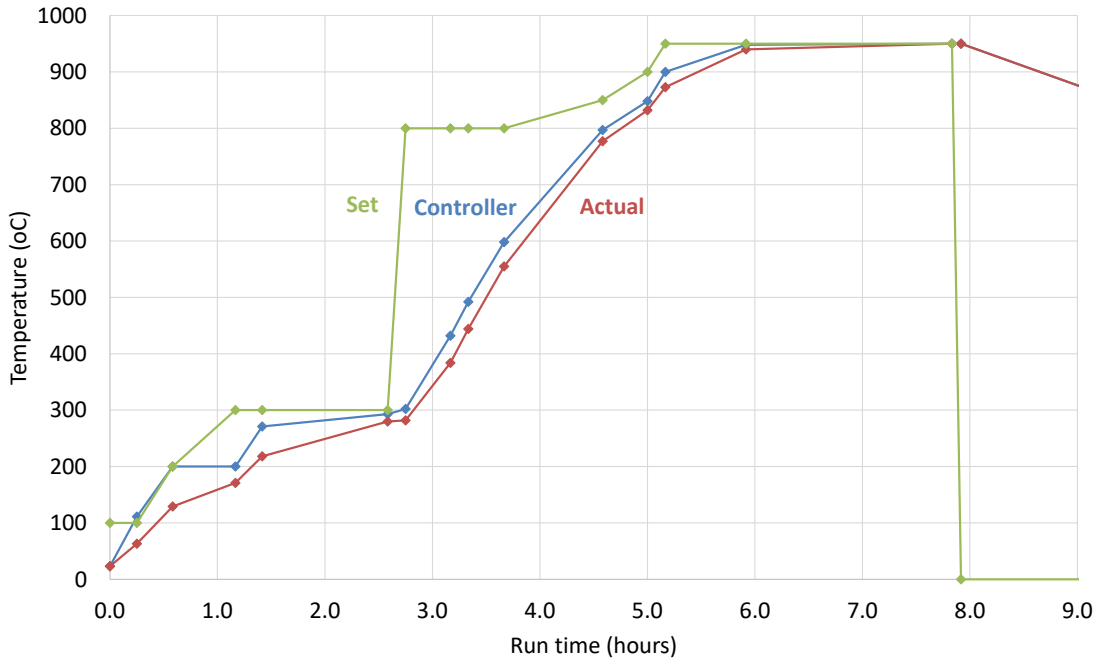

Figure 8.10 Temperature history for the debinding treatment in the box furnace. The 'Actual' temperature readings are from a thermocouple adjacent to the samples.

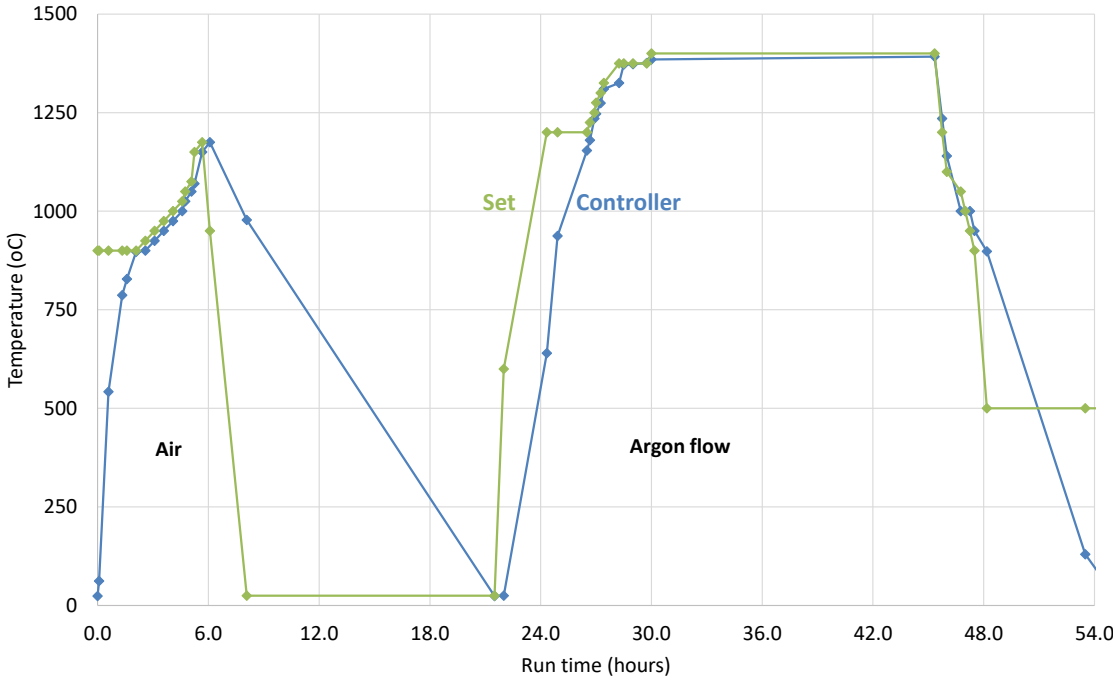

Figure 8.11 Temperature history for the sintering treatment in the sealed tube furnace. The initial heating run was aborted in order to turn introduce a flow of argon.

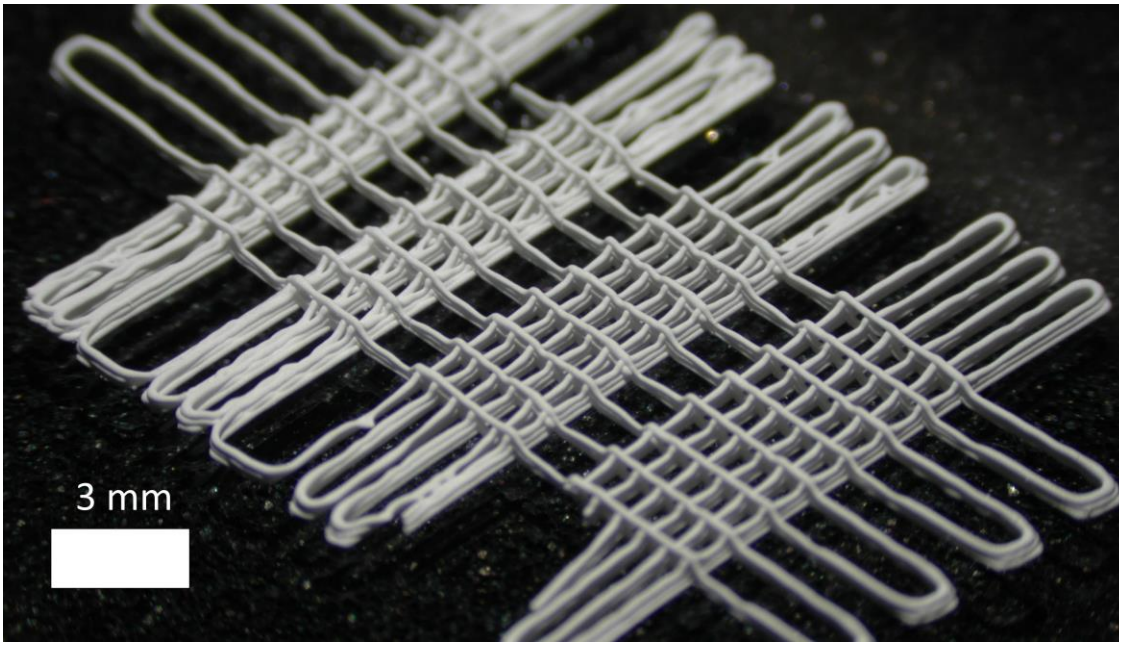

Figure 8.12 Succesfully sintered lattice sample, showing the white colour of pure alumina and minimal change to geometry, apart from several cracks and breakages from handling.

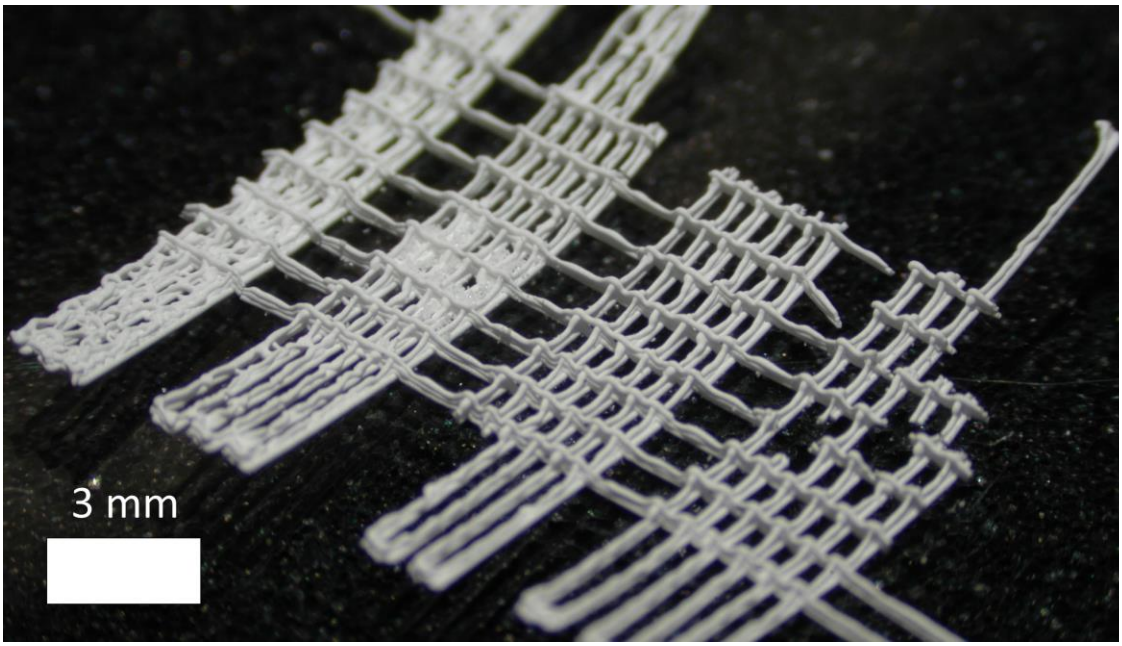

Figure 8.13 Poorly sintered lattice, showing significant warping, trapped powder and breakages within the lattice sections.

The de-binding step ran according to the plan shown in Figure 8.10, with the samples losing the blue colour imparted by the LJ210. For this first run, an additional K-type thermocouple was placed in the furnace next to the sample to give readings that were more representative of the sample temperature. However, the sintering step was interrupted. The tube furnace must be sealed airtight for use and initially it was heated with the trapped, static air. During heating, it was decided a flow of argon would be preferable to protect the furnace form possible oxidative damage, but simply turning the gas flow on while the tube was hot could cause it to crack, so the furnace was cooled and reheated with flowing argon. The heat input from this aborted run was not expected to have significantly contributed to the sintering, as it did not exceed 1,200 ^{o}C and had no dwell period. The full temperature history is shown in Figure 8.11.

The resulting parts were carefully lifted from the coarse powder beds. Two of the four samples were not significantly visually altered by the sintering process, other than several cracks in filaments between lattice sections, as seen in Figure 8.12. The other two samples showed various degrees of warping and had some of the coarse powder stuck in their pores, as seen in Figure 8.13. The powder was likely not bonded with the lattice as it fell away from the other samples, but no attempt was made to clear the powder until the durability of the samples was established. The curling of two samples could have resulted from either the material rearrangement during sintering or insufficient support from the powder bed, allowing the sample to sag.

During handling, it was observed that the sintered samples were harder and more durable than the green body samples. To check for shrinkage, a sintered sample was placed on an acetate film and laid over a green sample. No difference in size was visible by inspection, limiting any linear shrinkage to less than 5 % and probably no more than 1 %.

8.4 Post-sinter imaging

The sintered lattice samples were prepared for the SEM in the same way as the green samples, producing Figure 8.14 and Figure 8.15. The low sintering temperature resulted in a very porous structure, which was difficult to continuously coat with sputtered metal. This led to poor charge dissipation and created difficulties in capturing good images of the samples. Charge building up on the surface caused drift in the image, so to avoid blurring scans had to be performed quickly. Multiple scans could be averaged together to improve the signal-to-noise ratio in the image. Excessive charge build-up can damage the sample, creating dark spots that develop during imaging.

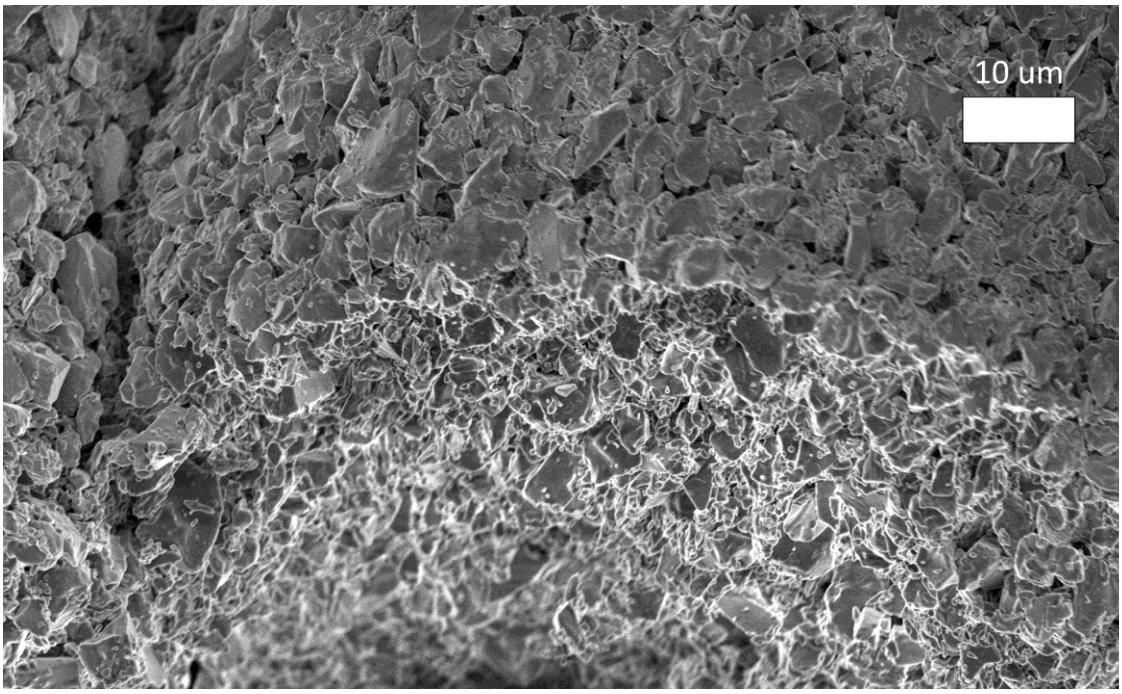

Figure 8.14 SEM image of a sintered lattice sample, showing the fracture surface (lower half) and outer surface (upper half) of a filament, along with a joint between stacked filaments (far left).

These images made it clear that the sintering process was very limited, with little diffusion of the alumina, as the shapes of the original particles were still plainly visible. Compared to the original powder, shown in Figure 5.1, the smallest particles were less prevalent and the edges of individual particles appeared more rounded.

These features had the highest surface area to volume ratios, so were the first to lose material during sintering. This confirmed some diffusion occurred, along with the fact that the sintered samples had some appreciable strength.

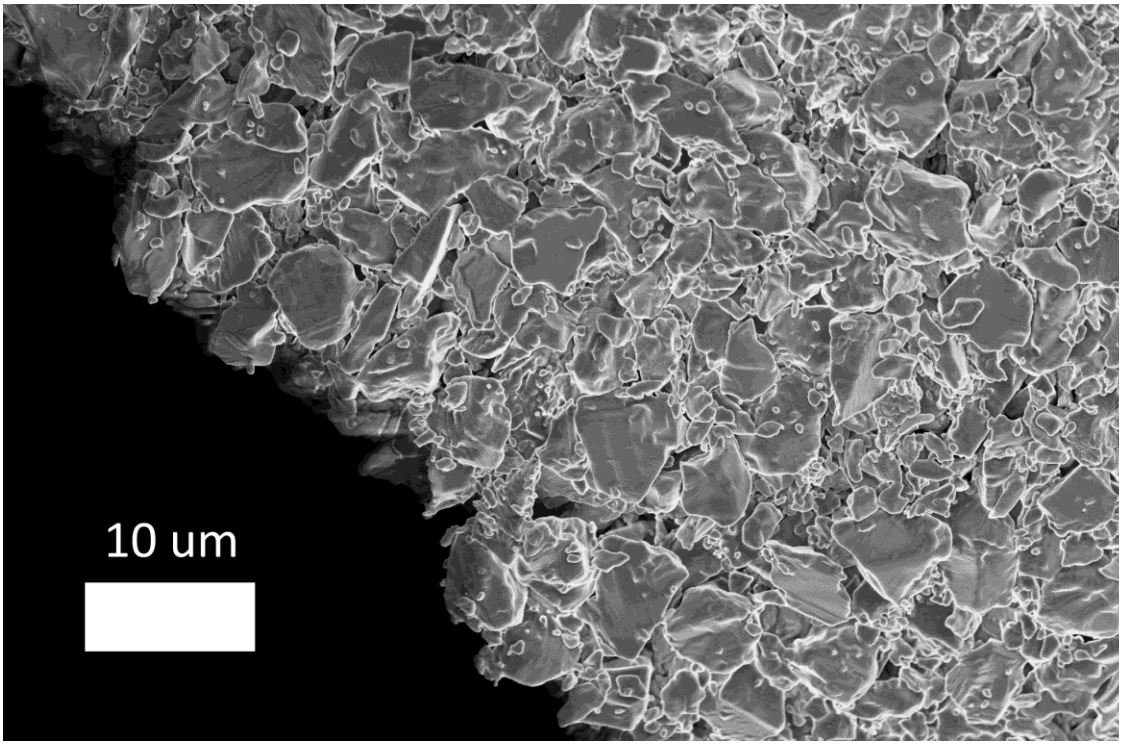

Figure 8.15 SEM image of a sintered lattice sample, looking at the outer surface of a filament next to a fracture plane.

With the waxes removed, the distribution of alumina particles was clearer and it continued to appear consistent throughout the filament. However, it was possible that there was some rearrangement during sintering, after the wax had burnt off but before strong bonds were formed between the particles. There was no measurable large-scale shrinkage in the samples, due to the low degree of material consolidation, so if there was small-scale rearrangement of the particles it would be expected that larger voids or similar defects might have formed. No such defects were seen, so it could be concluded that any particle movement was very small and the distribution of the particles within the deposited filament was initially uniform.

These SEM images, when combined with the negligible sample shrinkage, suggested that the alumina particles were very nearly or already in contact with each other in the solidified ink. One concern when formulating the ink was that if the solid volume fraction of the ink was not sufficiently close to the theoretical limit there would be relatively large distances between the ceramic particles and the sample would collapse after de-binding. This work has shown that 50 vol% was above this lower limit, but establishing if the limit exists and the value of it is left for future work. Inks with lower solid fractions, when marginally sintered as the samples presented here have been, would produce very high porosity rods, with might be advantageous in catalytic or biological applications. Attempting to sinter fully such low volume fraction inks would produce high shrinkage and possibly lead to cracking. Higher solid fractions would leave less porosity with marginal sintering and result in less shrinkage with more complete sintering.

8.5 Mechanical testing

Sintered lattices, of the shape described in Figure 7.1 and built with three layers, were broken into sections of constant filament spacing. Only the 0.6 and 0.5 mm spacing sections were tested, as these were more likely to be properly formed without filaments crossing between adjacent walls. The universal tester recorded the force on and position of the knife as it was lowered, with the results for two lattices shown in Figure 8.16. Each lattice section comprised six beams in parallel across the gap, each made of three stacked filaments, with seven perpendicular beams. This was very different from the typical geometry of rectangular or circular bars used for bend tests, but testing the strength of a single filament was impractical with the available equipment. The perpendicular filaments prevented twisting or buckling of the spanning beams and the knife was positioned so that the edge was between the junction points, so that the loading point was on a beam with a relatively consistent cross-section. Figure 8.4 shows the profile of the spanning beams, from which it was clear that the filament junctions would increase the stiffness of the beam. However,

the peak stress in a three-point bend is seen directly under the middle loading point, so only the material properties in this region affected the results below.

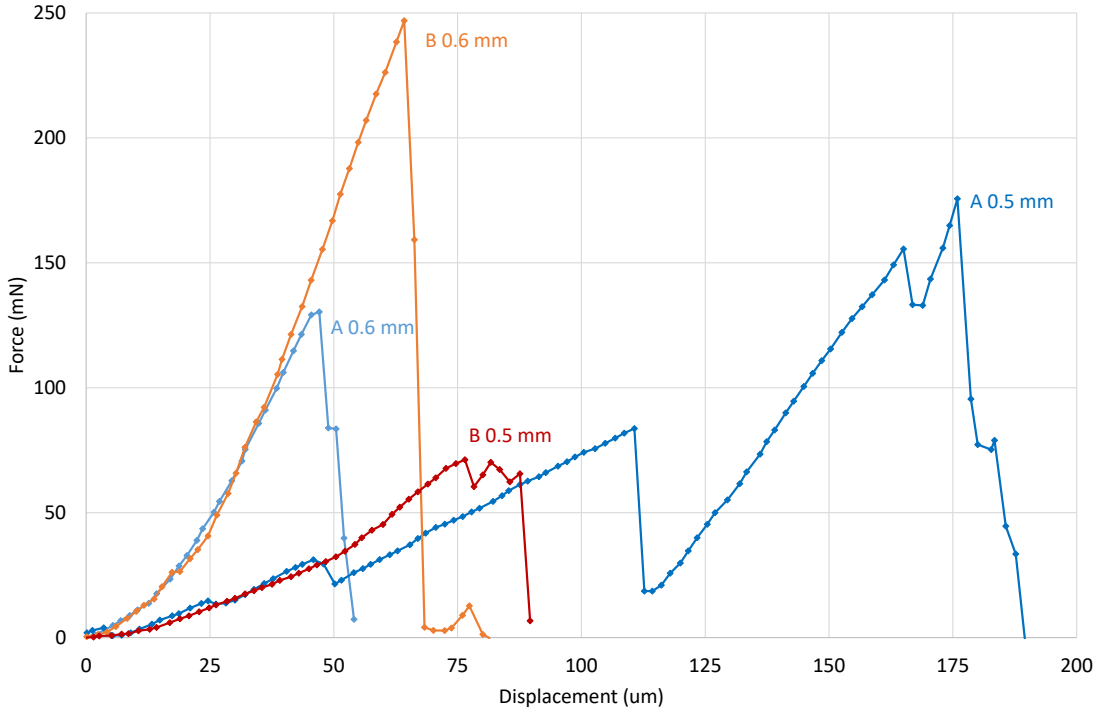

Figure 8.16 Force versus displacement graphs for two sections of two lattices (A and B), with each section having a beam spacing of 0.5 or 0.6 mm. The displacement values are relative, with each line shifted so that the force begins to rise at zero displacement.

To calculate the expected properties of the lattice if it was made from solid alumina, each beam was modelled as three vertically stacked cylinders, touching at a single point, with the full section being six of these in parallel. Figure 8.6 shows the actual cross-section is made of overlapping circles, but this assumption greatly simplifies the calculation. The second moment of area, I_x for a circle through its centre is given in equation 8-1, where r is the radius of the circle, and the parallel axis theorem can be used to calculate the second moment of area for the top and bottom circle around the axis of the middle circle. This is given in equation 8-2, where A is the area of the offset section and d is the distance by which it is offset. Equation 8-3 gives the second moment of area for the beam, I_{beam}.

8-1 $$I_x = \frac{1}{4}\pi r^4$$

8-2 $$I_{x'} = I_x + Ad^2$$

8-3 $$I_{beam} = \frac{1}{4}\pi r^2(3r^2 + 8d^2)$$

From standard beam bending equations, it is straightforward to derive relationships between the measurements in Figure 8.16 and the flexural strength, $\sigma_{flexural}$, and Young's modulus, *E,* shown in equations 8-4 and 8-5 respectively, where *F* is the force, *L* is the length of loaded beam, *y* is the distance from the central axis and δ is the displacement. Note that for equation 8-5, the two points must be on a straight section of the curves shown in Figure 8.16. It was assumed that the loading system was perfectly rigid and that the measured displacement was the deflection of the sample.

8-4 $$\sigma_{flexural} = \frac{1}{6}\left(\frac{F_{max}Ly_{max}}{4I_{beam}}\right)$$

8-5 $$E = \frac{1}{6}\left(\frac{(F_2 - F_1)L^3}{48I_{beam}(\delta_2 - \delta_1)}\right)$$

Based on measurements from Figure 8.6, the average filament diameter for these lattices was taken as 100 μm. The average peak force for the four samples was 156 mN and the Young's modulus calculation was based on the 'B 0.6 mm' curve, as it was the steepest. The lower gradient curves are due to warping of the samples causing the span, *L*, to be larger or due to only a subset of the beams being in contact with the knife, so part of the sample was not loaded. The results of the calculations are given in Table 8.1 along with some example values for bulk alumina. The assumptions about the sample geometry and the inconsistencies in the samples themselves severely limited the precision of these calculations.

From the images presented in Section 8.4, the mechanical properties of the sintered samples were expected to be a fraction of those for solid alumina, due to both the solid volume fraction of 50 % and the limited bonding between particles. This meant that

strength and stiffness values in the range of 15 to 18 % of the bulk properties were well within the expected range. The samples produced here were not suitable for load bearing applications, not only due to the comparatively lower strength but also because of the variability in strength, which was more than a factor of two from highest to lowest. This was partly due to the random and sparse connections within the porous filaments and partly due to the test method. Attempting to use rigid tooling to load six parallel beams of variable dimensions inevitably led to one or two beams initially taking the full load. With a brittle material such as alumina, these beams may fail before any other beams encounter the tools. This sequential loading of the beams caused the multiple peaks seen for the 'A 0.5 mm' curve of Figure 8.16, where the different slopes of each peak was proportional to the number of beams in contact with the tools. Alternatively, the high local forces might lead to crushing of the filament, which could have been responsible for the oscillations and jumps in force values. Avoiding these issues with a different method might show less variation in the strength, with more samples tending toward the higher strength of the 'B 0.6mm' sample.

	Bulk alumina	Sintered sample	**Relative performance**
Flexural strength $\sigma_{flexural}$ (MPa)	260	40	15 %
Young's modulus E (GPa)	370	69	19 %

Table 8.1 Measured mechanical properties of the sintered lattice samples compared to typical values for bulk alumina.

Although this testing used a small sample set and involved several simplifications, it did show that the samples underwent significant consolidation during sintering. The ink formulation and electrospinning process did not prevent the powder particles bonding well and producing continuous alumina.

8.6 Conclusions

Imaging of the green body lattices confirmed several properties proposed or assumed earlier in this work. First, the cross-section of the deposited filaments was very close to circular, as assumed, but the area that flattens against the substrate was larger than expected and could be as large as half the diameter of the filament. Second, the ink still being molten as it hit the deposition surface led to good bonding with previous filaments, but allowed surface tension to cause successful bridges to be thinner than fully supported filament, in turn leading to bulging at the ends of the bridge. Third, the dimensions of the lattice samples were accurate and there was negligible shrinkage from the cooling and solidification of the wax.

The samples survived removal of the binders and sintered successfully after 15 hours at just under 1,400 ^{o}C. The resulting samples were stronger than the green samples and showed negligible shrinkage, but half of them suffered some degree of warping. It was not known whether the warping was due to consolidation within the sample or poor support of the sample. Some cracking was also observed, although for the successful sample this was mainly in weaker regions and could have been caused during handling.

SEM of the sintered samples revealed a very low degree of consolidation, with the original particles still distinct. The distribution of particles was found to be uniform throughout the filament, including at the outer surface and joints between filaments. No large voids or defects were seen on the outer or fracture surfaces, indicating minimal particle movement during de-binding and sintering and a good dispersion of particles in the original ink. The success of this marginal sintering suggests that lower solid fraction inks might be used to produce high porosity sintered filaments, but that better sintering of the ink used in this work might produce large shrinkages.

Three-point bend testing of sections of sintered lattices showed their strength and stiffness to be around 15 and 18 % compared to solid alumina respectively. This was in line with the highly porous structure, but showed that the product of the electrospinning process can be sintered into continuous ceramic.

9 Overall Conclusions and Future Work

Electrospinning is a technique that has been used for decades to produce fine filaments and meshes of polymers. More recently, inks that are more viscous have been used to produce straight jets and the technique adapted to a direct-write technology. The overall aim of this work was to extend this use to include inks with a high solid content, in order to provide a direct route to additive manufacture of ceramic parts with feature sizes down to 200 μm.

9.1 Attainment of research aims

1. **Create a system capable of producing patterns with high resolution**

Given the limitations of the motion platform and syringe pump, the smallest filament that could be reliably patterned was just over 100 μm in diameter, exceeding the 200 μm target. The key limits were the maximum deposition speed of the three-axis stage and minimum flow rate of the syringe pump. In experiments on the rotary stage, which could achieve higher speeds, filaments as thin as 25 μm were produced.

2. **Formulate a suitable ink**

The final ink composition, used for the work described in Chapters 7 and 8, met all the requirements laid out in Section 1.1, with some caveats on long-term stability. A carrier liquid based on alkanes ensured low conductivity and by using paraffin wax, the ink quickly solidified after leaving the nozzle, fixing the shape of the ink over long time scales. The addition of large volume fractions of alumina gave the ink shear-thinning properties, helping minimise flow over short timescales while keeping the viscosity in the region of 1,000 mPa s at the shear rates expected in the nozzle. The

inclusion of a UV-curable wax allowed for deposited patterns to be placed in a furnace and have the organic components burnt out without loss of shape. At 50 vol%, the alumina content was high enough that samples retained their shape after partial sintering. The ink suffered from some sedimentation of the alumina and showed signs of separation if kept molten for several hours. Long-term storage in the solid state alleviated these problems, but evaporation of limonene, added as a thinner, was a concern when the storage period was longer than a week.

3. Investigate electrospinning conditions

Electrostatic modelling showed that adding a conductive shroud around the nozzle, electrically connected to it, would produce a more consistently vertical electric field, potentially helping direct the jet straight down toward the substrate. This also reduced the peak electric field, which was typically located at the nozzle and limited the voltage that can be applied. Thermal models of the jet suggested that little cooling would occur in flight and that most heat loss was through the substrate, taking up to 0.5 seconds after impact for a filament to fully solidify.

An empirical equation for predicting minimum electro-jet width was established for an oil-based ink. Using the nozzle height, flow rate and applied voltage as variables, the relative importance of each condition was found to be in that order, from most to least important. An average electric field between the nozzle and substrate of 2.0 to 2.5 kV/mm was found to give the most robust jet. The investigated range of nozzle sizes had a minor effect on the minimum jet width, whereas the substrate speed had a major effect, with a faster substrate producing thinner jets. It was also found that the dimensions of the deposit were entirely determined by the substrate speed, as the ink was still liquid upon hitting the substrate. Reducing the viscosity of the ink could produce thinner jets, but the jets were then stable over a smaller range of voltages.

4. Investigate patterning ability

Several limiting behaviours were identified when trying to create layered patterns with this process. First, the electro-jet was attracted to previously deposited filaments when the spacing between them was less than 0.5 mm, depending upon the conditions.

This appears to have been due to the dielectric properties of the ink warping the electric field. This made patterning filaments with a spacing of less than their diameter impossible, but meant that stacking filaments vertically was very reliable. Second, the jet had difficulty bridging gaps unsupported, such as the space between two filaments in a previous layer. A gap as large as four filament diameters could be spanned with a success rate of 71%, although this was only achieved on the second layer of the test lattices. Third, the flexibility of the jet caused sharp corners to become rounded, with a minimum radius of around 0.4 mm. Further to this minimum radius, deviations in the filament path were observed up to 2 mm from a 90^{o} corner. The minimum radius could be reduced by increasing the deposition speed, but exceeding 20 mm/s induced significant oscillations in the three-axis stage.

5. **Produce pure ceramic parts**

Samples were successfully sintered, but due to the maximal temperatures attainable with the equipment used, only bonding of the powder particles occurred, with minimal consolidation of the ceramic. Imaging of the samples after sintering showed a uniform distribution of alumina particles and a high porosity structure. Half of the sintered samples suffered from warping during sintering, although this might have been due to poor contact with the supporting powder bed rather than changes within the sample itself. The ceramic parts had around 15 % of the strength of pure alumina, in line with their high porosity.

9.2 Future work

The formulation of the inks could be improved in several ways. Ideally, the need for a thinner additive would be removed by using a lower viscosity UV-curing additive. The replacement UV-curable material could be solid at room temperature, allowing it to also replace the paraffin wax entirely, or liquid at room temperature and continue to be blended with the paraffin wax. Alternatively, further exploration of evaporative inks could reduce or remove the need for de-binding and achieve higher packing densities in the deposited ink while maintaining low viscosities in the nozzle.

The patterning process could be improved with a more rigid motion platform, enabling higher deposition speeds to be explored. Integrating voltage and motion control together, so that the applied voltage can be increased as the nozzle is raised, would also enable exploration of taller patterns. This work identified the difficulty in closely spacing filaments due to attraction between the electro-jet and deposited material, but the intentional patterning of adjacent filaments to produce solid sheets of material was not investigated.

The third major area for future investigation is the use of alternative powdered materials and their processing. Only minor material consolidation was achieved in this work, so the primary question is whether samples can survive or even achieve consolidation to beyond 90 % of bulk density. This would require temperatures in excess of 1,700 ^{o}C with the powder used here. A finer alumina powder could allow for full consolidation at lower temperatures, as well as the potential for finer filaments. The inclusion of sintering aids, such as silicon dioxide, could improve consolidation with any alumina powder. In addition to investigation into near full density parts, exploring how low the solid loading of the ink can be while remaining able to be sintered could lead to very high porosity rods, with applications in filtering, catalysis and cell growth. The latter two areas would also benefit from the use of different ceramics, for example using hydroxyapatite powder to build lattices for hard tissue reconstruction, which would also use lower sintering temperatures.

10 REFERENCES

Amplitude sweeps :: Anton Paar Wiki [WWW Document], n.d. . Anton Paar. URL https://wiki.anton-paar.com/en/amplitude-sweeps/ (accessed 5.9.18).

Angammana, C.J., Jayaram, S.H., 2011. Analysis of the Effects of Solution Conductivity on Electrospinning Process and Fiber Morphology. IEEE Trans. Ind. Appl. 47, 1109–1117. https://doi.org/10.1109/TIA.2011.2127431

Anton, F., 1934. Process and apparatus for preparing artificial threads. US1975504 A.

Bellini, A., 2002. Fused deposition of ceramics: a comprehensive experimental, analytical and computational study of material behavior, fabrication process and equipment design. Drexel University.

Bisht, G.S., Canton, G., Mirsepassi, A., Kulinsky, L., Oh, S., Dunn-Rankin, D., Madou, M.J., 2011. Controlled Continuous Patterning of Polymeric Nanofibers on Three-Dimensional Substrates Using Low-Voltage Near-Field Electrospinning. Nano Lett. 11, 1831–1837. https://doi.org/10.1021/nl2006164

Brown, T.D., Dalton, P.D., Hutmacher, D.W., 2016. Melt electrospinning today: An opportune time for an emerging polymer process. Prog. Polym. Sci. 56, 116–166. https://doi.org/10.1016/j.progpolymsci.2016.01.001

Brown, T.D., Dalton, P.D., Hutmacher, D.W., 2011. Direct Writing By Way of Melt Electrospinning. Adv. Mater. 23, 5651–5657. https://doi.org/10.1002/adma.201103482

Cloupeau, M., Prunet-Foch, B., 1994. Electrohydrodynamic spraying functioning modes: a critical review. J. Aerosol Sci. 25, 1021–1036. https://doi.org/10.1016/0021-8502(94)90199-6

Cloupeau, M., Prunet-Foch, B., 1989. Electrostatic spraying of liquids in cone-jet mode. J. Electrost. 22, 135–159. https://doi.org/10.1016/0304-3886(89)90081-8

Cutler, I.B., Bradshaw, C., Christensen, C.J., Hyatt, E.P., 1957. Sintering of Alumina at Temperatures of 1400°C. and Below. J. Am. Ceram. Soc. 40, 134–139. https://doi.org/10.1111/j.1151-2916.1957.tb12589.x

Dalton, P.D., Vaquette, C., Farrugia, B.L., Dargaville, T.R., Brown, T.D., Hutmacher, D.W., 2013. Electrospinning and additive manufacturing: converging technologies. Biomater. Sci. 1, 171–185. https://doi.org/10.1039/C2BM00039C

Deitzel, J.M., Kleinmeyer, J.D., Hirvonen, J.K., Beck Tan, N.C., 2001. Controlled deposition of electrospun poly(ethylene oxide) fibers. Polymer 42, 8163–8170. https://doi.org/10.1016/S0032-3861(01)00336-6

Doshi, J., Reneker, D.H., 1993. Electrospinning process and applications of electrospun fibers. IEEE, pp. 1698–1703. https://doi.org/10.1109/IAS.1993.299067

Edwards, M.D., Mitchell, G.R., Mohan, S.D., Olley, R.H., 2010. Development of orientation during electrospinning of fibres of poly(ε-caprolactone). Eur. Polym. J. 46, 1175–1183. https://doi.org/10.1016/j.eurpolymj.2010.03.017

Erkalfa, H., Misirli, Z., Baykara, T., 1995. Densification of alumina at 1250 °C with MnO2 and TiO2 additives. Ceram. Int. 21, 345–348. https://doi.org/10.1016/0272-8842(95)96207-6

Feng, J.J., 2002. The stretching of an electrified non-Newtonian jet: A model for electrospinning. Phys. Fluids 1994-Present 14, 3912–3926. https://doi.org/10.1063/1.1510664

Fernandez De La Mora, J., Navascues, J., Fernandez, F., Rosell-Llompart, J., 1990. Generation of submicron monodisperse aerosols in electrosprays. J. Aerosol Sci., Proceedings of the 1990 European Aerosol Conference 21, S673–S676. https://doi.org/10.1016/0021-8502(90)90332-R

Finney, J.L., 1970. Random packings and the structure of simple liquids. I. The geometry of random close packing. Proc R Soc Lond A 319, 479–493. https://doi.org/10.1098/rspa.1970.0189

Gañán-Calvo, A.M., Dávila, J., Barrero, A., 1997. Current and droplet size in the electrospraying of liquids. Scaling laws. J. Aerosol Sci. 28, 249–275. https://doi.org/10.1016/S0021-8502(96)00433-8

German, R.M., Suri, P., Park, S.J., 2008. Review: liquid phase sintering. J. Mater. Sci. 44, 1–39. https://doi.org/10.1007/s10853-008-3008-0

Gratson, G.M., Lewis, J.A., 2005. Phase Behavior and Rheological Properties of Polyelectrolyte Inks for Direct-Write Assembly. Langmuir 21, 457–464. https://doi.org/10.1021/la048228d

Greulich, M., Greul, M., Pintat, T., 1995. Fast, functional prototypes via multiphase jet solidification. Rapid Prototyp. J. 1, 20–25.

Griffith, M.L., Halloran, J.W., 1996. Freeform Fabrication of Ceramics via Stereolithography. J. Am. Ceram. Soc. 79, 2601–2608. https://doi.org/10.1111/j.1151-2916.1996.tb09022.x

Gu, D.D., Meiners, W., Wissenbach, K., Poprawe, R., 2012. Laser additive manufacturing of metallic components: materials, processes and mechanisms. Int. Mater. Rev. 57, 133–164. https://doi.org/10.1179/1743280411Y.0000000014

Hales, T., Adams, M., Bauer, G., Dang, T.D., Harrison, J., Hoang, L.T., Kaliszyk, C., Magron, V., Mclaughlin, S., Nguyen, T.T., Nguyen, Q.T., Nipkow, T., Obua, S., Pleso, J., Rute, J., Solovyev, A., Ta, T.H.A., Tran, N.T., Trieu, T.D., Urban, J., Vu, K., Zumkeller, R., 2017. A FORMAL PROOF OF THE KEPLER CONJECTURE. Forum Math. Pi 5. https://doi.org/10.1017/fmp.2017.1

Hamid, Q., Snyder, J., Wang, C., Timmer, M., Hammer, J., Guceri, S., Sun, W., 2011. Fabrication of three-dimensional scaffolds using precision extrusion deposition with an assisted cooling device. Biofabrication 3, 034109. https://doi.org/10.1088/1758-5082/3/3/034109

Hochleitner, G., Jüngst, T., Brown, T.D., Hahn, K., Moseke, C., Jakob, F., Dalton, P.D., Groll, J., 2015. Additive manufacturing of scaffolds with sub-micron filaments via melt electrospinning writing. Biofabrication 7, 035002. https://doi.org/10.1088/1758-5090/7/3/035002

Hon, K.K.B., Li, L., Hutchings, I.M., 2008. Direct writing technology—Advances and developments. CIRP Ann. - Manuf. Technol. 57, 601–620. https://doi.org/10.1016/j.cirp.2008.09.006

Huang, Y., Bu, N., Duan, Y., Pan, Y., Liu, H., Yin, Z., Xiong, Y., 2013. Electrohydrodynamic direct-writing. Nanoscale 5, 12007–12017. https://doi.org/10.1039/C3NR04329K

Huang, Z.-M., Zhang, Y.-Z., Kotaki, M., Ramakrishna, S., 2003. A review on polymer nanofibers by electrospinning and their applications in nanocomposites. Compos. Sci. Technol. 63, 2223–2253. https://doi.org/10.1016/S0266-3538(03)00178-7

Hutmacher, D.W., Dalton, P.D., 2011. Melt Electrospinning. Chem. – Asian J. 6, 44–56. https://doi.org/10.1002/asia.201000436

Jafari, M.A., Han, W., Mohammadi, F., Safari, A., Danforth, S.C., Langrana, N., 2000. A novel system for fused deposition of advanced multiple ceramics. Rapid Prototyp. J. 6, 161–175. https://doi.org/10.1108/13552540010337047

Jaworek, A., Krupa, A., 1999. Jet and drops formation in electrohydrodynamic spraying of liquids. A systematic approach. Exp. Fluids 27, 43–52. https://doi.org/10.1007/s003480050327

Kataoka, T., Kitano, T., Sasahara, M., Nishijima, K., 1978. Viscosity of particle filled polymer melts. Rheol. Acta 17, 149–155. https://doi.org/10.1007/BF01517705

Kim, H.-W., Song, J.-H., Kim, H.-E., 2005. Nanofiber Generation of Gelatin–Hydroxyapatite Biomimetics for Guided Tissue Regeneration. Adv. Funct. Mater. 15, 1988–1994. https://doi.org/10.1002/adfm.200500116

King, B.H., Dimos, D., Yang, P., Morissette, S.L., 1999. Direct-Write Fabrication of Integrated, Multilayer Ceramic Components. J. Electroceramics 3, 173–178. https://doi.org/10.1023/A:1009999227894

Kitano, T., Kataoka, T., Shirota, T., 1981. An empirical equation of the relative viscosity of polymer melts filled with various inorganic fillers. Rheol. Acta 20, 207–209. https://doi.org/10.1007/BF01513064

Kolathodi, M.S., Rao, S.N.H., Natarajan, T.S., Singh, G., 2016. Beaded manganese oxide (Mn2O3) nanofibers: preparation and application for capacitive energy storage. J. Mater. Chem. A. https://doi.org/10.1039/C6TA01948J

Ku, B.K., Kim, S.S., 2002. Electrospray characteristics of highly viscous liquids. J. Aerosol Sci. 33, 1361–1378. https://doi.org/10.1016/S0021-8502(02)00075-7

Lee, H., Kim, J., Jang, Y., Byun, D., 2014. Direct Alignment and Patterning of Silver Nanowires by Electrohydrodynamic Jet Printing. Small 10, 3918–3922. https://doi.org/10.1002/smll.201400936

Lee, J., Lee, S.Y., Jang, J., Jeong, Y.H., Cho, D.-W., 2012. Fabrication of Patterned Nanofibrous Mats Using Direct-Write Electrospinning. Langmuir 28, 7267–7275. https://doi.org/10.1021/la3009249

Lee, J.W., Lee, I.H., Cho, D.-W., 2006. Development of micro-stereolithography technology using metal powder. Microelectron. Eng., Micro- and Nano-Engineering MNE 2005 Proceedings of the 31st International Conference on Micro- and Nano-Engineering 83, 1253–1256. https://doi.org/10.1016/j.mee.2006.01.192

Lewis, J.A., Smay, J.E., Stuecker, J., Cesarano, J., 2006. Direct Ink Writing of Three-Dimensional Ceramic Structures. J. Am. Ceram. Soc. 89, 3599–3609. https://doi.org/10.1111/j.1551-2916.2006.01382.x

LITHOJET™ 210 Etch Resist [WWW Document], 2018. URL http://www.seacole.com/wp-content/uploads/2016/04/LithoJet-210-Datasheet-11-2010.pdf

Lombardi, J.L., Calvert, P., 1999. Extrusion freeforming of Nylon 6 materials. Polymer 40, 1775–1779. https://doi.org/10.1016/S0032-3861(98)00402-9

Marlin firmware [WWW Document], 2018. URL https://github.com/MarlinFirmware/Marlin (accessed 5.1.18).

Medellín-Castillo, H.I., Pedraza Torres, J.E., 2009. Rapid Prototyping and Manufacturing: A Review of Current Technologies 609–621. https://doi.org/10.1115/IMECE2009-11750

Mestel, A.J., 1996. Electrohydrodynamic stability of a highly viscous jet. J. Fluid Mech. 312, 311–326. https://doi.org/10.1017/S0022112096002029

Mora, J.F.D.L., Loscertales, I.G., 1994. The current emitted by highly conducting Taylor cones. J. Fluid Mech. 260, 155–184. https://doi.org/10.1017/S0022112094003472

Morissette, S.L., Lewis, J.A., Cesarano, J., Dimos, D.B., Baer, T., 2000. Solid Freeform Fabrication of Aqueous Alumina–Poly(vinyl alcohol) Gelcasting

Suspensions. J. Am. Ceram. Soc. 83, 2409–2416. https://doi.org/10.1111/j.1151-2916.2000.tb01569.x

Morissette, S.L., Lewis, J.A., Clem, P.G., Cesarano, J., Dimos, D.B., 2001. Direct-Write Fabrication of Pb(Nb,Zr,Ti)O3 Devices: Influence of Paste Rheology on Print Morphology and Component Properties. J. Am. Ceram. Soc. 84, 2462–2468. https://doi.org/10.1111/j.1151-2916.2001.tb01036.x

Nadkarni, S.S., Smay, J.E., 2006. Concentrated Barium Titanate Colloidal Gels Prepared by Bridging Flocculation for Use in Solid Freeform Fabrication. J. Am. Ceram. Soc. 89, 96–103. https://doi.org/10.1111/j.1551-2916.2005.00646.x

Nangrejo, M., Ahmad, Z., Edirisinghe, M., 2010. Generation of ceramic–ceramic layered composite microstructures using electrohydrodynamic co-axial flow. Ceram. Int. 36, 1217–1223. https://doi.org/10.1016/j.ceramint.2010.01.012

Niu, H., Lin, T., Wang, X., 2009. Needleless electrospinning. I. A comparison of cylinder and disk nozzles. J. Appl. Polym. Sci. 114, 3524–3530. https://doi.org/10.1002/app.30891

Pokorny, M., Klemes, J., Zidek, O., Dollinger, C., Ozcebe, G., Singh, S., Vladimir Velebny, Ghaemmaghami, A.M., Wolfova, L., Vrana, N.E., 2017. Electrohydrodynamic printing as a method to micropattern large titanium implant surfaces with photocrosslinkable structures. Biomed. Phys. Eng. Express 3, 015002. https://doi.org/10.1088/2057-1976/3/1/015002

Prasad, T.V., Brown, K.W., Thomas, J.C., 1994. Diffusion coefficients of organics in high density polyethylene (HDPE). Waste Manag. Res. 12, 61–71. https://doi.org/10.1016/S0734-242X(94)90021-3

Ragucci, R., Bellofiore, A., Cavaliere, A., 2004. Polarity Inversion in Electrohydrodynamic Spraying. Combust. Sci. Technol. 176, 889–905. https://doi.org/10.1080/00102200490428512

Rak, Z.S., 2000. Advanced shaping techniques in advanced ceramics. Cfi-Ceram. Forum Int. 77, 6-+.

Reis, N., Ainsley, C., Derby, B., 2005. Ink-jet delivery of particle suspensions by piezoelectric droplet ejectors. J. Appl. Phys. 97, 094903. https://doi.org/10.1063/1.1888026

Repetier-Host [WWW Document], 2018. . Repetier. URL http://www.repetier.com/documentation/repetier-host/ (accessed 8.18.15).

Seerden, K.A.M., Reis, N., Evans, J.R.G., Grant, P.S., Halloran, J.W., Derby, B., 2001. Ink-Jet Printing of Wax-Based Alumina Suspensions. J. Am. Ceram. Soc. 84, 2514–2520. https://doi.org/10.1111/j.1151-2916.2001.tb01045.x

Shin, Y.M., Hohman, M.M., Brenner, M.P., Rutledge, G.C., 2001. Experimental characterization of electrospinning: the electrically forced jet and instabilities. Polymer 42, 09955–09967. https://doi.org/10.1016/S0032-3861(01)00540-7

Shor, L., Darling, A., Starly, B., Sun, W., Guceri, S., 2005. Precision extruding deposition of composite polycaprolactone/hydroxyapatite scaffolds for bone tissue engineering, in: Bioengineering Conference, 2005. Proceedings of the IEEE 31st Annual Northeast. Presented at the Bioengineering Conference, 2005. Proceedings of the IEEE 31st Annual Northeast, pp. 172–173. https://doi.org/10.1109/NEBC.2005.1431978

Smay, J. e., Gratson, G. m., Shepherd, R. f., Cesarano, J., Lewis, J. a., 2002. Directed Colloidal Assembly of 3D Periodic Structures. Adv. Mater. 14, 1279–1283. https://doi.org/10.1002/1521-4095(20020916)14:18<1279::AID-ADMA1279>3.0.CO;2-A

Son, W.K., Cho, D., Park, W.H., 2006. Direct electrospinning of ultrafine titania fibres in the absence of polymer additives and formation of pure anatase titania fibres at low temperature. Nanotechnology 17, 439. https://doi.org/10.1088/0957-4484/17/2/016

Spivak, A.F., Dzenis, Y.A., 1998. Asymptotic decay of radius of a weakly conductive viscous jet in an external electric field. Appl. Phys. Lett. 73, 3067–3069. https://doi.org/10.1063/1.122674

Sun, D., Chang, C., Li, S., Lin, L., 2006. Near-Field Electrospinning. Nano Lett. 6, 839–842. https://doi.org/10.1021/nl0602701

Taylor, G., 1964. Disintegration of Water Drops in an Electric Field. Proc. R. Soc. Lond. Math. Phys. Eng. Sci. 280, 383–397. https://doi.org/10.1098/rspa.1964.0151

Technical basis for a unified classification system for advanced ceramics (No. 15), 1993. , Technical Working Area 14. VAMAS.

Thermal-FluidsPedia | Natural convection on cylinders and spheres [WWW Document], 2018. URL https://www.thermalfluidscentral.org/encyclopedia/index.php/Natural_convection_on_cylinders_and_spheres (accessed 4.11.18).

Theron, A., Zussman, E., Yarin, A.L., 2001. Electrostatic field-assisted alignment of electrospun nanofibres. Nanotechnology 12, 384. https://doi.org/10.1088/0957-4484/12/3/329

Travitzky, N., Bonet, A., Dermeik, B., Fey, T., Filbert-Demut, I., Schlier, L., Schlordt, T., Greil, P., 2014. Additive Manufacturing of Ceramic-Based Materials. Adv. Eng. Mater. 16, 729–754. https://doi.org/10.1002/adem.201400097

Vaezi, M., Seitz, H., Yang, S., 2013. A review on 3D micro-additive manufacturing technologies. Int. J. Adv. Manuf. Technol. 67, 1721–1754. https://doi.org/10.1007/s00170-012-4605-2

Viscosity of Paraffin Wax – viscosity table and viscosity chart :: Anton Paar Wiki [WWW Document], n.d. . Anton Paar. URL https://wiki.anton-paar.com/en/paraffin-wax/ (accessed 7.14.19).

Wang, D.Z., Jayasinghe, S.N., Edirisinghe, M.J., 2005. Instrument for electrohydrodynamic print-patterning three-dimensional complex structures. Rev. Sci. Instrum. 76, 075105. https://doi.org/10.1063/1.1942531

Wei, C., Dong, J., 2013. Direct fabrication of high-resolution three-dimensional polymeric scaffolds using electrohydrodynamic hot jet plotting. J. Micromechanics Microengineering 23, 025017. https://doi.org/10.1088/0960-1317/23/2/025017

Williams, C.B., Mistree, F., Rosen, D.W., 2011. A Functional Classification Framework for the Conceptual Design of Additive Manufacturing Technologies. J. Mech. Des. 133, 121002–121002. https://doi.org/10.1115/1.4005231

Xue, L.A., Chen, I.-W., 1991. Low-Temperature Sintering of Alumina with Liquid-Forming Additives. J. Am. Ceram. Soc. 74, 2011–2013. https://doi.org/10.1111/j.1151-2916.1991.tb07825.x

Yalamaç, E., Trapani, A., Akkurt, S., 2014. Sintering and microstructural investigation of gamma–alpha alumina powders. Eng. Sci. Technol. Int. J. 17, 2–7. https://doi.org/10.1016/j.jestch.2014.02.001

Zeleny, J., 1914. The Electrical Discharge from Liquid Points, and a Hydrostatic Method of Measuring the Electric Intensity at Their Surfaces. Phys. Rev. 3, 69–91. https://doi.org/10.1103/PhysRev.3.69

Zhao, X., Evans, J.R.G., Edirisinghe, M.J., Song, J.H., 2002. Ink-jet printing of ceramic pillar arrays. J. Mater. Sci. 37, 1987–1992. https://doi.org/10.1023/A:1015247131016

Zhou, H., Green, T.B., Joo, Y.L., 2006. The thermal effects on electrospinning of polylactic acid melts. Polymer 47, 7497–7505. https://doi.org/10.1016/j.polymer.2006.08.042

11 APPENDICES

APPENDIX A – MECHANICAL DRAWINGS OF SYRINGE PUMP

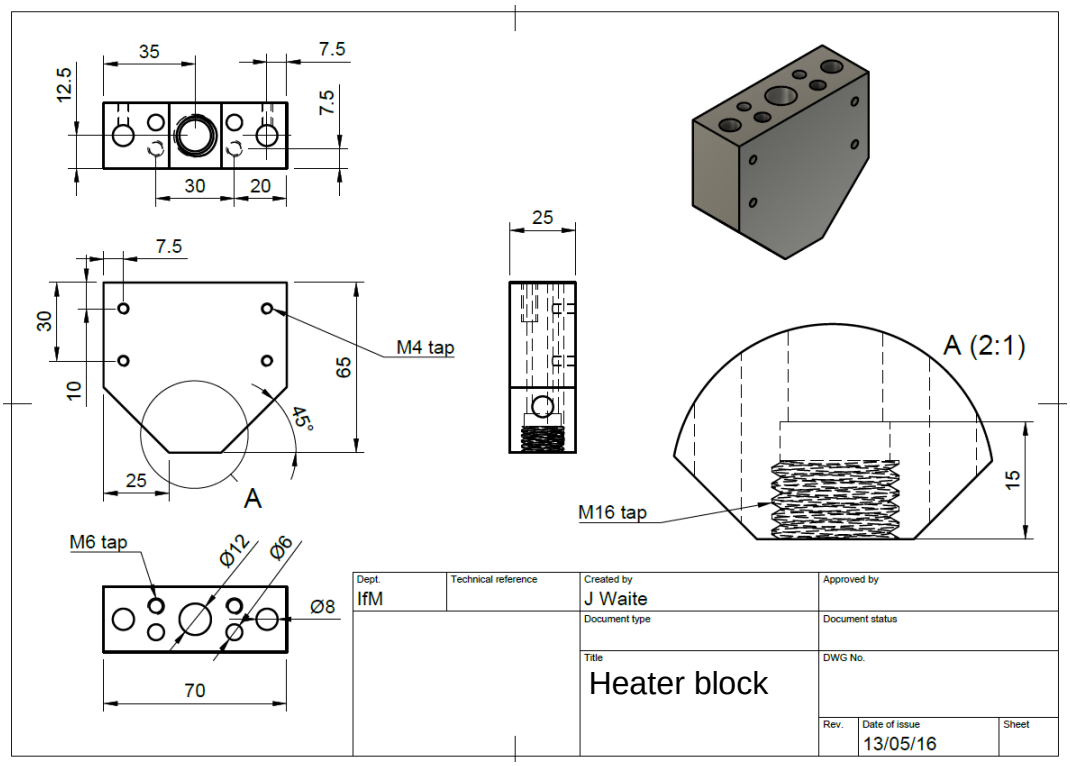

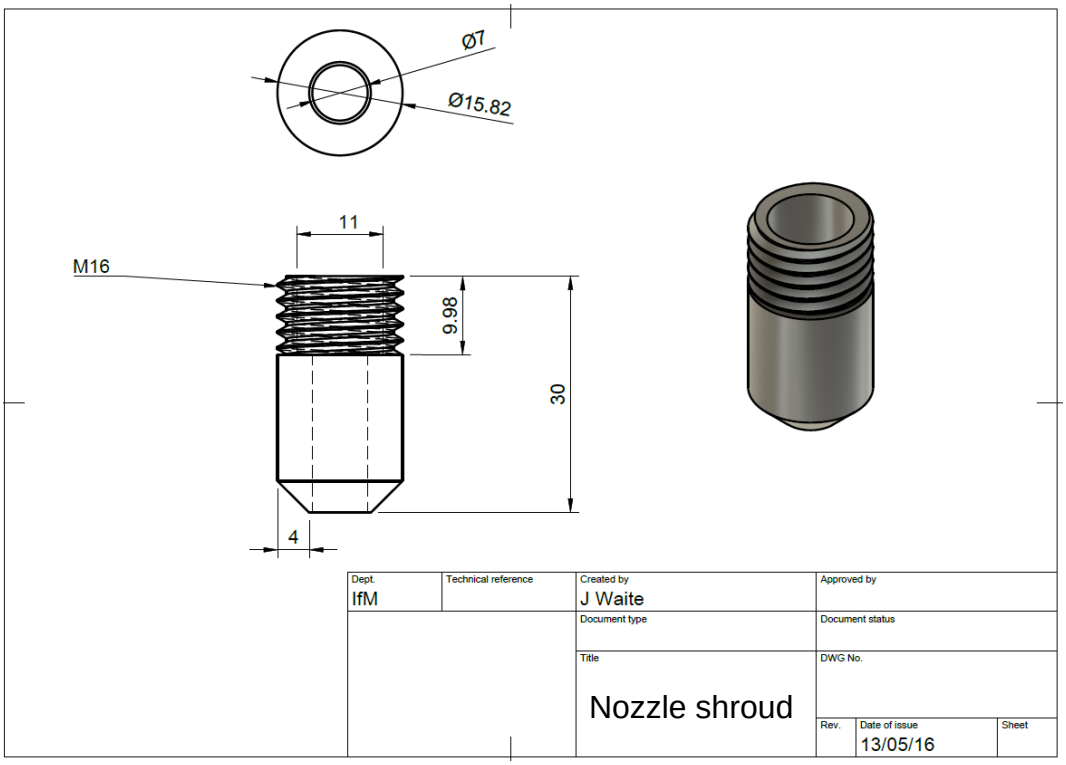
Ø7
Ø15.82
11
M16
9.98
30
4
Dept.
IfM
Technical reference
Created by
J Waite
Approved by
Document type
Document status
Title
Nozzle shroud
DWG No.
Rev.
Date of issue
13/05/16
Sheet

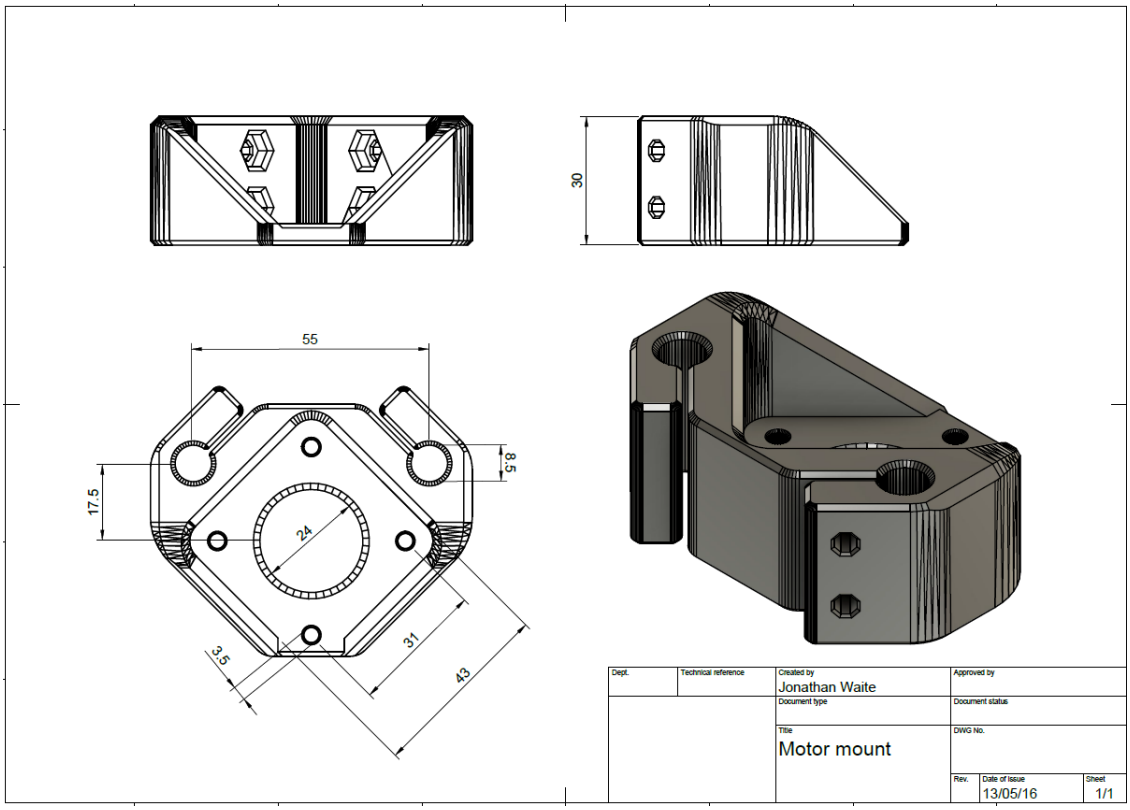
30
55
8.5
17.5
24
3.5
31
43
Dept.
Technical reference
Created by
Jonathan Waite
Approved by
Document type
Document status
Title
Motor mount
DWG No.
Rev.
Date of issue
13/05/16
Sheet
1/1

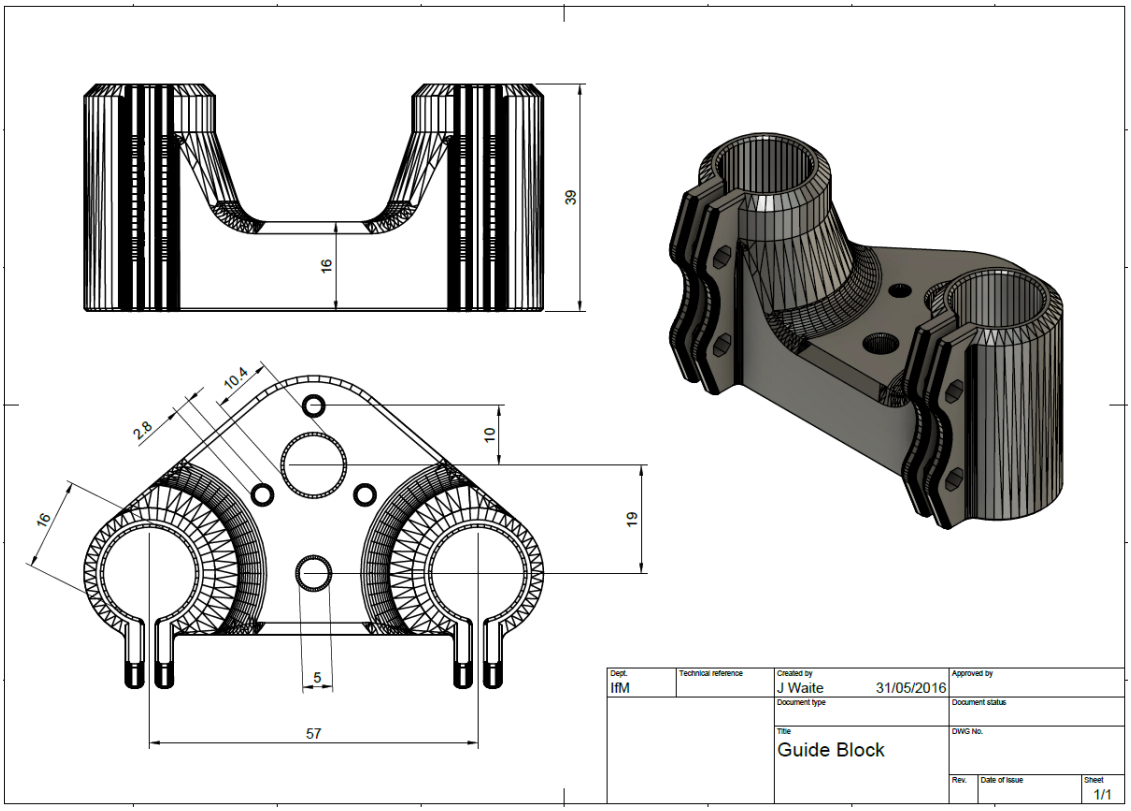

Dept.	Technical reference	Created by	Approved by
IfM		J Waite 31/05/2016	
		Document type	Document status
		Title: Guide Block	DWG No.
			Rev. / Date of issue / Sheet: 1/1

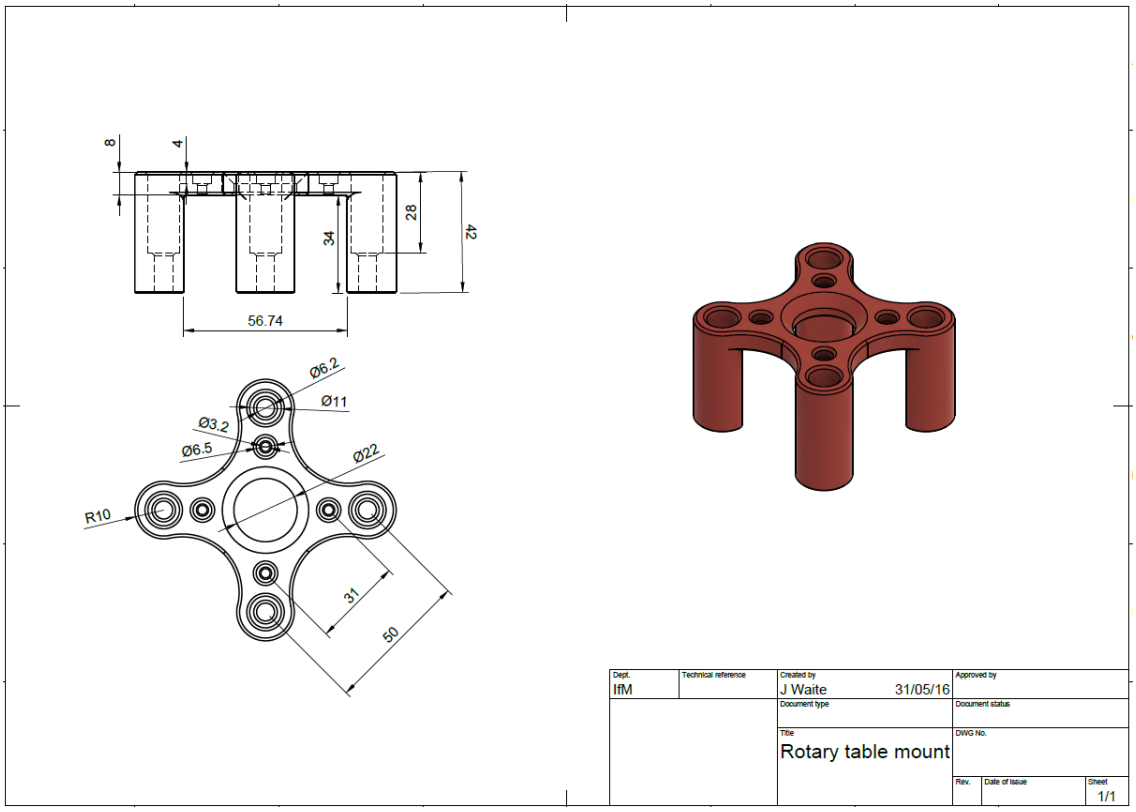

Dept.	Technical reference	Created by	Approved by
IfM		J Waite 31/05/16	
		Document type	Document status
		Title: Rotary table mount	DWG No.
			Rev. / Date of issue / Sheet: 1/1

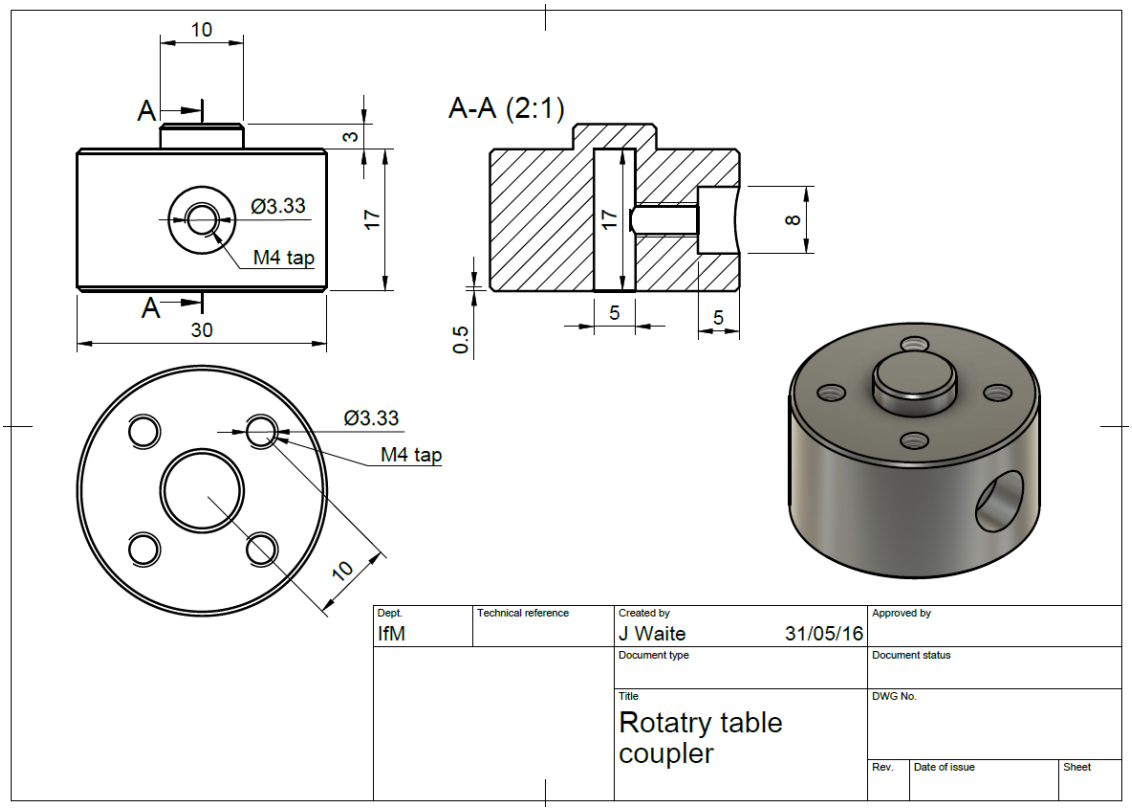
10
A
3
17
Ø3.33
M4 tap
A
30
A-A (2:1)
17
8
0.5
5
5
Ø3.33
M4 tap
10
Dept.
IfM
Technical reference
Created by
J Waite
31/05/16
Approved by
Document type
Document status
Title
Rotatry table coupler
DWG No.
Rev.
Date of issue
Sheet

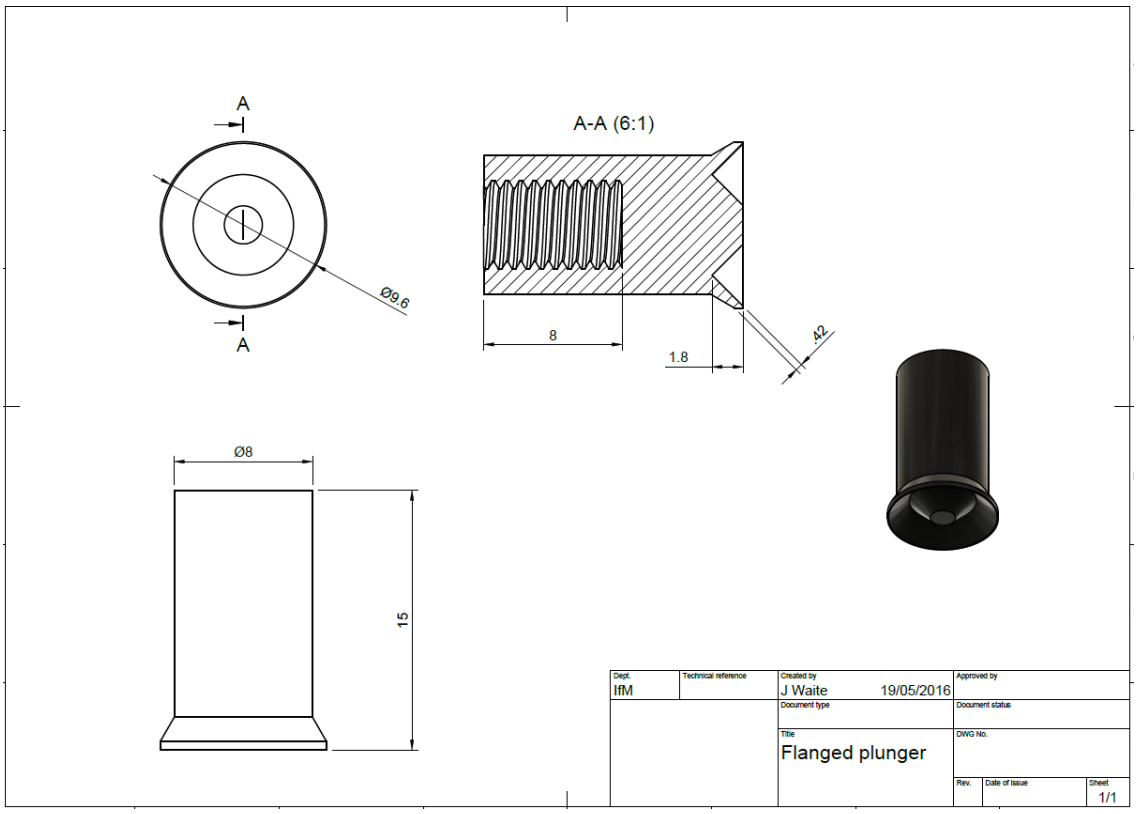
A
Ø9.6
A
A-A (6:1)
8
1.8
Ø2
Ø8
15
Dept.
IfM
Technical reference
Created by
J Waite
19/05/2016
Approved by
Document type
Document status
Title
Flanged plunger
DWG No.
Rev.
Date of issue
Sheet
1/1

APPENDIX B – EQUIPMENT WIRING DIAGRAMS

Motor control for syringe pump and rotary table:

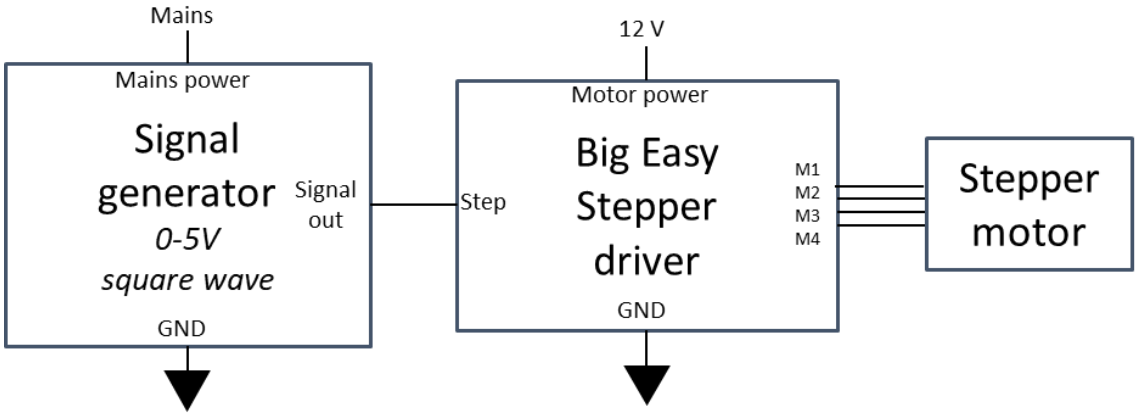

Heater control for syringe pump:

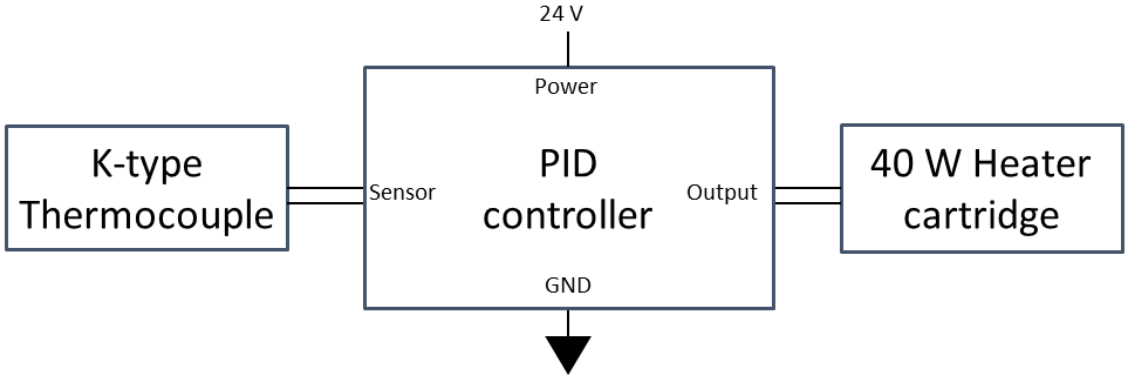

Motion control system:

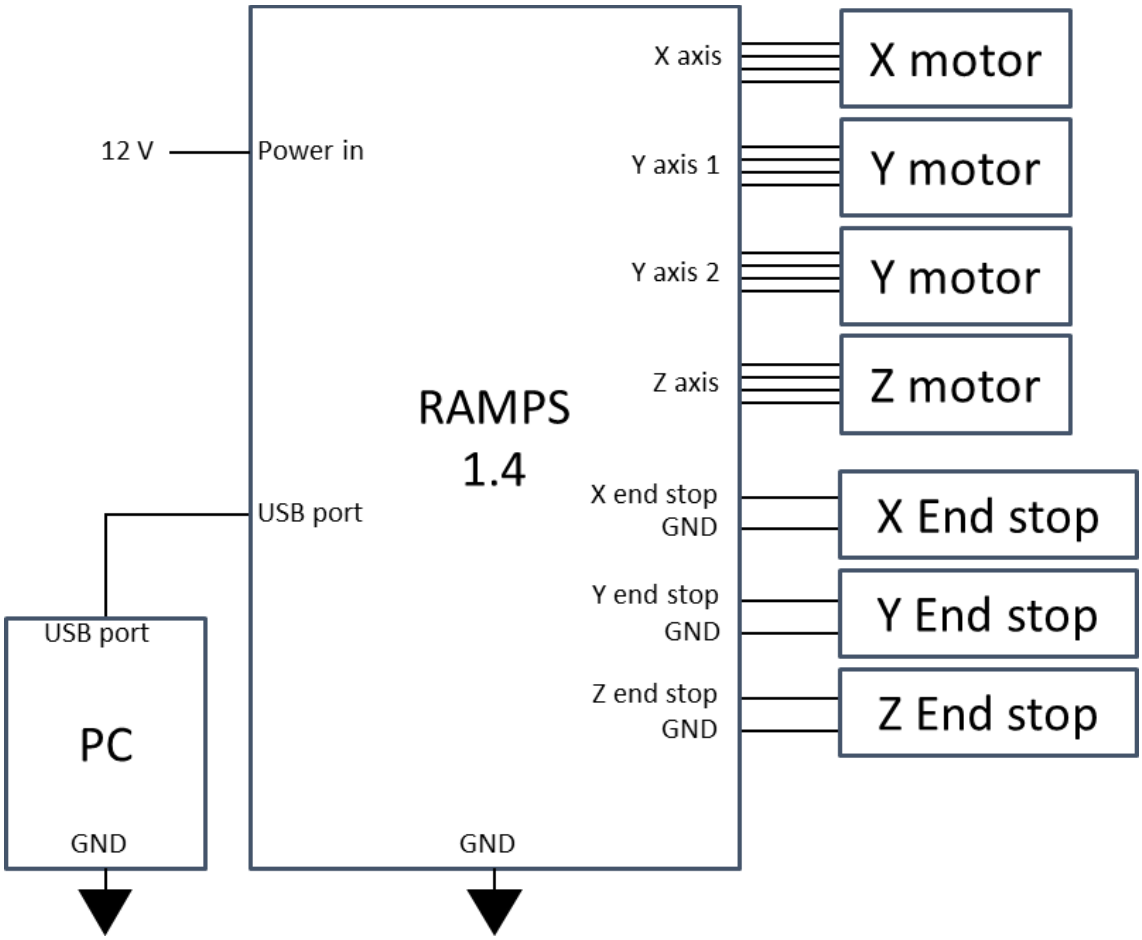

APPENDIX C – ELECTROSTATICS SIMULATION MATLAB CODE

```
% This script is written and read by pdetool and should NOT be
edited.
% There are two recommended alternatives:
% 1) Export the required variables from pdetool and create a
MATLAB script to perform operations on these.
% 2) Define the problem completely using a MATLAB script. See
http://www.mathworks.com/help/pde/examples/index.html for
examples of this approach.
function pdemodel
[pde_fig,ax]=pdeinit;
pdetool('appl_cb',5);
set(ax,'DataAspectRatio',[1 0.95121951219512191 1]);
set(ax,'PlotBoxAspectRatio',[4.0999999999999996
2.7333333333333329 1]);
set(ax,'XLim',[-4.0999999999999996 4.0999999999999996]);
set(ax,'YLim',[-0.10000000000000001 5.0999999999999996]);
set(ax,'XTickMode','auto');
set(ax,'YTickMode','auto');
% Geometry description:
pderect([-0.20000000000000001 0.20000000000000001 7 3],'R2');
pderect([-4 4 5 0],'R1');
pdepoly([ -4, -0.5, -0.5,],[ 6, 6, 3,], 'P1');
pdepoly([ 0.5, 0.5, 4,],[ 6, 3, 6,], 'P2');
pderect([-5 -1 8 4],'R3');
pderect([5 1 8 4],'R4');
set(findobj(get(pde_fig,'Children'),'Tag','PDEEval'),'String','
R1-(R2+R3+R4)')
% Boundary conditions:
pdetool('changemode',0)
pdesetbd(20,'dir',1,'1','0')
pdesetbd(19,'dir',1,'1','0')
pdesetbd(18,'dir',1,'1','0')
pdesetbd(17,'dir',1,'1','0')
pdesetbd(16,'dir',1,'1','0')
pdesetbd(15,'dir',1,'1','0')
pdesetbd(10,'neu',1,'0','0')
pdesetbd(9,'neu',1,'0','0')
pdesetbd(8,'neu',1,'0','0')
pdesetbd(7,'neu',1,'0','0')
pdesetbd(6,'neu',1,'0','0')
pdesetbd(5,'neu',1,'0','0')
pdesetbd(4,'dir',1,'1','0')
pdesetbd(3,'dir',1,'1','0')
pdesetbd(2,'dir',1,'1','5')
pdesetbd(1,'dir',1,'1','0')
```

```
% Mesh generation:
setappdata(pde_fig,'Hgrad',1.3);
setappdata(pde_fig,'refinemethod','regular');
setappdata(pde_fig,'jiggle',char('on','mean',''));
setappdata(pde_fig,'MesherVersion','preR2013a');
pdetool('initmesh')
pdetool('refine')
pdetool('refine')
% PDE coefficients:
pdeseteq(1,'1.0','0.0','0','1.0','0:10','0.0','0.0','[0 100]')
setappdata(pde_fig,'currparam',['1.0';'0  '])
% Solve parameters:
setappdata(pde_fig,'solveparam',char('0','7056','10','pdeadwors
t','0.5','longest','0','1E-4','','fixed','Inf'))
% Plotflags and user data strings:
setappdata(pde_fig,'plotflags',[2 1 1 1 1 1 3 1 0 0 0 1 1 0 0 1
0 1]);
setappdata(pde_fig,'colstring','');
setappdata(pde_fig,'arrowstring','');
setappdata(pde_fig,'deformstring','');
setappdata(pde_fig,'heightstring','');
% Solve PDE:
pdetool('solve')
```

APPENDIX D – ELECTRO-JET IMAGE ANALYSIS MATLAB CODE

```
%Calculate minimum width and deposit height for images of EHD
jets
groupSize = 3;
%Default values - not guaranteed to run
scale = 1;
startHeight = 1;
clearHeight = 100;
finishHeight = 2000;
%widthThresh = 0.6; %replaced with auto-scaling in image loop
slopeSample = 75; %+-rows to average for jet angle correction
%Get parameters from file in image folder
fileID = fopen('scale.txt','r');
if fileID>=0    %does the file exist?
    numbers = fscanf(fileID,'%f'); %file should contain only
numbers on separate lines
    if ~isempty(numbers)    %file can be blank
        scale = numbers(1); %px/mm
        if length(numbers)>1
            startHeight = numbers(2); %ignore top of image to
speed processing
            if length(numbers)>2
                clearHeight = numbers(3); %look for deposit
below this height
                if length(numbers)>3
                finishHeight = numbers(4); %remove reflected
jet, but not deposit
                end
            end
        end
    end
    fclose(fileID);
end
pictures = ls('*.jpg'); %get list of images
%Predefine arrays
N = size(pictures,1); %number of images
widths = zeros(N,finishHeight-startHeight); %record full
profile of jet
minWidths = zeros(N,1);
aveMinWidths = zeros(N/groupSize,1);
lowMinWidths = aveMinWidths;
highMinWidths = aveMinWidths;
heights = minWidths;
aveHeights = aveMinWidths;
lowHeights = aveHeights;
highHeights = aveHeights;
```

```
firstEdge = zeros(finishHeight-startHeight,1);
lastEdge = firstEdge;
%Image processing - extract data from images
for j = 1:N
    %import current image
    fullImage = imread(pictures(j,:));
    workingImage = fullImage(startHeight+1:finishHeight,:,:);
%trim to area of interest
    %simplify image
    level = graythresh(workingImage); %Otsu's method
    BWImage = -1*(im2bw(workingImage, level)-1); %reduce to
two-tone and invert so jet is white
    %reduce to vector of widths
    widths(j,:) = sum(BWImage,2)'/scale;
    %extract deposit height
    widthsCut=widths(j,clearHeight-startHeight:finishHeight-
startHeight); %ensure nozzle is out of image
    widthThresh = max(widthsCut)/2; %crude scalable threshold
    widthsCut=max(widthsCut,widthThresh)-widthThresh; %make all
values outside deposit zero
    top = find(widthsCut,1);    %get index of leading edge
    bottom = find(widthsCut,1,'last');  %get index of trailing
edge
    heights(j) = (bottom-top)/(2*scale);    %account for
reflection
    %Slope and broken jet correction
    [tempMin, minRow] = min(widths(j,1:bottom)); %find
narrowest horizontal
    if tempMin>0    %not broken
        for row=1:finishHeight-startHeight
            firstEdge(row) = find(BWImage(row,:),1); %find
leftmost edge of jet
            lastEdge(row) = find(BWImage(row,:),1,'last');
%find rightmost edge of jet
        end
        leftSlope = mean(gradient(firstEdge(minRow-
slopeSample:minRow+slopeSample))); %calculate average gradient
around area of interest
        rightSlope = mean(gradient(lastEdge(minRow-
slopeSample:minRow))); %only look above to avoid curvature due
to deposit
        slope =  mean([leftSlope,rightSlope]);
        minWidths(j) = tempMin*cosd(atand(slope)); %estimate
perpendicular width
    else    %jet broken
        minWidths(j) = 0;
    end
end
%Data averaging with checks
```

```
for k = 1:N/groupSize %put images under the same conditions
together
    %Width data
    wValues = minWidths(groupSize*(k-1)+1:groupSize*k); %data
of interest
    goodData = find(wValues);   %get indeces of non-zero data
    errs = groupSize-size(goodData,1); %check how many broken
jets
    if errs <= 1 %assume jet is stable
        aveMinWidths(k) = mean(wValues(goodData)); %only
average non-zero values
    else    %jet unstable, set zero
        aveMinWidths(k) = 0;
    end
    lowMinWidths(k) = min(wValues);
    highMinWidths(k) = max(wValues);
    %Height data
    hValues = heights(groupSize*(k-1)+1:groupSize*k); %data of
interest
    aveHeights(k) = mean(hValues);  %there is always a deposit,
broken jets are already highlighted in width data
    lowHeights(k) = min(hValues);
    highHeights(k) = max(hValues);
end
%Write summary data
csvwrite('averages.csv',vertcat(lowMinWidths',aveMinWidths',hig
hMinWidths',lowHeights',aveHeights',highHeights'));
%Write full jet profiles
csvwrite('widths.csv',vertcat(minWidths',heights',widths'));
```

APPENDIX E - ELECTRO-JET IMAGE ANALYSIS VERIFICATION

Images A1-A7, left to right:

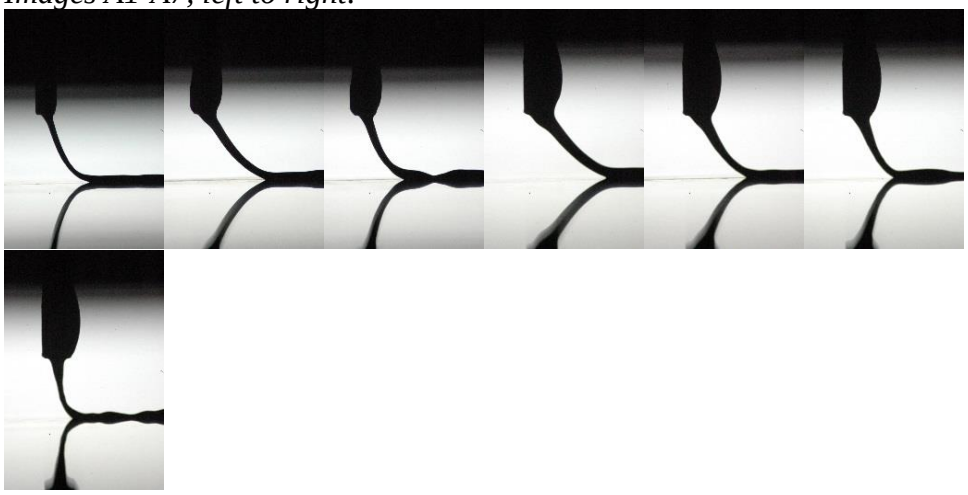

Images B1-B3:

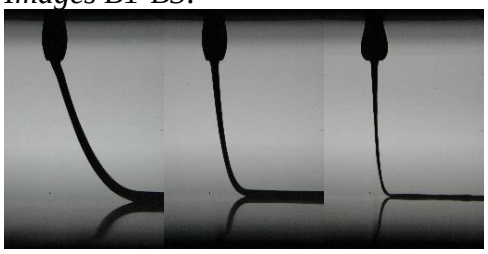

Images C1-C3, D1 and D2:

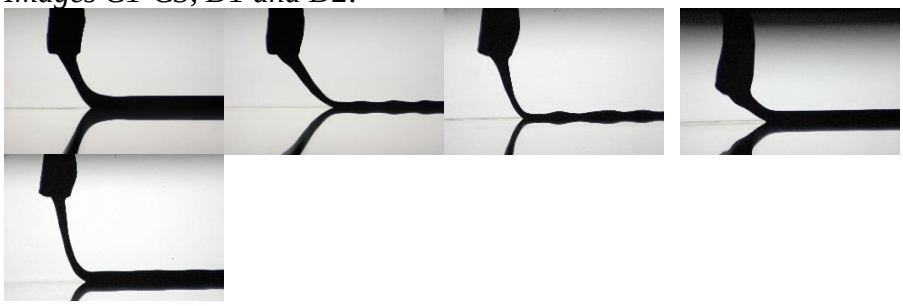

Difference between script measurement and manual measurement for each image:

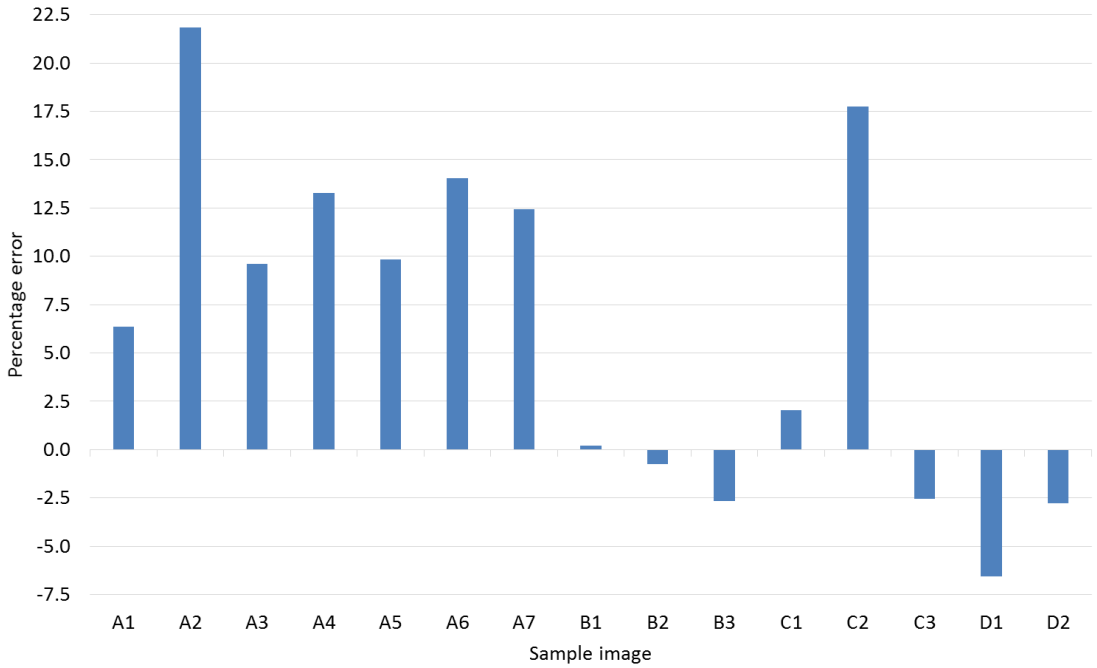
22.5
20.0
17.5
15.0
12.5
10.0
7.5
5.0
2.5
0.0
-2.5
-5.0
-7.5
Percentage error
A1
A2
A3
A4
A5
A6
A7
B1
B2
B3
C1
C2
C3
D1
D2
Sample image

APPENDIX F – G-CODE GENERATION MATLAB CODE

Lattice shown in Figure 7.1:

```
fileID = fopen('BiDirStrip.txt','w');
lineFormat = 'G1 X%3.2f Y%3.2f E%3.5f\r\n';
feedrate = 20;
Nx = 3;
Ny = 4;
x = [0.6,0.5,0.4,0.3];
Ke = ((100/1000)/9.6)^2;
gapx = 1;
gapy = 1;
Layer2Extra = 4;
y = (Ny*2-1)*gapy+2*Layer2Extra;
X = sum(x)*2*Nx+gapx*(length(x)-1)+2*Layer2Extra;
space = 1;
fprintf(fileID,';Feedrate = %3.1f mm/s\r\n',feedrate);
fprintf(fileID,';Extrusion multiplier = %1.4g
um/mm\r\n',Ke*1000);
fprintf(fileID,'G91\r\nG1 E0.1 F50\r\nG1 X%3.1f Y%3.1f
F5000\r\nG1 F%-
5.0f\r\n\r\n',Layer2Extra+space,space,feedrate*60);
%Vertical lines
for n = 1:length(x)
    fprintf(fileID,';Steps of %1.2f mm\r\n',x(n));
    for k=1:Nx
        pos = [0,  y;
               x(n),  0;
               0,  -y;
               x(n),  0];
        for i = 1:length(pos)
fprintf(fileID,lineFormat,pos(i,1),pos(i,2),Ke*norm(pos(i,:)));
        end
    end
    fprintf(fileID,'G1 X%3.1f\r\n\r\n',gapx);
end
fprintf(fileID,'G1 X%3.1f Y%3.1f\r\n',Layer2Extra-
gapx,Layer2Extra-gapy);
fprintf(fileID,'\r\n;Layer Two\r\n');
%Horizontal lines
for j = 1:Ny
    pos = [0,  gapy;
          -X, 0;
           0,  gapy;
           X,  0];
    for i = 1:length(pos)

fprintf(fileID,lineFormat,pos(i,1),pos(i,2),Ke*norm(pos(i,:)));
```

```
    end
end
fprintf(fileID,'G1 X%3.1f F5000\r\nG1 Y-%3.1f F5000\r\nG1 E-0.2
F200\r\n',space,(2*Ny-1)*gapy+Layer2Extra+space);
fprintf(fileID,'G1 X-%3.1f
F5000\r\nG90\r\n',2*(space+Layer2Extra)+2*Nx*sum(x)+gapx*(lengt
h(x)-1));
if fileID>=3
    fclose(fileID);
end
```

Angled crossing pattern described in Figure 7.2:

```
fileID = fopen('Overlaps.txt','w');
lineFormat = 'G1 X%3.2f Y%3.2f E%3.5f\r\n';
feedrate = 20;
N = 3;
angles = [20,15,10,7.5,5];
y = 15;
x = y.*tand(angles)/2;
Ke = ((100/1000)/9.6)^2;
gap = 0.5;
space = 1;
fprintf(fileID,';Feedrate = %3.1f mm/s\r\n',feedrate);
fprintf(fileID,';Extrusion multiplier = %1.4g
um/mm\r\n',Ke*1000);
fprintf(fileID,'G91\r\nG1 E0.1 F50\r\nG1 X%3.1f Y%3.1f
F5000\r\nG1 F%-5.0f\r\n\r\n',space,space,feedrate*60);
for n = 1:length(x)
    fprintf(fileID,';Steps of %1.2f mm\r\n',x(n));
    fprintf(fileID,';Angle of %1.3f deg\r\n',atand(2*x(n)/y));
    for k=1:N
        pos = [x(n),   0;
               0,      y;
               -x(n),  0;
               2*x(n),-y;
               gap,    0];
        for i = 1:length(pos)
fprintf(fileID,lineFormat,pos(i,1),pos(i,2),Ke*norm(pos(i,:)));
        end
    end
    fprintf(fileID,'G1 X%3.1f\r\n\r\n',space);
end
fprintf(fileID,'G1 Y-%3.1f F5000\r\nG1 E-0.2 F200\r\n',space);
fprintf(fileID,'G1 X-%3.1f
F5000\r\nG90\r\n',2*sum(x)*N+gap*N*length(x)+space*(length(x)+1
));
if fileID>=3
    fclose(fileID);
```

```
end
```

Hollow cylinder shown in Figure 7.8:

```
fileID = fopen('Circle.txt','w');
lineFormat = 'G1 X%3.3f Y%3.3f E%3.5f\r\n';
feedrate = 20;
N = 30;
layers = 10;
zshift = 0.1;
R = 0.5;
space = 1;
theta = 360/N;
Ke = ((100/1000)/9.6)^2;
fprintf(fileID,';Feedrate = %3.1f mm/s\r\n',feedrate);
fprintf(fileID,';Extrusion multiplier = %1.4g
um/mm\r\n',Ke*1000);
fprintf(fileID,'G91\r\nG1 E0.1 F50\r\nG1 X%3.2f Y%3.2f
F5000\r\nG1 F%-5.0f\r\n\r\n',R+space,space,feedrate*60);
fprintf(fileID,';Diameter = %2.1f mm\r\n',R*2);
for n = 1:layers
    fprintf(fileID,';Layer %2d\r\n',n);
    for k=1:N
        pos = [R*(sind(k*theta)-sind((k-1)*theta))
               R*(1-cosd(k*theta)-(1-cosd((k-1)*theta)))];
        fprintf(fileID,'G1 X%3.3f Y%3.3f Z%3.5f
E%3.5f\r\n',pos(1),pos(2),zshift/N,Ke*norm(pos(:)));
    end
end
fprintf(fileID,'G1 Y-%3.2f F5000\r\nG1 E-0.2 F200\r\n',space);
fprintf(fileID,'G1 X-%3.2f F5000\r\n',R+space);
fprintf(fileID,'G1 Z-%3.5f F1000\r\nG90\r\n',zshift*layers);
if fileID>=3
    fclose(fileID);
end
```